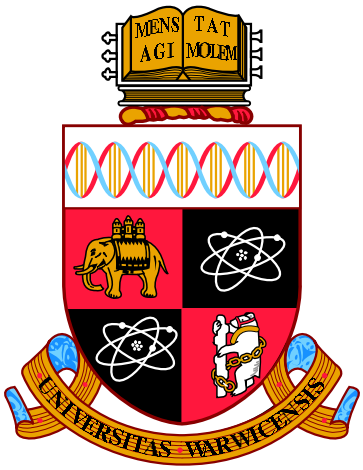

Electronic Structure Studies of Exotic Phenomena Using Magnetic Compton Scattering

by

David Alexander Kersh

Thesis

Submitted to the University of Warwick

for the degree of

Doctor of Philosophy

Department of Physics

January 2016

THE UNIVERSITY OF WARWICK

Contents

List of Figures

List of Tables

Abbreviations

AC Auto correlation

AFM Antiferromagnetic

AFQ Antiferroquadropolar

AMF Around Mean Field

AMPW Asymmetric Multipole Wiggler

BL08w The beamline used at SPring-8

BZ Brillouin Zone

CCD Charge-coupled Device

CPA Coherent Potential Approximation

DDCSCS Doubly Differential Compton Scattering Cross Section

DFT Density Functional Theory

DOS Density of States

DSP Degree of Spin Polarisation

DZ Double Zeta

EDX Energy Dispersive X-ray Spectroscopy

EMD Electron Momentum Density

EMPW Elliptical Multipole Wiggler

EOS Equation of State

ESRF European Synchrotron Radiation Facility

FP Full Potential

FSM Fixed Spin Moment

FT Fourier Transform

FWHM Full Width Half Maximum

GAMESS General Atomic and Molecular Electronic Structure System

GGA Generalised Gradient Approximation

GPIB General Purpose Interface Bus

HT Hankel Transformation

IBZ Irreducible Brillouin Zone

ID Insertion Device

KN Klein-Nishina

KS Kohn-Sham

LAPW Linearised Augmented Planewave

LCAO Linear Combination of Atomic Orbitals

LDA Local Density Approximation

linac Linear Accelerator

LSDA Local Spin Density Approximation

MCA Multi Channel Analyser

MCP Magnetic Compton Profile

MCS Magnetic Compton Scattering

NMR Nuclear Magnetic Resonance

PCAR Point Contact Andreev Reflection

PND Polarised Neutron Diffraction

PSU Power Supply Unit

RHF Relativistic Hartree-Fock

RKKY Ruderman-Kittel-Kasuya-Yosida

SCF Self Consistent Field

SEM Scanning Electron Microscopy

SOC Spin Orbit Coupling

SPring-8 Super Photon Ring 8 GeV

SPR-KKR Spin Polarised Relativistic Korringa-Kohn-Rostoker

SPR-LMTO Spin Polarised Relativistic Linear Muffin Tin Orbital

SQuID Superconducting Quantum Interference Device

SR Synchrotron Radiation

TZV Triple Zeta Valence

UV Ultra Violet

VSM Vibrating Sample Magnetometer

VTI Variable Temperature Insert

WTBS Well-Tempered Gaussian Basis Set

XC Exchange Correlation

XMCD X-ray Magnetic Circular Dichroism

XRD X-ray Diffraction

Acknowledgements

It is with a deep appreciation that I first thank my supervisor, Dr. Jon Duffy. Without his guidance, none of this would have been possible. Thanks to his expertise and enthusiasm for physics, the person I was at the start of this project is very different to the person I've become at the end. I'd like to think for the better.

In addition, I would like to thank our fellow Compton scatterers, Dr. Sean Giblin, Dr. Jon Taylor and Prof. Steve Dugdale. Their expertise, knowledge and cynicism was invaluable to my scientific pursuits. Additional thanks goes to Dr. David Ernsting, Dr. David Billington and Tom Millichamp, who have guided me through the world of DFT and kept me company during our various *cultural* escapades.

Thanks needs to go to Dr. Martin Lees and Dr. Oleg Petrenko. Without their patience, I would surely be banned from using any of the equipment in the ground floor of the Physics building. Mo Saghir and Joel Barker also require thanks for their help with my magnetometry work.

Thanks needs to be extended to Dr. Tom Hase for his guidance, and giving me the numerous teaching opportunities he provided. Were it not for him, I would surely be a grossly inferior educator. In addition, I would like to thank Dr. Gavin Bell for introducing me to the vibrant world of ale, dodgy curries and early progressive rock music.

I would like to thank Ally Caldecote. She has been a constant source of motivation for me and has been invaluable to me as a friend and as an educator.

I would like to give my love and thanks to my family. Their unconditional support has been unparalleled, to which I owe them greatly.

Finally, I would like to thank all my friends. Thanks for letting me hang around with you and giving me a floor to sleep on.

Declarations

This thesis details my own independent research, except where explicitly acknowledged in the text. It has been submitted to the University of Warwick in support of my application for the degree of Doctor of Philosophy. It has not been submitted to any other institution. All work took place under the supervision of Dr. J. A. Duffy and Dr. T. P. A. Hase between October 2011 and October 2015.

Published Work

- D. Billington, D. Ernsting, T. E. Millichamp, C. Lester, S. B. Dugdale, **D. A. Kersh**, J. A. Duffy, S. R. Giblin, J. W. Taylor, P. Manuel, D. D. Khalyavin and H. Takatsu, *Magnetic Frustration, Short-range Correlations and the Role of the Paramagnetic Fermi Surface of* $PdCrO_2$, Scientific Reports, 2015, **5**, 12428.

Abstract

The presented thesis investigates the spin densities of three exotic magnetic materials: Co_2MnSi, a proposed *half-metallic* material which has gathered much interest in recent years due to the very high spin polarisation measured in thin films. CeB_6, a *Kondo* material with a very complex phase diagram where the nature of the origin of the magnetism remains controversial and finally $Ca_3Co_2O_6$, a complicated low-dimensional system where the electronic structure of the magnetic sites is poorly studied and controversial. These studies would not be possible were it not for the improved statistical quality and greatly enhanced experimental capacity, achieved by upgrading the experimental setup on the BL08W beamline at the SPring-8 synchrotron.

The primary technique used to investigate the magnetic properties of these materials was *Magnetic Compton Scattering*. This technique directly probes the spin-dependent electron momentum density of a material, enabling an isolated measurement of its spin moment. In addition, through comparison with theoretical models, the technique can be used to gain insight into the electronic structure of the material, and determine which bands contribute to the magnetism in the system. These theoretical models were calculated using *ab initio* methods such as Density Functional Theory (DFT). In addition to magnetic Compton scattering, a range of complementary experimental techniques have been used to provide further useful analysis for these materials. This includes techniques such as SQuID magnetometry, Energy Dispersive X-ray Spectroscopy, Powder X-ray Diffraction and Laue Diffraction.

The upgrade to the BL08W beamline at the SPring-8 synchrotron in Hyōgo, Japan was prompted by technical issues which were present at the ID15 beamline at ESRF in Grenoble, France. Modelling the stray field effects proved the presence of such a powerful magnet would not impact the electron beam during operation, ensuring the magnet could be used on the beamline without affecting other experiments. Upgrading the 3 T cryostat at SPring-8 to the 9 T Oxford Instruments *Spectromag* magnet improved the experimental capacity - the range of physical phenomenon which can be measured, considerably.

The study of Co_2MnSi marks one of the first *bulk* investigations of the potential half-metal. A single crystal was measured along the [100], [110] and [111] directions using magnetic Compton scattering. Modelling of the system was performed using the ELK DFT code which calculated the system to be a half-metal with a 5 μ_B spin moment. Comparing the experimental and theoretical profiles yielded good agreement, with the theoretical profiles very accurately modelling the broadness and tails of the MCPs but with deviations at low momentum. Comparing the anisotropies found very good agreement between the experimental and theoretical profiles. Characterisation of the material was performed using SQuID magnetometry, Energy Dispersive X-ray Spectroscopy and

Powder X-ray Diffraction. The SQuID work found the sample to saturate at 5 μ_B, in very good agreement with the theoretical calculation and literature. Studying the stoichiometry of the system, the EDX suggested a small Co-Si disorder, with the excess Si occupying the Co sites. Finally, Powder XRD using a Co and Cu source was used to probe the disorder in the sample by comparing the differences in the anomalous scattering from the two sources. Due to fluorescence and a poor background:noise ratio, this study remained inconclusive. However, the good agreement between the DFT work and the measured magnetic Compton Profiles, the anisotropies and the SQuID work contribute strong evidence for the half-metallicity of Co_2MnSi.

A sample of CeB_6 was measured along the [100] and [110] directions using magnetic Compton scattering. A small anisotropy between the two directions was found which prompted a further investigation. DFT calculations were capable of reproducing an anistropy but were inadequate in describing the shapes of the MCPs. The $4f$ profiles of the Ce ion were calculated using the GAMESS code. None of the calculated orbitals were found to be in good agreement with the experimental data. A calculation which combined the Ce $4f_{x(z^2-y^2)}$ orbital with the calculated $2p$ orbitals of the B_6 octahedra found excellent agreement with the experimental data. A fixed-spin moment calculation performed using DFT where a small moment was allocated to the B sites did not improve agreement with the experimental data. This result gives strong indication that the spin-density of CeB_6 requires both a Ce and B moment to be described adequately.

The final experimental chapter measured a sample of $Ca_3Co_2O_6$ along the c axis using magnetic Compton scattering. Modelling the CoO_6 trigonal site in GAMESS gave non-physical results for describing the data. This lack of physicality was reproduced in the Co_3O_{12} and Co_5O_{18} calculations. Removing the O atoms from the calculation improved agreement with the experimental data considerably, finding the orbital contributions to be physical. The results of this work suggest $Ca_3Co_2O_6$'s electron momentum density originates entirely from the Co trigonal site in the 3+ state, with no spin-density originating from the O sites.

Chapter 1

Introduction

The work in this thesis details the upgrade of the BL08W beamline's cryostat and the investigation into three materials which have utilised the newly available experimental capacity. The materials investigated all exhibit a plethora of exotic physical phenomena. Co_2MnSi is a proposed half-metallic ferromagnet, CeB_6 is a strongly correlated system with a complex phase diagram and $Ca_3Co_2O_6$ is a one-dimensional $3d$ ferrimagnetic system with a poorly understood band structure. The range of physical phenomena examined here is vast and complicated. Probing the band structure of these materials has been performed primarily using one technique.

The technique used to study these materials at SPring-8 has been *Magnetic Compton Scattering* (MCS). MCS requires very high energy circularly polarised X-rays to probe the spin-polarised *Electron Momentum Density* (EMD). Analysis of this data is possible through the modelling of the system using *Density Functional Theory* (DFT) methods to create a band and orbital specific picture of the system. Additionally, MCS is a highly accurate probe of a material's *spin* moment. Combining these measurements with a complementary technique such as SQuID magnetometry means an accurate picture of a material's magnetism can be painted.

1.1 Aim and Motivations

The main aims of this project were as follows:

- Relocate and install the Oxford Instruments 9 T Superconducting Magnet from the ID15A beamline at ESRF to the BL08W beamline at SPring-8. This upgrade to BL08W's original capabilities means a larger range of physical phenomena can be studied using a more powerful and stable beam source.
- Probe the EMD of Co_2MnSi and model the system using DFT in order to attempt to characterise the system and determine the degree of spin polarisation in the material. This can be achieved through the comparison between the experimental data and theoretical models combined with a study of the directional dependent anisotropy.
- Determine the spin density contributions to the EMD of CeB_6. There is much controversy surrounding the origins of magnetism in CeB_6. Current literature suggests the magnetism originates from the $4f$ band, in disagreement with previous literature which suggests a more $5d$ character. MCS is an excellent technique for probing the EMD and when combined with *ab initio* techniques, the true nature of the magnetism can be determined. An accurate measurement is only now possible due to the BL08W magnet upgrade.
- Earlier work has investigated the orbital occupation of the EMD in $Ca_3Co_2O_6$ however this model was unsuccessful in describing the measured experimental data. The upgrade to BL08W combined with new advances in *ab initio* techniques has enabled a more accurate study of the system to be possible.

1.2 A Brief Introduction to Magnetic Compton Scattering

Compton scattering is the inelastic scattering of a photon by an electron as depicted in figure 1.1. This scattering process is dictated by the equation

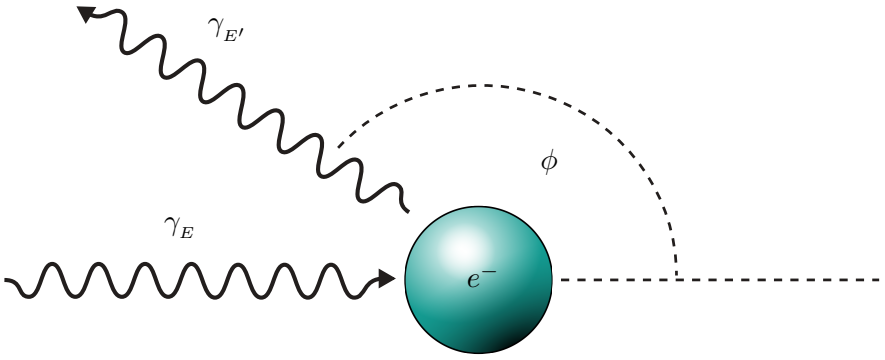

Figure 1.1: The inelastic scattering of a photon by an electron, as described by the Compton effect. An incident photon γ with energy E scatters off an electron e^-, shifting its energy to E'. The angle of the scattering event is ϕ.

$$E' = \frac{E}{1 + (E/m_e c^2)(1 - \cos\phi)} \tag{1.1}$$

which is called the *Compton Shift*. Here, E and E' are the incident and scattered photon energies respectively, ϕ is the scattering angle, m_e is the rest mass of the electron and c is the speed of light. This shift in energy can be written in terms of the electrons' initial momentum $\mathbf{p}$ as

$$E' - E = \frac{\hbar^2 \mathbf{q}^2}{2m_e} + \frac{\hbar \mathbf{q} \cdot \mathbf{p}}{m_e} \tag{1.2}$$

where $\mathbf{q} = \mathbf{k} - \mathbf{k}'$ is the scattering vector and $\hbar$ is the reduced Planck constant. As such, Compton scattering can be used to probe the momentum density of the electrons in a material.

Magnetic Compton Scattering elaborates on this scheme by magnetising the sample with a magnetic field, polarising the electrons of the sample in the process. By measuring the sample with higher energy, circularly polarised X-rays and flipping the field between measurements, the *Magnetic Compton Profile* (MCP) can be determined. The MCP is characteristic of only the unpaired, magnetic electrons in the system and through various forms of modelling and data analysis, insight into the magnetic properties of the

system can be determined.

1.3 Chapter Overview

Chapter 2 serves as an introduction to how the electrons of a material behave in a solid. The concept of a band structure is discussed and an overview of the various types of magnetic interactions are given.

In chapter 3, the reader is introduced to the Hartree-Fock method for solving a many electron system. This is then extended to the famous Density Functional Theory method which is used to analyse the majority of the experimental work in this thesis. Methods for optimising a calculation and converging to an accurate result are described and a brief overview of SPR-KKR and GAMESS codes are given.

Chapter 4 introduces the theory and mechanisms behind MCS to the reader. A brief history of the technique is given where the technique's importance to the development of quantum mechanics is emphasised. The idea of a scattering cross-section is presented which leads onto the means in which the magnetic scattering can be studied. Quantities which need to be optimised to improve the statistics and quality of the data are also discussed and a discussion on the analysis of measured data is provided. Finally, an overview of some of the complementary techniques for MCS is given.

Chapter 5 introduces the SPring-8 synchrotron and the BL08W beamline. Synchrotron radiation is studied and the various insertion devices are compared. The magnet upgrade is detailed with the work studying the impact of the magnet's presence at the beamline being detailed. An overview of the software upgrade is provided with the main functions being detailed.

Chapter 6 details the study of the half-metallic compound Co_2MnSi in an attempt to determine its spin polarisation. The *Magnetic Compton Profile* was measured along the [100], [110] and [111] directions and was modelled using the ELK DFT code. The models were found to be in good agreement with the experimental data and excelled at modelling the anisotropy in the sample. Extensive work also went into characterising

the sample through the use of energy dispersive X-ray diffraction, SQuID magnetometry and powder X-ray diffraction.

The next experimental chapter, chapter 7, details the attempts to model the heavy fermion Kondo system CeB_6. Following on from the work in the mid 2000s by Cooper *et al.*, the upgrade to the magnet at SPring-8 meant a far more accurate set of measurements for the compound were possible. The old data's fitting was compared to the new data's and a new model was developed using DFT and GAMESS.

Chapter 8 is the final experimental chapter, revisiting the 1D complex oxide $Ca_3Co_2O_6$. The material was remeasured in order to improve upon the statistics of the data collected during a previous project. The higher precision data suggested the original model, where the total MCP is comprised mainly from a large $3d_{xz,yz}$ contribution and a moderate $3d_{x^2-y^2,xy}$ contribution, did not agree with the new experimental data. Several different models have been developed which attempt to model the new experimental data in the wake of this new data.

The final chapter, chapter 9, summarises the work which has been culminated to produce this thesis whilst providing ideas for future work in the field and possible experiments which can be expected to be performed in the future.

Chapter 2

Electrons in Solids and Magnetism

The aim of this chapter is to introduce the concept of a crystal to the reader followed by a discussion on how the atoms and electrons in the crystal are described. This will naturally lead on to how the electrons in materials dictate the properties of those materials. The chapter will end with a discussion on magnetism.

In condensed matter physics, it is not necessarily the minutia of the atom itself which is of interest to theorists and experimentalists. Instead, it is about how these atoms, and their electrons, interact with other atoms (and *their* electrons too). For their interactions dictate the vast majority of the interesting properties and phenomena exhibited by materials. The phase of all the materials studied in this thesis are *Crystalline Solids*. Crystalline solids are characterised by a highly ordered arrangement of atoms, forming a crystal *lattice*.[1]

2.1 Crystal Structure

The *Crystal Structure* of a material is the periodic arrangement of atoms which form a solid. The crystal is defined in terms of its *unit cell*, the most basic, repeating structure which can describe the total crystal. The primitive lattice vectors, $\mathbf{a}_1$, $\mathbf{a}_2$ and $\mathbf{a}_3$ define

the lattice and are therefore nearly always treated as a set of axes. Any point $\mathbf{R}$ along the crystal lattice can be defined as

$$\mathbf{R} = l_1\mathbf{a}_1 + l_2\mathbf{a}_2 + l_3\mathbf{a}_3 \tag{2.1}$$

where $\{l_1, l_2, l_3\} \in \mathbb{Z}$. The domain of all possible values for $\mathbf{R}$ is called *real* space. The volume of the unit cell can be calculated by $V = |\mathbf{a}_1 \cdot \mathbf{a}_2 \times \mathbf{a}_3|$. In total, there are 14 different types of lattices (distinct due to their different symmetries) called the *Bravais* lattices.[2] Of these 14 Bravais lattices, there are 230 unique space groups which define the symmetry of the crystal. Figure 2.1 compares the three cubic Bravais lattices. The

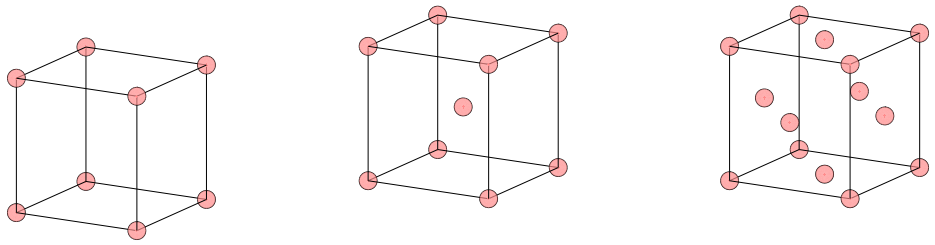

(a) Simple Cubic Structure (spacegroup = 195)

(b) Body-centred Cubic Structure (spacegroup = 197)

(c) Face-centred Cubic Structure (spacegroup = 196)

Figure 2.1: The three cubic Bravais lattices.

space group is important for defining a solid as it dictates the symmetry of the atomic arrangements in the lattice. Additionally, *Wyckoff* positions are required which define the positions of the atoms inside the crystal lattice.[3] Finally, the lattice parameters and (and lattice angles for hexagonal lattices) are required. These can be measured experimentally using diffraction-based techniques such as Powder *X-ray Diffraction* (XRD),[4] neutron diffraction[5] and electron diffraction.[6] Theoretically, the structure can be calculated using various *ab initio* techniques and the Birch-Murnaghan model (see Chapter 3).

2.2 The Reciprocal Lattice

While the primitive lattice vectors define the crystal lattice, the *reciprocal* lattice vectors are used to define the reciprocal lattice. There exists an analogous set of vectors $\mathbf{G}$ for every possible set of real space vectors $\mathbf{R}$. The reciprocal lattice vector is important as it will be shown that the properties of a system can be described in terms of just a subset of the reciprocal lattice. A more rigorous definition is that all vectors of the reciprocal lattice must satisfy the equation

$$e^{i(\mathbf{G}\cdot\mathbf{R})} = 1. \tag{2.2}$$

The reciprocal lattice vectors $\mathbf{b}_1$, $\mathbf{b}_2$ and $\mathbf{b}_3$ are defined as

$$\mathbf{b}_1 = 2\pi\frac{\mathbf{a}_2 \times \mathbf{a}_3}{\mathbf{a}_1 \cdot \mathbf{a}_2 \times \mathbf{a}_3}, \quad \mathbf{b}_2 = 2\pi\frac{\mathbf{a}_3 \times \mathbf{a}_1}{\mathbf{a}_1 \cdot \mathbf{a}_2 \times \mathbf{a}_3}, \quad \mathbf{b}_3 = 2\pi\frac{\mathbf{a}_1 \times \mathbf{a}_2}{\mathbf{a}_1 \cdot \mathbf{a}_2 \times \mathbf{a}_3}, \tag{2.3}$$

where the denominator is the volume V of the unit cell.[7] The primitive and reciprocal lattice vectors are orthogonal to each other, satisfying the relation

$$\mathbf{a}_i \cdot \mathbf{b}_j = 2\pi\delta_{ij} \tag{2.4}$$

where δ_{ij} is the *Kronecker* delta function.[8] Analogous to $\mathbf{R}$, $\mathbf{G}$ is defined as

$$\mathbf{G} = m_1\mathbf{b}_1 + m_2\mathbf{b}_2 + m_3\mathbf{b}_3, \tag{2.5}$$

where incidentally, $\{m_1, m_2, m_3\} \in \mathbb{Z}$.

The primitive cell defined in reciprocal space is called the *Brillouin* zone (BZ). It is constructed by bisecting the connecting points defined in reciprocal space. The BZ is of critical importance because the periodic properties of a crystal can be described entirely within the *first* BZ, the most basic construction in reciprocal space possible. The BZ is also important for theoretical, computer based calculations since the properties of an entire system can be calculated solely from a small *wedge* (the *irreducible* Brillouin zone (IBZ)), easing the computational burden and improving the accuracy significantly.

Figure 2.2 plots the calculated first BZ for Ni, a material described by the FCC structure. Visualising the first BZ is useful particularly for calculating the *Band Structure* plot of a

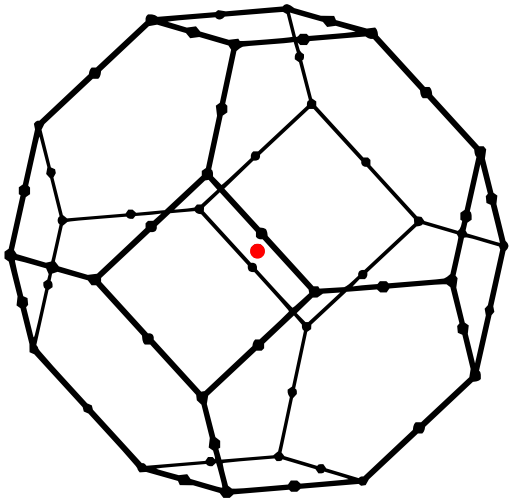

Figure 2.2: The first BZ of Ni, an element which crystallises into an FCC structure.

material. The shapes of the bands change with the direction $\mathbf{k}$ points along so choosing a *path* which encompasses all the essential features of the band structure is crucial to describing the electronic structure of a studied material.

2.3 Energy Levels and Bands

The quantum mechanical description of an atom suggests the electrons occupy different *orbitals* around a nucleus, each with a defined energy. The energy levels are calculated as eigenvalues of the Schrödinger equation, defined as

$$\left\{-\frac{\hbar^2}{2m_e}\nabla^2 + V(\mathbf{r})\right\}\psi(\mathbf{r}) = E\psi(\mathbf{r}) \tag{2.6}$$

where $\hbar$ is the reduced Planck constant, m_e is the mass of the electron, $V(\mathbf{r})$ is some external potential and $\psi(\mathbf{r})$ is an electronic eigenstate, dependent on the spatial coordinate $\mathbf{r}$ which defines the electron's position in space.

For an eigenstate dependent on only one spatial coordinate (and therefore, only one

electron), solving this equation gives the energy eigenvalues for the H atom.[9] The energy eigenvalues represent the possible energy levels for which the single H electron can occupy. For higher order elements, more spatial coordinates are required to describe the positions of the electrons, increasing the number of terms the wavefunction depends on i.e. $\psi(\mathbf{r}) \Rightarrow \psi(\mathbf{r}_1, \mathbf{r}_2, ..., \mathbf{r}_n)$. As more atoms are introduced to a system, the electrons form molecular orbitals, each with a discrete energy level. When describing the atoms and electrons in a solid (where the number of electrons approaches $\sim 10^{23}$), the energy levels become so dense that they start to form a *continuum*.

2.3.1 Energy Bands

As atoms come into close proximity to one another, the orbitals create *bonding* and *anti-bonding* orbitals, forming a continuum called a *band*. This has been shown pictorially in figure 2.3. Using Na as an example, as the two atoms are brought closer together, their single filled $3s^1$ orbitals hybridise, forming a lower energy Na $3s^2$ bonding orbital and an unfilled, higher energy anti-bonding orbital. The newly formed molecule's energy levels are then plotted as a function of interatomic separation[10] where a is the lattice parameter of Na. The point at which the atomic separation is equal to the lattice parameter of the material is where the energy level is minimised. This separation is the

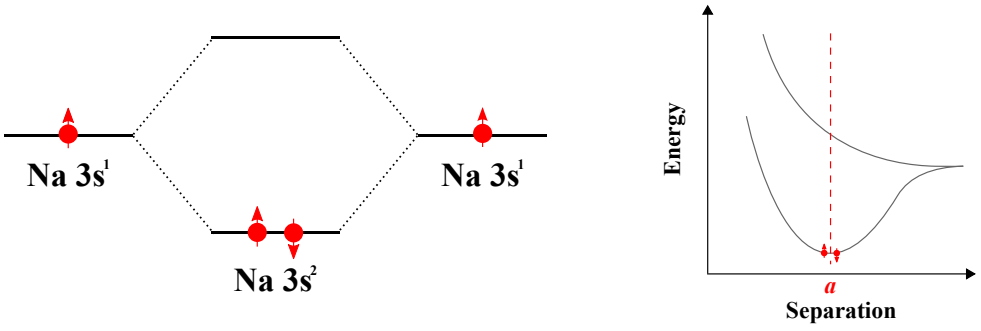

Figure 2.3: The creation of a bonding (occupied) and anti-bonding (unoccupied) orbital as a result of the close proximity of two Na $3s^1$ orbitals. The bonding orbital created is a lower energy doubly filled Na $3s^2$ orbital. The unoccupied anti-bonding orbital sits higher in energy. The energy has also been plotted as a function of inter-atomic separation where the $3s^2$ pair sits at the lowest possible energy, found when the inter-atomic separation is equal to the lattice parameter.

point at which equilibrium is reached between the repulsive and attractive potentials acting on the atoms. Such potentials have a general form of

$$V_{ij}(\mathbf{r}_{ij}) = V_{\text{repulsive}}(\mathbf{r}_{ij}) + V_{\text{attractive}}(\mathbf{r}_{ij}) \tag{2.7}$$

defined in terms of atom i and atom j.[11,12]

As more electrons are introduced to this system, more bonding and anti-bonding pairs are generated. Since the Pauli exclusion principle abhors degeneracy in the energy levels, these doubly filled Na $3s^2$ energy levels occupy orbitals which are very close together in energy. Eventually, as the number of electrons tends to that of an actual solid ($\sim 10^{24}$), the energy levels can no longer be clearly identified. Instead, occupied and unoccupied *energy bands* are formed, as shown in figure 2.4. When the number of electrons resembles

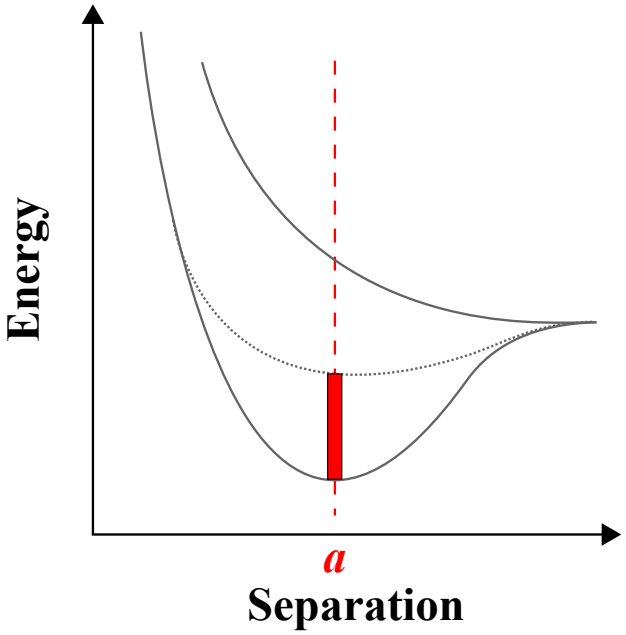

Figure 2.4: The Na $3s^2$ energy band (red) generated as a result of Na atoms coming together to form a solid. The number of electrons present is on the order of $\sim 10^{23}$. Above the dotted line are the unoccupied anti-bonding states.

the number in a solid, the differences between the occupied, bonding energy levels are

too small to be identified. The bonding energy levels now form a continuum of occupied states, called a band.

The energy-band view of electronic bonding can explain why certain materials have certain properties. The band *structure* (the shape and character of these bands) is a good means of characterising a material's conductive properties (such as a metal, semiconductor, or insulator). In the case of Na, the unoccupied states are situated directly next to the occupied band. To be more succinct, the energy band is *half-filled*. Applying an electric field to Na, the electrons will be subjected to an increase in kinetic energy, promoting them into the unoccupied states. This is why Na is a metal. It can freely promote electrons into higher energy levels.[13]

This model of electronic bands does not possess any predictive capabilities. Various models have been proposed for studying the electronic structure of materials, the earliest of which was the Drude model.[14,15] The free-electron model developed upon the Drude model through the application of Fermi-Dirac statistics.[16] While the free-electron model was a significant improvement upon the Drude model, its approximation (that $V(\mathbf{r}) = 0$) is a very poor approximation for all materials. The success of the free-electron model lies in its ability to predict metallic properties correctly in certain materials (such as Na). It however, fails to characterise other materials correctly such as metallic properties in Ca and semiconducting properties in Si.

2.4 Electrons in a Periodic Potential

Non-metallic materials are characterised by the presence of a band gap at the Fermi energy, E_{F}. To give a more accurate description of the electrons' physics, a potential must be applied. The electrons, even in metals, are not completely free since they move through an array of ions which form the crystal lattice. This array of ions form a periodic crystal potential. This model is often called the *Nearly Free-Electron Model*.

For the crystal potential $V(\mathbf{r})$ of a system to be periodic, it must satisfy the expression

$$V(\mathbf{r} + \mathbf{R}) = V(\mathbf{r}). \tag{2.8}$$

The potential, $V(\mathbf{r})$, now being a periodic function, can be described in the form of a Fourier series. This enables the periodic potential to be defined as

$$V(\mathbf{r}) = \sum_{\mathbf{G}} V_{\mathbf{G}} e^{i\mathbf{G}\cdot\mathbf{r}}. \tag{2.9}$$

Equations 2.8 and 2.9 are used to derive the reciprocal lattice criteria in equation 2.2[1].

The *Born-von Karman periodic boundary conditions* are employed in order to find a suitable wavefunction to describe the motion of the electrons through the periodic potential.[17] The boundary condition infers the wavefunction be a plane-wave of the form

$$\psi(\mathbf{r}) = e^{i(\mathbf{k}\cdot\mathbf{r}-\omega t)} \tag{2.10}$$

where ω is the angular frequency and $\mathbf{k}$ is the wave vector. This plane-wave is subject to the boundary conditions which result from the intrinsic symmetry of the crystal. If $j \in \{1, 2, 3\}$ the boundary condition becomes

$$\psi(\mathbf{r} + l_j \mathbf{a}_j) = \psi(\mathbf{r}). \tag{2.11}$$

Recalling that l_j is the number of unit cells in the j^{th} direction, N, the number of unit cells in the crystal, is simply

$$N = \prod_j l_j. \tag{2.12}$$

Likewise in equation 2.2, this implies

$$e^{il_j \mathbf{k}\cdot\mathbf{a}} = 1. \tag{2.13}$$

What is important about the Born-von Karman boundary condition is that it shows the periodicity of $\psi(\mathbf{r})$ is identical to the periodicity of $V(\mathbf{r})$. That is, $\psi(\mathbf{r} + \mathbf{R}) = \psi(\mathbf{r})$. This would only be true if the wavefunctions were degenerate ($\psi(\mathbf{r})$ and $\psi(\mathbf{r} + \mathbf{R})$ have the same energy eigenvalue). In the case that the wavefunctions are non-degenerate, the

[1] $e^{i\mathbf{G}\cdot(\mathbf{r}+\mathbf{R})} = e^{i\mathbf{G}\cdot\mathbf{r}}$ can only be true if $e^{i\mathbf{G}\cdot\mathbf{R}} = 1$ since $e^{i\mathbf{G}\cdot(\mathbf{r}+\mathbf{R})} = e^{i\mathbf{G}\cdot\mathbf{r}} e^{i\mathbf{G}\cdot\mathbf{R}}$.

periodicity of ψ is

$$\psi(\mathbf{r}+\mathbf{R}) = Cu_{\mathbf{k}}(\mathbf{r}) \tag{2.14}$$

where $u_{\mathbf{k}}(\mathbf{r})$ is some function with the same periodicity of the crystal lattice. The normalisation constraints imposed on the wavefunction requires that $|C|^2 = 1$, therefore C can be related to equation 2.13, i.e.,

$$C = e^{il_j\mathbf{k}\cdot\mathbf{a}} = e^{i\mathbf{k}\cdot\mathbf{r}} = 1. \tag{2.15}$$

Inserting this expression back into equation 2.14 gives an important function called a *Bloch wave*,[18] explicitly defined as

$$\psi_{\mathbf{k}}(\mathbf{r}) = e^{i\mathbf{k}\cdot\mathbf{r}}u_{\mathbf{k}}(\mathbf{r}) \tag{2.16}$$

Theorem 2.1. *The eigenstates $\psi(\mathbf{r})$ of the Hamiltonian $\hat{\mathcal{H}} = \frac{-\hbar^2}{2m}\nabla^2 + V(\mathbf{r})$ can be chosen to have the form of a plane-wave multiplied by a function with the periodicity of the Bravais lattice:*

$$\psi_{n\mathbf{k}}(\mathbf{r}) = e^{i\mathbf{k}\cdot\mathbf{r}}u_{n\mathbf{k}}(\mathbf{r}) \tag{2.17}$$

where

$$u_{n\mathbf{k}}(\mathbf{r}+\mathbf{R}) = u_{n\mathbf{k}}(\mathbf{r}) \tag{2.18}$$

While the introduction of Bloch's theorem has been given from within the context of electronic states, Bloch's theorem is true for *any* particle which propagates through a lattice with a periodic potential. More so, this formalism makes no assumptions regarding the strength of this periodic potential. The energy eigenvalue $\epsilon_n(\mathbf{k})$ is periodic in reciprocal space i.e. $\epsilon_n(\mathbf{k}+\mathbf{G}) = \epsilon_n(\mathbf{k})$. This reinforces the concept that only the states inside the first Brillouin zone need be solved to describe the properties of the entire crystal.[19]

Importantly, $\mathbf{k}$ here in equation 2.17 is not a general wavevector but a wavevector which exists only inside the first Brillouin zone. The additional subscript, n, is called the *band index*. Each set of $u_{n\mathbf{k}}(\mathbf{r})$ describes a set of electronic states whose energies lie on a

dispersion curve [2]. This is the concept of a *band structure*. For each band n, there will be a number of possible wavefunctions, distinguished by their $\mathbf{k}$. The way these bands are filled determines the type of material (be it a metal, insulator, semiconductor, or perhaps, a more exotic type).

2.5 Band Structure

Application of a periodic potential enables study of a crystal to be localised entirely within the first BZ. It also creates band gaps at the Fermi Energy, E_{F} for certain materials. Studying the band structure for a real, 3D crystal is difficult because the band energy now depends on a 3D $\mathbf{k}$ and the BZ becomes more complicated. A common way to calculate the band structure in *lieu* of these issues is through the use of *ab initio* electronic structure calculations (see chapter 3). Figure 2.5 plots the band structure of Si - a material famous for its semiconducting properties. The figure plots $E - E_{\mathrm{F}}$ as a function of $\mathbf{k}$. The lines represent the shapes of the dispersion relation as they *evolve* throughout $\mathbf{k}$ space. The Greek characters denote certain high-symmetry points inside the BZ and are specific to each type of unit cell. At $E = 0$, a region has formed which is free of any bands which is the aforementioned *band-gap*. This band gap means that no electrons can freely be promoted to the unoccupied bands which line at $E \geq 0$ without a larger energy input. This is what gives Si its semiconducting properties.[20] A metal would have bands which cross E_{F} and this would be reflected in the band structure plot. In conclusion, the band structure is one of the most powerful means of characterising the macroscopic (and often the microscopic) properties of a material.

2.6 Magnetism

The notion of a band structure can be applied to the development of magnetism in a material. Magnetism originates from the presence of *electron magnetic dipole moments* (often referred to as *spins*) and their alignment within the material. There is a

[2] The dispersion relationship is the function $E = E(\mathbf{k})$.

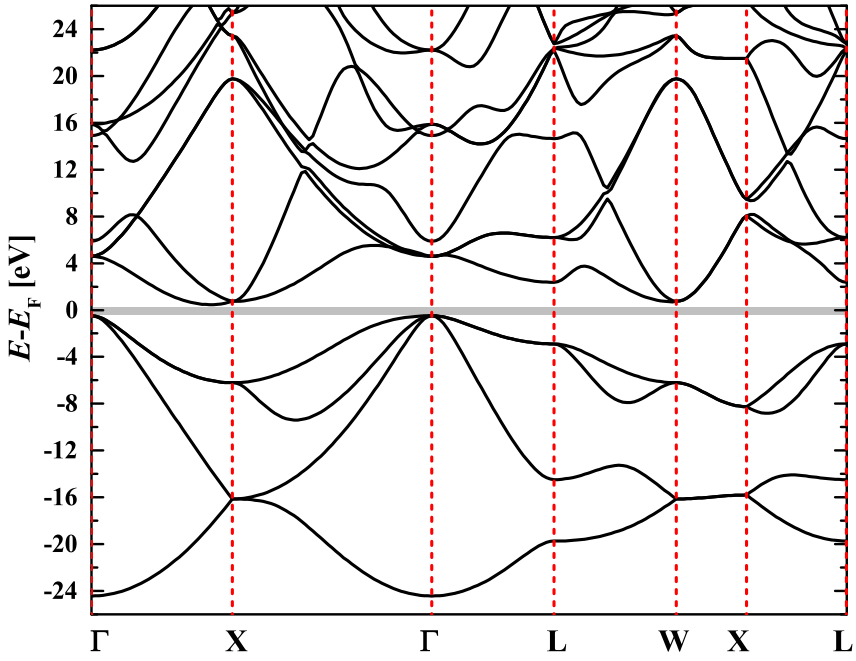

Figure 2.5: Calculated electronic band structure of Si plotted along $\Gamma \rightarrow$ L in reciprocal space. The region shaded in grey is the band-gap, indicating that Si is a semiconducting material. Band structure calculated using the ELK DFT code.

wide range of different magnetic orderings which have been observed in physics, some of which are illustrated in figure 2.6. The magnetic ordering of a material is heavily dependent on the arrangement of the magnetic moments and how the system reacts to an applied magnetic field. *Diamagnetism* is the weakest form of magnetism and is found in all materials. In a diamagnetic material, the electron spins will oppose an applied magnetic field. *Paramagnetism* is stronger than diamagnetism and is characterised by the alignment of a material's electron dipole moments with a sufficiently large magnetic field. When the applied magnetic field is removed, the spins lose their alignment. Below the so-called *Curie Temperature* T_{C}, a material may develop a spontaneous alignment of its spins. This is called *Ferromagnetism*. Ferromagnetism is a strong, long range ordering of the electron spins where the material will retain a net magnetisation even in the absence of an applied magnetic field. If a magnetic field is applied opposite to the alignment of the electron spins, they will only change their polarisation after a

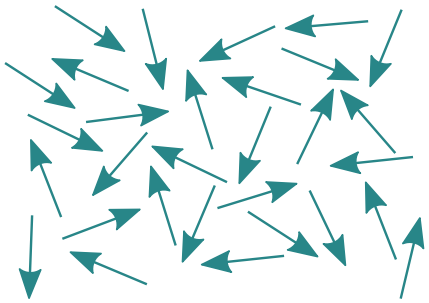

(a) No Ordering

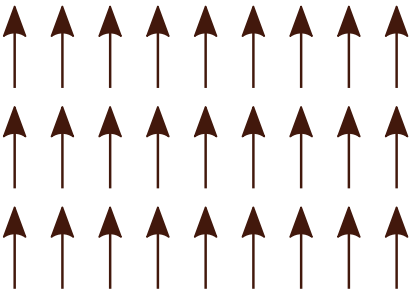

(b) Ferromagnetism (Observed in Co_2MnSi)

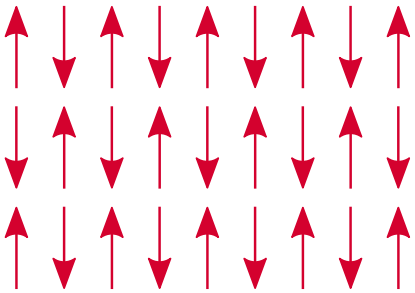

(c) Antiferromagnetism (Observed in CeB_6 and $Ca_3Co_2O_6$)

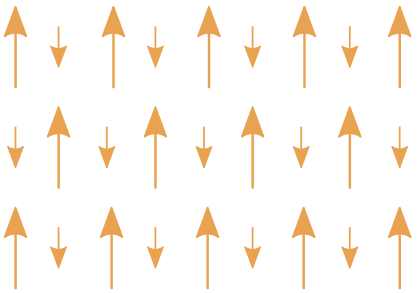

(d) Ferrimagnetism (Observed in $Ca_3Co_2O_6$)

Figure 2.6: The types of magnetic ordering which were encountered within this thesis. The arrows represent the direction and magnitude of the magnetic moments in the material.

sufficiently large magnetic field is applied. This phenomenon is called hysteresis. For some materials, *Antiferromagnetism* will develop where the net magnetisation of the sublattices which comprise the material develop a spontaneous alignment anti-parallel to each other. *Ferrimagnetism* is a similar phenomenon to antiferromagnetism however the magnitudes of the sublattices' magnetisations are different.

These types of ferroic ordering are very strong and do not develop solely from the electron magnetic dipole interaction. They develop from a type of interaction called the *Exchange* interaction.

2.6.1 The Exchange Interaction

For many materials, magnetic ordering occurs as a result of the exchange interaction. The exchange interaction is a quantum mechanical phenomenon which occurs as a result

of the Pauli exclusion principle and Hund's rules.[21] The electrons of a system must obey exchange symmetry[3] and cannot occupy the same quantum mechanical state. These conditions restrict the electrons to certain states and force them to not occupy like-states (this is also often called *Pauli repulsion*). In a material such as Fe, the magnetic moments align parallel to each other because this is the state which minimises the exchange interaction. All other arrangements of the electrons require more energy than that of a parallel arrangement of magnetic moments.

For a system of localised magnetic moments which interact via the exchange interaction, the exchange *energy* over all electrons i and j of a many-electron system is defined as

$$E_{\mathrm{x}} = -\sum_{ij} \mathcal{J}_{ij} \left(\mathbf{S}_i \cdot \mathbf{S}_j \right) \tag{2.19}$$

where $\mathcal{J}_{ij}$ is the exchange interaction between spins $\mathbf{S}_i$ and $\mathbf{S}_j$.[22]

Direct Exchange

Electrons which are close enough to have a large overlap of their electronic wavefunctions tend to interact via *Direct* exchange interactions. This is a strong, short range coupling which diminishes as the ionic separation increases. When the atoms are close together, the electrons occupy the intermediary space because this is where the Coulomb interaction is minimal. This spatial overlap forces the electrons to have opposing spins and as a result, direct exchange is responsible for causing antiferromagnetic ordering in materials.

Indirect Exchange

Over large inter-atomic separations, the *Indirect* exchange interaction contributes to the electronic coupling in a material. The more formal name of this interaction is the *Ruderman-Kittel-Kasuya-Yoshida* (RKKY) interaction. This type of exchange interaction is often mediated by the conduction electrons of metals due to their long range,

[3] $\psi(\mathbf{r}_1, \mathbf{r}_2) = -\psi(\mathbf{r}_2, \mathbf{r}_1)$

de-localised nature.[23]

2.6.2 Spin-Orbit Coupling

An electron's total magnetic moment is dependent not only on the spin angular momentum of the electron but also its orbital angular momentum. The interaction between the spin and orbital angular momenta cause shifts and splitting of the electron energy levels. This contributes an additional term to the Hamiltonian, $\mathcal{H}_{\mathrm{SO}}$, defined as

$$\mathcal{H}_{\mathrm{SO}} = \frac{e\hbar^2}{2m_e c^2 r}\frac{\mathrm{d}V(\mathbf{r})}{\mathrm{d}\mathbf{r}}\mathbf{S}\cdot\mathbf{L} \tag{2.20}$$

where e is the charge of the electron and $\mathbf{S}$ and $\mathbf{L}$ are the spin and orbital angular momenta of the electron, respectively. This phenomenon is called *Spin-Orbit Coupling*. For materials which exhibit large orbital moments (such as $4f$ systems), the spin-orbit coupling will be strong and as a result, will need to be considered when attempting to accurately describe the band structure. For materials where the orbital moment is small (such as in most $3d$ alloys[4]), the spin-orbit coupling is negligible.[23]

2.6.3 Spin-split Bands

Very many materials have non-integer magnetic moments per atom. This value is not possible within the framework that magnetism originates solely from the unpaired electrons in a system. This type of magnetism is due to the spin-splitting of the bands of a material. Sometimes in a material, due to the interaction with the molecular potential, it is energetically favourable for the spin-up and spin-down bands to be unequal in terms of their populations. An example DOS has been sketched in figure 2.7 which shows the spin-split spin up and down bands of a ferromagnet. The energy change ΔE due to spin-down electrons moving into the spin-up band is

$$\Delta E = \frac{1}{2}n(E_{\mathrm{F}})(\delta E)^2(1 - U_n(E_{\mathrm{F}})) \tag{2.21}$$

[4]This is not the case for all $3d$ compounds. For example, in chapter 8, the calculations find a significant orbital moment in $Ca_3Co_2O_6$.

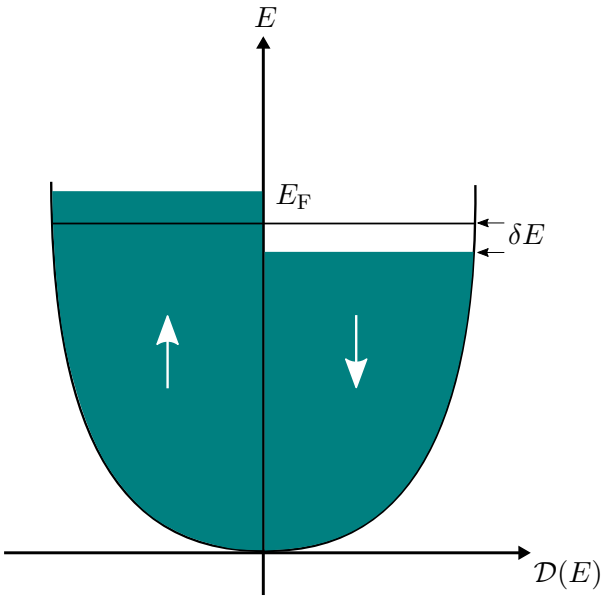

Figure 2.7: Sketch of the DOS of a ferromagnetic material. The spin splitting of the spin-up (↑) and spin-down (↓) is what gives the compound its net, magnetic spin moment.

where $n(E_{\mathrm{F}})$ is the number of electrons at E_{F}, δE is the increase in energy as a result of moving electrons into the spin up band, and $U_n(E_{\mathrm{F}})$ is the *Stoner Parameter*. For materials which satisfy

$$U_n(E_{\mathrm{F}}) \geq 1, \tag{2.22}$$

spontaneous ferromagnetism will occur in the material.

Chapter 3

Theoretical Techniques

In this chapter the main theoretical methods for calculating the electronic structure of materials will be discussed. The work in this thesis will see applications of several different types of theoretical technique. These are the *Hartree-Fock* method, *Density Functional Theory* (DFT) through the use of the *Full Potential Linearised Augmented Planewave* (FP-LAPW), the *Spin-Polarised Fully-Relativistic Korringa-Kohn-Rostoker* (SPR-KKR) methods, and the *Molecular Orbital Wavefunction Method*.

3.1 Introduction

These techniques exist essentially to evaluate the time independent Schrödinger equation,

$$\hat{\mathcal{H}}\psi(\mathbf{r}) = E\psi(\mathbf{r}) \tag{3.1}$$

where $\hat{\mathcal{H}}$ is the Hamiltonian, $\psi(\mathbf{r})$ is the wavefunction for an electron at position $\mathbf{r}$, and E is the energy eigenvalue for the electron.

Before studying this equation further, it is important to discuss *why* it might be interesting to evaluate this equation (and why it's actually impossible for nearly all practical applications).

Consider the unit cell of Ni - a popular material studied heavily with MCS[24] and mea-

sured on nearly all experiments for calibration reasons (see chapter 4). With the space group $Fm\text{-}3m$, the unit cell consists of two atoms, each with one nucleus and 28 electrons. This would result in a wavefunction of 174 dimensions (3 for each electron and nucleus). Explicity, $\hat{\mathcal{H}}$ can be defined as

$$\hat{\mathcal{H}} = -\frac{\hbar^2}{2M_i}\sum_{i=1}^{N}\nabla^2_{\mathbf{R}_i} + \frac{1}{2}\sum_{i=1}^{N}\sum_{j>i}^{N}\frac{Z_i Z_j e^2}{|\mathbf{R}_i - \mathbf{R}_j|} - \frac{\hbar^2}{2m}\sum_{i=1}^{n}\nabla^2_{\mathbf{r}_i} - \sum_{i=1}^{N}\sum_{j=1}^{n}\frac{Z_i e^2}{|\mathbf{R}_i - \mathbf{r}_j|} + \frac{1}{2}\sum_{i=1}^{n}\sum_{j>i}^{n}\frac{e^2}{|\mathbf{r}_i - \mathbf{r}_j|} \tag{3.2}$$

where $\hbar$ is the reduced Planck constant,[25] M_i is the mass of nucleus i, $\mathbf{R}_i$ is the position of nucleus i, ∇ is the *del* operator[1], Z_i is the atomic number of nucleus i, e is the charge of the electron,[25] m is the mass of the electron and $\mathbf{r}_i$ is the position of electron i. The indices N and n are over the total number of nuclei and electrons respectively[2]. This Hamiltonian is often called the *Multi-Atom-Multi-Electron* Hamiltonian. From left to right, there are five terms in total which are as follows: The kinetic energy of the nuclei, the Coulomb repulsion between the nuclei, the kinetic energy of the electrons, the Coulomb attraction between the nuclei and the electrons and the Coulomb repulsion between the electrons. Inserting this Hamiltonian into the Schrödinger equation gives the *Multi-Atom-Multi-Electron* Schrödinger equation

$$\hat{\mathcal{H}}\Psi(\mathbf{R}_1, \cdots, \mathbf{R}_N; \mathbf{r}_1, \cdots, \mathbf{r}_n) = E\Psi(\mathbf{R}_1, \cdots, \mathbf{R}_N; \mathbf{r}_1, \cdots, \mathbf{r}_n). \tag{3.3}$$

This is an extremely complicated eigen-equation to solve, of which there is no known analytical solution. To contextualise just how difficult this equation is to solve, consider that a typical solid has roughly $n \sim 10^{24}$ electrons. Using this Hamiltonian, there will be $3n$ electronic coordinates to solve. Hartree-Fock Theory and its extension, Density Functional Theory find their applications in providing an approximate solution to this problem.

[1] This operator is often also called the *Nabla* operator.

[2] The double sum is because it's a sum over the available *pairs* of electrons in the system. This is why j is dependent on i and not independent. If j was independent of i, the electron-electron interaction pairs would start to be counted twice

3.1.1 The Born-Oppenheimer Approximation

Before studying how to overcome this technical challenge of $3n \sim 10^{24}$ electrons, one approximation can be made immediately to ease the computational burden. This is called the *Born-Oppenheimer* approximation.

The mass of the nuclei are a factor of ~ 1800 greater than the electron. This means that the electrons possess a higher momentum than the slow, heavy, lattice-bound nuclei. The Born-Oppenheimer approximation as a result, infers that the nuclei do *not* move when compared to the high momentum electrons. This means that the Coulomb interaction between the nuclei can be solved classically and the nuclear kinetic energy can be removed. The attractive potential between the electrons and the now *frozen* nuclei is referred to as the *external background* potential, $V_{\text{ext}}(\mathbf{r}_i)$. The Hamiltonian can now be written as

$$\hat{\mathcal{H}} = -\frac{\hbar^2}{2m}\sum_{i=1}^{n}\nabla^2_{\mathbf{r}_i} - \sum_{i=1}^{n}V_{\text{ext}}(\mathbf{r}_i) + \frac{1}{2}\sum_{i=1}^{n}\sum_{j>i}^{n}\frac{e^2}{|\mathbf{r}_i - \mathbf{r}_j|}. \tag{3.4}$$

A more compact notation is preferred for writing this Hamiltonian. Rewriting the now *Many Electron* Schrödinger equation gives

$$\left[\hat{T}_e(\mathbf{r}) + \hat{V}_{\text{ext}}(\mathbf{r}) + \hat{V}_{ee}(\mathbf{r},\mathbf{r}')\right]\psi(\mathbf{r_i}) = \epsilon_i\psi(\mathbf{r_i}) \tag{3.5}$$

where the following substitutions have been made:

$$\hat{T}_e(\mathbf{r}) = -\frac{\hbar^2}{2m}\sum_{i=1}^{n}\nabla^2_{\mathbf{r}_i}, \tag{3.6}$$

$$\hat{V}_{\text{ext}}(\mathbf{r}) = -\sum_{i=1}^{n}V_{\text{ext}}(\mathbf{r}_i), \tag{3.7}$$

$$\hat{V}_{ee}(\mathbf{r},\mathbf{r}') = \frac{1}{2}\sum_{i=1}^{n}\sum_{j>i}^{n}\frac{e^2}{|\mathbf{r}_i - \mathbf{r}_j|}. \tag{3.8}$$

This is still a very difficult equation to solve. The Coulomb interactions between the different electrons ($\hat{V}_{ee}(\mathbf{r},\mathbf{r}')$) still scales extremely poorly with systems which might actually be of interest to study.

It is at this point where different paradigms to solving the Schrödinger equation emerge. This thesis will explore two of these methods: the *Hartree-Fock* method and DFT.

3.2 The Hartree-Fock Method

The Hartree-Fock method is at its core, the treatment of a many body system by inferring it to be constructed entirely of non-interacting electrons (set $\hat{V}_{ee}(\mathbf{r}, \mathbf{r}') = 0$). This is a very simplistic approximation to make, for it is the electronic interactions (and in many cases, the strong electronic correlations) which are responsible for much of the magnetic phenomena studied in this thesis. Even so, one positive consequence of this assumption is that the many body wavefunction $\psi(\mathbf{r}_i)$ can now be separated into a product of non-interacting wavefunctions i.e.,

$$\psi_{\mathrm{HP}}(\mathbf{r}_i) = \phi_1(\mathbf{r}_1)\phi_2(\mathbf{r}_2)\cdots\phi_N(\mathbf{r}_N) \tag{3.9}$$

which is called a *Hartree Product*. These *orbitals* only depend on 3 coordinates as opposed to 3N coordinates and so, make it much simpler to solve the many body Schödinger equation. However, one serious problem with this setup is that the Hartree product does not satisfy the *Anti-symmetry Principle*[3]. For example, in the case of two electrons (such as in a He atom), the Hartree product is

$$\psi_{\mathrm{HP}}(\mathbf{r}_1, \mathbf{r}_2) = \phi_1(\mathbf{r}_1)\phi_2(\mathbf{r}_2) \tag{3.10}$$

If electron 1 and 2 are swapped over, the Hartree product becomes

$$\psi_{\mathrm{HP}}(\mathbf{r}_2, \mathbf{r}_1) = \phi_1(\mathbf{r}_2)\phi_2(\mathbf{r}_1) \tag{3.11}$$

the only way to obtain the negative of the original Hartree product is if

$$\phi_1(\mathbf{r}_1)\phi_2(\mathbf{r}_2) = -\phi_1(\mathbf{r}_2)\phi_2(\mathbf{r}_1) \tag{3.12}$$

[3]This is a result of the fact that electrons are *fermions*. The wavefunction *must* change sign if two electrons are exchanged.

which is not true in this case. This means the wavefunction ψ_{HP} is not a valid wavefunction for describing two electrons because it does not obey the anti-symmetry principle.

There is no way to solve this issue unless an extra degree of freedom is introduced. This is the *spin* of the electron, which is either α (spin *up*) or β (spin *down*).[26] The spin of the electron arises from its intrinsic angular momentum[4]. As a result, instead of describing the wavefunction $\phi(\mathbf{r})$ exclusively *spatially*, spin in addition is now considered. These *spin orbitals* take the form $\chi(\mathbf{r}, \omega) = \phi(\mathbf{r})\omega$ where $\omega \in \{\alpha, \beta\}$. The Hartree Product can now be rewritten as

$$\psi_{\text{HP}}(\mathbf{r}_1, \mathbf{r}_2, \omega_1, \omega_2) = \frac{1}{\sqrt{2}} \left[\chi_1(\mathbf{r}_1, \alpha)\chi_2(\mathbf{r}_2, \beta) - \chi_1(\mathbf{r}_2, \alpha)\chi_2(\mathbf{r}_1, \beta)\right]. \tag{3.13}$$

This wavefunction now satisfies the antisymmetry principle for any choice of χ_1 and χ_2.

For wavefunctions which depend on more than two electrons, the Hartree Product needs to be represented as a *Slater Determinant*.

The Slater Determinant

For N electrons, the Hartree product which generally violates the anti-symmetry principle can be written as a Slater Determinant of the form

$$\psi_{\text{HP}}(\mathbf{r}_i, \omega) = \frac{1}{\sqrt{N!}} \det \begin{bmatrix} \chi_1(\mathbf{r}_1, \omega) & \chi_2(\mathbf{r}_1, \omega) & \cdots & \chi_N(\mathbf{r}_1, \omega) \\ \chi_1(\mathbf{r}_2, \omega) & \chi_2(\mathbf{r}_2, \omega) & \cdots & \chi_N(\mathbf{r}_2, \omega) \\ \vdots & \vdots & \ddots & \vdots \\ \chi_1(\mathbf{r}_N, \omega) & \chi_2(\mathbf{r}_N, \omega) & \cdots & \chi_N(\mathbf{r}_N, \omega) \end{bmatrix} \tag{3.14}$$

where the coefficient $1/\sqrt{N!}$ is a normalisation factor. The Slater Determinant has some interesting qualities. It changes sign whenever the positions of two electrons are exchanged, it does not distinguish between individual electrons (they are all the same) and it disappears if two electrons have identical coordinates or wavefunctions (implicitly

[4] An additional *orbital* angular momentum is also present in electrons, however for many systems, the orbital angular momentum is absent.

satisfying the Pauli-exclusion principle[5]). The Slater Determinant's ability to adapt to electrons exchanging position falls more generally under the branch of interactions known as *exchange interactions* (some of which have been discussed in the previous chapter). While the Hartree Product (or more broadly, the Hartree-Fock paradigm in general) suggests that the electrons initially are completely non-interacting, the Slater Determinant representation of the Hartree Product incorporates an electron exchange interaction.[27]

With the anti-symmetry being accounted for by the Slater determinant, Fock modified the initial Hamiltonian to give

$$\left\{-\frac{h^2}{2m}\nabla^2 + V_{\text{ext}}(\mathbf{r}) + \sum_{j\neq i}^{n}\int \mathrm{d}\mathbf{r}\frac{e^2\left|\psi_j(\mathbf{r})\right|^2}{\left|\mathbf{r}_j-\mathbf{r}\right|}\right\}\psi_i(\mathbf{r}) - \sum_{j\neq i}^{n}\delta_{i,j}\int \mathrm{d}\mathbf{r}'\frac{e^2}{|\mathbf{r}'-\mathbf{r}|}\psi_j^*(\mathbf{r}')\psi_i(\mathbf{r}')\psi_j(\mathbf{r}) \tag{3.15}$$

which can be recognised as the initial Hamiltonian (equation 3.4) with an additional *exchange interaction* term which arises due to the anti-symmetry of the Slater determinant wavefunction. The presence of the Kronecker delta $\delta_{i,j}$ causes the term to vanish for $i \neq j$. This arises from the Pauli exclusion principle and forbids electrons with the same spin from occupying the same region in space.

Solving this equation calculates the Hartree-Fock groundstate energy E_0^{HF}. This is performed by minimising the function with respect to varying the orbital wavefunctions and external potential. This is done *iteratively* until the change in E_0^{HF} and $V_{\text{ext}}(\mathbf{r})$ are minimised. The inclusion of the exchange interaction term significantly improves upon the results of the Hartree-Fock theory but it is important to note that this Hamiltonian does not account for electron *correlations*.

3.3 Density Functional Theory

There are many issues facing the Hartree-Fock method. While the Slater Determinant is able to account for the exchange interactions the electrons in the system might un-

[5]The Pauli Exclusion Principle requires that two Fermions may not occupy the same quantum mechanical state.

dergo, no correlation effects are considered. These play a very dominant role in complex compounds and strongly correlated systems. There is also the dependence on a well defined set of single-particle orbitals which create the Slater Determinant. DFT is able to approximate the correlation effects in electrons instead of ignoring them and does not depend on the orbitals which are used to solve the Schrödinger equation. Instead, DFT defines the system in terms of its electron density,

$$n(\mathbf{r}) = \sum_i |\psi_i(\mathbf{r})|^2 \tag{3.16}$$

and defines the energy as a functional of this electron density i.e. $E[n]$. As was the case in the description of the Hartree-Fock method, the Born-Oppenheimer approximation is assumed.

3.3.1 The Hohenberg-Kohn Theorems

Before exploring the idea of representing the energy of a system of atoms and their electrons as a functional of the electron density, two very important theorems need to be discussed.[28]

Theorem 3.1. *The external potential $\hat{V}_{\text{ext}}(\boldsymbol{r})$, and hence the total energy, is a unique functional of the electron density $n(\boldsymbol{r})$.*

This energy *functional* $E\left[n(\mathbf{r})\right]$ can be written in terms of the external potential $v_{\text{ext}}(\mathbf{r})$ as

$$E\left[n(\mathbf{r})\right] = \int n(\mathbf{r})\hat{v}_{\text{ext}}(\mathbf{r})\mathrm{d}\mathbf{r} + F\left[n(\mathbf{r})\right] \tag{3.17}$$

where $F\left[n(\mathbf{r})\right]$ is an unknown functional of the electron density $n(\mathbf{r})$. Next, a Hamiltonian for the system can be constructed in such a way that the electron wavefunction $\Psi = \psi(\mathbf{r}_i)$ which minimises the expectation value gives the groundstate energy

$$E\left[n(\mathbf{r})\right] = \langle\Psi|\hat{\mathcal{H}}|\Psi\rangle\,. \tag{3.18}$$

The Hamiltonian can be rewritten as

$$\hat{\mathcal{H}} = \hat{F} + \hat{V}_{\text{ext}} \tag{3.19}$$

where $\hat{F}$ is the electronic Hamiltonian consisting of the kinetic energy operator $\hat{T}$ and electron-electron interaction operator $\hat{V}_{\text{ee}}$

$$\hat{F} = \hat{T} + \hat{V}_{\text{ee}} \tag{3.20}$$

The electronic Hamiltonian $\hat{F}$ is the same for all N electron systems, so $\hat{\mathcal{H}}$ is completely defined by the number of electrons N and external potential v_{ext}.

Proof. Suppose there are two different potentials $\hat{V}_{\text{ext}_1}$ and $\hat{V}_{\text{ext}_2}$ which will give the same electron density $n(\mathbf{r})$. These two potentials belong to two different Hamiltonians $\hat{\mathcal{H}}_1$ and $\hat{\mathcal{H}}_2$ which act upon two different, distinct wavefunctions $\Psi_1(\mathbf{r})$ and $\Psi_2(\mathbf{r})$, respectively. Invoking the *Variational Principle*[29] gives

$$E_1 = \langle \Psi_1 | \hat{\mathcal{H}}_1 | \Psi_1 \rangle < \langle \Psi_2 | \hat{\mathcal{H}}_1 | \Psi_2 \rangle \,. \tag{3.21}$$

Recall that the Hamiltonians can be written as follows

$$\hat{\mathcal{H}}_1 = \hat{F} + \hat{V}_{\text{ext}_1} \tag{3.22}$$

$$\hat{\mathcal{H}}_2 = \hat{F} + \hat{V}_{\text{ext}_2} \tag{3.23}$$

and as a result, through substitution, the following relation can be derived for the Hamiltonian

$$\hat{\mathcal{H}}_1 = \hat{\mathcal{H}}_2 + \hat{\mathcal{H}}_1 - \hat{\mathcal{H}}_2 \tag{3.24}$$

Going back to equation 3.21, the inequality can be rewritten as

$$E_1 < \langle \Psi_2 | \hat{\mathcal{H}}_2 | \Psi_2 \rangle + \langle \Psi_2 | \hat{\mathcal{H}}_1 - \hat{\mathcal{H}}_2 | \Psi_2 \rangle \tag{3.25}$$

which finally gives the relation

$$E_1 < E_2 + \int n_0(\mathbf{r}) \left[V_{\text{ext}_1} - V_{\text{ext}_2}\right] \mathrm{d}\mathbf{r}. \tag{3.26}$$

Doing the same treatment of E_2 gives

$$E_2 < E_1 - \int n_0(\mathbf{r}) \left[V_{\text{ext}_1} - V_{\text{ext}_2}\right] \mathrm{d}\mathbf{r}. \tag{3.27}$$

Adding together equations 3.26 and 3.27 finally gives the relation

$$E_1 + E_2 < E_2 + E_1 \tag{3.28}$$

This is clearly a violation and as a result, through proof by *reductio ad absurdum*, no two external potentials can give the same electron density - there is a one-to-one correspondence between the electron density and the external potential. □

Theorem 3.2. *The groundstate energy can be obtained variationally: the density that minimises the total energy is the exact groundstate energy.*

Since the first theorem proves the external potential $\hat{V}_{\text{ext}}$ is uniquely determined by the density (and in turn, this external potential uniquely determines the ground state wavefunction), all other observable quantities in the system are also uniquely determined. This means the energy can be written as a functional of the density, i.e.,

$$E = E[n(\mathbf{r})]. \tag{3.29}$$

A very important consequence of this is that if every Energy E has a corresponding electron density $n(\mathbf{r})$, an electron density which gives the minimum energy E_0 must exist.

Proof. The ground state energy E_0 will have a corresponding ground state electron density $n_0(\mathbf{r})$ calculated by

$$E_0[n_0(\mathbf{r})] = \langle \Psi_0 | \hat{\mathcal{H}}_0 | \Psi_0 \rangle \,. \tag{3.30}$$

Employing the variational principle again, a different electron density $n(\mathbf{r})$ will give a higher energy

$$E_0[n_0(\mathbf{r})] = \langle \Psi_0 | \hat{\mathcal{H}}_0 | \Psi_0 \rangle < \langle \Psi | \hat{\mathcal{H}}_0 | \Psi \rangle = E \tag{3.31}$$

hence, there exists an electron density - the ground state electron density, which minimises this expectation value of the energy, giving the ground state energy. □

Looking back at equation 3.5, recall that the Hamiltonian is currently comprised of three components,

$$E[n(\mathbf{r})] = \langle \Psi | \hat{\mathcal{H}} | \Psi \rangle = \langle \Psi | \hat{T}_e | \Psi \rangle + \langle \Psi | \hat{V}_{\text{ext}} | \Psi \rangle + \langle \Psi | \hat{V}_{ee} | \Psi \rangle \,. \tag{3.32}$$

We can reinsert the unknown functional $\hat{F}[n(\mathbf{r})] = \hat{T}_e + \hat{V}_{\text{ee}}$ (equation 3.20) to get

$$E[n(\mathbf{r})] = \hat{V}_{\text{ext}}[n(\mathbf{r})] + \hat{F}[n(\mathbf{r})] \tag{3.33}$$

What is important to note about equation 3.33 is that each term is now dependent entirely on the electron density $n(\mathbf{r})$. The problem is that there is still no way of solving this equation because $\hat{F}[n(\mathbf{r})]$ is still unknown.

3.3.2 The Kohn-Sham equations

It was about a year later that Kohn and Sham developed a method for calculating the ground state density - a method[30] which is now called *Density Functional Theory* (DFT). Instead of considering a fully interacting system with a real potential, a fictional, non-interacting system where the electrons move within what is called the *Kohn-Sham* (KS) single-particle potential, $\hat{V}_{\text{KS}}(\mathbf{r})$ is considered. This paradigm generates the famous KS equation[6]

$$\left[-\frac{\hbar}{2m} \nabla^2_{\mathbf{r}} + \hat{V}_{\text{KS}}(\mathbf{r}) \right] \chi_i(\mathbf{r}) = \epsilon_i \chi_i(\mathbf{r}) \tag{3.34}$$

where, as in equation 3.14, a wavefunction of a non-interacting set of particles can be rewritten as a Slater determinant of single-particle orbitals $\chi_i(\mathbf{r})$. ϵ_i is the appropriate

[6]Here, as in the previous section, the wavefunction $\chi_i(\mathbf{r})$ is also dependent on the spin ω of the electron as well as the position $\mathbf{r}$. This ω has been removed but its dependence is implied.

energy eigenvalue of each of the non-interacting single particle wavefunctions and as before, the electron density $n(\mathbf{r}) = \sum_{i=1}^{N} |\chi_i(\mathbf{r})|^2$. The KS potential, is a proposed substitution for $\hat{F}$ and is defined as

$$\hat{V}_{\mathrm{KS}}(\mathbf{r}) = \hat{V}_{\mathrm{ext}}(\mathbf{r}) + \hat{V}_{\mathrm{H}}(\mathbf{r}) + \hat{V}_{\mathrm{XC}}(\mathbf{r}) \tag{3.35}$$

where $\hat{V}_{\mathrm{ext}}$ is again, an effective potential created as a result of the fixed nucleic Coulomb repulsion, $\hat{V}_{\mathrm{H}}$ is the *Hartree Potential*, defined as

$$\hat{V}_{\mathrm{H}}(\mathbf{r}) = \int \frac{n(\mathbf{r})}{|\mathbf{r} - \mathbf{r}'|} \mathrm{d}\mathbf{r}' \tag{3.36}$$

and $\hat{V}_{\mathrm{XC}}$ is the *exchange-correlation* (XC) potential, defined as

$$\hat{V}_{\mathrm{XC}}(\mathbf{r}) = \frac{\delta E_{\mathrm{XC}}[n(\mathbf{r})]}{\delta n(\mathbf{r})}. \tag{3.37}$$

An important point is that solving the KS equation, will (in principle) give the exact groundstate electron density $n_0(\mathbf{r})$. Unfortunately, the issue now is that the XC functional $E_{\mathrm{XC}}[n(\mathbf{r})]$[7] is unknown. As a result, many approximations have been developed for this functional. Famous examples include the *Local Density Approximation* (LDA)[31] (and its spin polarised equivalent, the Local *Spin* Density Approximation (LSDA)) and the *Generalised Gradient Approximation* (GGA).[32] In terms of Energy, these two functionals will take the general form of

$$E_{\mathrm{XC}}^{\mathrm{LSDA}}([n(\mathbf{r})], \omega) = \int \epsilon_{\mathrm{XC}}[n(\mathbf{r}), \omega] n(\mathbf{r}) \mathrm{d}\mathbf{r} \tag{3.38}$$

$$E_{\mathrm{XC}}^{\mathrm{GGA}}([n(\mathbf{r})], \omega) = \int \epsilon_{\mathrm{XC}}[n(\mathbf{r}), \nabla n(\mathbf{r}), \omega] n(\mathbf{r}) \mathrm{d}\mathbf{r}. \tag{3.39}$$

The LDA XC functional is dependent solely upon the value of the electron density at each point in space while the GGA XC functional also depends on how the electron density varies from point to point (hence $\nabla n(\mathbf{r})$).

[7] If an exact, analytical solution for $E_{\mathrm{XC}}[n(\mathbf{r})]$ were to be found, this would be a huge deal for computational and theoretical chemistry. Much like the Hohenberg-Kohn theorems, the existence of the XC functional tells us a solution exists, but gives no insight into what that solution may be.

Often, these approximations find less than satisfactory results, however. A famous example is the failure of the LDA to predict the correct structure of Fe. Using the LDA, Fe's most stable structure is a non-magnetic face centred cubic structure,[33] contrary to the ferromagnetic, body centred cubic structure found in nature. The GGA predicts the correct structure.

3.3.3 The SCF Method

To summarise what has been discussed up till now, solving the KS equation requires the Hartree Potential V_{H} to be defined, but in order to define V_{H}, the electron density $n(\mathbf{r})$ needs to be known, this in turn requires a definition of the single-electron KS orbitals $\chi(\mathbf{r})$ which in turn, are found by solving the KS equation. This kind of paradigmatic loop can be solved *iteratively* through what is called the *Self Consistent Field* (SCF) method and is depicted in figure 3.1 as a flowchart. Before discussing this figure, an important comment needs to made on the idea of *convergence*. A DFT code will typically *converge* a calculation with respect to two quantities: the change in total energy of the system ΔE_{tot} and the change in KS potential energy ΔV_{KS}. Convergence is achieved when these two quantities have become sufficiently small from iterating over the SCF loop [8].

The first step in the DFT calculation is to calculate the external potential V_{ext}. The code will generally do this based on the input the user gives. The input will typically be the positions of the atomic nuclei, their Z (or species in DFT nomenclature) and their spacings (lattice parameters, primitive axes angles, etc.). Following this, the code will make a *guess* for $n(\mathbf{r})$. Now the SCF loop starts where the electron density is inserted and the KS potential is calculated. This in turn, is used to solve the KS equation whose eigenstates can then be used to calculate a new electron density. At this point, the code will find ΔE_{tot} and ΔV_{KS}. If the change is large, the code will generate a new electron density based upon the old one (Broyden Mixing[34]) and restart the SCF loop. If the change is small and meets the convergence criteria, the SCF loop will finish and the

[8] Actually, there are other important quantities for checking the convergence of a DFT calculation, but these quantities are variables which are separate from the SCF loop and will be discussed later.

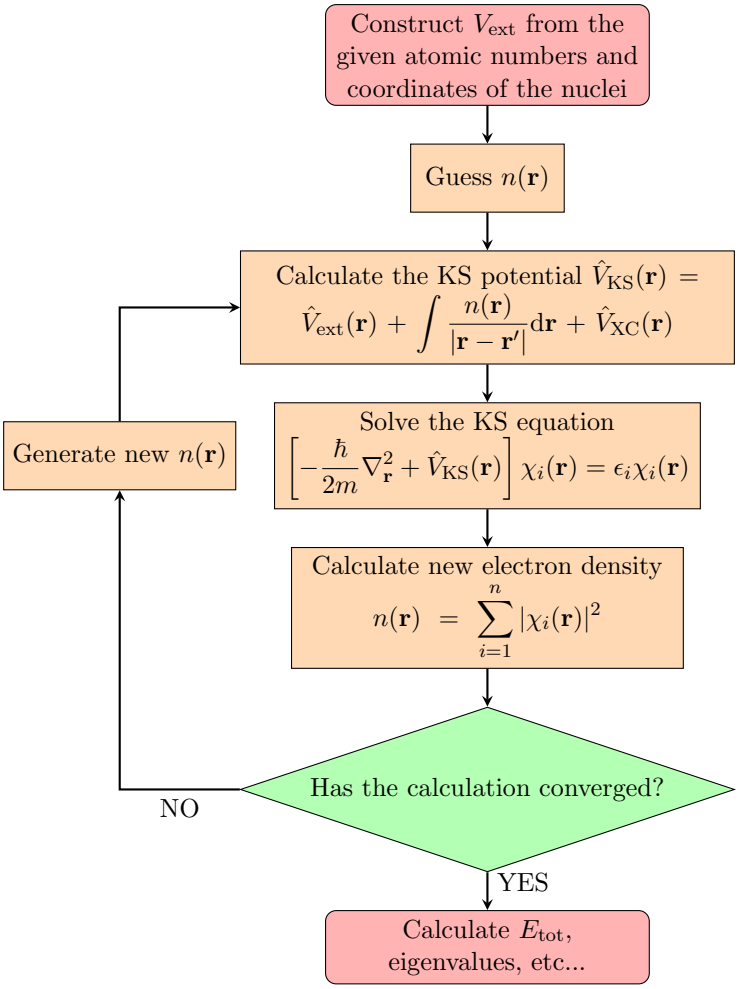

Figure 3.1: Flowchart depicting the self consistent field method for computing a DFT calculation using the KS equation.

various quantities of interest will be computed.

3.4 The Linearised Augmented Planewave Method

A substantial bulk of the theoretical work performed in this thesis has utilised a method for solving the KS equation by separating the wavefunctions χ_i into a set of two distinct sets of basis functions. This method is called the *Linearised Augmented Planewave* (LAPW) method.[35] The method proposes the approximation that, near the atomic nucleus, the potential and wavefunctions are similar to those inside the atom. They vary strongly, but are nearly spherical in shape. Further away from the nucleus, in the *interstitial* region between atomic nuclei, the potential and wavefunctions are smoother.

The LAPW method separates the definitions of the wavefunctions into two regions as a result: the interstitial region and the spherical region (figure 3.2, and in these different regions the wavefunctions are defined differently. Explicitly, these definitions of the

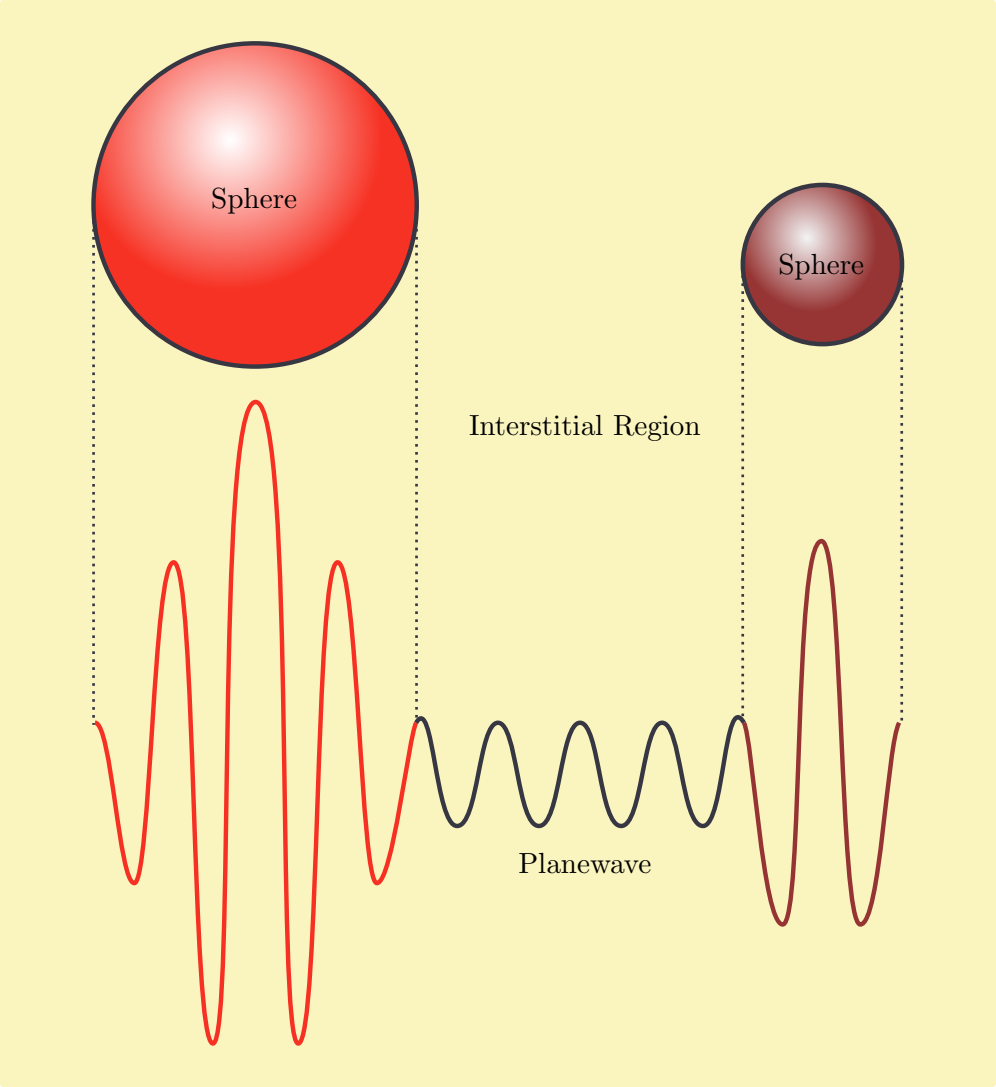

Figure 3.2: Sketch of the basic principle behind the LAPW method. Inside a specified radius, the wavefunction is described using a radial function whereas outside the sphere, the wavefunction is described using a planewave. The boundary behind these two different regions must retain the value and gradient of the functions.

wavefunctions are

$$\psi(\mathbf{r}) = \begin{cases} \Omega^{-\frac{1}{2}} \sum_{\mathbf{G}} c_{\mathbf{G}} e^{i(\mathbf{G}+\mathbf{k})\cdot\mathbf{r}} & \mathbf{r} \in \text{interstitial} \\ \sum_{lm} \left(A_{lm} u_l(r) + B_{lm} \dot{u}_l(r) \right) Y_{lm}(\mathbf{r}) & \mathbf{r} \in \text{sphere} \end{cases} \tag{3.40}$$

where Ω is the volume of the unit cell, $\mathbf{G}$ is the general reciprocal lattice vector, $\mathbf{k}$ is the principle wave vector, A_{lm}, B_{lm} and $c_{\mathbf{G}}$ are expansion coefficients, u_l is a solution to the radial Schrödinger equation at each band energy, $\dot{u}_l = \partial u_l / \partial E$, and Y_{lm} is the radial component of the wavefunction. Solving the expansion coefficients requires that the wavefunctions inside the sphere match the planewaves at the sphere-interstitial boundary in both value and gradient. Once the LAPWs have been defined, the solutions yield band energies for each value of $\mathbf{k}$. The DFT code which implements the LAPW method used in thesis is the ELK code.[36]

3.5 GAMESS

The *General Atomic* and *Molecular Electronic Structure System* (GAMESS)[37] is an *ab initio* quantum chemistry code which can calculate a set of self-consistent molecular wavefunctions, given an input molecule or cluster of atoms. These molecular orbitals are constructed through a linear combination of atomic orbitals (LCAO). More succinctly, the molecular wavefunction Φ is described using a basis set of a linear sum of atomic orbitals, i.e,

$$\Phi(\mathbf{r}) = \sum_k c_k \psi_k(\mathbf{r}) \tag{3.41}$$

where c_k are expansion coefficients calculated using the variational principle and ψ_k are a special type of wavefunction called a *basis function*. It is important that sensible values for these coefficients be given and it is the aim of the GAMESS code to calculate suitable values for these coefficients. Since GAMESS is a wavefunction based code, the method for solving the Schrödinger equation is done through the same means as the Hartree-Fock method. As in the Hartree-Fock and DFT sections, the expansion coefficients are calculated through an SCF loop.

The number of atomic orbitals ψ_k used is very important as they improve the accuracy of the calculation. To reach the exact Hartree product, an *infinite* number of atomic orbitals need to be used. This is quite an impossibility and so, much research has been invested into defining these so called *basis sets* to ease the computational burden, a very

large majority of which are hosted online at the EMSL Basis Set Exchange.[38] Examples of commonly used basis sets are

- *Minimal* - one atomic orbital is used for each occupied orbital in the atom (for example, one atomic orbital is used to model the $1s$ electron in H).
- *Double Zeta* (DZ) - two atomic orbitals are used for each occupied orbital in the atom. Gives better results because of more well described geometry, but still gives poor energy values.
- *Triple Zeta* (TZV) - three atomic orbitals for each atom, with the addition of a polarisation function.

The actual form of these atomic orbitals is often defined as a linear combination of Gaussian orbitals due to them being relatively light on a computational level.[39]

The wavefunctions calculated using GAMESS are processed using a software package called *wxMacMolPlt*.[40] wxMacMolPlt allows the visualisation and processing of GAMESS' outputs and in particular, allows the the user to export specific orbitals from the GAMESS output. In order to do this, the real space wavefunctions are sampled using an $N \times N \times N$ mesh enclosing the atom or molecule of interest. N is directly related to the resolution of the wavefunction (and therefore, also the MCP) so it is a necessity to make N as large as reasonably possible.

A number of operations are required in order to relate the real-space wavefunctions calculated in GAMESS to a momentum-space 1D MCP. These have been outlined by Saenz *et al.*[41] and adapted in figure 3.3. Starting from the outputted wavefunction $\psi_j(\mathbf{r})$, there are two different ways to calculate a MCP: The *Momentum-Space method* and the *Position-Space method*. The momentum-space method requires a *3D Fourier Transform* (3D-FT) of the wavefunction, yielding $\tilde{\psi}_j(\mathbf{p})$ which can then be used to calculated the momentum density $n_j(\mathbf{p})$. This subsequently can either be projected to give the spin dependent EMD (which can then be summed to give a directional MCP) or doubly integrated to give the 1D-EMD which can be integrated to give the directional MCP. The position-space method requires no determination of the EMD at all. Instead, determination of the *autocorrelation* (AC) functions $B_j(\mathbf{s})$ and $B_j(s)$ can be performed.

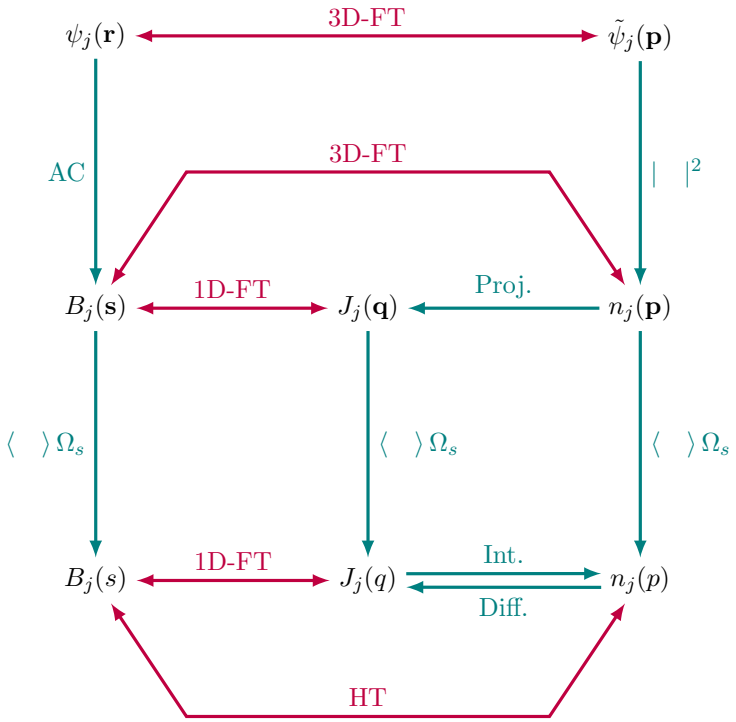

Figure 3.3: The scheme for calculating the directional specific MCP $J(\mathbf{q})$ and spherically averaged MCP $J(q)$ from an orbital j. 1D and 3D-FT are 1D and 3D Fourier transforms respectively, $|\ \ |^2$ is the modulus squared, AC is the autocorrelation, Proj. is the projection of the momentum density $n_j(\mathbf{p})$ along the scattering vector, $\langle\ \ \rangle\Omega_s$ is the spherical average obtained using double integration, Int. is an integration, Diff. is a differentiation and HT is the Hankel transformation.

3.6 The SPR-KKR Method

The *Spin-Polarised Relativistic Korringa-Kohn-Rostoker* (SPR-KKR) method[42] has been used in this thesis for studying the disorder effects in Co_2MnSi. Initially, the theory for the multiple scattering of electrons in a solid was formalised by Korringa in terms of wavefunctions[43] but later on, was generalised in terms of Green's functions by Kohn and Rostoker.[44]

SPR-KKR is a Green's function based method for solving the Kohn-Sham equations. Rather than attempting to find the single electron states $\chi_i(\mathbf{r})$, the KKR method instead calculates the corresponding single-electron, multiple-scattering Green's function $G(\mathbf{r}, \mathbf{r}', E)$, defined by

$$\left[E + \frac{\hbar^2}{2m}\nabla^2 - V(\mathbf{r})\right] G(\mathbf{r}, \mathbf{r}', E) = \delta(\mathbf{r} - \mathbf{r}'). \tag{3.42}$$

From this equation, useful, observable quantities can be calculated. For example (and perhaps most importantly), the electron density can be calculated as

$$n(\mathbf{r}) = -\frac{1}{\pi}\Im\left(\int_{-\infty}^{E_F} G(\mathbf{r},\mathbf{r}',E)\mathrm{d}E\right) \tag{3.43}$$

which can be solved by self consistently solving equation 3.42 by varying the effective potential $V(\mathbf{r})$.

The code has been developed with the aim of calculating the spectroscopic properties of magnetic solids and as such, has support for calculating the spectra of techniques such as X-ray Absorption Spectroscopy, X-ray Magnetic Circular Dichroism and importantly (for the applications of this thesis), MCPs. Site specific MCPs can also be generated through editing the plotting files.

SPR-KKR can also model disorder in solids through the use of the *Coherent Potential Approximation* (CPA).[45] This has been used to model the effects of disorder introduced to the Co_2MnSi compound.

3.7 Convergence

The idea of convergence is extraordinarily important when using a computational code to calculate the electronic properties of a system. The predicted values of important macroscopic properties such as magnetic moment, Fermi level and band structure properties can vary greatly if a calculation is not sufficiently converged.

The goal of convergence is to minimise the total energy of the system. By setting a change in energy (and potential threshold), the calculation is *converged* once these two threshold criteria are reached. As an example, the default threshold values in ELK for the change in the KS potential and the change in total energy are 1×10^{-6} Hart. and 1×10^{-4} Hart. respectively. Only when the changes in the KS potential and total energy are smaller than these values will the calculation be converged. This section outlines a few of the other criteria which need to be monitored to return a successful calculation.

3.7.1 k-point Convergence

Arguably the most important parameter when it comes to the convergence of a DFT calculation is the number of k points used in the calculation. The more k points used, the larger the number of planewaves used to model the interstitial region of the system, hence, the calculation is more accurate[9]. Figure 3.4 shows how the total energy and total moment of a system changes as the number of k points is varied. Whilst there are other parameters which factor into the convergence of a calculation, the number of k points in this case plays a very dominant role. The number of k points used in a

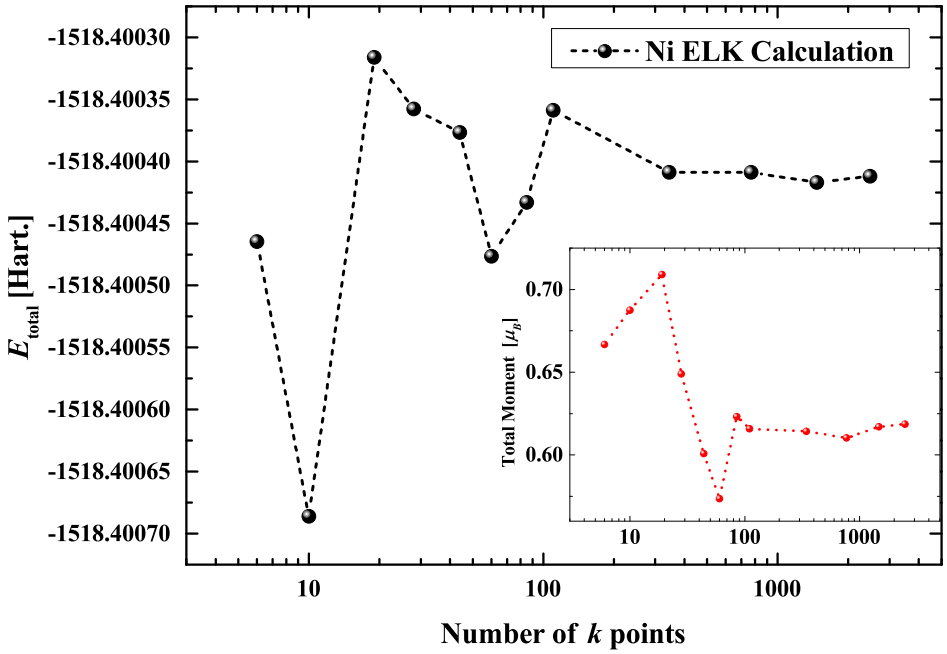

Figure 3.4: The convergence of a Ni calculation with respect to number of k points. Only after ~ 300 k points does the variation in total energy and total moment start to stabilise.

calculation is generally specified as along the three principal axes. If M is the number of k points, the specification will therefore be $M \times M \times M$. An important point is that because these k points are specified in reciprocal space, the number of k points required

[9]It's important to be careful when using the word *accurate* here. Accuracy does not mean the calculation is more representative of reality, accuracy is how little the results will change, should parameters such as the number of k points be changed.

is inversely proportional to the lattice parameters (the longer the lattice parameter, the less k points needed).

3.7.2 Energy Cutoff

As the interstitial planewaves are periodic, they need to obey Bloch's theorem (see §2.4), which describes the wavefunction of a particle in a periodic potential. Since $u_{\mathbf{k}}(\mathbf{r})$ is periodic, it can be expanded in terms of a unique set of planewaves, i.e.,

$$u_{\mathbf{k}}(\mathbf{r}) = \sum_{\mathbf{G}} c_{\mathbf{G}} e^{i(\mathbf{G}\cdot\mathbf{r})}. \tag{3.44}$$

Inserting equation 3.44 into equation 2.17 gives

$$\varphi_{\mathbf{k}}(\mathbf{r}) = \sum_{\mathbf{G}} c_{\mathbf{k}+\mathbf{G}} e^{i(\mathbf{k}+\mathbf{G})\mathbf{r}}. \tag{3.45}$$

Due to the sum being over $\mathbf{G}$, an issue arises for solids as there are an infinite number of possible $\mathbf{G}$ vectors. This initially suggests this function to be unsolvable. Fortunately, there is a way of limiting the number of $\mathbf{G}$ vectors which are included in the sum, and this is related to the E eigenvalues obtained when solving the Schrödinger equation with such wavefunctions.

Solutions of the Schrödinger equation will have kinetic energy

$$E = \frac{\hbar^2}{2m}|\mathbf{k}+\mathbf{G}|^2. \tag{3.46}$$

Solutions which give lower energy values are much more likely to physical compared to higher energies, and so a *cutoff* energy can be defined where wavefunctions which give certain E eigenvalues higher than the cutoff, will be disregarded. As a result, the infinite sum in equation 3.45 can be altered to only include solutions with kinetic energy less than the cutoff energy, defined as

$$E_{\text{cut}} = \frac{\hbar^2}{2m}G_{\text{cut}}^2 \tag{3.47}$$

This reduces equation 3.45 to

$$\varphi(\mathbf{r}) = \sum_{|\mathbf{k}+\mathbf{G}|<G_{\text{cut}}} c_{\mathbf{k}+\mathbf{G}} e^{i(\mathbf{k}+\mathbf{G})\cdot\mathbf{r}}. \tag{3.48}$$

This means that E_{cut} is another parameter which must be investigated when attempting to converge a DFT calculation. Figure 3.5 shows how varying E_{cut} affects the total energy of a Ni calculation.

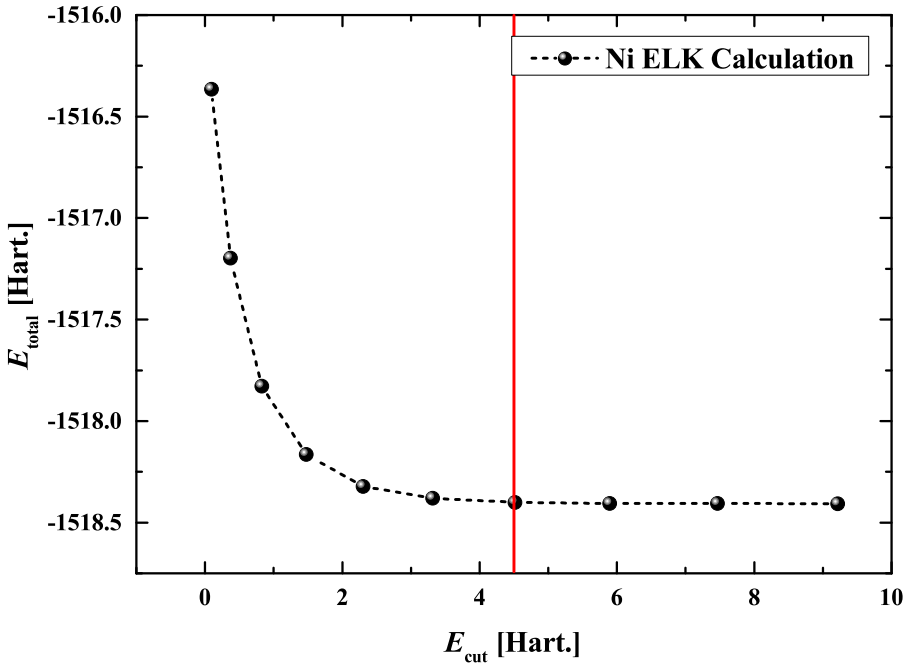

Figure 3.5: The convergence of a Ni calculation with respect to the cut-off energy E_{cut}. The LDA XC functional was used with 300 k points. The red line is the code's default value for E_{cut} ($\sim$ 4.5 Hartree for Ni). Clearly, this is a very reasonable default value as at this value, the change in E_{total} is very small. However for other systems, convergence with respect to E_{cut} needs to be checked as macroscopic quantities such as total moment (and therefore, the band structure of the material) will vary drastically if the calculation is poorly converged.

3.7.3 Lattice and Geometry Optimisation

Lastly, convergence (or perhaps, optimisation) of the structure of the system is necessary to obtain accurate groundstate properties for a system. This is quite important for rare-

Earth materials (such as CeB_6) due to the narrowness of the $4f$ band. The sharp $4f$ band's position relative to E_F will drastically change the macroscopic properties of such a material. As such, finding the correct ground-state lattice parameter is very important. This lattice parameter may not be exactly the same as the experimental lattice parameter due to the fact that DFT is working within a fictitious set of KS orbitals, at 0 K. As a result, it is important to study how the macroscopic properties and band structure of the system vary with changes in the lattice parameter.

The general procedure for optimising the structure of a material is to calculate the groundstate for a range of different lattice parameters, and then fit some equation of state (EOS) function to find the minimum value for the lattice constant. Figure 3.6 shows the lattice parameter optimisation of a Ni unit cell. This is quite a trivial exercise

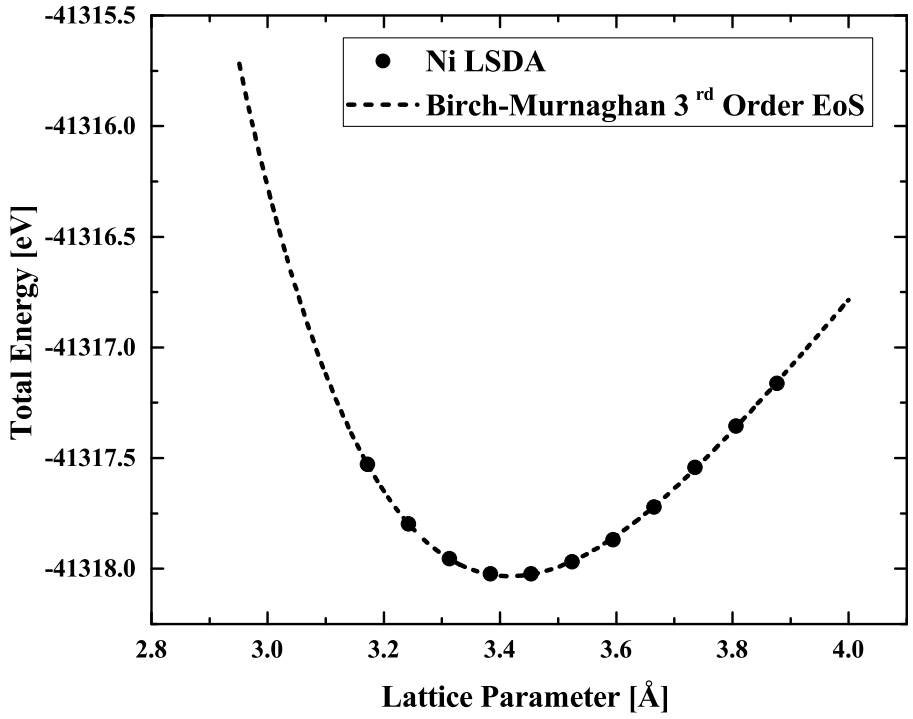

Figure 3.6: The lattice optimisation for the unit cell of Ni. The calculation was performed with ELK using the LSDA XC functional with 44 k points per calculation.

for cubic systems but for less symmetric systems, it becomes a more iterative process. For example, in the worst case scenario, where lattice parameters $a \neq b \neq c$, there are

too many variables to change in order to fit a simple EOS. Instead, it becomes another SCF-esque problem where the parameters are all varied slightly and the total energy is compared to the original calculation. This can also be done for the positions of the atoms themselves inside the unit cell as well as for the angles α, β and γ which define the coordinate system.

Chapter 4

The Theory of Compton Scattering and Experimental Magnetic Compton Scattering

In this chapter, the theoretical aspects behind the most prevalent experimental technique deployed in this thesis; high energy *Magnetic Compton Scattering* (MCS) will be discussed. Additionally, the various methods for analysing MCS data have been detailed Before discussing the technique further, it would be sensible to have a brief look at the principle behind the *Compton* effect.

Compton scattering is the inelastic scattering of a photon by an electron[1]. The scattered photon will experience a *shift* in its energy as a result of the collision (hence it being inelastic) and will travel in a different direction with a different energy. This change in energy is called the Compton *shift*. The situation has been pictured in figure 4.1 which depicts the Compton scattering of a photon by an electron.[46] From this scheme, the Compton shift is defined as

$$\lambda' - \lambda = \Delta\lambda = \frac{h}{m_e c}(1 - \cos\phi) \tag{4.1}$$

[1]It need not always be an electron which plays the role of the scatterer in Compton scattering, any charged particle will satisfy this mechanism. In this entire thesis however, an electron will always be the scatterer.

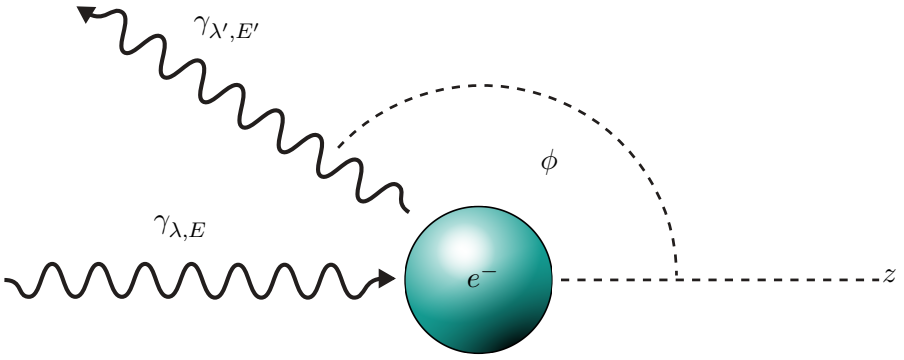

Figure 4.1: The inelastic scattering of a photon γ with wavelength λ and energy E by an electron, as described by the Compton effect. The inelastic scattering results in a photon with wavelength λ' and energy E'. The angle of the scattering event is ϕ. The scattering vector is defined along the z direction.

where λ and λ' are the wavelengths of the incident and scattered photon respectively, h is Planck's constant, m_e is the mass of the electron, c is the speed of light and ϕ is the scattering angle. In this picture, the electron is *stationary*, requiring its momentum to be zero ($|\mathbf{p}| = 0$). The scattering vector is defined to point along the z direction as the simplifies the formulae defined later. It is often more useful to write this equation in terms of the respective energies of the photon, in which case the Compton shift is defined as

$$E' = \frac{E}{1 + (E/m_e c^2)(1 - \cos\phi)}. \tag{4.2}$$

This shift in energy can be directly observed on a Compton scattering experiment by observing the spectrum measured as shown in figure 4.2. Here, the large, lower energy peak corresponds to the photons inelastically scattered by the electrons in the sample. These photons will experience a Compton shift in their wavelength and hence, will have energy E'. The small peak at high energy is the *elastic line* which corresponds to the photons which have been elastically scattered by the sample. These photons will not experience a Compton shift in their wavelength resulting in their scattered energy being the same as the incident photon energy, E. The peaks experience a broadness due to

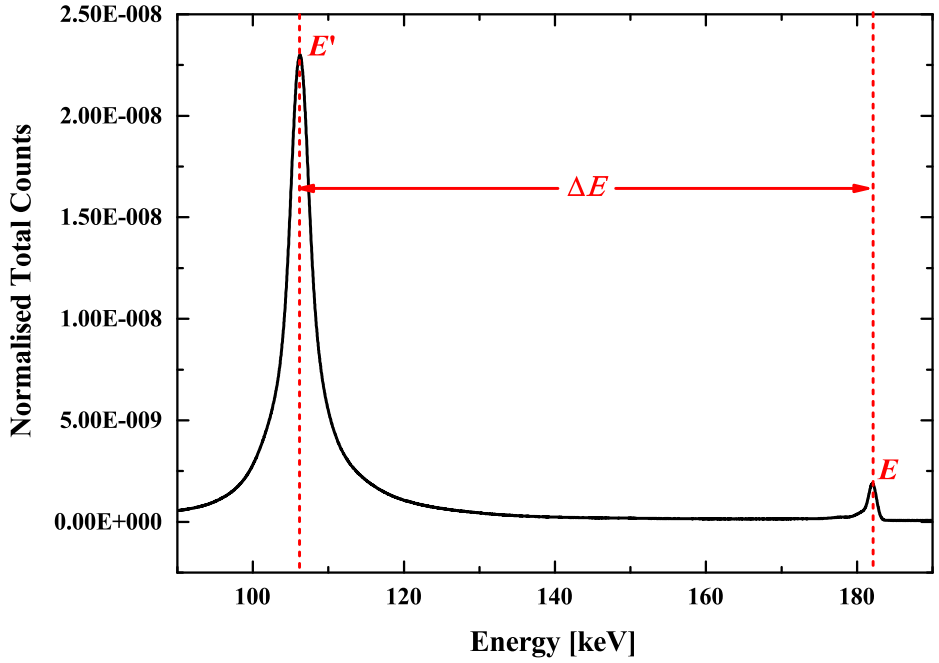

Figure 4.2: Energy spectrum of a $TbMn_2O_5$ sample measured on the BL08W beamline at SPring-8. The scattering angle is ~ 173 °. The left peak is the Compton profile and the right peak is the elastic line. The difference between these two peaks is the Compton shift.

the electronic motion in the sample.

4.1 History of Compton Scattering

4.1.1 Discovery of the Compton Effect

With the proposal of the *Photoelectric effect* by Einstein, much debate still surrounded the properties of radiation. Experiments such as the double slit experiment suggested that light acted much in the same way a wave might whilst the photoelectric effect suggested light had the properties of a particle. Between 1921 and 1922, Arthur H. Compton performed X-ray scattering experiments which gave very explicit evidence for the particle like properties of light. Compton used Mo K_α X-rays on samples of pyrex and graphite, and observed their shift in wavelength. He found that the shift was proportional to $\sin^2(\phi/2)$ and was able to generalise the relationship by deriving

the expression in equation 4.1. In 1923, these findings were later published in Physical Review.[47] The absolute evidence that light has particle-like properties was rewarded by the Nobel Prize in 1927 for the "discovery of the effect named after him".[48]

4.1.2 Early probing of the Electron Momentum Density

While the Compton effect's discovery made a monumental change to the intellectual landscape at the time, the applications of the effect weren't considered until the very early 1930s when DuMond recognised the importance of the electron motion in producing the Doppler broadened spectra. Measuring the Compton profile of a Be sample with monochromated Mo K_α radiation, DuMond showed that the classical Maxwell-Boltzmann and Bohr-Sommerfeld models were inadequate in describing the measured Compton Profile. It was only with a new model, incorporating Fermi-Dirac statistics and a dependence on the Pauli-exclusion principle, did the theoretical description agree with the experimental data.

Only in the wake of very high energy synchrotron sources did high resolution Compton scattering start to become harnessed. As will be seen in the following sections, the incident X-ray energy has a huge impact on the quality and resolution of the data collected.

4.2 Scattering Cross-sections

Equation 4.1 derived by Compton is for when the electron is stationary. Electrons in materials do have motion and is evident in the broadening of the measured peaks in figure 4.2. For electrons which experience transfers in energy greatly above that of the binding energy, the interaction between the photon and the electron will be *impulsive*. For a reference, the energy of the X-rays produced on the BL08W beamline are ~ 220 keV. This means the potential the electron finds itself in before and after the interaction is the same, or more succinctly, the electron does not experience an excitation. With this *impulse approximation*, only the kinematics of the interaction need to be considered,

and the change in energy can be written as

$$E' - E = \Delta E = \frac{1}{2m_e}\left[\mathbf{p} + \hbar(\mathbf{k} - \mathbf{k}')\right]^2 = \frac{\hbar^2\mathbf{q}^2}{2m_e} + \frac{\hbar\mathbf{q}\cdot\mathbf{p}}{m_e} \tag{4.3}$$

where $\mathbf{p}$ is the initial momentum of the electron and $\mathbf{q} = \mathbf{k} - \mathbf{k}'$, the difference between the incident and scattered wavevectors of the scattered photon. This equation is essentially the energy lost as a result of the photo-electron interaction. The first term is the Compton shift as mentioned previously, only this time, there is an additional *Doppler broadening* term which scales linearly with the electron momentum $\mathbf{p}$.

It is now important to study the scattering cross-section for a Compton Scattering event. The scattering cross-section describes the strength of the interaction between the particles. To be more succinct, the scattering cross-section describes the likelihood of a scattering event occuring - it can be normalised to be a probability. For classical scattering (*Thomson* scattering), the cross-section is given by

$$\left(\frac{\mathrm{d}\sigma}{\mathrm{d}\Omega}\right)_{\mathrm{Tom}} = \frac{r_e^2}{2}\left(1 + \cos\phi\right) \tag{4.4}$$

where r_e is the classical (or Lorentz) radius of the electron. However, this does not take into account relativistic effects associated with the incident photon nor the scattering electron. As the incident energy increases towards a substantial fraction of mc^2, the Thomson scattering cross section becomes less valid. Klein and Nishina proposed a general form of the photon-electron scattering cross section, taking into account relativistic effects which the Thomson cross-section fails to incorporate.[49] The Klein-Nishina (KN) cross section is defined as

$$\left(\frac{\mathrm{d}\sigma}{\mathrm{d}\Omega}\right)_{\mathrm{KN}} = \frac{1/2r_e^2\left[1 + \cos^2\phi\right]}{\left[1 + 2\epsilon\sin^2\phi/2\right]^2}\left\{1 + \frac{4\epsilon^2\sin^4\phi/2}{\left[1 + \cos^2\phi/2\right]\left[1 + 2\epsilon\sin^2\phi/2\right]}\right\} \tag{4.5}$$

where $\epsilon = E/m_e c^2$. Plotting the KN cross-section for different incident energies is shown in figure 4.3. Here we can see that for very low energies, the cross-section tends towards that of a cosine function (as the cross-section is proportional to $\cos\phi$ in the Thomson scattering regime). For higher energies, the cross-section becomes more and

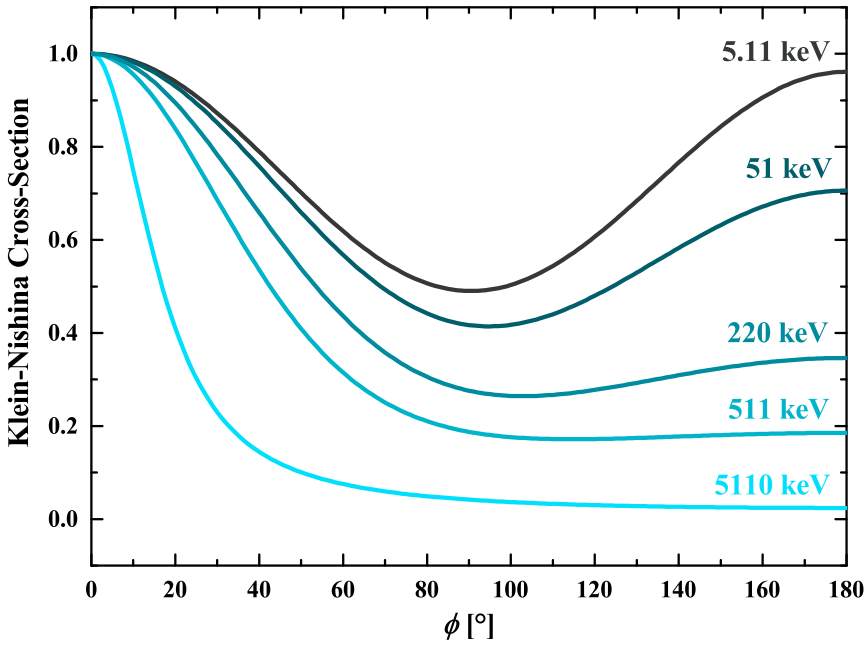

Figure 4.3: Klein-Nishina cross-section as a function of angle. As the incident energy E increases, the amount of back scattering drops drastically. For very low energies, the curve becomes more symmetric, reminiscent of the classical Thomson cross-section.

more asymmetric as relativistic effects play a more crucial role. As a result, the amount of back-scattered radiation diminishes greatly.

The KN cross-section however does not depend upon any parameters relating to the target electron (it is still considered stationary). The Compton scattering cross-section needs to be defined in order to give a more adequate description of the interactions at play during a Compton scattering event.

In 1954, Lipps and Tolhoek examined the work by Klein and Nishina but to take into account the type of scattering depicted in a Compton scattering event.[50,51] They presented the Compton scattering cross-section as

$$\frac{\mathrm{d}\sigma}{\mathrm{d}\Omega} = \frac{r_e^2}{4}\left(\frac{k'^2}{k^2}\right)\left[(1+\cos^2\phi) + (k-k')(1-\cos\phi) + \xi_1\sin^2\phi - \xi_3(1-\cos\phi)\hat{\boldsymbol{\varsigma}}\cdot(\mathbf{k}+\mathbf{k}'\cos\phi)\right] \tag{4.6}$$

which can then be separated into the charge and magnetic Compton scattering cross-

sections as

$$\left(\frac{\mathrm{d}\sigma}{\mathrm{d}\Omega}\right)_{\text{charge}} = \frac{r_e^2}{4}\left(\frac{k'^2}{k^2}\right)\left[(1+\cos^2\phi)+(\mathbf{k}-\mathbf{k}')(1-\cos\phi)+\xi_1\sin^2\phi\right] \tag{4.7}$$

$$\left(\frac{\mathrm{d}\sigma}{\mathrm{d}\Omega}\right)_{\text{mag}} = -\frac{r_e^2}{4}\left(\frac{k'^2}{k^2}\right)\left[\xi_3(1-\cos\phi)\hat{\boldsymbol{\varsigma}}\cdot(\mathbf{k}+\mathbf{k}'\cos\phi)\right]. \tag{4.8}$$

Here, ξ_1 and ξ_3 are Stokes parameters for the linearly and circularly polarised incident photons respectively, and $\hat{\boldsymbol{\varsigma}}$ is a unit vector for the direction of the electrons' spin polarisation. This can be manipulated with the application of an external magnetic field. The magnetic cross-section's dependence on ξ_3 is the reason circularly polarised X-rays are required. Linearly polarised X-rays would give a weaker magnetic signal compared to circularly polarised X-rays. This is because since the MCP is the result of a difference measurement, keeping the helicity of the incident radiation fixed allows the magnetic cross-sections to change sign with the reversal of the applied magnetic field. If linearly polarised X-rays were used, this difference measurement would not be possible.

Investigating the ratio of the charge and magnetic cross-sections (equations 4.7 and 4.8 respectively) give valuable insight into the scattering angle dependence of the cross-sections. The ratio of the magnetic signal to the charge signal is called the *magnetic effect*, R, written as

$$R = \frac{(\cos\phi-1)\xi_3\dfrac{\hbar E}{m_e c^2}\left[\cos\phi\cos\alpha+\dfrac{E'}{E}\cos(\phi+\alpha)\right]}{1+\cos^2\phi+\xi_1\sin^2\phi+\dfrac{\hbar(E-E')}{m_e c^2}(1-\cos\phi)} \tag{4.9}$$

where α is the angle between the incident photon direction and the magnetic field.[52] Figure 4.4 plots the magnetic effect against the scattering angle for a range of incident energies. As can be seen, a large magnetic signal requires the scattering angle to be as large as possible. It can also be seen that increasing the energy of the incident photons greatly enhances the magnetic signal. The consequences of the magnetic effect's dependence on energy and scattering angle influences the design of a MCS experiment in order to enhance the magnetic effect as much as possible.

These cross-sections are not able to provide anything which the experimentalist can

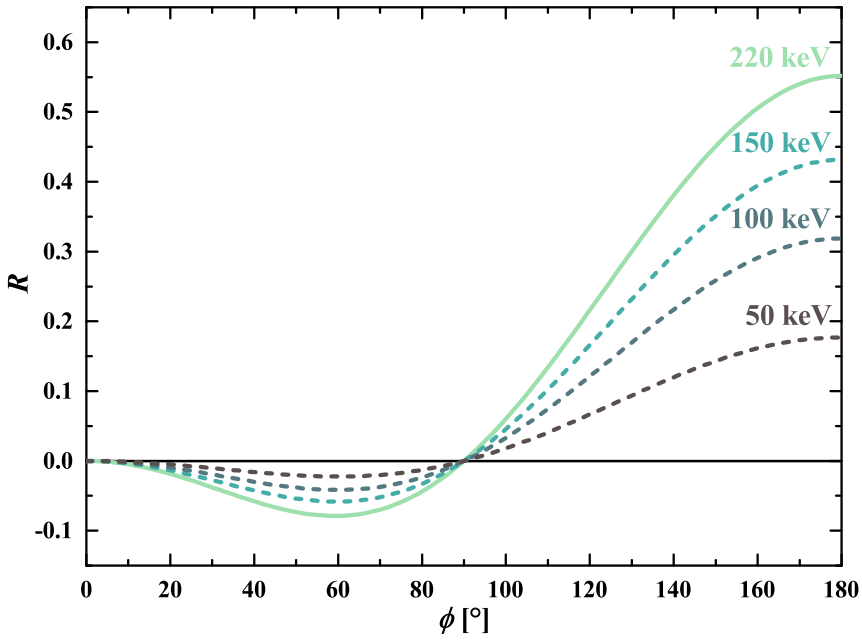

Figure 4.4: The magnetic effect, R plotted against the scattering angle, ϕ. For the fixed parameters, $\xi_1 = \xi_3 = 1$, $\alpha = (180 - \phi)/2$ where $\phi = 180$, $m_e c^2 = 511$ keV and $\hbar = 1$. The greatest magnetic signal is achieved when the angle and incident energy is large. The line representing $E = 220$ keV is solid because this is the energy of the incoming x-ray radiation on BL08w.

observe *experimentally*. While they provide insight into how the incident beam must be chosen (the coupling of the linearly and circularly polarised components, the scattering angle, the incident energy, etc.), they do not provide actual quantities which can be measured. For this, the *Doubly Differential Compton Scattering Cross-Section* (DDCSCS) needs to be introduced.

4.3 The DDCSCS and Compton Profiles

4.3.1 The Doubly Differential Compton Scattering Cross-Section

The DDCSCS can be written as a linear combination of the two Compton cross-sections as

$$\frac{\mathrm{d}^2\sigma}{\mathrm{d}E'\mathrm{d}\Omega} = \left(\frac{\mathrm{d}\sigma}{\mathrm{d}\Omega}\right)_{\text{charge}} J(p_z) + \left(\frac{\mathrm{d}\sigma}{\mathrm{d}\Omega}\right)_{\text{mag}} J_{\text{mag}}(p_z) \tag{4.10}$$

where $J(p_z)$ and $J_{\mathrm{mag}}(p_z)$ are the charge and *Magnetic Compton Profiles* (MCP) respectively.[53] They are one dimensional projections of the electronic and spin momentum densities, along the scattering vector z, defined as

$$J(p_z) = \frac{1}{n}\iint_{-\infty}^{\infty} \rho(\mathbf{p})\mathrm{d}\mathbf{p}_x\mathrm{d}\mathbf{p}_y \tag{4.11}$$

$$J_{\mathrm{mag}}(p_z) = \frac{1}{\mu}\iint_{-\infty}^{\infty} \left(\rho^{\uparrow}(\mathbf{p}) - \rho^{\downarrow}(\mathbf{p})\right)\mathrm{d}\mathbf{p}_x\mathrm{d}\mathbf{p}_y \tag{4.12}$$

where $\rho(\mathbf{p})$ is the momentum density of the electrons, $\rho^{\uparrow}(\mathbf{p})$ is the momentum density of the electrons polarised to be spin up, and $\rho^{\downarrow}(\mathbf{p})$ is the momentum density of the electrons polarised to be spin down. If the area under $J(p_z)$ is normalised to the number of electrons per formula unit (the atomic number), the area under $J_{\mathrm{mag}}(p_z)$ will be the spin moment per formula unit, μ_{spin}, i.e,

$$\int J(p_z)\mathrm{d}p_z = Z \tag{4.13}$$

$$\int J_{\mathrm{mag}}(p_z)\mathrm{d}p_z = \mu_{\mathrm{spin}}. \tag{4.14}$$

The reason magnetic Compton scattering is a probe of solely the total spin moment and insensitive to the magnetic orbital moment of a system is another consequence of the impulse approximation. Due to the very high energies involved, the interaction time is too short for the orbital motion of the electrons to be *sensed*.[54] This makes MCS an excellent probe of not only the spin moment of a system, but of a system's ground-state phenomena too. No excitations are observed using this technique.

$J_{\mathrm{mag}}(p_z)$ can be separated from $J(p_z)$ due to its dependence on ξ_3. Coupling to ξ_3 with the use of incident circularly polarised radiation means that the experimenter has two terms which can be reversed (have their sign changed) in order to isolate the MCP. The first way is by changing the helicity of the incident radiation. The second way is by reversing the magnetisation across the sample, changing the sign of $\hat{\boldsymbol{\varsigma}}$. Since the MCP is the difference between the spin-up and spin-down momentum densities, computation of the MCP causes a complete cancellation of any charge affects as well as background contributions to the profile.

4.3.2 Profile Shape

The Doppler broadening term in equation 4.3 means that the shape of the Compton profiles is heavily dictated by the momenta of the electrons. Tightly bound, core electrons have greater momenta compared to more delocalised electrons which are reflected in the larger contributions to the MCP at lower momentum. Figure 4.5 compares the theoretical *Relativistic Hartree-Fock* (RHF) profiles of the Co $3d$ orbital and the Ce $4f$ orbital. The Co $3d$ profile is more narrow than the Ce profile due the magnetic,

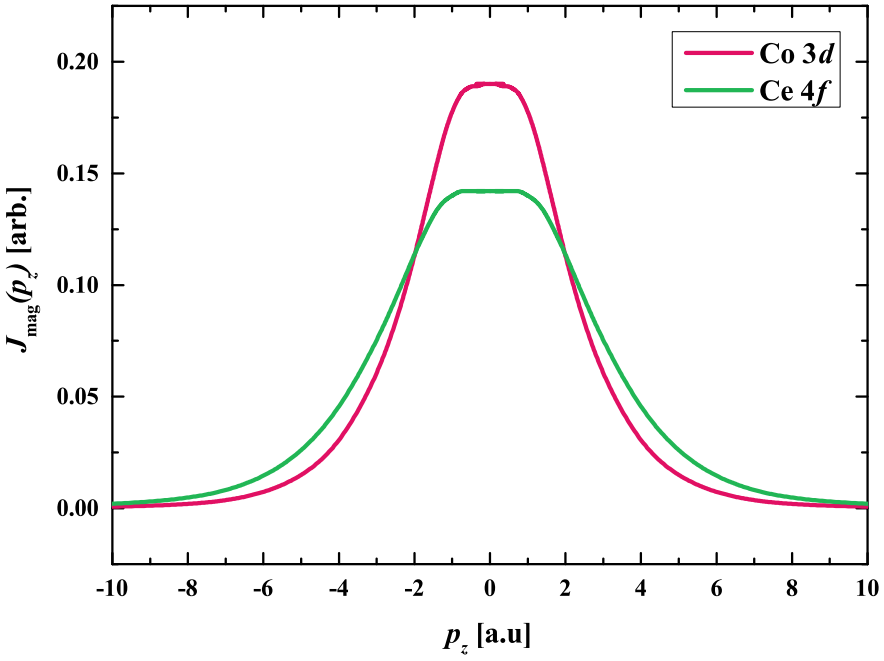

Figure 4.5: Theoretical Relativistic Hartree-Fock MCPs calculated for the Co $3d$ and Ce $4f$ bands. Both profiles have been normalised to the same area. The Ce $4f$ electrons are more localised than the Co $3d$ electrons and so, the Ce profile is broader than the Co profile.

unpaired electrons of Co occupying the $3d$ band. These d electrons are very delocalised and therefore, have a lower momenta, giving greater contributions to the MCP at low momentum values. Conversely, the Ce $4f$ profile is broader, indicating that instead, the magnetic electrons contributing to the profile are more localised. The real-space wavefunction $\psi(\mathbf{r})$ is related to the momentum-space wavefunction $\tilde{\psi}(\mathbf{p})$ by a 3D Fourier transform. A very broad, delocalised wavefunction in $\mathbf{r}$ will have narrow features in $\mathbf{p}$.

The momentum density $\rho(\mathbf{p})$ is then explicitly defined as

$$\rho(\mathbf{p}) = |\tilde{\psi}(\mathbf{p})|^2 = \frac{1}{(2\pi\hbar)^3}\left|\int_{-\infty}^{\infty}\psi(\mathbf{r})e^{-i\mathbf{p}\cdot\mathbf{r}}\mathrm{d}\mathbf{r}\right| \tag{4.15}$$

Studying the broadness of a MCP is important in identifying the contributing electrons, especially when studying heavier elements and compounds comprised of these elements. An example of this can be seen in the work of McCarthy *et al.* where the superposition of a Sm and Mn RHF profile is required to describe the experimental MCP.[55]

4.4 Experimental Magnetic Compton Scattering and Data Analysis

Following the detailing of the theory of MCS, it is now important important to discuss how an experiment is carried out at the synchrotron. The general experimental procedure is described here. Samples are loaded into a *Variable Temperature Insert* (VTI) which is placed inside the magnet upside-down. This geometry needs to be accounted for when aligning samples as the rotations about certain axes will need to be reversed. Once the sample is loaded and rotated into the correct alignment, the beam hutch can be closed and the sample can be aligned. After the alignment has been achieved and the required input parameters have been specified (magnetic field, temperature, scan number, etc), the experiment can be initiated. Typically, the number of scans is set to 15. This means there will be 15 scans before the field is flipped. The first field (positive) is denoted A whilst the negative field direction is denoted as B. For efficiency, scans 16 to 45 are all B fields to save time on flipping. Scans 46 to 60 are A fields. Having an equal number of A scans to B scans simplifies the normalisation of the MCPs.

Correctly calibrating MCS data is crucial to obtaining accurate results. The first level of data processing comes from normalising the count rates obtained for the measured Compton profiles. Figure 4.6 plots the raw Compton profiles of a Ni measurement. The only post-processing performed has been this initial normalisation. The peaks of the Compton profile and the Pb $K_{\alpha_{1,2}}$ and $K_{\beta_{1,2}}$ fluorescence are shifted for the

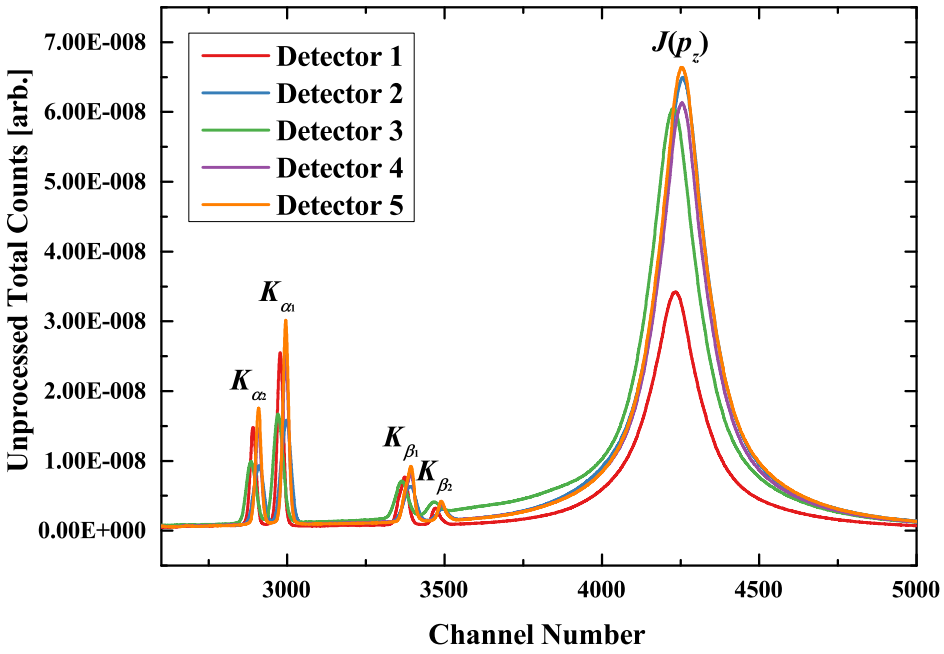

Figure 4.6: Unprocessed Ni [100] data collected at 1.7 K using an applied magnetic field of 1 T. Only 5 of the 10 detectors are shown for clarity. The different Compton profile peaks are in different positions due to needing calibration. This is accented by the shifting of the Pb $K_{\alpha_{1,2}}$ and $K_{\beta_{1,2}}$ peaks which are very well defined in energy. It is these fluorescence peaks which are used for calibration.

different detectors. In order to correct this, the energy spectra are calibrated based on the energies of the Pb absorption edges.[56] Since the absorption edges are well known, Gaussian profiles are fit to the energy peaks for the Pb. From this, the channel number of the peak can be determined and an energy calibration can be generated.

4.4.1 Relation between electron momentum and scattered photon energy

To move from an energy scale to a momentum scale along the scattering vector p_z, the relation derived by Holm[57] can be used,

$$p_z = \left[\frac{|\mathbf{q}|}{2} + \frac{(E' - E)}{2}\sqrt{1 + \frac{2mc^2}{E'E(1 - \cos\phi)}}\right] \cdot \frac{1}{\alpha mc^2}. \tag{4.16}$$

A factor of $1/\alpha mc^2 = 0.26817$ is necessary to give p_z in terms of atomic units (a.u.) and the energy in kilo-electron volts (keV). The scattering vector length, $|\mathbf{q}|$ is defined as

$$|\mathbf{q}| = |\mathbf{k}_1 - \mathbf{k}_2| = \sqrt{E'^2 + E^2 - 2E'E\cos\phi}. \tag{4.17}$$

Assuming the peak of the Compton profile has momentum $p_z = 0$, the scattering angle ϕ can be determined using the Compton equation (equation 4.2).

Using Holm's relation, the experimental data can now be accurately converted from an energy scale to a momentum scale. The next step is to sum the individual detector datasets (with the purpose being, to sum the individual detector's Compton profiles).

4.4.2 Detector quality using the Fisher-Pearson function

Out of the 10 detectors used, it is often the case that one or more will exhibit sub-optimal performance and create anomalous results. This is detrimental to the data quality of the MCP as non-physical artefacts can appear in the MCP's shape. As a result of this, it is very important to analysis the shapes of the detectors' Compton profiles and decide which detectors should not be included when summing the datasets.

A more quantitative way to perform this is to study the *skewness* of the Compton profiles. Since all the count rates are normalised, the low count rate of certain detectors is not necessarily indicative of poor performance. Skewness however is a strong indication that a detector is under-performing as the Compton profile *must* be symmetric (it must not be skewed). This is because there should be an equal number of electrons moving in one direction to another. It is unreasonable to assume the electrons will have a bias for a certain direction.

The Fisher-Pearson function[58] is a quantitative way to gauge the skewness of a distribution. The Fisher-Pearson *coefficient of skewness* γ_1 is defined in terms of the second

and third moments around the mean (m_2 and m_3 respectively), as

$$\gamma_1 = \frac{m_3}{m_2^{3/2}} = \frac{\frac{1}{n}\sum_{i=1}^{n}(x_i - \bar{x})^3}{\left[\frac{1}{n}\sum_{i=1}^{n}(x_i - \bar{x})^2\right]^{3/2}} \tag{4.18}$$

where n is the sample size and $\bar{x}$ is the mean.

For a perfectly symmetric distribution, γ_1 will have a value of 0. Any deviations from 0 indicate either positive or negative skewness to the distribution. Therefore, detectors which have a skewness close to 0 have a better performance than those which have a skewness deviating significantly from 0. Detectors with a large deviance should be neglected from the summation. Secondary to the analysis of the skewness is a comparison of the detectors' count rates. Significant variations in the count rates for each detector could suggest an issue with the scattering geometry of the experimental setup (or instead, an under-performing detector).

Finally, it is important to the compare the individual spectra for each detector. Any missing features or *glitches* in the spectra (such as discontinuities) could be symptomatic of data collection or detector issues. Identifying these issues is important to ensure a high quality set of data.

4.4.3 Magnetic Compton Profile Calculation

As seen in equation 4.12, to compute the MCP, the difference between the spin up and spin down polarised Compton profiles must be computed. After taking the difference, a symmetric MCP is generated as pictured in figure 4.7(a). The statistics of the MCP can be improved by exploiting the fact that the profile is *always* symmetric. By *folding* the profile and binning the data points (since this will double the number of data points), the statistics can be improved. In figure 4.7(b), the MCP has been folded and binned to produce the *folded* MCP.

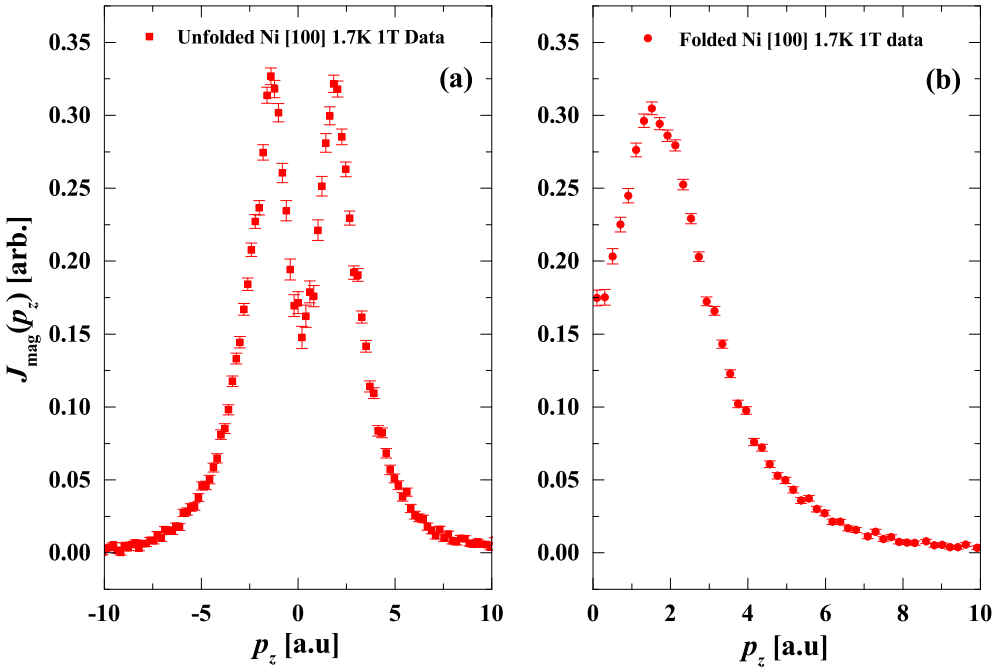

Figure 4.7: Comparison of unfolded and folded MCPs for a measurement of Ni [100] at 1.7 K in a field of 1 T. The symmetric nature of the MCP can be exploited in order to enhance the statistics of the MCP. Plot (a) is the unfolded Ni MCP and (b) is the folded Ni profile. The data points have also been *binned* in order to enhance the statistics further.

4.4.4 Error Propagation

The errors for a Compton profile are calculated using Poisson Counting statistics.[59] If an experiment yields a mean count of N, the best estimate of the error in this quantity is $\sqrt{N}$. This error is propagated conventionally when the detectors are summed and the profile folded, and binned.

4.4.5 Spin Moment Calculation

One of the key features of MCS is its ability to isolate the spin moment μ_{spin} of a magnetic system. The spin moment calculation is dependent on the *flipping ratio* F. F is defined as

$$F = \frac{I^{\uparrow} - I^{\downarrow}}{I^{\uparrow} + I^{\downarrow}} \tag{4.19}$$

where $I^{\uparrow}$ and $I^{\downarrow}$ are the integrated intensities for the spin up and spin down Compton profiles respectively. To obtain the μ_{spin} from the flipping ratio, a calibration must obtained since the various experimental parameters which dictate the values of the measured quantities will be subtly different each experiment. Using a sample with a well known and well studied spin moment as a calibration tool is imperative for extracting an accurate flipping ratio and subsequently, an accurate spin moment. Historically (and presently), this calibration sample is Ni, which has a spin moment of 0.56 μ_{B}[60].[61] The equation to calculate the spin moment of a sample μ_{S} is

$$\mu_{\text{S}} = \frac{F_{\text{S}}}{F_{\text{Ni}}} \times \frac{Z_{\text{S}}}{Z_{\text{Ni}}} \times 0.56. \tag{4.20}$$

where F_{S} is the flipping ratio of the sample, F_{Ni} is the flipping ratio of the Ni calibration sample, Z_{S} is the atomic number of the sample and Z_{Ni} is the atomic number of Ni.[62]

4.4.6 Experimental Resolution

The resolution of the projected momentum density along z is calculated using

$$\Delta p_z = \sqrt{\left(\frac{\partial p_z}{\partial E_1}\Delta E_1\right)^2 + \left(\frac{\partial p_z}{\partial E_2}\Delta E_2\right)^2 + \left(\frac{\partial p_z}{\partial \phi}\Delta \phi\right)^2}. \tag{4.21}$$

The experimental resolution is dependent on three terms: the energy broadening of the source, the energy broadening of the detector and an energy broadening term due to the geometry of the set up, respectively. It is this detector term which plays a dominate role in the experimental resolution. Charge-coupled devices (CCD) perform more optimally in this regard and so are often used in Charge Compton Scattering experiments to give a superior resolution. Unfortunately, their count rates are very low and so, solid-state based detectors are used for MCS experiments. While they offer worse resolution, they boast higher count rates which improve the statistics on the collected data. The apparatus on the BL08W allows an experimental resolution of 0.44 a.u. This value is useful when convoluting theoretically calculated MCPs.

4.5 Complementary Techniques

4.5.1 Laue Diffraction

MCS is very useful when used to study the various anisotropic magnetic phenomena inherent to the target sample. For example, Co_2MnSi (studied in Chapter 6) was measured along three different directions, giving very different MCP shapes along each. In order to measure these different crystallographic directions, the sample must first be aligned accurately. This is achieved using *Laue diffraction*.

Using Laue Diffraction, X-rays are scattered off the target sample (placed on a goniometer) into a camera. The captured image is indicative of the crystallographic orientation of the sample. By adjusting the goniometer appropriately, the sample can be rotated into the correct orientation and mounted. This section will focus on the *Back-reflection* Laue method (the camera is between the X-ray gun and the sample).

Bragg's law relates the X-ray wavelength λ, the interplanar distance d and the scattering angle θ by

$$n\lambda = 2d\sin\theta \tag{4.22}$$

where $n \in \mathbb{N}_{>0}$ is the planar index. The scattering angle for constructive interference is there 2θ. Laue diffraction only depends on the fact that the X-rays are back-scattered off the sample. Since d and θ are fixed, all crystallographic planes will contribute to a Laue spot. These spots are characteristic of the crystal's symmetry and aid in the alignment of the sample. Figure 4.8 gives the Laue diffraction pattern of a $Sr_3Ru_2O_7$ sample in the [100] direction. The camera has been centered on a high symmetry direction. This is indicated by the numerous white spots which are converging on the center of the image. Examining the image closer reveals that the spots converge on other points too. Aligning the crystal so that rotations of the sample around its z axis find other high symmetry directions is very important when attempting to measure anisotropy in the sample using MCS.

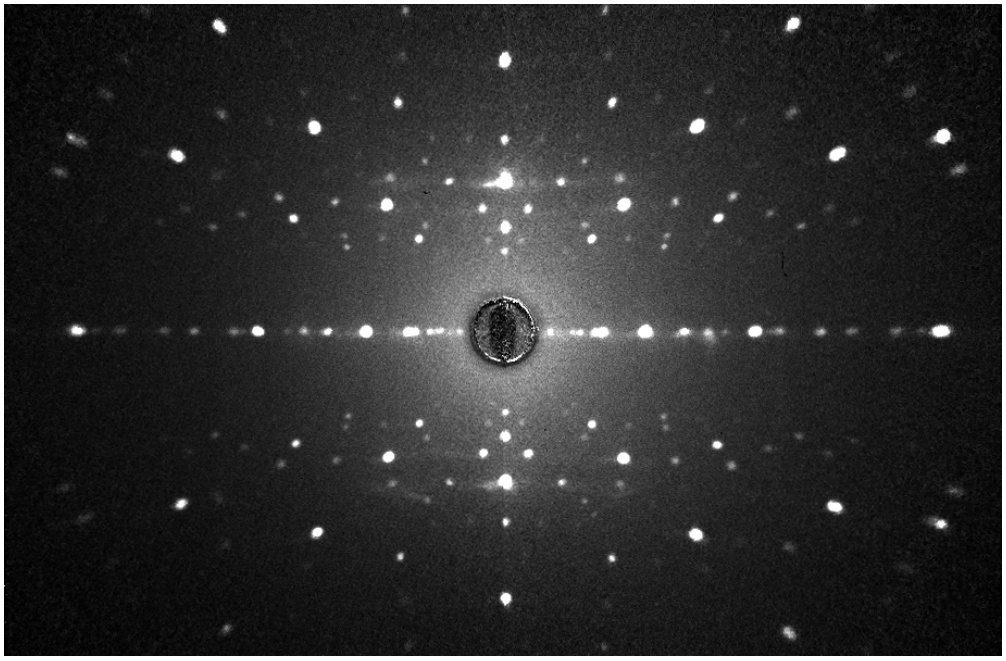

Figure 4.8: Back reflected Laue diffraction pattern of a $Sr_3Ru_2O_7$ along the [100] direction. The exposure time was a period of 10 minutes.

4.5.2 SQuID Magnetometry

While MCS is a direct probe of the spin moment of a magnetic system, the *Superconducting Quantum Interference Device* (SQuID) can be used to measure the *total* moment of a magnetic system. A measurement is performed by moving the sample through a set of superconducting coils, located inside a magnet. As the sample moves through the coils, an electric current is induced onto the coils. The coils and the SQuID itself form a closed superconducting loop. Any change in current caused by the induction is proportional to a change in magnetic flux.

The SQuID magnetometer can perform **M**v**H** (magnetic field vs applied magnetic field) measurements as well as **M**vT (magnetic field vs temperature) measurements as a means to characterise the sample's magnetic properties.

4.5.3 VSM

A *Vibrating Sample Magnetometer* (VSM) is another type of magnetometer which has been used for CeB_6's magnetometry (chapter 7). The VSM was used instead of the

SQuID because it can be cooled down to lower temperatures compared to the available SQuID magnetometers. Inside a uniform magnetic field, the sample is vibrated sinusoidally perpendicular to the applied magnetic field. The oscillating magnetic field of the sample induces a voltage in the detection coils. The voltage generated in these coils is proportional to the sample's total magnetic moment and as a result, **M**v**H** and **M**vT measurements can be made much like a SQuID magnetometer.[63,64]

4.5.4 Energy Dispersive X-Ray Spectroscopy

Energy Dispersive X-ray Spectroscopy (EDX) is a technique for determining the composition of a material. The principle behind EDX characterisation stems from the fact each element has a unique atomic structure. The different binding energies associated with the electrons of each element can be measured and weighted in order to form a qualitative characterisation of the material.

A high energy beam of charged electrons or an X-ray beam is focused incident to the sample. The bombardment of particles is essentially the photoelectric effect, removing electrons from the sample and creating electron holes in their place. When a higher state electron loses energy to *fall* down into this hole, an X-ray - characteristic of the element, is emitted. From the various counts obtained from different atoms in the sample, the EDX software will be able to calculate the compositional properties of the material.

While EDX is a very good gauge for the basic composition of a material, it in general is not an accurate tool for gauging the stoichiometry of the material as it can measure atomic weightings to an accuracy of approximately $\pm 10\%$. While atomic structure is unique for each material, the measured binding energies of atoms can often be very similar, causing their EDX spectral peaks to overlap, creating a large error when integrating.[65]

Chapter 5

The SPring-8 Synchrotron and the BL08W Upgrade

The majority of the work performed in this thesis has been collected and studied at the SPring-8 synchrotron's BL08W beamline in the Hyōgo prefecture, Japan. An important objective of this project was to upgrade the original cryostat on the BL08W beamline of SPring-8 to the 9 T Oxford Instruments magnet which was shipped from the ESRF synchrotron in Grenoble, France. The result of this upgrade enabled a much larger range of physical phenomenon to be studied due to increased experimental capacity.

This chapter discusses the SPring-8 facility and the BL08W beamline. Subsequently, some background behind synchrotron radiation is discussed in addition to some of the most important components of the beamline, followed by some documentation of the magnet upgrade and revisions to the software which were required. Finally, the last section documents many of the software elements which are integral to the running and operation of an MCS synchrotron experiment.

5.1 SPring-8 Overview

The Super Photon Ring 8 GeV (SPring-8) is one of the most powerful synchrotron facilities in the world. The SPring-8 synchrotron requires a *Linear Accelerator* (linac)

to be used as an injector for the synchrotron, accelerating electrons to about 1 GeV before being injected into the booster synchrotron. Inside the synchrotron, the electrons are then accelerated further to 8 GeV before being injected into the storage ring for experimental usage. The storage ring is 1436 m in circumference and is comprised of *cells*. Each cell is about 30 m long and contains two bending magnets, 10 quadrupole magnets and 7 sextupole magnets. These cells are divided by straight sections and it is here where insertion devices are installed for each beamline. The linac, booster synchrotron and storage ring have been labelled on the map provided in figure 5.1. Inside the storage ring is where the various beamlines are located. The beamline which

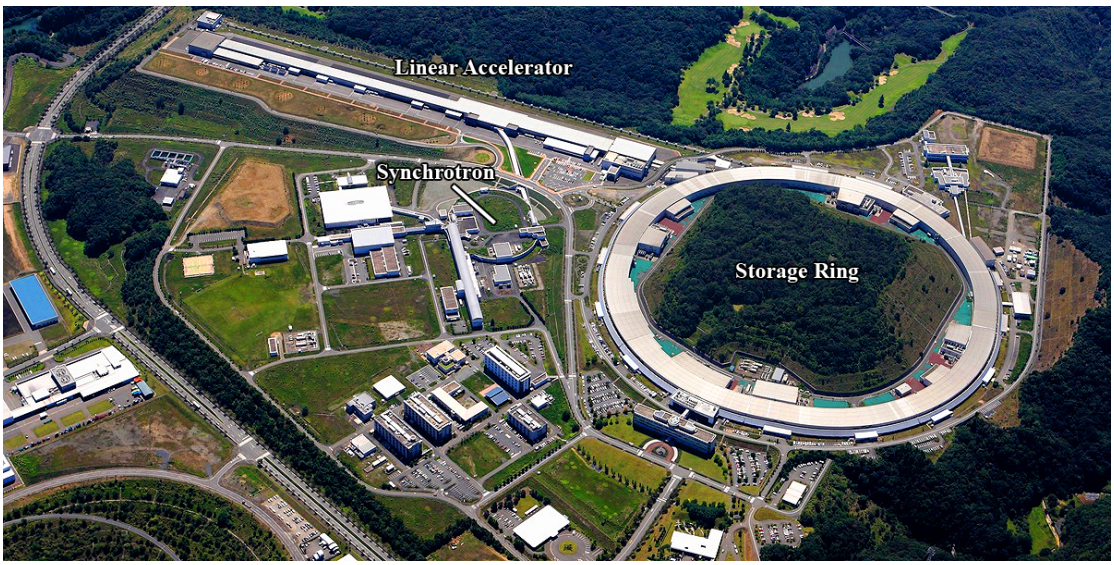

Figure 5.1: Map of the SPring-8 campus (image courtesy of Tōhoku University).

has been used for all MCS experiments described in this thesis is *BL08W*.

From studying equations 4.8 and 4.9, it can be seen that in order to improve the resolution of the experimental MCP, not only is a high energy incident beam required, but also a large scattering angle and circularly polarised radiation incident to the sample. Due to the high energy demands of magnetic Compton scattering (see figure 4.4), it is very important that the synchrotron provide very high energy circularly polarised photons. This is the reason why the BL08W beamline of SPring-8 is used for MCS experiments, no other source provides high enough energy, circularly polarised X-rays.

5.2 Synchrotron Radiation

The reason why high energy X-ray radiation is so important and demanded is due to its probing capacity. X-rays can probe deep into a sample (the degree of penetration is related to the energy of the photon and the electron density of the sample) and are also non-destructive (they do not make permanent changes to the material). X-rays can also however, be made to probe only the surface of a sample when made incident through shallow angles. As such, X-rays are excellent at both, bulk measurements, and surface sensitive measurements. High energy X-rays can also be diffracted by the periodic lattice of crystals due their very short wavelengths ($E = hc/\lambda$) and so, many different kinds of diffraction phenomena can be studied. Lower energy X-rays and UV photons can be used to study the binding energies and electronic properties of materials.[66] Finally, as seen in chapter 4, high energy X-rays are an absolute necessity when it comes to collecting high quality magnetic Compton scattering data.

Synchrotron radiation (SR) is generated tangentially to the velocity vector $\mathbf{v}$ of an electron. An electron accelerating around the storage ring generates SR in a very broad range of photon energies (from microwaves, to hard x-rays and γ-rays). Such a wide spectrum of different electromagnetic phenomena simply cannot be produced in other sources, especially photons in the ultraviolet (UV) / hard x-ray range. Hard x-rays production in particular has no rival.[67] The SR used for the experiments described in this thesis is generated entirely using bending magnets. These magnets are located around the storage ring, causing the electrons to travel radially at relativistic speeds ($\gamma \gg 1$). SR created by such means is excellent because of its spectral range, intensity, polarisation and collimation. The highly collimated light is a result of the *relativistic aberration*.

In the laboratory's frame of reference (denoted S'), the SR is relativistically aberrated ($|v| \sim c$), resulting in a higher spectral flux[1] radiated parallel to $\mathbf{v}$. The relativistic

[1]Spectral flux is not the only term used to quantify the *quality* of the emitted SR. A more common term is *brilliance* which is a slightly different quantity defined as the number of photons produced per second, within a solid angle of 1 (mrad^2), per cross-sectional area (mm^2), falling within an energy bandiwdth of 0.1 %.[68]

aberration formula is

$$\tan\theta = \frac{\sin\theta'}{\gamma(\cos\theta' + \beta)} \tag{5.1}$$

where $\beta = v/c$.[69] This function has been plotted in figure 5.2. For larger values of

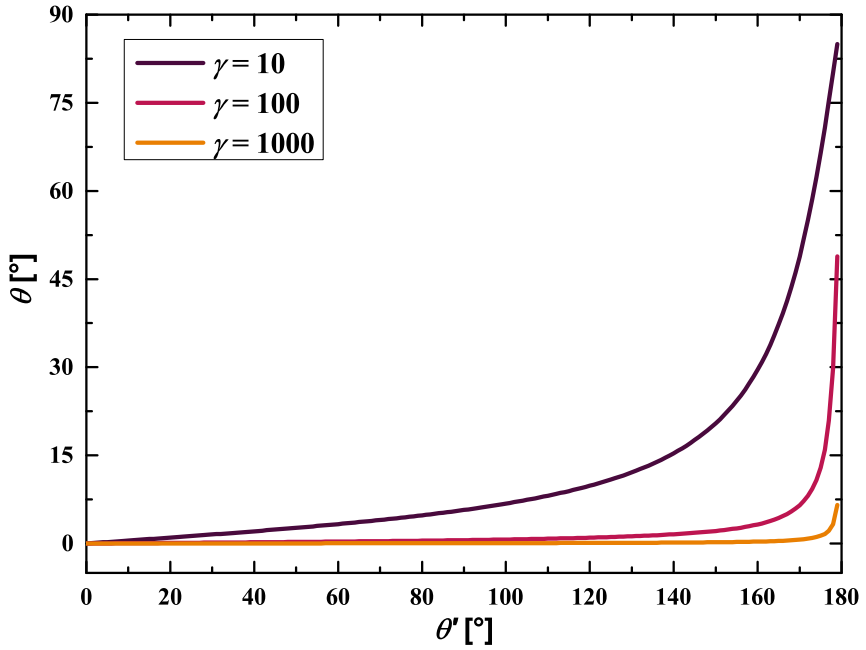

Figure 5.2: The relativistic aberration of photons emitted from an electron accelerated through a synchrotron. For simplicity, β has been set equal to 1. For large γ, almost all emitted radiation is forwardly projected.

γ, the radiated photons start to point more forwards (along $\mathbf{v}$). Schematically, the effect of this relativistic aberration is as shown in figure 5.3. For an electron orbiting the synchrotron ring at non-relativistic speeds ($|v| \ll c$), the emitted SR travels in all directions. At relativistic speeds however, the *headlights* effect arises where the SR is generated almost directly parallel to $\mathbf{v}$. It is due to this mechanism that synchrotron sources create radiation with brilliance several orders of magnitude larger than other radiation generation methods.

The spectral range of pure SR is very wide (a large range of frequencies are available). To correct this, a second stage of *tuning* is required before the SR can be utilised in experiments on the beamlines. The radiation needs to pass through an *insertion device*

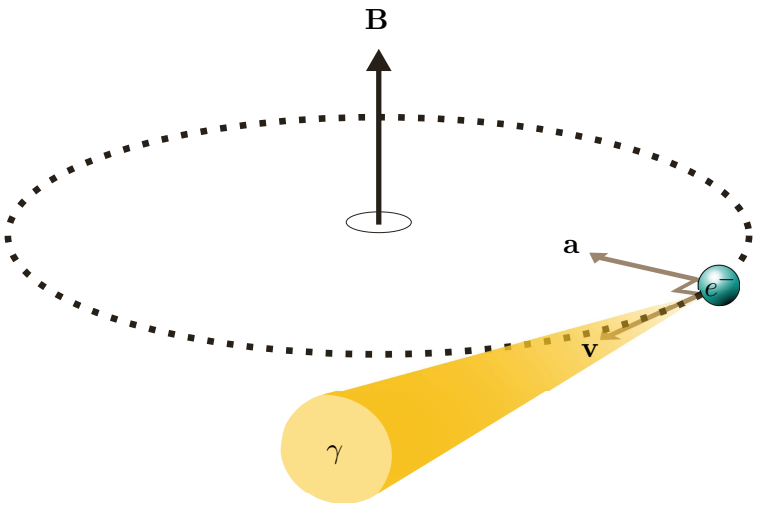

Figure 5.3: Schematic of an electron inside the storage ring of the synchrotron, emitting SR forwards due to the effects of relativistic aberration.

which in addition to focusing the beam, generates more flux.

5.2.1 Insertion Devices

Third-generation synchrotrons are notable for their inclusion of multiple so-called *Insertion Devices* (IDs), located at straight sections between the bending magnet sections of the synchrotron. The purpose of an ID is to generate even more flux and brilliance from the electron beam than from just solely the bending-magnets of the storage ring alone. This is done by oscillating the electrons along a path using an array of alternately polarised magnets.

IDs are characterised by how drastically the electrons are forced to deviate from their initial, straight path. An *undulator* creates very small oscillations in the initial path whereas a *wiggler* creates large oscillations (the path becomes *wiggly*). Quantitatively, IDs are distinguished by their *Strength* parameter, K, defined as

$$K = \frac{eB_0\lambda_{\mathrm{ID}}}{2\pi m_e c} \tag{5.2}$$

where B is the strength of the insertion device's magnetic field and λ_{ID} is the period

of the magnets along the insertion device.[70] For $K \ll 1$, the oscillation in the motion of the radiation is small and hence, the insertion device is an undulator. For $K \gg 1$, the oscillation in large and the insertion device is a wiggler. The limit of 1 is actually arbitrary and at $K \sim 1$, the ID presents characteristics of both an undulator and a wiggler. Figure 5.4 schematically compares the two different types of ID.

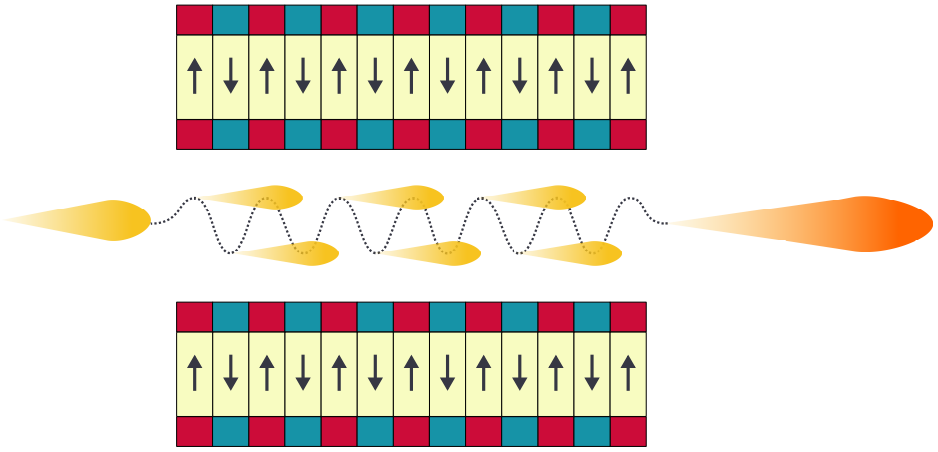

(a) Undulator

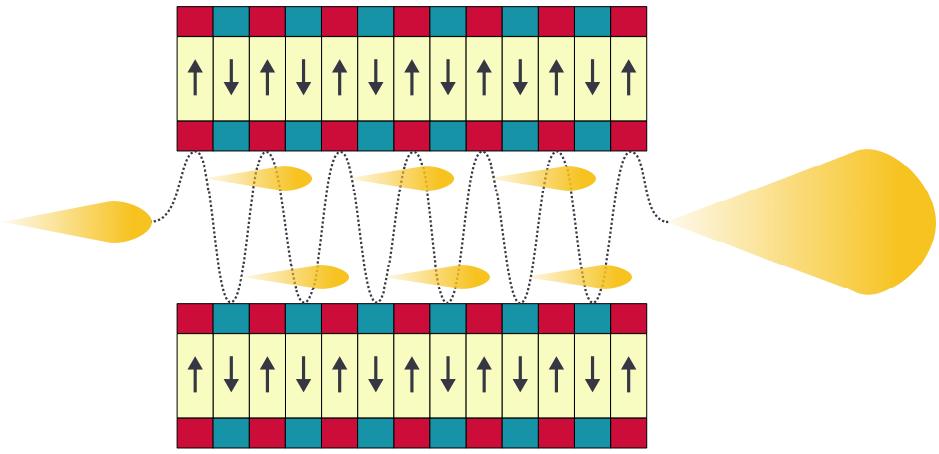

(b) Wiggler

Figure 5.4: Schematic representations of an undulator and wiggler ID. The extent of the oscillations of the electrons' path have been greatly exaggerated but the principle remains. As a result, undulators produce a highly concentrated (large flux and brightness) beam of SR with a narrow spectrum, whereas the wiggler produces a less concentrated, broader SR beam.

Undulator

The undulator produces a beam of radiation across a narrow spectrum due to the very small oscillation produced in the electron path. This causes the radiation *cones* to overlap and interfere with each other. Only certain wavelengths will interfere constructively and so the undulator will produce one fundamental frequency of radiation together with less intense, higher harmonic frequencies. The undulator's spectrum consists of a set of narrow lines, equally spaced by ΔE, defined as

$$\Delta E = \frac{2hc\gamma^2}{\lambda_{\mathrm{ID}}\left(1 + \frac{K^2}{2}\right)}. \tag{5.3}$$

Varying K enables the experimentalist to tune the insertion device to a specific set of energy bands. K's dependence on λ_{ID} means the gap between magnetic poles can be varied to choose the required energies for the experiment. For low values of K, the energy spectrum will be dominated by the root harmonic. As K is increased, the angular spread increases and so, more harmonics begin to appear.

Not only does the spacing of magnetic poles λ_{ID} have an effect on the spectral properties of the undulator produced radiation, but so to does the number of periods N produced by the $2N$ magnets of the undulator. The on-axis peak intensity I_n of the n^{th} harmonic of the undulator radiation is defined as

$$I_n = \alpha N^2 \gamma^2 \frac{\Delta\nu}{\nu} \frac{I}{e} F_n(K) \tag{5.4}$$

where α is the fine structure constant, $\Delta\nu/\nu$ is the relative spectral bandwidth of the harmonic peak, I is the current and $F_n(K)$ is the tuning function. As a result of $I \propto N^2$, the intensity scales greatly with the number of magnetic pairs in the undulator.

Wiggler

While the undulator produces a narrow spectrum of different specific wavelengths, the wiggler produces a smooth continuum. Wiggler-produced radiation does not overlap like

the radiation produced with an undulator as the angle of the electron path is too large. Wigglers therefore provide very high-power X-ray beams with a broad spectral range and so, the heat load applied to apparatus such as the monochromator can be very high. Carbon, due to its very high vaporisation temperature, is often used to absorb much of this unwanted radiation in order to protect the hardware down the ID line.[71]

Both types of insertion device produce linearly polarised radiation due to the symmetric design - the right-handed and left-handed circularly polarised radiation cancel out. In order to generate circularly polarised radiation, two methods can be employed:

1. Come *off-axis*, where the incident beam is not measured directly but instead, a component of the beam is measured at a certain angle.

2. Make the ID asymmetric.

Method two is preferred since coming off-axis affects the countrate significantly.

Intense circularly polarized X-rays are created using either an *elliptical multipole wiggler* (EMPW)[72] or an *asymmetric multipole wiggler* (AMPW).[73] Both types of wiggler incorporate an asymmetric array of magnets in order to generate circularly polarised X-rays. The EMPW design is the type of wiggler used on the BL08W beamline at SPring-8.

5.3 The BL08W Beamline

All of the MCPs collected and presented in this thesis were collected on the BL08W beamline at SPring-8. BL08W is the only beamline at SPring-8 which uses a wiggler for its insertion device. Incidentally, BL08W is also the highest energy beamline at SPring-8. The wiggler enables the creation of circularly polarised X-ray radiation which aids in isolating the magnetic cross-section from the charge cross-section (section 4.3). The X-ray energy range is 100 to 300 keV. Other than MCS and Charge Compton Scattering, the beamline is also used for high energy Bragg scattering and high energy fluorescent X-ray analysis.

The optics and experimental hutches are configured as shown in figure 5.5. The *Elliptical*

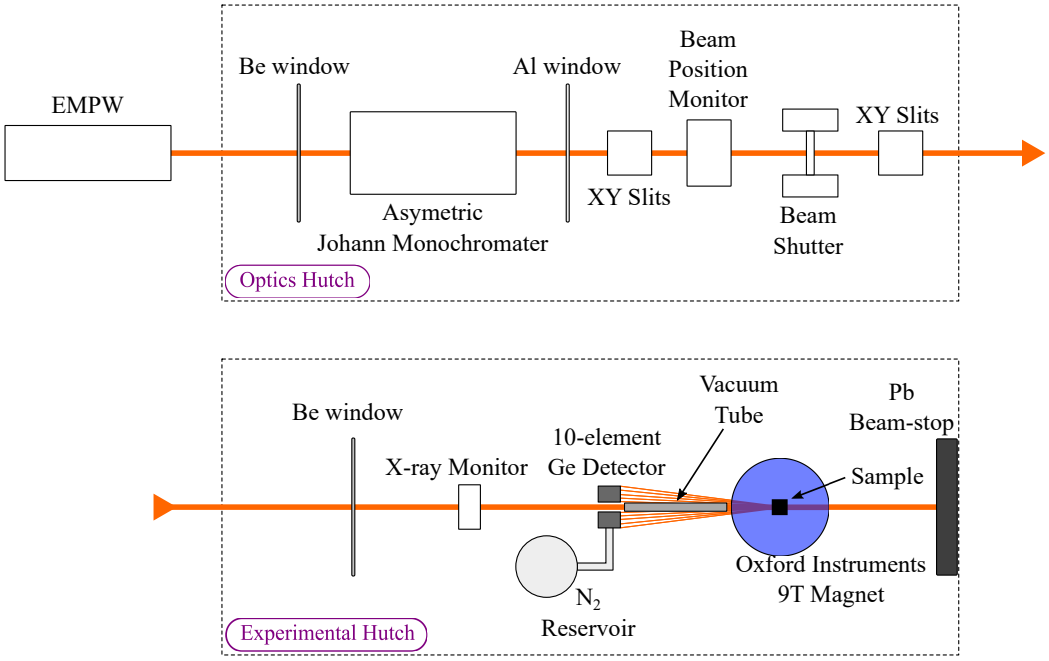

Figure 5.5: Schematic of the BL08W optics hutch and experimental hutch.

Multipole Wiggler (EMPW) can produce either linearly or elliptically polarised X-ray radiation. The X-rays are focused and monochromated using an assymetric *Johann-type* monochromator. The incident X-ray radiation scatters of the target sample situated inside the magnet where the scattered radiation strikes the detector.

5.3.1 Detector

The X-ray detector used on BL08W is a 10 Ge crystal solid-state detector.[74] The 10 crystals are arranged around the beam-opening, forming a perfect circle. The crystal arrangement allows for a scattering angle of $\sim 173\,^{\circ}$. It is beneficial to keep the scattering geometry consistent for each detector as the inherent symmetry of this setup simplifies the data analysis. The detector is cooled with liquid N_2 and needs to be refilled daily during an experiment. When an X-ray is absorbed, an electron-hole pair is generated resulting in a charge pulse. This charge pulse is normalised using a pre-amp and analysed using a 8190 channel *multi-channel analyser* (MCA) where the charge pulse is integrated and converted into a voltage pulse. This voltage pulse's value is proportional to the

energy of the sample-scattered photon which is incident to the detector. The conversion from the arbitrary channel number to actual photon energy is outlined in §4.4.

While the MCA is processing the charge pulse, any additional counts which contribute to the energy spectra are ignored. This is due to a phenomenon called *Dead-time*. Dead-time consequently prompts an efficiency problem to the experimentalist as one wishes to reduce dead-time whilst keeping the count-rate as high as possible. This refinement is generally achieved by reducing the size of the beam incident to the sample. Generally, a dead-time of more than 10 % is unacceptable. The beam *profile* is controlled by the XY slits in figure 5.5.

5.4 BL08W Magnet Upgrade

A primary objective of this project was the upgrade of the BL08W 3 T cryostat to the Oxford Instruments 9 T *Spectromag* Magnet which originally resided at the ID15 beamline at ESRF in Grenoble, France. The ID15 beamline has been subjected to numerous technical issues over the years of use and in addition, its ID is being change to one which does not produce circularly polarised X-rays. Moving the magnet to SPring-8 presents an opportunity to enhance the experimental capacity available when studying materials on BL08W. Figure 5.6 graphically conveys this enhancement in experimental capacity. Here, *experimental capacity* is defined as the area encompassed by the respective instrument on the graph. The original cryostat could be cooled to a temperature of 6 K and magnetised with an applied field of up to ± 3 T. In comparison, the Oxford Instruments 9 T Spectromag magnet can be cooled to ∼ 1.5 K and magnetised with an applied field of up to ± 9 T[2]. A comparison of the old and new setups is shown in figure 5.7.

5.4.1 Oxford Instruments 9 T Magnet

The Oxford Instruments 9 T *Spectromag* system (project number 25167) is the magnet used for all the MCS experiments described within this thesis. The magnet has

[2]In practice, the maximum magnetic fields available are slightly lower because generally, the magnet will quench before reaching such a high field. The cryostat is frequently quoted as being able to achieve 2.5 T and the Oxford Instruments Magnet will not be magnetised above 6.5 T.

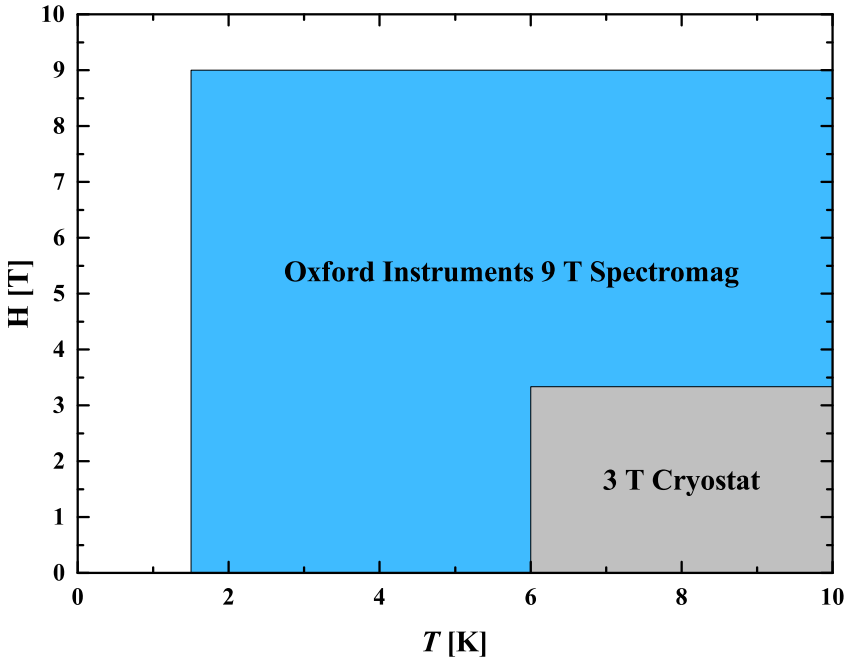

Figure 5.6: Graphical representation of the experimental capacities available for the 3 T cryostat situated on BL08W and the Oxford Instruments 9 T *Spectromag* magnet which was shipped from France. As can be clearly seen, the 9 T magnet massively increases the range of phenomena which can be studied at BL08W compared to the 3 T cryostat.

a maximum possible magnetic field of ± 9 T which is positioned to be aligned along the scattering vector. This means that when aligning samples for MCS experiments, no additional translations or rotations are necessary to align a sample beyond its initial alignment. The sample's temperature is controlled inside the VTI which can be controlled using a third party temperature controller (a Lakeshore 336 Cryogenic Temperature Controller). Operating the magnet is performed using an Oxford Instruments IPS 120-10 Superconducting Magnet *Power supply Unit* (PSU). The PSU is interfaced over a *General Purpose Interface Bus* (GPIB) controller with commands sent from the beamline software. §5.5 discusses how this software works and details the various commands sent to the magnet control system.

(a) 3 T Cryostat (b) 9 T Oxford Instruments *Spectromag*

Figure 5.7: The old 3 T cryostat and the new 9 T Oxford Instruments *Spectromag* magnet which replaced it.

5.4.2 Stray Field Precautions

A requirement for the usage of the new magnet on the beamline was that it must not interfere with the current setup established there. This includes no effects to neighbouring beamlines and more importantly, no effects whatsoever to the storage ring. Plotted in figure 5.8 is the experimental data for the stray field strength of the magnet at 9 T. The storage ring is located approximately 7 metres away from the magnet installation point in the beam hutch. In order to calculate the strength of the stray field at this distance, a *slice* was taken along the axis perpendicular to the storage ring and fit with a function $f(x) \propto 1/r^3$.[75] The results of this fitting are plotted in figure 5.9. The model

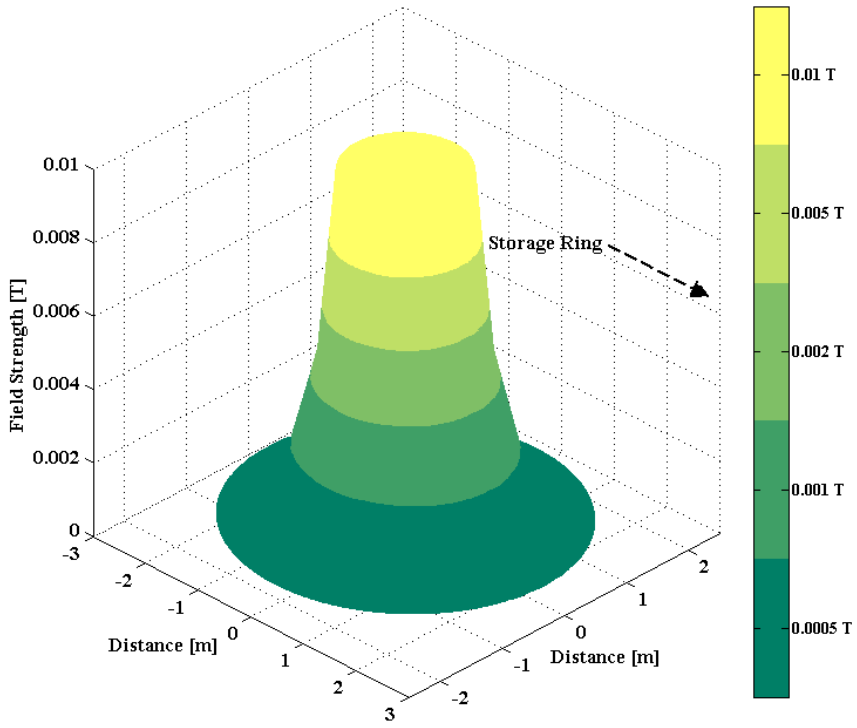

Figure 5.8: Experimental data collected for the stray field strengths of the Oxford Instruments 9 T magnet at different distances away from the magnet. The field strength drops off as following an inverse cube law.

(a generalised inverse cube law) very adequately describes the experimental data. At a distance of 7 m from the magnet (close to the storage ring of SPring-8), the field strength is $\sim 1.4 \times 10^{-5}$ T. This has no impact on the storage ring and as a result, the magnet can be used on the beamline without affecting other experiments or storage ring.

5.5 Magnet Operation

The magnet (and the whole experiment) is controlled using software written specifically for MCS experimental use. Elements of the software had to be rewritten after the magnet upgrade in order to allow the software to interface with the new hardware. Figure 5.10 displays the main window of the program. The following is a description of the different components of the software.

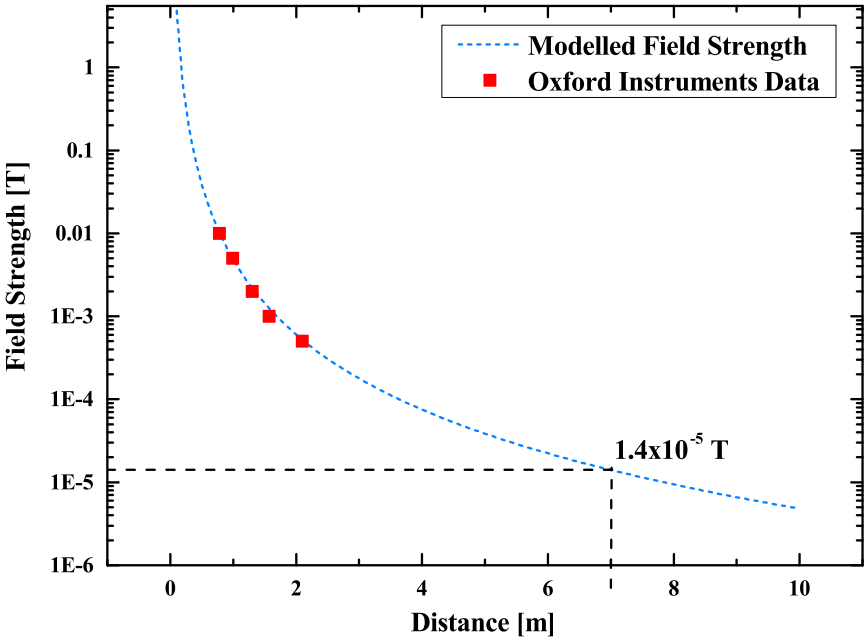

Figure 5.9: Stray field data attenuated perpendicular to the SPring-8 storage beam. The model calculates a field strength of 1.4×10^{-5} T when at a distance of 7 m away from the magnet.

5.5.1 Experiment Control

Figure 5.11 contains the window elements which are directly related to controlling the experiment. The parameters described here *must* be specified to run a MCS experiment.

- `FILE` specifies the name and location of the experimental files. Each cycle (and its scans) are automatically named by the software. Giving a sensible filename prefix ensures no confusion or complications arise.
- `A [T]` and `B [T]` specify the magnetic field magnitudes for the experiment. Spurious results will occur if these values differ in magnitude. The software will not allow values greater than 6.5 T due to the risk of the magnet quenching. If greater fields are required, this limit can be modified in the source code.
- `preset (sec)` specifies how long each scan is (this is by default set to 60 seconds).

Figure 5.10: Main window for the MCS experiment control software. This program allows the experimentalist to control MCS experiments and enables full configuration of the experimental setup. This means that the entire experiment can be controlled without accessing the experimental beam hutch.

Figure 5.11: Experimental parameters used to perform a MCS experiment.

- `Scans` specifies how many scans *per cycle* the software will collect data for until it flips the field (for example, 15 scans means there will be 60 scans total per cycle).
- `num. cycles` specifies the number of cycles the software will collect for until the program stops. This limit is seldom reached and so can be ignored.
- `START` starts the data collection process.

- `STOP` stops the data collection process.
- `Time` provides an approximate time for one cycle to be collected.
- `Clear` and its console window display the current status of the data collection process. This is useful as it allows the user to halt data collection at an appropriate time. Clicking `Clear` wipes the console window.
- `Slit` specifies the `Height` and `Width` of the incident beam with `Read` reading the values from the beam controller and `Set` sending values to the controller.
- `Stage` allows the sample stage to be positioned so the sample can be centred on the beam. `Read` and `Set` function identically to the `Slit` window. Sample alignment will be covered in a further section.

5.5.2 Temperature Control

The temperature can be set using the interface in figure 5.12. This interface will also plot the temperature for each scan during data collection. This is useful as it can be clearly seen graphically if there's spurious temperature control issues occurring.

Figure 5.12: Temperature control interface.

- `A` displays the *current* temperature of the LakeShore 336 temperature controller unit (units: Kelvin) output from terminal A. `B` displays the output from terminal B. When data collection is not active, values can be read by pressing the `Read` button.

- `SetValue` allows temperature values to be sent to the LakeShore. Input a value into the corresponding textbox and click `set` to send the value to the LakeShore.
- `GPIB` must be selected to connect the software to the LakeShore unit.
- The graph below the `LakeShore 336` section plots the *read* temperature against time as a red line. This plot is automatically updated during data collection.

5.5.3 Magnet Control

This section of the interface allows the user to send commands to the magnet PSU. This is very useful for benchmarking and testing purposes as well as reseting the software should any issues occur. The magnet control window is presented in figure 5.13.

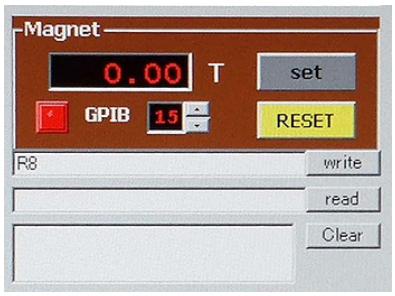

Figure 5.13: Magnet control interface.

- `Magnet` allows the user to set the magnetic field of the magnet to whichever value is entered into the textbox. Clicking `set` sends the appropriate commands to the magnet PSU and the magnet will start ramping.
- `RESET` will set the magnet's field to 0 T whilst also resetting the various variables which the software keeps track of to operate the manual. As a result, it is imperative that when the `STOP` button is pressed in the *experimental control* section, the `RESET` button is pressed before any further configurations are made.
- `write` and its respective textbox sends the input command to the magnet PSU. This is very useful for benchmarking.
- `read` reads the output from any commands sent to the magnet PSU. Again this is very useful for benchmarking. An important point is that the `read` button must

be clicked twice. The first click reads the value from the PSU. The second click wipes this value from the PSU's memory. If this is not done, the PSU will buffer these commands and spurious results will be produced.

- `Clear` clears the console window (to the left of the button). The console window shows every single command sent to the magnet PSU when the `Magnet` controls are used as well as during data collection. This is very useful when debugging.

5.5.4 Sample Alignment

This section of the interface helps in aligning the sample into the incident X-ray beam. This is important as if the beam *glances* the sample (does not hit purely the sample), it is difficult to normalise the data and the spin moment will be incorrectly determined. Figure 5.14 presents the interface elements related to aligning the sample. Before ex-

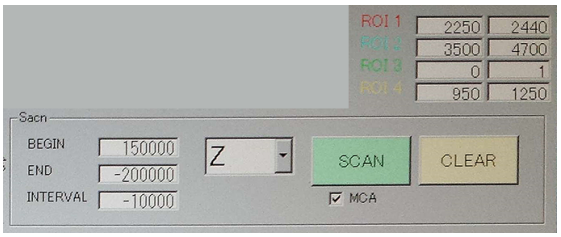

Figure 5.14: Sample alignment section of the interface.

plaining the various interface elements, the alignment procedure will be explained.

To align a sample in the beam, the Compton scattering is measured for the current sample position. As discussed in §4.4, various different types of X-ray energies will be detected. In order to align the sample, typically a piece of Sn foil will be positioned below the sample. This will fluoresce when exposed to the X-ray synchrotron radiation and will show up on the energy spectra. By specifying and plotting how these regions of energy change with sample position, the sample's shape and position can be determined and so, the alignment can be fixed on the sample.

- `ROI` specifies the *region of interest* in energy which will be plotted on the graph (for example, the Sn fluorescence energy range can be specified. Another common ROI is the Compton peak.

- The `Scan` section controls the ranges the sample position will be moved so a position profile can be measured. `Z` scans up and down the sample, `X` scans across the sample.
- `BEGIN` and `END` specify the positions to scan to and from respectively. `INTERVAL` specifies how many points will be measured between the two end points (and therefore, is directly related to the resolution of the scan). In `X`, an interval of 2500 equates to 1 mm. In `Z`, an interval of 32500 equates to 1 mm.
- `SCAN` initialises the scan.
- `CLEAR` wipes all data from the graphs.

The plot generated when scanning across a sample in `X` is plotted in figure 5.15. As can

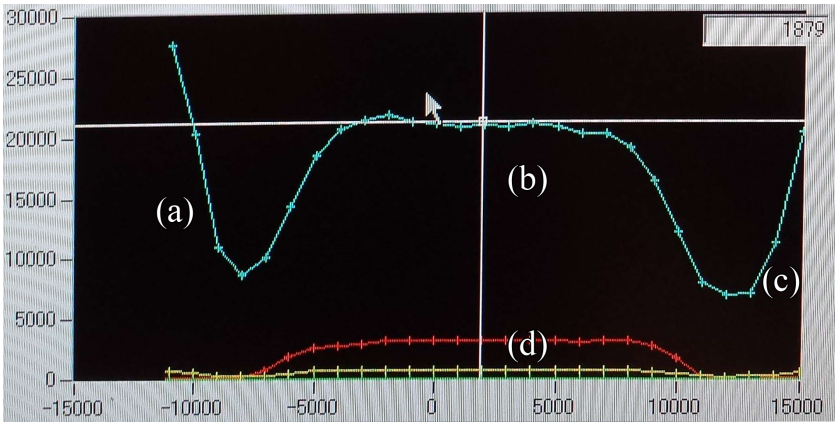

Figure 5.15: Sample alignment plot of the alignment of BaCuGeO. (a) and (c) are the sides of the sample space windows. (b) is the sample and (d) is the Ba fluorescence used to aid in finding the sample. The x axis represents the position in `X` of the sample and the y axis represents the count rate.

be seen, when scanning the sample, the sample shape profile can be identified. Centering on the profile will center the incident beam on the physical sample. By combining this procedure with changes to the beam shape and height, the apparatus can be *tuned* to give optimal measuring conditions.

5.6 Concluding Remarks

5.6.1 Summary

Modelling the stray field effects of the 9 T Oxford Instruments magnet proved the magnet would make no impact on the electron beam during operation. This concluded that the usage of the magnet on BL08W would not impact other experiments. The 9 T Oxford Instruments magnet was shipped to the BL08W beamline of SPring-8 successfully. Interfacing the magnet and the software was achieved by editing certain parts of the code to send messages to the PSU over the GPIB interface. A significantly improved experimental capacity is now possible since the magnet can reach lower temperatures and larger applied magnetic fields compared to the old cryostat. Examples of the improved statistical quality of the data can be seen in chapters 7 and 8. Additional functionality has been implemented into the control software such as the ability to benchmark the experimental setup by sending commands to the system and counting time approximations, so experimentalists can be informed of the cycle duration.

5.6.2 Future Work

A downside to the larger experimental capacity is the effect large magnetic fields have on the position of the sample inside the magnet. When flipping the magnetic fields, the increased helium flow in the magnet caused the sample environment to shrink, moving the sample's position relative to the incident beam. This can be observed as variations in the count rate as the beam hits less (or more) of the sample. This can produce difficulties when normalising the collected data and can make determination of the spin moment inaccurate if the incident beam moves off the sample due to this sample movement. This issue could be resolved by upgrading the magnet to isolate the sample environment from the helium flow when the field is flipped.

Chapter 6

Spin Polarisation Investigation of Co-based Full-Heusler Compound Co_2MnSi

High T_C half metallic ferromagnets are of significant interest due to their application in *Spin Transport Electronics* (Spintronics). This promising, emergent technology is sensitive not only to the charge of the electron (as is the case in electronics) but also the spin of the electron. It has been suggested that the introduction of a spin degree of freedom will provide higher performance compared to regular semiconductor based electronics as well as the potential for higher order transistor based technologies, decreased power consumption and non-volatility.[76] The combination of MCS experiments and theoretical work can be used to characterise a compound's electronic structure. By configuring the calculation (if necessary) to give an electronic structure which agrees with the experimental data, insight into the compound's degree of spin polarisation can be obtained. The EMD of Co_2MnSi was measured along three different directions on the BL08W beamline at SPring-8. The system was modelled using the ELK FP-LAPW and SPR-KKR DFT codes and compared to the experimental data. Along all three directions and their anisotropies, the theoretical results exhibit very good agreement with the experimental data, contributing to the evidence that Co_2MnSi is a half metal. Most

studies of these proposed half-metallic alloys have studied thin films of the material. This work marks the first attempt to investigate the degree of spin polarisation in a *bulk* material.

6.1 Introduction

Cobalt Manganese Silicon (Co_2MnSi) is a *Full-Heusler* compound[77] (chemical formula X_2YZ) predicted of having a half metallic character. This is characterised by a band structure which possesses a metallic majority channel whilst simultaneously possessing an insulating minority channel.[78–82] It is also notable for having the highest Curie temperature of the Heusler alloys with a T_C of ~985 K,[83–85] suggesting that its magnetic properties will be more *robust* at room temperature than the predicted half metals with lower T_C (such as NiMnSb[86]). Co_2MnSi crystallises into the $L2_1$ crystal structure with lattice parameter 5.645 Å.[85,87–89] The $L2_1$ structure is distinct in that it consists of four interpenetrating FCC lattices. In *Half-Heusler* compounds (chemical formula XYZ) have the $C1_b$ crystal structure. The crystal structure of both these types of materials have been plotted in figure 6.1.

6.1.1 Half-metallic Ferromagnets

It was in the early 1980s that the unusual magneto-optical properties of various Heusler alloys were investigated via study of their band structure through the means of DFT.[90] It was discovered that the intermetallic compound NiMnSb[91] had an unexpected band structure. Whilst the metallic and semiconducting (and insulating) band structures had been familiar for much of the 20th century, this was the first time both states had been observed in the same material. It was found that the electron majority states occupy E_F whereas there is the existence of a band gap in the minority channel. De Groot *et al.* described these materials as being *half metallic*.[90]

Figure 6.2 presents the DOS for NiMnSb as calculated using DFT. The calculation predicts the compound to have a 100% spin polarisation as indicated by the presence of

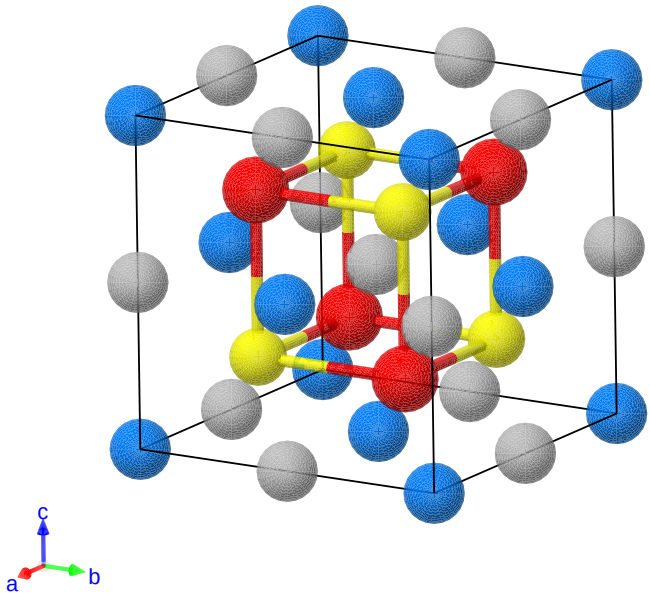

Figure 6.1: The full Heusler $L2_b$ structure. The X_1 sites are labelled as ●, the X_2 sites are labelled as ● (absent in Half-Heuslers), the Y sites are labelled as ● and the Z sites are labelled as ●.

a band gap in the minority channel. Due to this unique band structure, by definition, a half metal *must* be a ferromagnet with an integer total moment M.[1] The Slater-Pauling rule[92] is a useful tool in the prediction of half metals as it suggests that the total spin moments are related to the number of valence electrons in the compound. This relationship is described more succinctly in equations 6.1 and 6.2 where M_{half} and M_{full} are the total spin moments of the half and full-Heusler compounds (discussed in the proceeding section) respectively, and Z_{e^-} is the total number of valence electrons in the compound.

$$M_{\text{half}} = Z_{e^-} - 18 \tag{6.1}$$

$$M_{\text{full}} = Z_{e^-} - 24 \tag{6.2}$$

For example, in the case of NiMnSb (which has 22 valence electrons), the predicted total spin moment is 4 μ_{B}. In the case of Co_2MnSi (which has 29 valence electrons),

[1] This statement is not a *rigid* definition. This is the case for materials which exhibit little to no spin-orbit coupling (SOC). For the materials studied in this chapter, no spin-orbit interaction is expected.

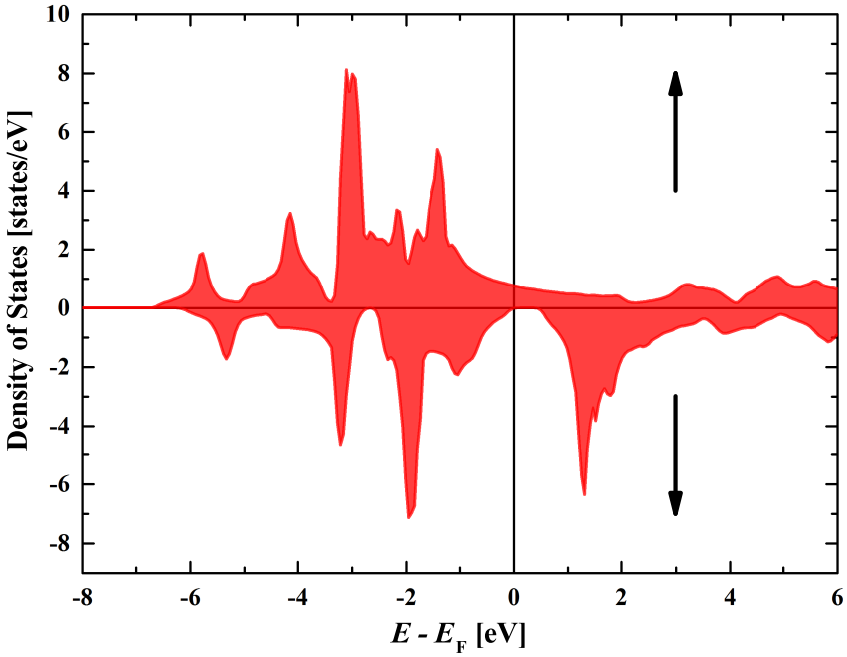

Figure 6.2: NiMnSb Total DOS calculated with the ELK FP-LAPW DFT code[36] using the Generalized Gradient Approximation exchange correlation functional. The black arrows mark the Majority (↑) and Minority (↓) spin channels. At 0 eV there is no DOS at E_F in the minority channel (indicative of a semiconducting or insulating material) whereas there is a non-zero DOS at E_F in the Majority channel. This character of DOS is archetypical of a Half-Metallic state.

this means the estimated total spin moment will be 5 μ_B.

6.1.2 Electronic Structure

The half metallic band structure observed in Co_2MnSi arises from the interaction between the p electrons of the Si sp hybridised band and the d electrons of the hybridised Co-Co bands and the Mn d band. The four sp bands can only be partially filled by the 4 valence electrons of the Si (valence $3s^2 3p^2$) and as a result, 4 unoccupied states remain, able to accommodate the available d electrons of the Co and Mn. Turning attention to the transition metals of the system, neglecting the Mn atoms for now, the Co atoms sit on a cubic lattice observing an octahedral symmetry (O_h) compared to the tetrahedral symmetry (T_d) of the whole crystal. The result of this is that some Co states will be

localised exclusively on the Co sites. It is therefore sensible to initially focus on the effects of the Co-Co hybridisation which can occur as a result of this symmetry and then look at how these hybridised bands interact with the Mn d and Si sp bands.

Figure 6.3 shows the possible hybridisations between the two Co atoms following the octahedral symmetry of the lattice. The e_g orbitals ($3d_{x^2-y^2}$ and $3d_{z^2-r^2}$) will only

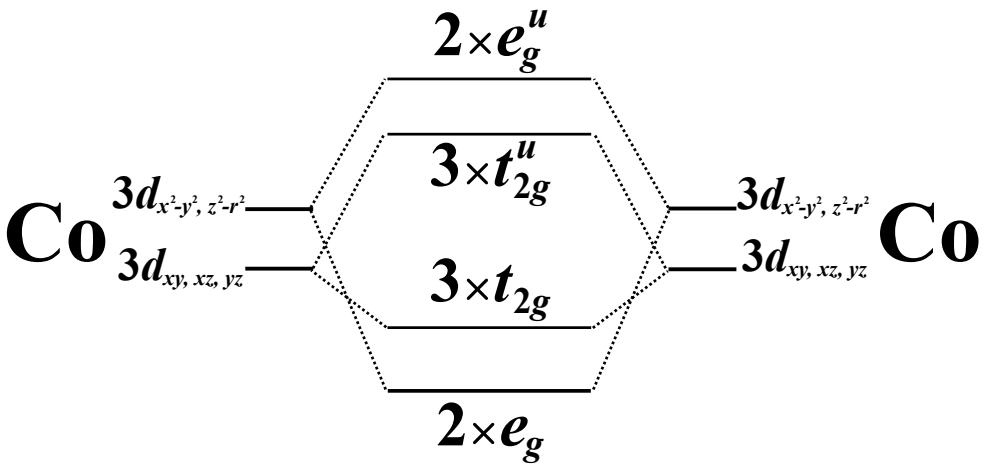

Figure 6.3: The possible ways in which the Co d orbitals can hybridise with each other.

couple to other e_g orbitals because of the symmetry. This means these orbitals can only interact with the e_g bands of other $3d$ atoms such as the Co and Mn. This argument also applies to the t_{2g} orbitals ($3d_{xy}$, $3d_{xz}$ and $3d_{yz}$). As a result of this, the Co e_g and t_{2g} orbitals form sets of doubly and triply degenerate bonding and anti-bonding orbitals respectively when interacting with another Co atom.

In figure 6.4, the doubly degenerate Co-Co e_g orbitals hybridise with the Mn e_g orbitals, creating a doubly degenerate e_g orbital which sits very low in energy, together with an e_g anti-bonding orbital. The Co-Co t_{2g} orbital hybridises with the Mn t_{2g} orbital, creating 6 new orbitals: the triple degenerate t_{2g} bonding orbital and the triply degenerate t_{2g} antibonding orbital. What now remains are the unoccupied Co-Co antibonding bands t_{1u} and e_u. Since there are no longer any Mn d orbitals to couple with, these orbitals do not hybridise with the Mn, instead sitting just below and above E_{F}. This band picture results in the opening of a small gap in the minority channel. The minority states close to E_{F} are localised at the Co and do not couple to the Mn.[92]

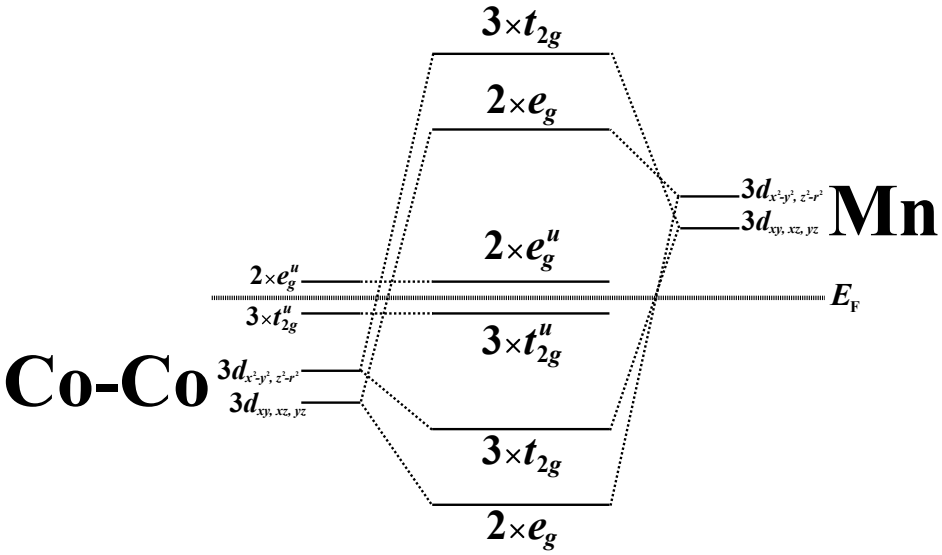

Figure 6.4: The result of the interaction between the Co-Co hybridised 3d orbitals and the Mn 3d orbitals.

6.1.3 Probing the Half-Metallic state

The primary issue within the study of half-metallicity is experimentally observing the state. Whilst various *ab initio* methods are very useful for predicting novel physics, the vast majority of these calculations study the ground state properties of the system, in a realm devoid of thermal excitations, or (as is often the case with transition metal based materials), spin-orbit interactions. Spin polarisation whilst being a relatively simple concept, is a challenging quantity to measure. One means of attempting to rigorously define the spin polarisation of a system is the *degree of spin polarisation* (DSP), defined as

$$P_n = \frac{N_\uparrow v_{F,\uparrow}^n - N_\downarrow v_{F,\downarrow}^n}{N_\uparrow v_{F,\uparrow}^n + N_\downarrow v_{F,\downarrow}^n} \tag{6.3}$$

where $N_\uparrow$ ($N_\downarrow$) is the DOS at E_F for the majority (minority) channel and $v_{F,\uparrow\downarrow}$ is the Fermi velocity. The index n dictates the different electrical transport regimes which may contribute to the DSP. For $n = 0$, no transport regime is considered and the DSP is defined purely in terms of the DOS. For $n = 1$, a ballistic electrical transport[93] regime is considered and for $n = 2$, a diffusive electrical transport regime is considered.[94] As a

result of these different regimes, the DSP value can change significantly depending on the experimental technique employed and this is one such factor as to why experimentally studying the spin polarisation is so difficult.

The techniques typically employed to measure the DSP are point-contact Andreev reflection (PCAR)[95–98] and spin-resolved photoemission spectroscopy.[99–101] Both of these techniques are very surface sensitive and do not take into consideration the bulk stoichiometry of the sample. This has historically caused widely varying experimental values for the DSP in predicted half metals, finding the DSP to be as much as ∼90% less than the theoretical value.[102–107] Factors which may lead to a reduction in the experimental DSP are atomic site disorder, poor stoichiometry and impurities in the sample.

6.1.4 Measurements of the DSP in Co_2MnSi

While theoretically, Co_2MnSi has been repeatedly calculated to be half-metallic, experimentally, observation of the half-metallic state in the Heusler alloys has been unsuccessful. Schmalhorst *et al.*[108] studied the transport properties of Co_2MnSi / AlO_x / Co-Fe magnetic tunnel junctions and measured an effective spin polarisation of 66 %. Herbort *et al.*[109] reported the spin polarisation of a $Co_2Cr_{0.6}Fe_{0.4}Al/AlO_x/Co_{0.7}Fe_{0.3}$ junction to be only 67 %. The study of the Giant Tunneling Magnetoresistance in a Co_2MnSi / AlO / Co_2MnSi interface by Sakuraba *et al.*[110] reported a markedly higher 83-89 % spin polarisation at 2 K. This value however collapsed upon heating the interface to ∼ 50 K.

As of recent, interest has been renewed in Co_2MnSi. Jourdan *et al.*[111] through the use of *in situ* ultraviolet spin-resolved photoemission spectroscopy measured a spin polarisation of ∼93% in Co_2MnSi. Not only was the determination of a large DSP encouraging, but additionally, comparison between their *ab initio* calculations and the experimental data gave exceptional agreement.

Many studies have been performed on the conductive and potential half-metallic properties on thin films of Co_2MnSi and other Heusler materials. As a result, they may not be representative of the bulk of the crystal. Little work has been performed on bulk

samples of the Heusler materials. This work details how MCS can be used to determine the degree of spin polarisation in the sample. We present the first bulk determination of the DSP by employing MCS on a bulk sample of Co_2MnSi.

6.1.5 Determination of the Spin Polarisation using Magnetic Compton Scattering

MCS can be used in determining the DSP of a material through the combination of experimental work and theoretical calculations. By fitting a theoretical MCP to the experimental data, the agreement between theory and experiment infers faith in the model. By *tuning* the model to the experimental data, insight into the electronic structure can be gained. This means that while MCS is not a direct probe of the DSP experimentally, the interplay between theoretical calculations and experimental work, and the agreement (or disagreement) between these two different paradigms gives valuable insight into the DSP and underlying electronic structure. To be more succinct, by making subtle changes to the band structure of the model, the model can be greatly enhanced to improve the agreement between the experimental and theoretical MCPs. The DSP can then be extracted from the most successful model. Unlike other methods of determining the DSP (as outlined in §6.1.3), using MCS to determine the DSP is performed exclusively on bulk samples, as opposed to the thin film work which dominates much of the literature.

To improve the confidence in the fitting, several directions need to be measured and compared to theoretical profiles simultaneously. This also enables the agreement between the theoretical and experimental anisotropies in the EMD to be studied. Unlike the measured MCPs, the 1D anisotropies will be comprised of only the itinerant electronic EMD contributions. These contributions are well described using DFT and can be used as an additional layer to critique the theoretical-experimental agreement.

In the following work, we have measured three directions. The anisotropies for both the experimental data and the theoretical calculations have been calculated totalling six data sets which seek agreement with the theoretical calculations.

6.2 Crystal Growth and Characterisation

6.2.1 Composition

Stoichiometry of the Heusler compounds plays a significant role in the various observable properties in the materials due to changes in the band structure. The Heuslers have been theoretically observed to undergo shifts in their band structure as the stoichiometry is altered.[112–114] This work has used two different methods to probe the disorder of the sample. EDX and powder XRD. The latter technique is a significantly more *involved* process which has been discussed in §6.5.

The EDX results find that compositionally, the sample used has a potential excess of Si which populates the Co sites. This measurement was performed using an *area* scan, in which a region of the sample is specified and measured by the equipment as opposed to one very specific point on the sample. The ratio of Co to Mn to Si was found to be 48/25/27 suggesting the possibility of a small disorder introduced to the Co sites with Si. However, EDX as suggested in the §4.5.4 is unreliable for high precision atomic weightings.

Along with the general inaccuracy of the EDX technique, EDX is quite surface sensitive. Figure 6.5 presents the surface of the sample, measured using an electron microscope. Several regions of the sample's surface can be identified as having poor homogeneity in comparison to the rest of the sample. These regions are assumed to be points where the material has not been completely melted, creating discontinuities on the surface. MCS is a bulk measurement of the sample and will ignore a lot of these surface defects but they may still be indicative of why the stoichiometry of the sample should be scrutinised.

6.2.2 SQuID Magnetometry

Another technique used to characterise the sample was a SQuID magnetometer. While the DSP is a very important quantity in regards to determining the half-metallic character of proposed half-metals, another quantity which can be used is the spin moment. As discussed previously, the Slater-Pauling rule requires a half-metallic material to have

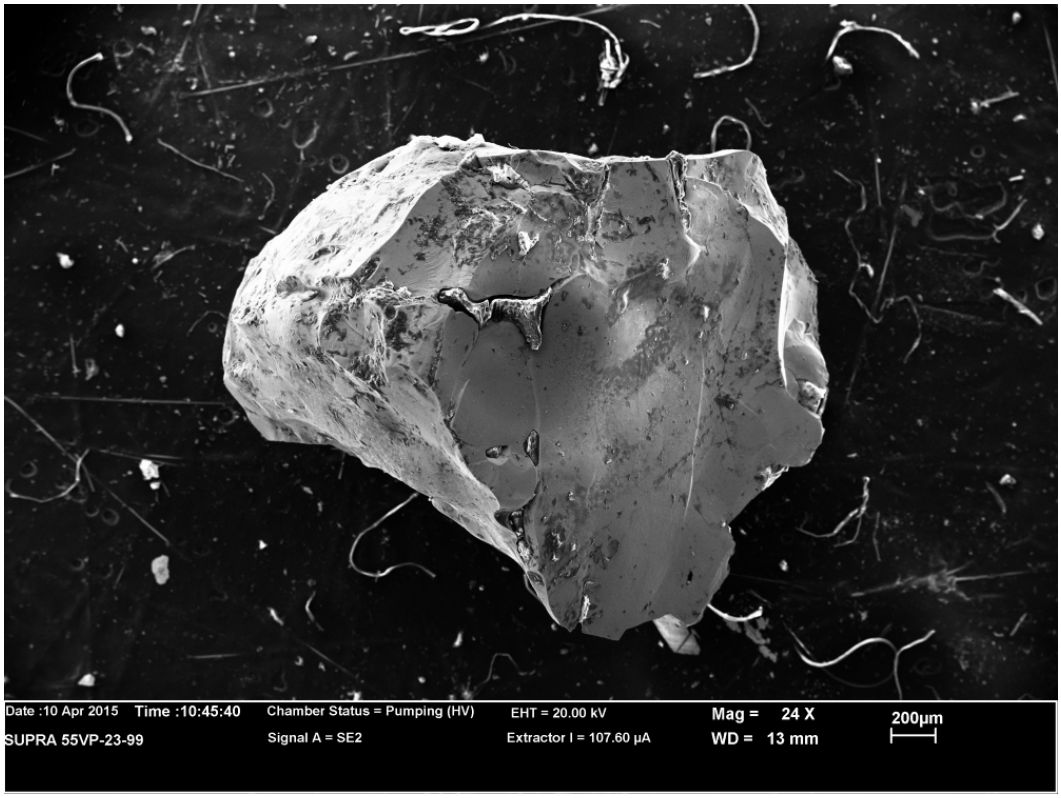

Figure 6.5: The surface of the measured Co_2MnSi using secondary electrons in the EDX apparatus.

an integer total moment. Both MCS and SQuID magnetometry can provide valuable insight into magnetic properties of these materials in order to find evidence for their half-metallicity (provided no orbital moment is found). The SQuID magnetometer was used to measure the characteristic **M**v**H** and **M**vT profiles of Co_2MnSi for a number of reasons. Co_2MnSi has a very large T_C of 985 K. This characteristic should be observable in its MvT profile as the change in moment from 2 K to 300 K will be small. The MvH was measured to compare to Co_2MnSi's calculated 5 μ_B total moment.

Figure 6.6 shows the results for the Co_2MnSi MvH. The sample was kept at a constant temperature of 2 K and the applied magnetic field was ramped up to a maximum value of $\pm$ 1.5 T. The very small hysteresis suggests Co_2MnSi to be a soft ferromagnet. The sample saturates at a total moment of $5.00 \pm 0.01 \mu_B$/f.u., in excellent agreement with the predicted Slater-Pauling behaviour, literature and DFT calculations. The data was processed using the correct Co_2MnSi stoichiometry. As a result, the agreement between the measured moment and the calculated moment is evidence of a pure, stoichiometric

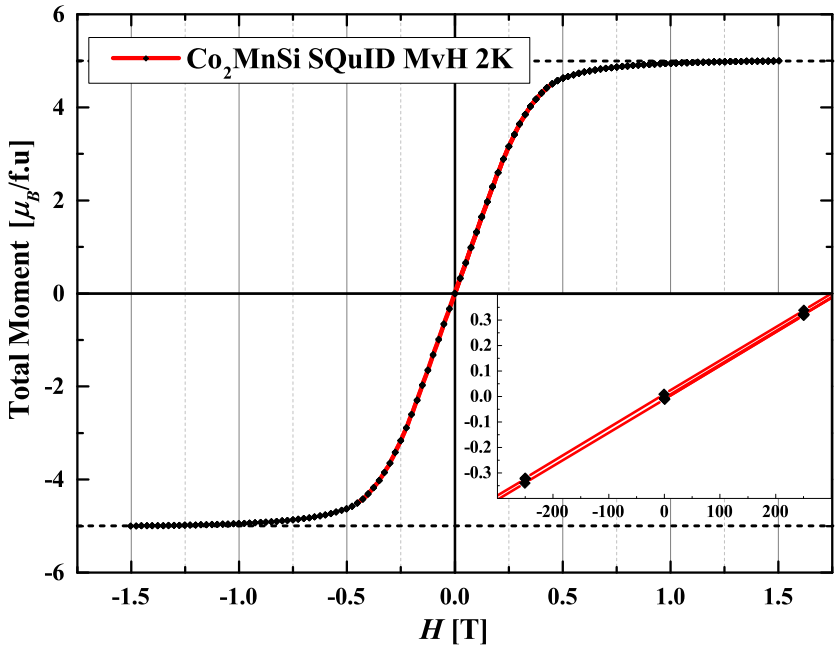

Figure 6.6: SQuID magnetometry for Co_2MnSi [100] direction at 2 K. The sample saturates at a total spin moment of 5.00 μ_B/f.u. The inset shows the very small amount of hysteresis about the origin.

sample. Since no orbital moment is expected in the case of Co_2MnSi, the SQuID results can be treated as a measurement of purely the spin moment of the system. The integer moment measured is indicative of the potential half-metallic character of the sample.

6.3 Theoretical Calculations

Self consistent field (SCF) calculations were carried out using the full potential linearised augmented planewave method as described by the ELK FP LAPW code. The aim of these calculations is to describe the measured MCPs and their anisotropies in order to determine the electronic structure of the system. Small modifications to the band structure may be necessary to improve agreement with the experimental data. These changes in the band structure have been observed through varying the lattice parameter and the inclusion of U to simulate correlation effects. Macroscopic quantities of interest are the total and site specific spin moments and how they compare to the SQuID

magnetometry and literature. Following this, studies into the structural properties and possible correlation effects of the system were performed to observe effects in the band structure (and therefore the magnetic properties) of the system.

6.3.1 Lattice Optimisation

A lattice optimisation was performed in order to determine the lattice parameter which would minimise the ground state energy of the calculation. A range of calculations were performed where the lattice parameter was varied by up to ±10%. The resulting ground state energies were then fit with the 3rd order Birch-Murnaghan equation of state,[115] defined as

$$E(V) = E_0 + \frac{9V_0B_0}{16}\left\{\left[\left(\frac{V_0}{V}\right)^{\frac{2}{3}} - 1\right]^3 B_0' + \left[\left(\frac{V_0}{V}\right)^{\frac{2}{3}} - 1\right]^2 \left[6 - 4\left(\frac{V_0}{V}\right)^{\frac{2}{3}}\right]\right\} \quad (6.4)$$

where P is the pressure, V_0 is the original volume, V is the new deformed volume, B_0 is the bulk modulus, and B_0' is the derivative of the bulk modulus with respect to pressure i.e.,

$$B_0 = -V\left(\frac{\partial P}{\partial V}\right)_{P=0} \quad (6.5)$$

and

$$B_0' = \left(\frac{\partial B}{\partial P}\right)_{P=0}. \quad (6.6)$$

The results for the lattice optimisation are plotted in figure 6.7. The calculated energy values have very strong agreement with the predicted BM curve. The energy is minimised for a lattice parameter value of $a = 5.659$ Å, in exceptional agreement with the reported experimental values of the literature.[87,103,116]

Varying the lattice parameter also indicates a *robustness* to Co_2MnSi's theoretical half metallic properties. A change in the lattice parameter from a range of $\sim \pm 6\%$ makes no impact to the total moment, retaining the integer value. However, there is a significant change to the band structure of the compound as the Mn and Co moments vary as the lattice parameter is varied. This can be seen in figure 6.8 where the total, Co and

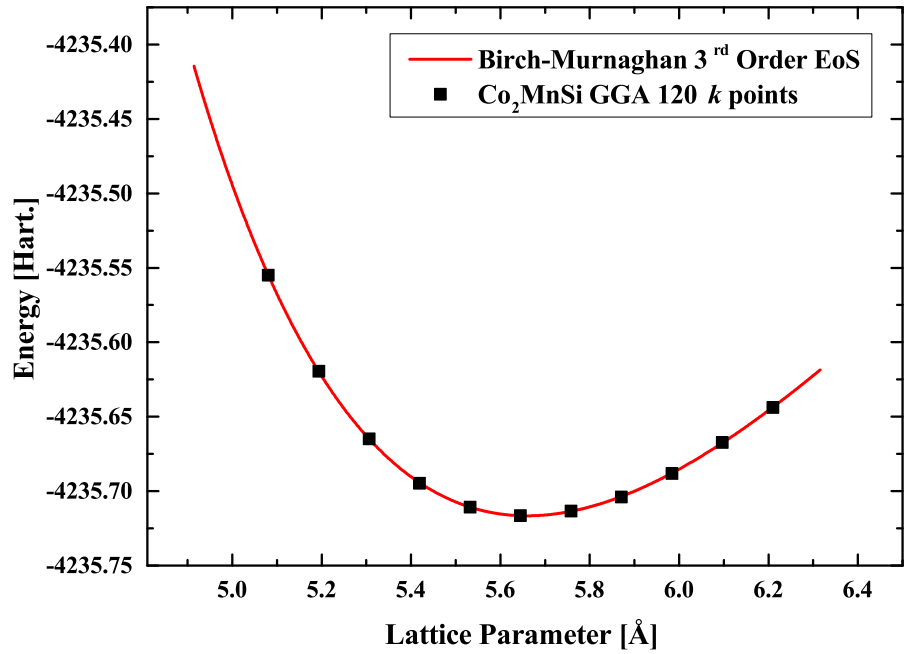

Figure 6.7: The lattice optimisation of Co2MnSi as performed in the ELK code. The lattice parameter was varied by up to ±10% and fit with the BM 3rd order equation of state. The minimum lattice parameter was found to be 5.659Å.

Mn moments have been plotted as a function of the lattice parameter. As the lattice parameter is increased, the Mn contribution to the total moment increases alongside a decrease in Co moment. These changes may be reflected in the individual contributions to the total EMD from the Co and Mn sites. Since both elements are $3d$ transition metals, this changes to the EMD will only occur at very low momentum. The broadness of their contributions to the EMD will be identical for larger momenta.

To conclude, a moderate change to the lattice parameter does not make any discernible difference to the total magnetic moment of Co_2MnSi. However, the moments of the Co and Mn which contribute to this total moment do change. The varying of these Co and Mn contributions to the EMD may be able to account for discrepancies between theory and experiment at low momentum but they will not affect the broadness of the MCPs. For all proceeding DFT work, the lattice parameter used will be 5.659 Å.

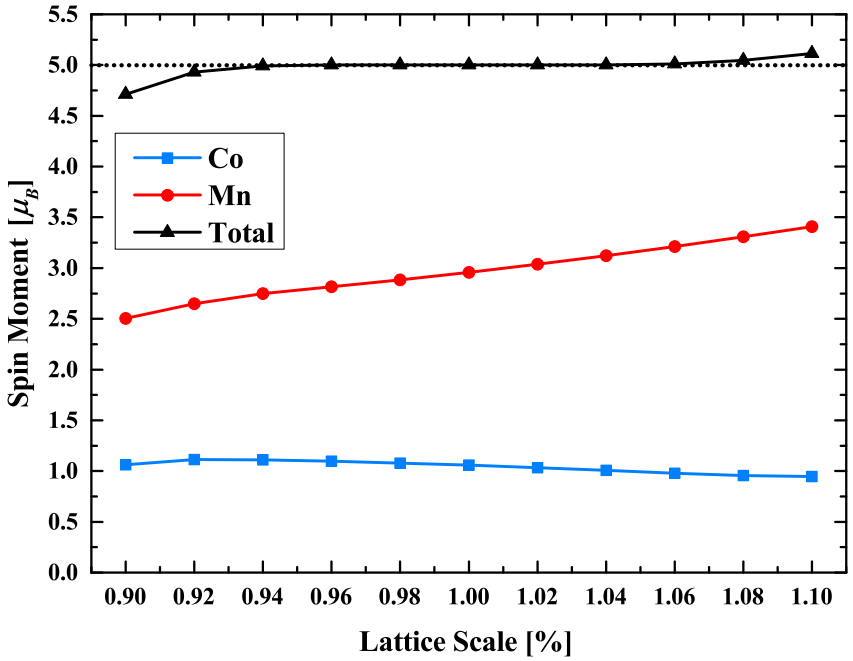

Figure 6.8: Relationship between the lattice parameter of Co_2MnSi and the calculated spin magnetic moments. Only very large changes ($> \pm$ 6 %) destroy the half metallic properties of the compound.

6.3.2 Calculation Details

The GGA XC functional[32] was used and the change in Energy convergence criteria was to the order of 1×10^{-4}eV. The calculation was converged with $35 \times 35 \times 35$ k points which was then limited to 1140 k points inside the irreducible BZ. E_{cutoff} was set to 137.74 eV. Spin orbit coupling was not used.

6.3.3 GGA Results

The SCF converged to a total magnetic moment of 5.00 μ_B, expected of the compound when taking into consideration the Slater-Pauling rule described in equation 6.2. The site specific total moments were calculated to be 1.06 μ_B for Co, 2.96 μ_B for Mn and -0.05 μ_B for Si. This is in very good agreement with the available literature.[117–121] This is in stark contrast however, with the X-ray Magnetic Circular Dichroism (XMCD) results of Wang *et. al.*[103] who found the Co moment to be 1.20 μ_B and the Mn moment

to be 2.6 μ_B. This could be due to underestimation of the moment due to issues with the sum rules used in XMCD. Also, as with many surface sensitive techniques, atomic disorder near the surface can significantly impact macroscopic quantities such as the total moment. This could also mean that the theoretical calculation has calculated the site specific moments incorrectly. Comparing the theoretical calculation to the experimental MCS results gives an additional experimental technique to compare the theory to.

The site specific DOS has been plotted in figure 6.9. Much like the calculated moments from the SCF, the DOS is in very good agreement with the literature. At E_{F}, a band gap of ~ 0.6eV is observed in the minority spin channel. This result, combined with the integer total spin moment of 5.00 μ_B, satisfies the half metallic criteria motivating this work. Studying the partial DOS shows the minority states around E_F which form the band gap are comprised mostly of the Co 3d band. Neither of these peaks couple to the Mn 3d band suggesting them to be of t_{1u} and e_u character. As a result, the peak just below E_F is the $3 \times t_{1u}$ state and the peak just above E_F is the $2 \times e_u$ state. This is the reason why the band gap is small.

6.4 Analysis of Magnetic Compton Profiles

Co_2MnSi MCPs were measured in a magnetic field of 1T at 300K on the BL08w beamline at SPring-8. The [100], [110] and [111] directions were measured so multiple directions could be compared to the theoretical calculations. Alignments were performed through the use of back-scattered Laue diffraction, prior to the experiment.

The theoretical [110] profile can be seen in figure 6.10. The unconvoluted and convoluted profiles have been plotted against one another to show how dramatic an effect convolution can have on the shape of a theoretical MCP. The usefulness of convolution is in its attempt to mimic the resolution of the actual experimental data. Often (and is quite clearly the case here), the Umklapp features present in metallic MCPs are very pronounced in theoretical MCPs. Convolution often alludes to why the umklapp features are not so prominent in the experimental data.

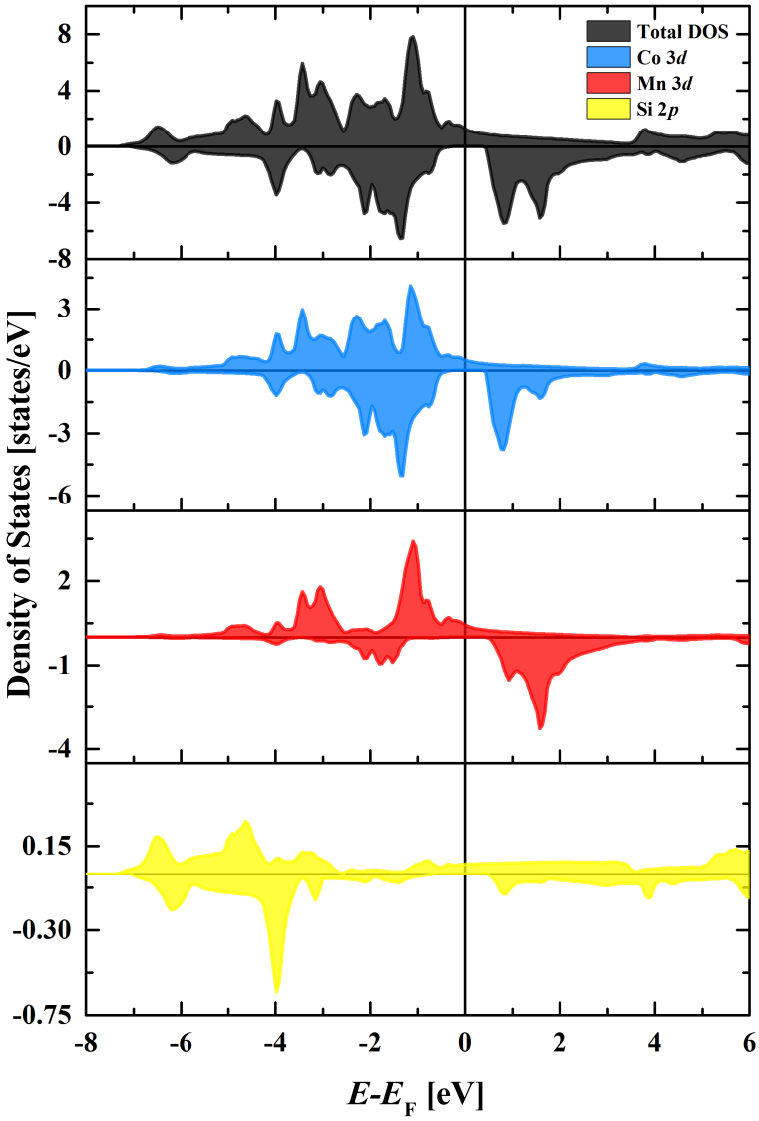

Figure 6.9: The calculated DOS of Co_2MnSi together with the partial DOS of the compositional atoms.

Figure 6.11 plots the experimental MCPs against the theoretical MCPs calculated. The areas of all profiles have been normalised to 1 for the purpose of comparison and the theoretical profiles have been convoluted using a gaussian of FWHM = 0.44 a.u. When studying multiple directions using MCS, it is beneficial to not only measure the direction specific MCPs in order to study how the shapes change, but to also calculate the *anisotropy* itself. The anisotropy is determined by calculating the difference between

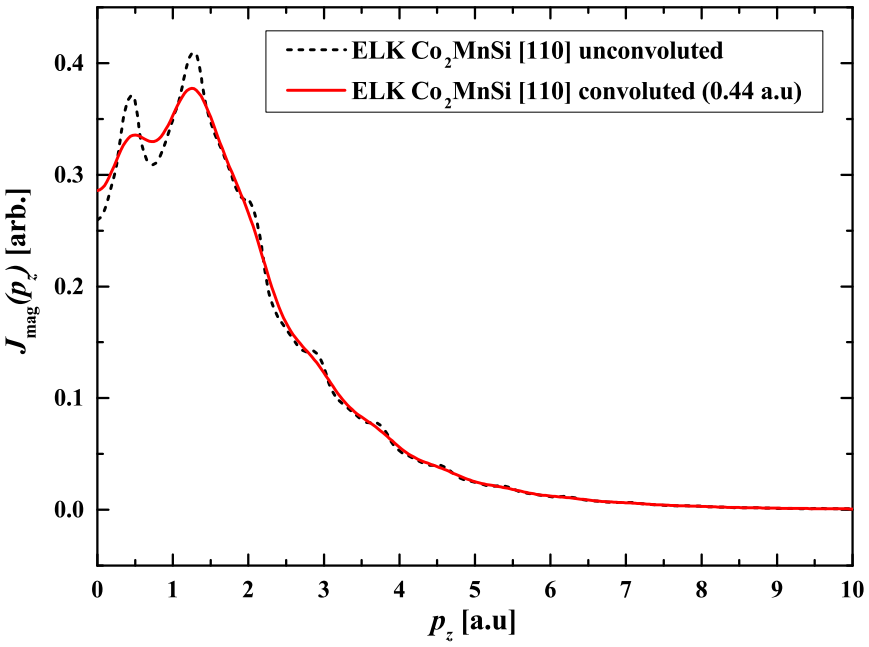

Figure 6.10: Theoretical [110] convoluted and unconvoluted profiles. The unconvoluted profile shows the presence of *Umklapp* features, typical in a material which has a metallic (or in this case, partially metallic) band structure. The convolution was performed using a gaussian of FWHM = 0.44a.u.

two directional MCPs. This has the effect of removing the less anisotropic, localised contributions to the MCP (higher momentum contributions). Since DFT calculations are quite apt in describing the more localised contributions to the MCP, the *anisotropic* MCP gives a much more *pure* plot of the itinerant components of the MCP. Comparing the experimental and theoretical anisotropies may therefore be a better indicator of the calculation's ability to model the itinerant region of the EMD than comparing the experimental directional MCPs to the theory. As such, the experimental and theoretical anisotropies have been included in the figure. The agreement with the experimental data is very good, with the calculations capturing the broadness and the periodic Umklapp features. Even at low momentum, where contributions are due to the more itinerant electrons of the material, the agreement is very reasonable. While there are deviations present between the data and calculations, compared to the earlier experiments,[24,122] the results of the *ab initio* calculations are encouraging. Turning attention to the anisotropy,

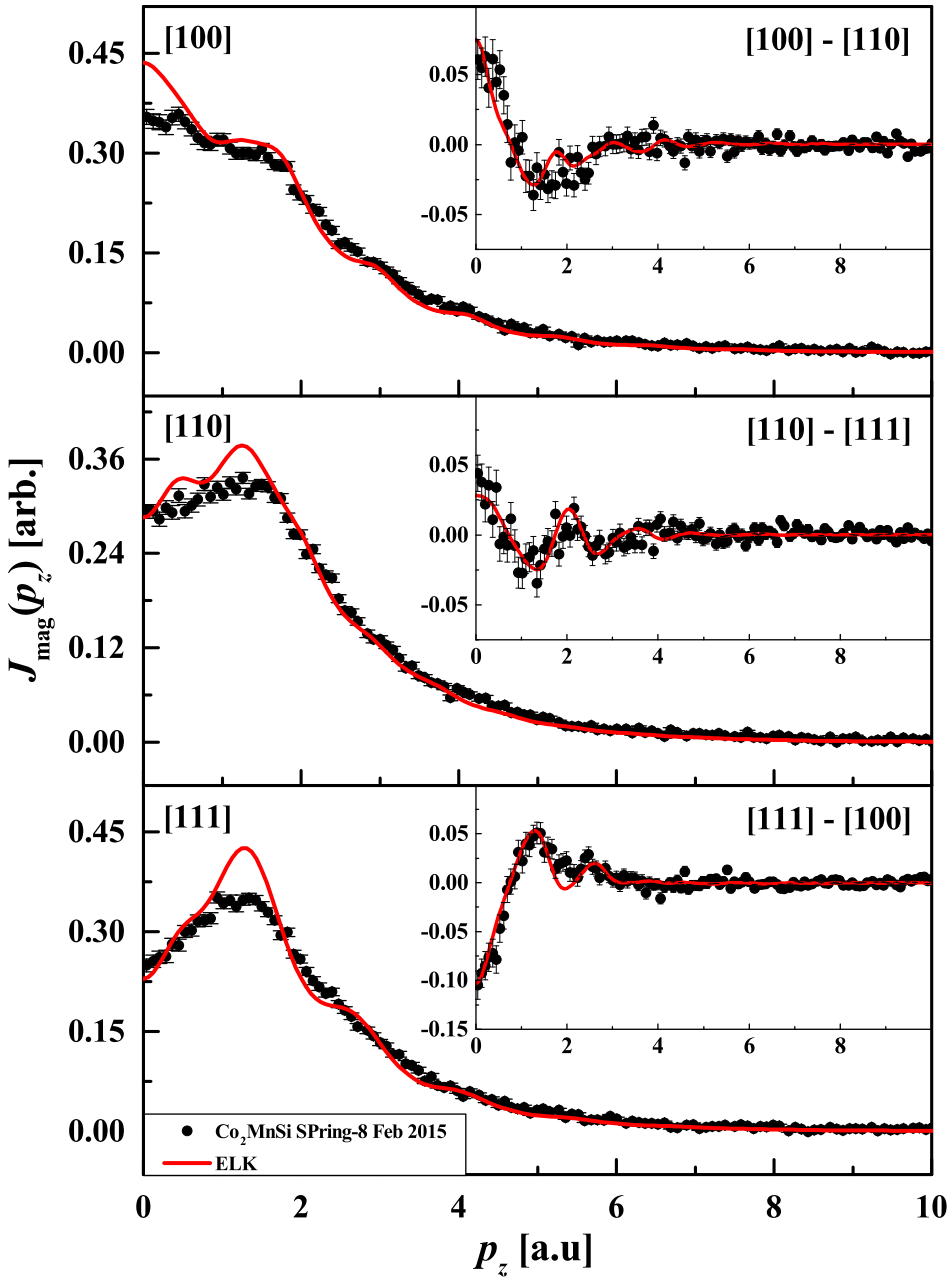

Figure 6.11: Experimental Co_2MnSi along the [100], [110] and [111] directions plotted against theoretical profiles calculated in ELK. The insets plot the experimental anisotropy against the theoretical anisotropy.

it can be seen that the agreement is again, excellent, with the oscillatory features and general shape being very well described by the DFT calculation.

6.4.1 Directional Analysis

For the [100] direction, the calculation captures the essential features of the experimental data very well. Unlike the other two directions, there is no low momentum dip in the experimental profile of the [100] direction, and this is captured in the calculation. The broadness is also replicated well and the Umklapp features seen in the theoretical profile can be observed in the experimental data at 1.5, 3 and 4 a.u.

Likewise, the theoretical [110] profile has very good agreement with the experimental data, matching the broadness of the data and replicating the slight low energy dip seen in the data. At this level of convolution, the Umklapp features cannot be seen much like the theoretical profile, the data resembles that of a smooth curve. Unlike the theoretical calculation however, the experimental data only has one peak at low momentum instead of two. The absence of this peak may be an anomaly due to the binning used to generate this data. The data points in this momentum region oscillate slightly indicating that with higher statistics, a feature may develop.

The [111] calculation captures the broadness of the data and replicates the low energy *dip* well, but like the [110] direction, seems to over-estimate the peak in the profile at about 1.5 a.u. Contrary to the other two directions, the [111] direction has very large Umklapp features which do not seem to be observed in the experimental data.

6.4.2 Anisotropy Analysis

Turning attention to the anisotropies, the calculations very well reflect how the electron momentum distribution changes in momentum space. The general shapes of all the anisotropies are very well reproduced. As was the case with the MCPs, the anisotropies' experimental periodicity seems to be shrouded possibly due to the experimental resolution as in the [100]-[110] and [111]-[100] profiles, the subtle peak at 2 a.u is not replicated well by the data. For the [110]-[111] anisotropy, which has larger, broader periodic features, the periodicity and shape of the experimental anisotropy is very well reproduced by the calculation.

To summarise, the agreement between the experimental data and the GGA calculation is very impressive. Except for perhaps the [111] direction (due to its failure to adequately describe the shape of the experimental data), the calculation captures the momentum space distribution of Co_2MnSi very well. To extend the work further, an investigation into how electron correlation affects the EMD was performed in order to see how this will change the shapes and character of the MCPs.

6.4.3 Correlation effects study using GGA+U

For many compounds, the LDA or GGA exchange correlation functionals are sufficient for generalising the interactions (or lack of interactions) between the itinerant, valence electrons of the system. Turning off the Coulomb interaction and treating the electrons as a homogenous electron gas (LDA) and taking into consideration, the change in electron density permeating that *sea* (GGA) can produce very accurate results. For systems which are more *correlated*, where the Coulomb interactions are not only strong between different electrons, but also the electrons' own self interaction, different approaches can be implemented to account for this *correlation* effect. Since variations in the lattice parameter yield no discernible impact on the MCPs, investigating how strongly correlated the electrons are, and what affect this correlation has on the band structure of Co_2MnSi is very useful to test how rigorous Co_2MnSi's band structure is.

In the same vein as similar work from the past,[123] the on-site electron correlation will be simulated using the GGA+U method.[124] The following work investigates how the band structure and magnetic moments are affected with the application of U. For all calculations, $J = 0.88$ eV and the *Around Mean Field* (AMF) double counting scheme[125] was employed. Calculations were performed where U was applied to the Co d electrons, the Mn d electrons, and both Co and Mn d electrons. No calculations were performed where U was applied to the Si as the Si $2p$ electrons are too low in energy to affect the magnetic properties and band gap of the compound.

$U_{\mathbf{Co}}$ Calculations

Applying U to the Co d electrons results in a very subtle change to the electronic and magnetic structure of the system. Figure 6.12(a) shows how the spin moments of Co_2MnSi with the application of U to the Co d electrons.

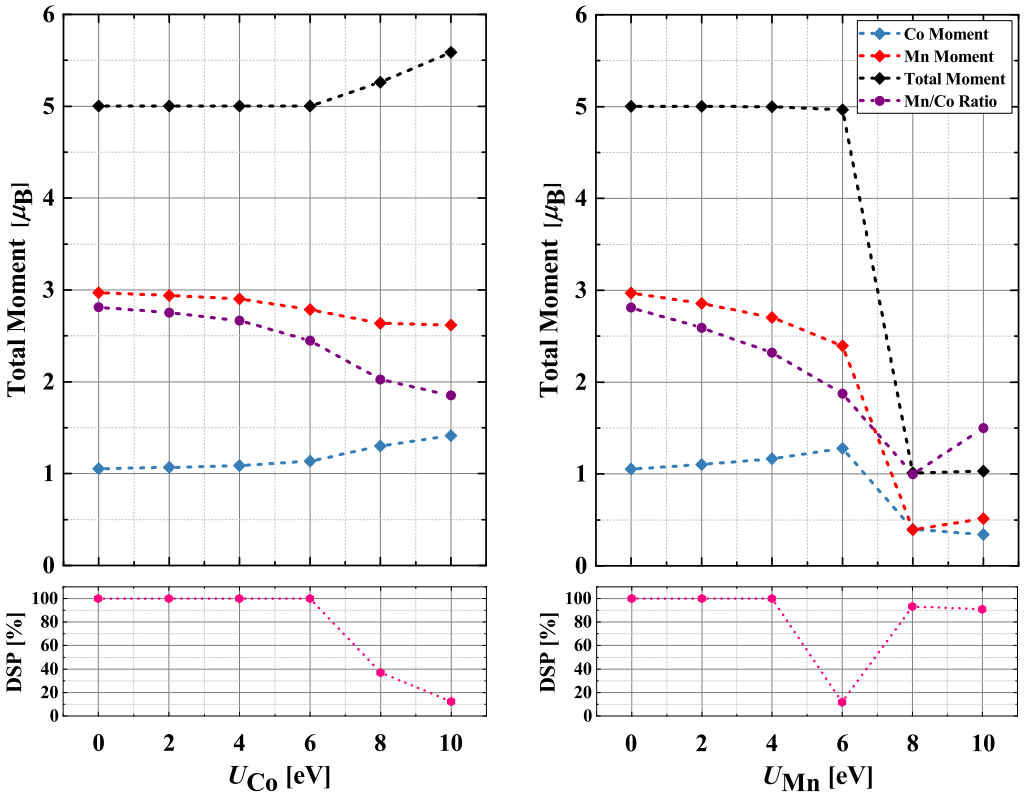

Figure 6.12: Spin moment quantities and DSPs calculated for applied U_{Co} (a) and U_{Mn} (b).

As U is increased, a change in ratio between the Mn and Co spin moments is observed which is why the total moment remains at 5.00 μ_B. Since the band structure is shifted minimally for smaller U values, the MCPs reflect this with very small deviations from the base GGA result. At $U > 6$ eV, the change in Mn:Co ratio continues, increasing the total moment above 5.00 μ_B, destroying the half-metallicity. It is concluded that correlation affects in the Co atoms play no role in changing the Co_2MnSi model. However, it is unlikely the correlation effects present in Co will be of such a magnitude and hence, are not considered to be of physical significance. To conclude, attempting to model Co's

correlation results in minimal changes to the electronic structure of Co_2MnSi.

$U_{\mathbf{Mn}}$ Calculations

For the effects of U on the Mn d electrons, much like the Co results, for $U < 6$ eV, the effects on the band structure and magnetic structure are minimal. Figure 6.12(b) plots the spin moments of Co_2MnSi with the application of U to the Mn d electrons. Much like with the applied Co U, for $U < 6$ eV, the total moment remains at a constant 5.00 μ_B as the Mn:Co ratio shifts. Compared to the Co U results, the change in Mn and Co moments is larger creating a more significant change in the band structure. This peaks at $U = 6$ eV where the DSP drops significantly. As for higher values, the magnetic structure completely changes as the total moment drops to ~ 1.01 μ_B. At this value, the DSP increases again as the total moment has approached an almost integer value. As evidenced from the magnetometry (§6.2.2) the total moment of Co_2MnSi is not this small and so the results for $U > 6$ eV can be interpreted as being non-physical. Much as is the case with Co, Mn's correlation effects are not thought to be this high in energy.

$U_{\mathbf{Co,Mn}}$ Calculations

In these sets of calculations, keeping the $U_{\mathrm{Co}} : U_{\mathrm{Mn}}$ ratio fixed to $1 : 1$, U was increased from 0 eV to 10 eV. Consistent with the previous two sets of calculations, the Mn:Co total moment ratio falls until at $U = 6$ eV where the half-metallicity is destroyed and the spin moment drops to 2.39 μ_B.

Attention must be drawn to the fact that a 6×6 matrix of different calculations can be performed for the case where U_{Co} and U_{Mn} are both varied. Future work could attempt to calculate these different elements of the matrix.

As a result of this correlation investigation, the theoretical work makes quite a substantial case for the lack of correlation effects in Co_2MnSi.

6.4.4 Relationship between Site-Disorder and Magnetic Moment

Studying how the effects of disorder change the band structure (and thus, magnetic properties) may be important for understanding analysing the Co_2MnSi data. Numerous studies investigating the disorder in the compound have been performed using DFT since variations in the stoichiometry of the Heusler materials may lead to explanations as to why they are half-metallic (or equally, why they are not). Picozzi *et al.* investigated the four most likely types of disorder to occur in Co_2MnSi. The following are ranked in terms of theoretical formation energy ΔE from smallest to largest:[126]

1. Mn $\rightarrow$ Co non-stoichiometric disorder
2. Co $\rightarrow$ Mn non-stoichiometric disorder
3. Co $\leftrightarrow$ Mn stoichiometric disorder
4. Mn $\leftrightarrow$ Si stoichiometric disorder

Other types of disorder are energetically unfavourable and hence, were not studied. The results from FLAPW-GGA calculations suggested that the non-stoichiometric disorder introduced from Co atoms substituting Mn atoms drastically lowered the spin polarisation, introducing Co states into the minority band at E_F. Conversely, non-stoichiometric disorder of Co atoms by Mn makes no impact on the minority states of Co_2MnSi preserving the half-metallicity. Whilst the formation energies are reported as being different, experimentally, these types of disorder are equally prevalent and so, it is predicted that non-stoichiometric disordering of Co and Mn atoms will play a dominant role in the destruction of Co_2MnSi's half-metallicity. Galanakis *et al.* find in contradiction with Picozzi *et al.* changes to the spin polarisation of Co_2MnSi when stoichiometric Mn $\leftrightarrow$ Si disorder is modelled.[127] Even small concentrations of $\sim 5\%$ cause changes to the total moment of the system, destroying the half-metallicity.

Finally, Pandey *et al.* found (also using the CPA) that for very small disorder (changes of a fraction of 1 %), quite significant changes can occur to the total moment of the system.[128] As such, being able to compare disorder effects to the experimental MCS and SQuID data will prove to be very useful in the analysis of this compound.

6.5 Powder X-ray Diffraction

To experimentally investigate the disorder and quality of the sample, powder X-ray Diffraction (XRD) was used to study the crystal structure and disorder of the sample. XRD was performed using Cu K_α radiation ($\sim$ 1.5418 Å) from an angle 2θ of 25° to 125° for a duration of 24 hours. Cu K_α was used due to the heavy Co fluorescence created when using a Mo source.

An initial Rietveld refinement[129] was performed using the GSAS[130,131] code. The lattice parameter was determined to be 5.652 ± 0.001 Å, in very good agreement with the literature and theoretical calculations. The model found no improvement when disorder was taken into account contributing to the evidence that the sample was stoichiometric. The Rietveld refinement has been plotted in figure 6.13. In general, the Rietveld

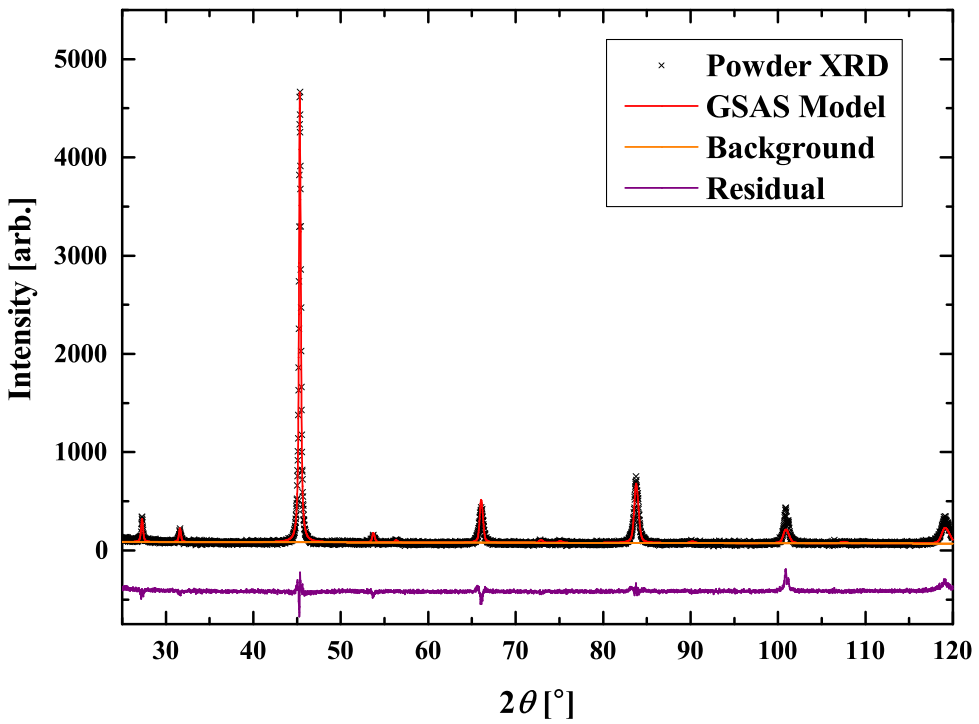

Figure 6.13: XRD diffractogram captured for Co_2MnSi powder using Cu K_{α_1} and Cu K_{α_2} X-ray radiation.

refinement models the data very adequately. At larger angles however, the peak inten-

Site	X sites	Y sites	Z sites
Co	$2-\gamma-\beta$	γ	β
Mn	γ	$1-\alpha+\gamma$	α
Si	β	α	$1-\alpha-\beta$

Table 6.1: Definition of the number of constituent atoms in Co_2MnSi, related to the disorder parameters α, β and γ.

sities are underestimated for the [440] and [620] reflections. Unfortunately, due to the energy of Cu K_α radiation, the Co in the compound fluoresces, reducing the XRD signal significantly. This can cause quite a considerable change to the measured intensities of the XRD peaks. As a result, while the measured reflections are counted at their appropriate angles, the intensities may not be believable due to issues with the measured background.

Takamura *et al.*[132] devised a different means of measuring the atomic disorder of full-Heusler materials as demonstrated by their analysis of the disorder in Co_2FeSi thin films. This new technique involves using Powder XRD with a Cu K_α and Co K_α source. While the different sources will shift the scattered peaks in 2θ due to their energy differences, another difference arises due to the X-ray anomalous scattering from the two sources.[133] Quantitatively determining the on-site disorder for the full-Heusler is expressed using three disorder parameters α, β and γ and determined from a physical model proposed by Niculescu *et al.*[134] Here, α represents the the exchange between the Mn and Si atoms, β represents the exchange between the Co and Si atoms, and γ represents the exchange between the Co and Mn atoms. Once the disorder parameters have been determined, calculating the composition of Co_2MnSi can be performed by referring to table 6.1. In order to determine these disorder parameters, the peak intensities of the (111), (002) and (220) reflections from the XRD data need to be determined, for these can then be related to the atomic scattering factors of the Co, Mn and Si. Figure 6.14 plots the calculated atomic scattering factors for both the Cu K_α and Co K_α sources.[135] Here, the atomic scattering factors for each element have been plotted as a function of $sin\theta/\lambda$, where θ is the scattering angle and λ is the incident X-ray wavelength.

Processing the data from the two XRD data sets requires they be normalised to the

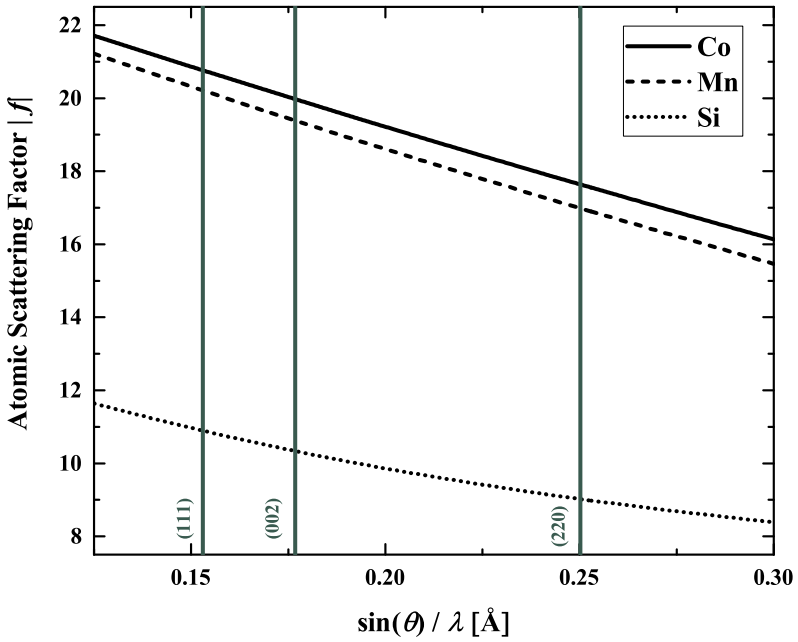

Cu K_α Source

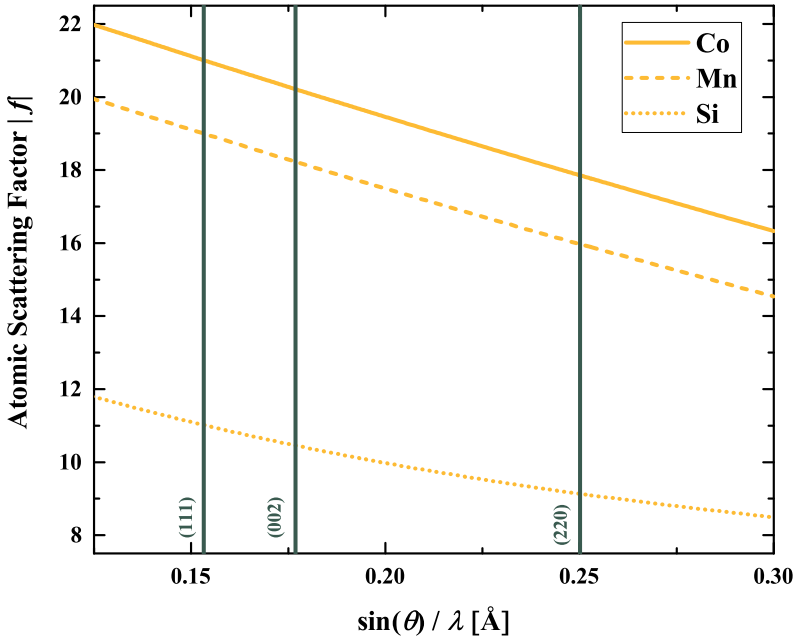

Co K_α Source

Figure 6.14: Calculated atomic scattering factors for Co, Mn and Si from Cu K_α and Co K_α sources.

intensity of the (220) reflection. The crystal structure factor[83] for the (220) direction ${F_{220}}^2$ is related to the atomic scattering factors by

$$F_{220} \propto 2f_{\mathrm{Co}} + f_{\mathrm{Mn}} + f_{\mathrm{Si}} \tag{6.7}$$

where f_{Co}, f_{Mn} and f_{Si} are the atomic scattering factors of Co, Mn and Si respectively. After the datasets have been normalised, the (111) and (002) reflections can be used to determine α, β and γ using the following two simultaneous equations:

$$F_{111} \propto (1 - 2\alpha - \beta)(f_{\mathrm{Mn}} - f_{\mathrm{Si}}) + (\gamma - \beta)(f_{\mathrm{Co}} - f_{\mathrm{Fe}}) \tag{6.8}$$

$$F_{002} \propto (1 - 2\beta)(f_{\mathrm{Co}} - f_{\mathrm{Si}}) + (1 - 2\gamma)(f_{\mathrm{Co}} - f_{\mathrm{Fe}}). \tag{6.9}$$

The collected Co K_α source data is plotted with the Cu K_α source data in figure 6.15. This style of analysis, where the peak intensities of two different datasets are compared

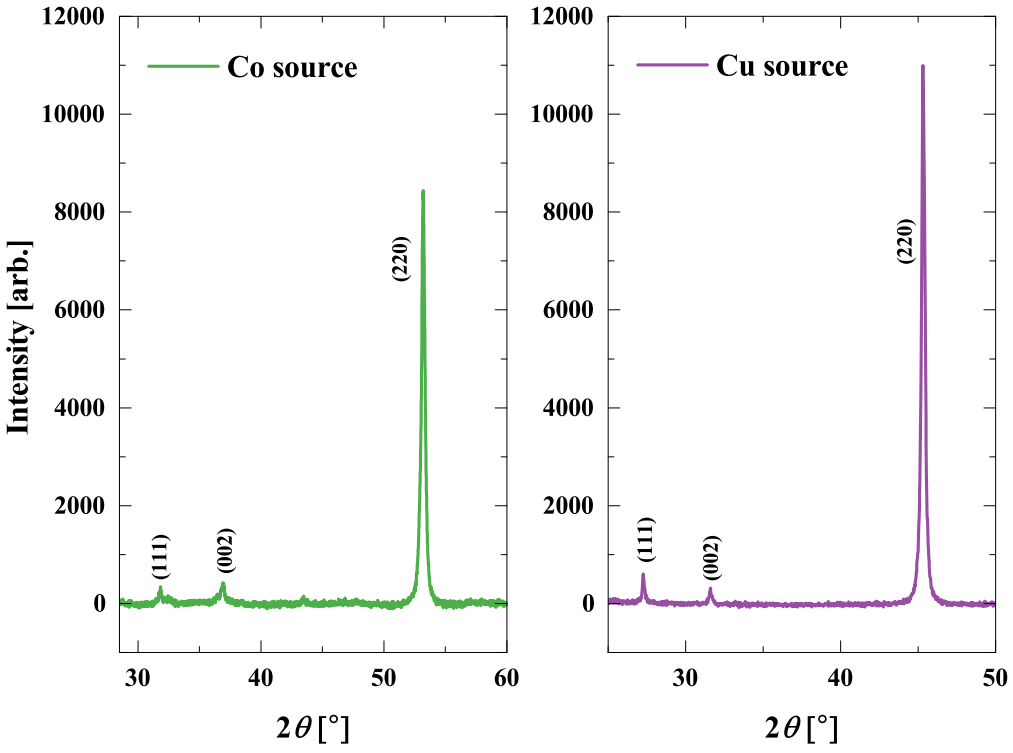

Figure 6.15: Measured XRD patterns for Co K_α and Cu K_α X-ray sources.

[2]The intensity I of a reflected peak is equal to the square of the crystal structure factor i.e. $I = F^2$.

is heavily dependent on a high signal to noise ratio. The values for α, β and γ were found to be 0.081, 0.007 and 0.513, respectively. These values suggest a significant amount of disorder between the Co and Mn atoms with a small disorder between the Mn and Si and a negligible disorder between the Co and Si. When considering the success of the theoretical work combined with the 5 μ_B total moment measured using the SQuID, and EDX work which suggested a small disorder between the Co and Si sites, it is not feasible for the sample to possess this level of disorder between the Co and Mn sites. For further analysis of the disorder to continue, a higher quality data set for the Co source needs to be measured.

6.6 Concluding Remarks

6.6.1 Summary

The EMD of Co_2MnSi was determined by measuring the directional dependent MCP along the [100], [110] and [111] directions. The system was modelled using the ELK FP-LAPW DFT code with the GGA exchange correlation functional which calculated a 100 % spin polarisation at E_F. From the calculation, the three directional MCPs were calculated and compared to the experimental data. For all three directions, the general broadness of the profiles find very good agreement with the experimental profiles while the [110] and [111] profiles overestimate the low momentum peak. Computing the anisotropy of the system finds very good agreement with the experimental data. Extensions to this theoretical work through the use of the Hubbard U model do not improve upon the initial *ab-initio* calculation.

The quality of the sample has been brought into question regarding its stoichiometry due to the variations in concentrations measured using the EDX technique. The original sample was a large chunk comprised of multiple single crystals. Isolating a sample which could be measured using MCS required the use of a diamond saw. Furthermore, the surface of the sample studied using a SEM has regions of discontinuity and inhomogeneity, suggesting the sample has not been annealed or grown sufficiently. Using SQuID

magnetometry, a saturation moment of 5 μ_B was measured (with the assumption that the sample is purely Co_2MnSi, in agreement with literature), reinforcing the notion that the bulk of the sample is stoichiometric. A further effort was made to study Co_2MnSi's stoichiometry through the use of powder XRD. While the modelled Rietveld refinement was in good agreement with the measured XRD data, the abundance of fluorescence generated with the Cu K_α source meant a significant background contributed to the XRD results, hindering an accurate measurement of the stoichiometry.

6.6.2 Future Work

More work is required to study the stoichiometry and composition of the sample. Of highest priority is to further study the sample using powder XRD. Obtaining two very high quality data sets from a Cu source and a Co source should allow the determination of the composition using the analytical technique of Takamura *et al.* The robustness of this compositional analysis is crucial for finalising the theoretical models used for comparison with the experimentally determined EMD. Further insight can be gained by modelling disorder in the sample using the SPR-KKR DFT code, which will most likely warrant a large study of the potential disorders available to the system.

Chapter 7

Characterisation of the Spin-Density of the Heavy Fermion Kondo system CeB_6

Magnetic Compton Scattering was used to collect high precision spin density data of the Kondo material CeB_6. The nature of the magnetism in CeB_6 is controversial. A multitude of *Polarised Neutron Diffraction* (PND) experiments have attempted to rectify this with discrepancies over whether the CeB_6 spin density originates from the $4f$ or $5d$ bands. In addition, the potential inclusion of a B contribution is also controversial. This material was initially measured to test the new magnet setup to observe how accurately the system could measure low spin moment systems. Due to the significantly improved statistics, an anisotropy was detected between the [100] and [110] directions which prompted a further study of the material. In addition to the improved statistics, the theoretical techniques employed are much more sophisticated than the previous study. The DFT and Hartree-Fock based codes used to study the momentum density of this system provided far greater insight than what was previously possible.

7.1 Introduction

The CsCl structured Hexaborides have attracted vast interest over the last few decades due to their anomalous transport properties and diverse magnetic phenomena. Examples include the superconductors, YB_6,[136,137] GdB_6, which have two magnetic structure changes at successive phase transitions,[138,139] SmB_6, which exhibits an *intermediate valence state*,[140,141] and CeB_6, a system which exhibits dense Kondo behaviour and a very complex magnetic phase diagram.[142]

Cerium Hexaboride (CeB_6) is a rare-Earth based f-electron compound which crystallises into a CsCl structure where the B octahedra occupy the Cl site. Surrounding these B octahedra are the Ce^{3+} ions which occupy a cubic lattice (figure 7.1). CeB_6 has seen

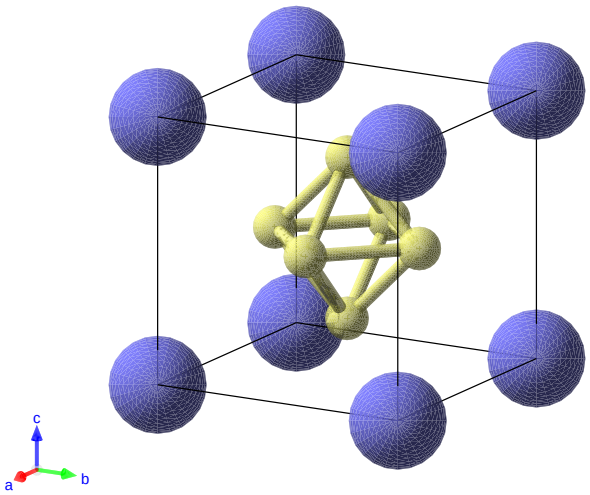

Figure 7.1: The cubic Pm-3m unit cell of CeB_6. Encompassed by the Ce ions (●) which occupy the corners of the cubic unit cell is the B (○) octahedra. Crystal structure adapted from the work of Blum *et al.*[143]

fervent study due in large to its very complex phase diagram which exhibits three different types of magnetic order: a paramagnetic phase (which exhibits the Kondo effect), an antiferromagnetic (AFM) phase, and an antiferro-quadrupolar (AFQ) phase which is characterised by a staggered, antiferromagnetic arrangement of magnetic moments.[144] The phase diagram can be seen in figure 7.2. These phase transitions were evidenced by the sharp peaks apparent in the specific heat measurements by Fujita *et al.*[145] At 2.4 K,

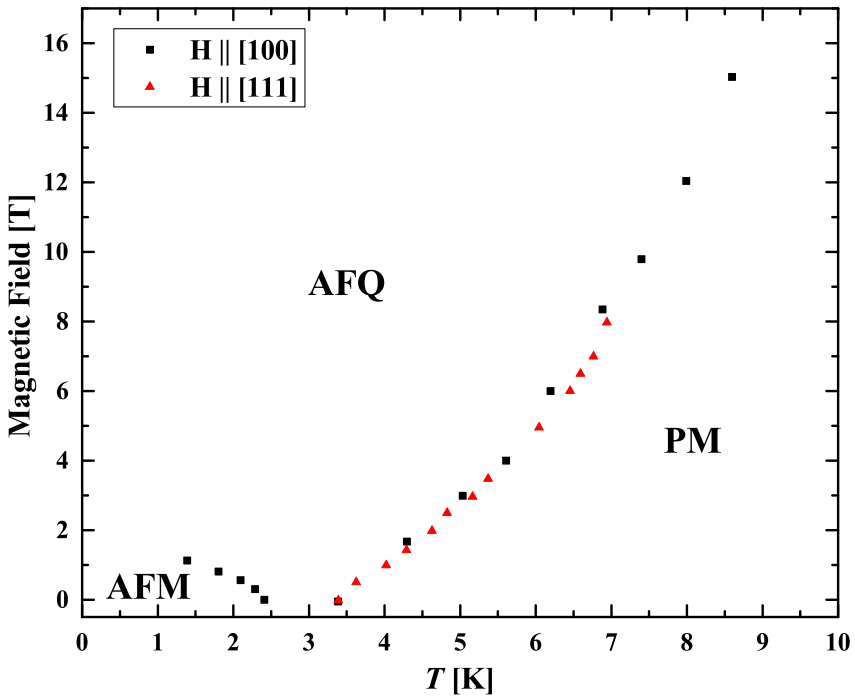

Figure 7.2: The magnetic phase diagram for CeB_6 obtained for a magnetic field applied along the [100] and [111] directions. The phase diagram shows the regions of the three paramagnetic (PM), antiferro-quadrupolar and antiferromagnetic phases present in CeB_6's phase diagram. The figure has been adapted from reference.[144]

a sharp peak develops, observing the transition into CeB_6's AFM phase. Additionally, a weaker peak is observed at 3.2 K relating to the so-called *antiferroquadrupolar* (AFQ) state. As is apparent from Fujita *et al.* and Effantin *et al.* this phase can be controlled with the application of large magnetic fields.

To add further complications to the phase diagram, Uimin *et al.*[146,147] proposed that within T_{AFQ}, it is possibly to destroy the AFQ state with the onset of a very large magnetic field ($\sim$ 20 T) however no experimental evidence of this has been observed for fields up to 18 T.[144,148] Takigawa *et al.* have also proposed that the AFQ phase has no magnetic moment in the absence of a magnetic field. AFQ, AFM and even ferromagnetic properties develop as a result of the application of a magnetic field.[149]

CeB_6 also exhibits the *Kondo* effect.[150,151] Within the paramagnetic phase of CeB_6, the *Kondo* effect can be observed with an increase in resistivity occuring at $T < 100$ K.

This effect can be suppressed with the application of a magnetic field. The observation of this phenomena implies the existence of localised moments in the compound.[152]

7.1.1 Crystal Field Effects

It has been a long time since the discovery of this AFQ state in CeB_6, and even now, the ordering mechanism behind its development is poorly understood. Whilst there have been numerous theories regarding the crystalline-electric field (CEF) excitations,[153–155] the first experimentally verified results were the result of Zirngieble *et al.*'s Raman and Neutron spectroscopy measurements in 1984.[156]

The ground state of CeB_6 is the Γ_8 quartet which is separated in energy by a gap of 46 meV from the more energetic Γ_7 doublet. The fourfold degenerate groundstate enforces two spin and two orbital degrees of freedom. The $4f^1$ electron of the Ce^{3+} ion with angular momentum $J = 5/2$ has eigenstates

$$|+,\uparrow\rangle = \sqrt{\frac{5}{6}}\left|\frac{5}{2}\right\rangle + \sqrt{\frac{1}{6}}\left|-\frac{3}{2}\right\rangle \tag{7.1}$$

$$|+,\downarrow\rangle = \sqrt{\frac{5}{6}}\left|-\frac{5}{2}\right\rangle + \sqrt{\frac{1}{6}}\left|\frac{3}{2}\right\rangle \tag{7.2}$$

$$|-,\uparrow\rangle = \left|\frac{1}{2}\right\rangle \tag{7.3}$$

$$|-,\downarrow\rangle = \left|-\frac{1}{2}\right\rangle \tag{7.4}$$

where $\sigma \in \{\uparrow,\downarrow\}$ are the spin quantum numbers and $\tau \in \{+,-\}$ are the orbital quantum numbers.[157] When in the paramagnetic state, σ and τ align paramagnetically, in the AFM state, σ and τ align antiferromagnetically, and in the AFQ state, σ aligns paramagnetically and τ aligns antiferromagnetically. As such, it can be concluded that the AFQ is the result of an arising *orbital* AFM state whilst the AFM state is the result of the coexistence between the spin and orbital AFM states. In 2001, the AFQ ordering was experimentally observed by Nakao *et al.* with wave vector $\mathbf{Q}_{\mathrm{AFQ}} = (\frac{1}{2},\frac{1}{2},\frac{1}{2})$.[158]

7.1.2 Anomalous and Non-anomalous Spin Density

Whilst many models of CeB_6 have been verified with the successful observation and determination of the AFQ ordering, little evidence has been produced for the nature and origin of the magnetic order. Predicting the nature of the origin of the magnetic moment in CeB_6 is difficult and studying the spin density of the system would help develop a better picture of the ordering in the AFQ phase. Early neutron diffraction work by Boucherle *et al.*[159] identified a primarily $4f$ contribution in intermetallic Ce compounds. Saitoh *et al.* attempted to probe the spin density using PND.[160] They noted that the distribution of the magnetic form factors was not as continuous as the expected spherical nature in reciprocal space. This hints at the possibility of the magnetic electrons in Ce being more delocalised in nature, indicative of the more delocalised $5d$ electrons as opposed to the more localised $4f$ electrons. In addition, their results suggest the presence of a small B spin density, centered on the B_6 octahedra. This work was later refuted by Givord *et al.*[161] who (also using neutron diffraction methods) reaffirmed that like the Ce based intermetallic compounds, the magnetisation was localised only on the Ce ions and was $4f$ in nature. Hanzawa[162] argues a transfer of spin density from the $4f$ states of the Ce to the $2p$ states of the B occurs in the presence of a magnetic field across the sample.

An issue with PND is the fact it measures the total moment of the contributing ions. It is insensitive to the itinerant spin moments. Since CeB_6 has a very large orbital moment relative to its spin moment, most of the spin moment contributions are lost in noise during measurements. In addition, no anisotropy is observed in the literature.

More recently, the inelastic neutron scattering work of Jang *et al.*[163] suggests more complicated physics is at work behind the system. They observed a ferromagnetic instability in the system which gives support to the possible presence of ferromagnetic correlations in the system. Their results also suggest that a model dependent on the AFM coupling of the dipolar and multipolar moments of the Ce $4f$ is not adequate in describing the essential physics of the system. Meanwhile, the *Nuclear Magnetic Resonance* (NMR) work of Friemel *et al.*[164] observed an additional, weak magnetic

exciton mode, separate from the previously observed AFM and AFQ orderings.

What is clear is that the origin and localisation of the magnetic electrons in CeB_6 is a controversial and exciting topic. Probing the EMD of the compound may yield valuable insight into the nature of its magnetism. With the upgrade to BL08W, CeB_6 was measured in order to the test the setup when studying low spin moment systems. Due to the improved statistical quality, an anisotropy was observed, prompting a further study with the aim of measuring an even higher quality set of data. In addition to the experimental improvements, access to more advanced modelling techniques with the use of GAMESS and ELK FP-LAPW DFT codes allows for greater insight into the material to be gained.

7.2 Magnetic Compton Profiles

A single crystal of CeB_6 was prepared by the Superconductivity and Magnetism group at the University of Warwick through the use of the floating zone method. The sample was measured on the BL08w beamline at SPring-8 in January 2013 and May 2014. The sample was cooled to 1.7 K and a field of $\pm$ 1 and $\pm$ 6 T was used, enabling the probing of the AFM and AFQ phases of the system, respectively. Due to the lack of statistical accuracy in the 1 T data, this work focuses exclusively on the analysis of the 6 T data (the AFQ phase).

7.2.1 Comparison with RHF Profiles

With a new data set collected, it is of much intellectual value to make comparisons to the $4f$ and $5d$ Ce RHF profiles. In figure 7.3, the RHF profiles have been convoluted with a Gaussian of FWHM = 0.44 a.u and fit to the experimental data. With this new and improved data set, both the $5d$ and the $4f$ profiles fail to capture the broadness of these features. The $5d$ now fails to capture the broadness of the low momentum region of the experimental data, overestimating the contribution to the MCP at 0 a.u. At $p_z = 1$ a.u., the $5d$ profile underestimates the broadness of the profile. Conversely, the

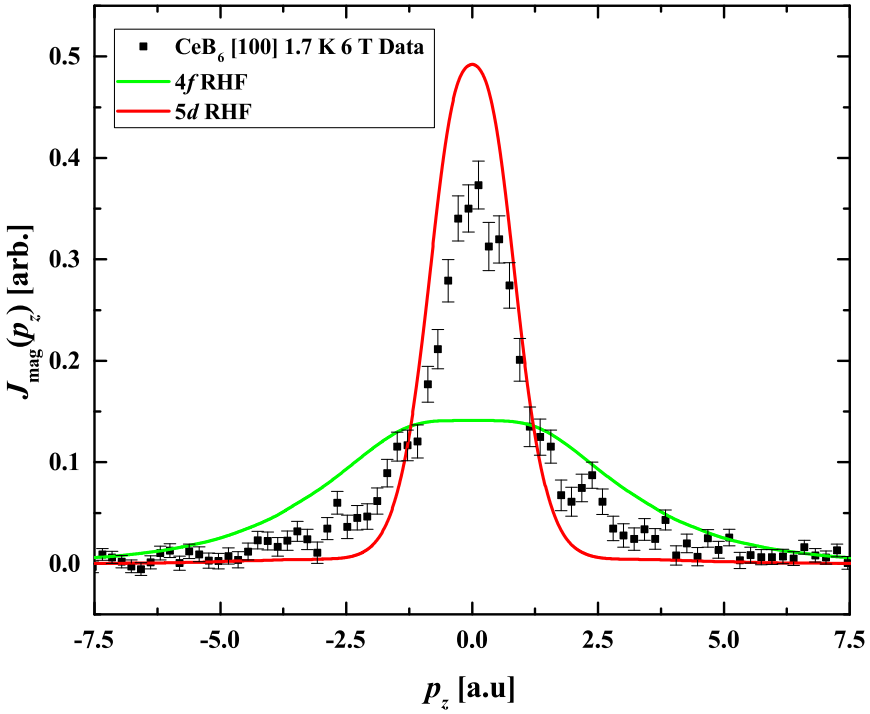

Figure 7.3: Comparison of the CeB_6 data collected at SPring-8 in 2014. Plotted against the experimental data are the $4f$ and $5d$ RHF profiles which have been fit to the data. The data remains unfolded due to the MCP being partially asymmetric. Due to the greatly enhanced statistics, it can be seen that neither the $4f$ nor the $5d$ profiles are capable of capturing the essential features of the experimental MCP.

$4f$ profile greatly underestimates the low momentum contribution but improves on the broadness of the profile at $p_z = 1$ a.u. In conclusion, it is clear from these results that the RHF free atom model fails to replicate the results measured. This causes disagreement with the early work of Cooper *et al.* who suggests that CeB_6 is characterised by a $5d$ moment.[165] Here, neither the $4f$ nor the $5d$ profile find agreement with the measured profiles. In order to proceed further, it is clear a more advanced means of modelling the CeB_6 system is necessary.

7.2.2 Observation of Anisotropy in the EMD

With the significant improvement to the statistics of the MCPs measured at SPring-8, an anisotropy between the [100] and [110] was found. Figure 7.4 presents the [100]

and [110] MCPs of CeB_6 measured at 1.7 K in a field of 6 T. Both profiles have been normalised to the same area. The anisotropy measured is subtle but observable at $p_z < 2$

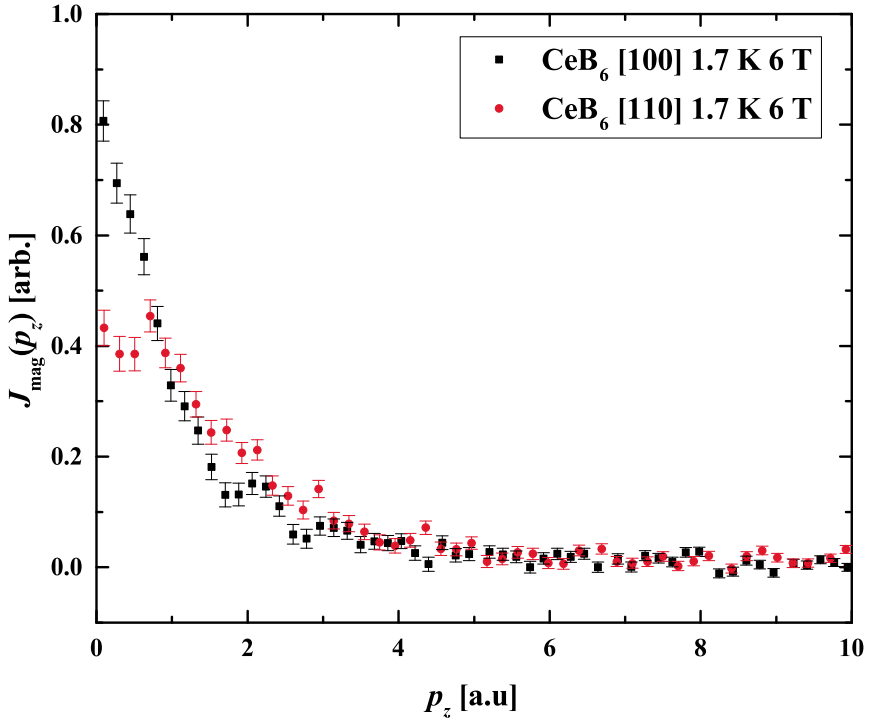

Figure 7.4: Comparison of CeB_6 [100] and [110] measured directions, measured at 1.7 K in a field of 6 T at SPring-8. The [110] has a smaller magnetic signal and is less narrow than the [100] direction.

a.u. where the [110] profile starts to broaden compared to the [100]. Additionally, the [100] profile has a larger contribution at lower momentum, resulting in a larger peak compared to the [110].

Calculation of the spin moments for the [100] and [110] directions was performed using a Ni flipping ratio of $-(6.40 \pm 0.04) \times 10^{-3}$. The spin moments were found to be antiparallel to the applied magnetic field. The [100] direction yielded a spin moment of $-0.286 \pm 0.007\ \mu_B$ and the [110] yielded a spin moment of $-0.252 \pm 0.006\ \mu_B$. The difference in measured spin moments for the two directions emphasises the small but observable anisotropy in the system.

The observation of anisotropy in the spin density is one which has yet to be discussed

in the literature. Its discovery prompted the following investigation into the system. A consequence of this anisotropy is that the success of theoretical models now depends on accurately replicating both measured directional MCPs. For the subsequent fitting, the areas under the MCPs will normalised to 1 in order to make direct comparisons between the shapes of the MCPs.

7.3 Magnetometry

A *Vibrating Sample Magnetometer* (VSM) was used to measure the total magnetic moment of the sample along the [100] and [110] directions at a temperature of 1.7 K with an applied field of up to 6 T. As shown in the phase diagram (figure 7.2), a transition from the AFM phase to the AFQ phase is expected. Using a magnetometer to measure the total moments of the system will enable the orbital moments for the [100] and [110] directions to be determined when compared to the measured spin moments from the MCS experiments. The VSM magnetometry results have been plotted in figure 7.5. The curves deviate significantly from one another indicating a high degree of anisotropy between the [100] and [110] directions. Evident in both curves is the transition from the AFM phase to the AFQ phase which occurs at ~ 2.10 T for the [100] direction and ~ 1.26 T for the [110]. Interestingly, the [110] actually appears to undergo two phase transitions as features in the curve are identified below 1.26 T. These are the AFM transitions which occur because the magnetic structure shifts from a double wave vector character to a single wave vector.[144,166]

Comparing the measured total moments of the VSM magnetometry to the measured spin moments measured using MCS, the directional orbital moments can be isolated. These values are contained within table 7.1. A very large anti-parallel orbital moment

Direction	Spin Moment [μ_B]	Orbital Moment [μ_B]	Total Moment [μ_B]
[100]	-0.286 ± 0.007	1.128 ± 0.006	0.844 ± 0.009
[110]	-0.252 ± 0.006	1.172 ± 0.005	0.920 ± 0.008

Table 7.1: Measured total and spin moments and calculated orbital moments of CeB_6 along the [100] and [110] directions. Note the the spin moment is anti-parallel to the orbital moment.

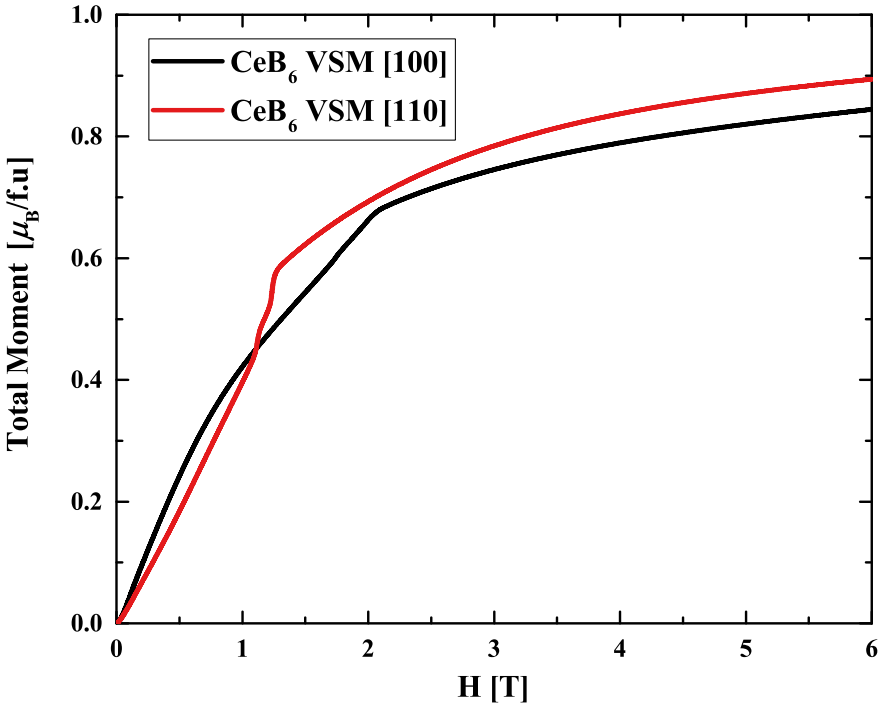

Figure 7.5: MvH measurements of CeB_6 made using a VSM along the [100] and [110] directions. The total magnetic moments measured at 6 T are 0.84 μ_B for the [100] direction and 0.89 μ_B for the [110] direction.

almost five times larger than the spin moment is measured, originating from the Ce $4f$ electron. Due to CeB_6's complicated phase diagram, attempting to replicate these values using DFT will be very difficult. Instead, calculating the correct sign of the spin and orbital moments (alongside the correct order of magnitude of the moments) will be imperative to obtaining a reasonable model of the system.

7.4 Electronic Structure Investigation

To extend the theoretical work beyond the RHF free atom approach, electronic structure calculations have been performed using two methods: the FP-LAPW DFT method employed using the ELK code and a wavefunction based method using GAMESS.

7.4.1 Calculation Details

The electronic structure of CeB_6 has been modelled using the ELK FP-LAPW code. For all calculations performed, spin-orbit coupling was turned on. In order to converge the calculations, `rgkmax` was set to `6.0`.

The electronic structure work of Suvasini *et al.*[167] was used as an initial suggestion for the placement of the Ce and B core/valence electron states. This initial calculation placed the Ce $4f^1$, $5d^1$ and $6s^2$ states into the valence. However, these calculations were found to converge to a non-magnetic groundstate when replicated. Instead, the valence states of the Ce were described as $4f^1$, $5s^2$, $5p^6$, $5d^1$ and $6s^2$ and the valence states of the B were described as $2s^2$ and $2p^1$. All other electron states were treated as core states. This calculation converged to a spin-polarised ground-state and it is this calculation which will be analysed in the proceeding sections.

7.4.2 Lattice Optimisation

An immediate difficulty in modelling CeB_6 using DFT relates to its very narrow $4f$ band which lies close to E_F. This means that very subtle changes in the band structure can have significant effects on the macroscopic properties (in particular, the magnetic moment). As a result of this, optimising the lattice parameter is essential to calculating the true groundstate properties of the system. The lattice optimisation was performed by varying the lattice parameter within a range of $\pm$ 10 %. Figure 7.6 presents the BM plot for CeB_6 calculated with the GGA exchange correlation functional using 1000 k points within the IBZ. The BM 3rd order equation of state fitting to the data found the minimum lattice parameter to have a value $a_0 = 4.135$ Å, in excellent agreement with the literature.[143,167,168] All subsequent ELK work used this lattice parameter as a result.

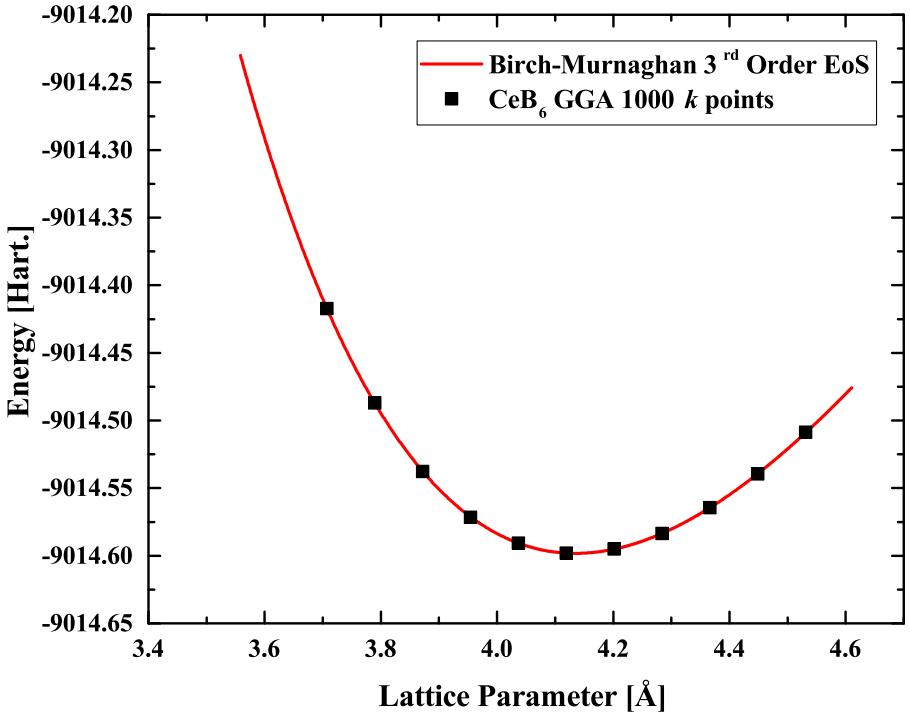

Figure 7.6: The lattice optimisation of CeB_6 as performed using the ELK code. The lattice parameter was varied by as much as ± 10 % of the lattice parameter quoted by Suvasini *et al.* as 4.119 Å.[167] and fit using the BM 3rd order equation of state. The minimum lattice parameter was found to be 4.135 Å, in excellent agreement with the quoted value.

7.4.3 Band Structure Study

Figure 7.7 plots the DOS of CeB_6. Immediately apparent is the very narrow $4f$ band which sits near E_F in both spin channels. The DOS at E_F is dominated by the Ce f contribution. The contributions at $E - E_F < 2$ eV are comprised mainly of B p states which are hybridised with the B s states. There are also minimal contributions from Ce s, p and d states. Above E_F is where the DOS is comprised predominantly from unoccupied d states. The magnetic moment seems to originate from the asymmetry in the DOS generated by the majority and minority Ce $4f$ peaks. The sharpness of these peaks makes it crucial that the band structure from the calculation is satisfactory as very small deviations in this band structure will create significant changes to the magnetic properties of the material.

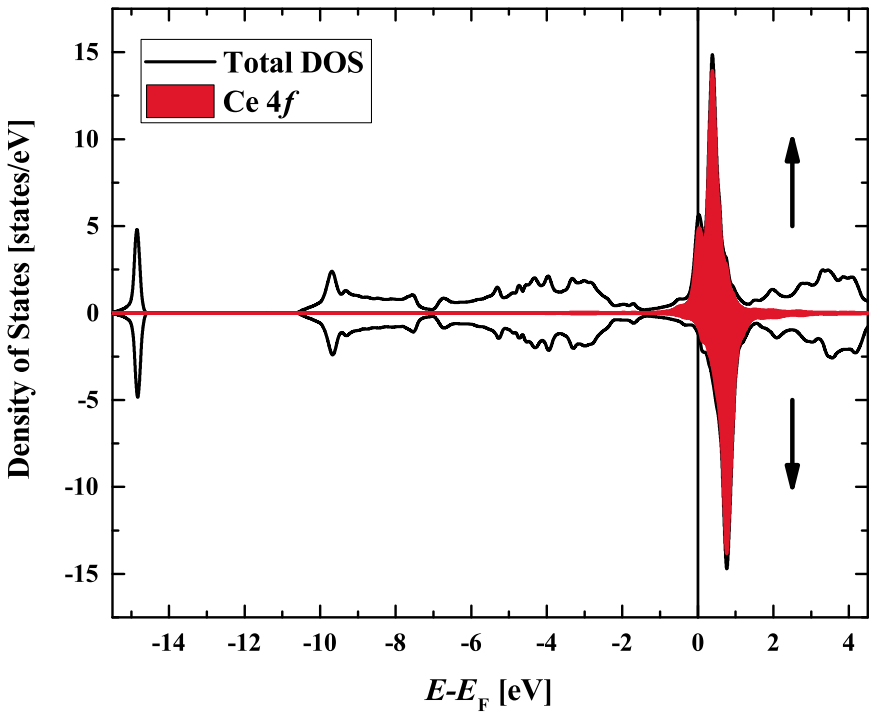

Figure 7.7: Spin polarised DOS of CeB_6. The arrows denote their respective spin channels. E_F is dominated by Ce $4f$ states.

Figure 7.8 plots the calculated non-magnetic band structure of CeB_6 where the Ce $4f$ electron is treated in the valence. The band structure is in very reasonable agreement with the calculation of Suvasini *et al.* Deviations from their calculations are likely due to differences in calculation method used. The ELK code is a *full potential* code whereas the *Fully Relativistic Spin-Polarised Linear Muffin Tin Orbital* (SPR-LMTO) method[169] used by Suvasini *et al.* is a fully relativistic calculation. In the ELK calculation, an additional term is present in $\hat{\mathcal{H}}$ to account for SOC. This does not allow the ELK code to qualify as a fully-relativistic calculation however. Both theoretical paradigms for calculating the properties of CeB_6 therefore have their inherent strengths and weaknesses. As a result, small deviations in the calculated band structure are to be expected. In particular, there is quite a deviation in which bands cross E_F and this is reflected in the shapes of the Fermi surfaces (see §7.4.4).

Calculations were also performed using the LDA exchange correlation functional. Ex-

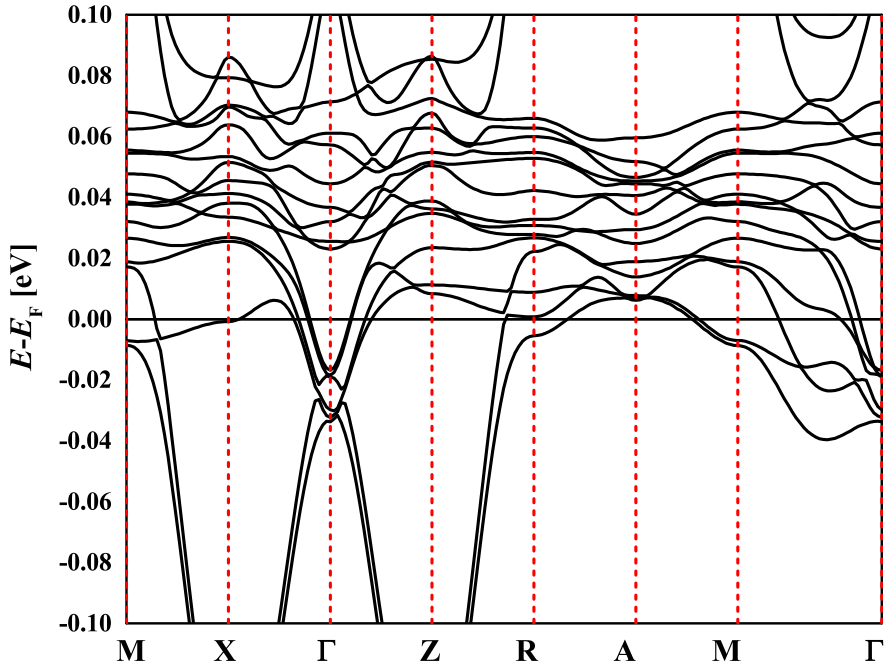

Figure 7.8: Non-magnetic band structure plot of CeB_6 with the Ce $4f$ electron treated as valence.

amining the DOS between the two different schemes showed no discernible difference between the two schemes. Table 7.2 compares several quantities of interest between the two functionals. Comparing the LDA and GGA exchange correlation functionals, the GGA calculates a lower energy groundstate than that of the LDA. Examining the calculated total, spin and orbital moments finds both functionals give very similar results for the material's magnetic properties. The difference between the DOS at E_F is also very

E_{XC}	Total Energy [Hart.]	DOS at E_F	Total Moment [μ_B]	Spin Moment [μ_B]	Orbital Moment [μ_B]
LDA	-9006.69896	192.60108	0.2197	-0.2684	0.4881
GGA	-9014.59817	181.46936	0.2405	-0.2895	0.5300

Table 7.2: Comparison of the LDA and GGA ELK calculations for CeB_6. Changing the exchange correlation functional appears to make minimal changes to the various properties of the material. Note the magnetic moment values will be slightly lower than expected since they are calculated only over the muffin-tins.

small. In conclusion, the GGA makes a very small change over the LDA. Both functionals give the same character to the material. Examining the differences in the calculated EMDs will give a better and more quantitative comparison of the two functionals as the differences will be easily identifiable in the calculated MCPs and 2D-EMD plots.

7.4.4 Fermi Surface Calculations

As with all metallic materials, CeB_6 has a Fermi surface. Various investigations have been performed using either the de Haas-van Alphen effect or positron annihilation radiation (2D-ACAR) to probe the Fermi surface of CeB_6 and sister compound LaB_6.[167,170,171] Attempting to replicate their work can reinforce confidence in the electronic structure calculation we have chosen to calculate the EMD from. The resulting Fermi surface calculated is heavily dependent on the treatment of the Ce $4f$ electron as being part of the core or a valence state. As such, both types of calculation were performed. An $80 \times 80 \times 80$ mesh of k points was used in reciprocal space to accurately calculate the non-magnetic Fermi surface. The Fermi surfaces calculated from treating the single Ce $4f$ electron in the core and as valence have been plotted in figure 7.9. The *core* calculation is characterised by the development of a single band crossing E_F, generating

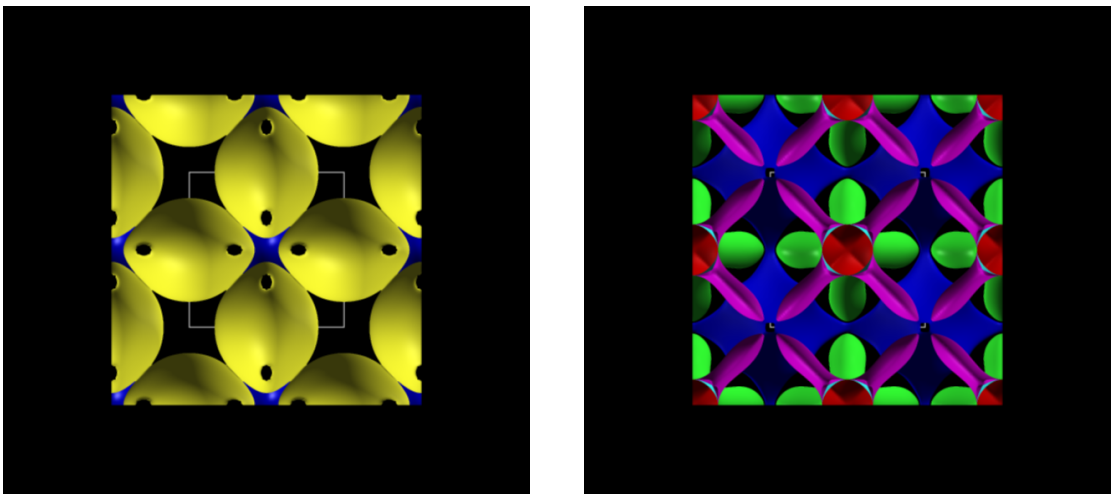

$4f^1$ Core $\qquad$ $4f^1$ Valence

Figure 7.9: The calculated Fermi Surfaces for CeB_6 where the single Ce $4f^1$ electron has been treated as either a core or valence state. The projection is along the principle axis.

a set of periodic oval shapes with small *holes* along the larger radii. This calculation is in excellent agreement with the Fermi surface measurements of LaB_6 studied in the available literature.[170,171] This is reasonable since La lacks an outer $4f$ electron. Setting Ce's $4f$ electron to be a core state forces the electron to be described with a purely symmetric, localised wavefunction, effectively making it inert. Fermiologically, this creates a calculation which is not dissimilar to that of a LaB_6, and this is reflected in the stellar agreement between the calculated core-$4f$ Fermi surface and the measured LaB_6 Fermi surface.

The second Fermi surface was calculated with the Ce $4f$ electron being treated as a valence state. Now the Ce $4f$ electron's wavefunction is described as a planewave. The Fermi surface from this calculation is characterised by the development of three bands, crossing the Fermi level. This results in a significantly more complicated Fermi Surface when compared to the core-$4f$ calculation. The widest band (coloured in blue) contributes the greatest to the DOS and is characterised by a set of *cones* which point along **b** in the BZ. The second and third bands contribute significantly less to the DOS and originate in the corners of the unit cell. This calculation disagrees quite significantly with Suvasini *et al.*'s work primarily due to the high sensitivity the Fermi surface's topology has to changes in the band structure. This makes sense when returning to the calculated band structure and DOS plots (section) which while giving very reasonable agreement with the Suvasini calculations, the band structure plot in particular displays subtle variations in band structure around E_F which cause the deviations in Fermi surface agreement.

7.5 Identifying Anisotropy in the Theoretical EMD

As discussed in the previously in §7.2.2, the anisotropy in CeB_6 is small but observable. It would be interesting to see how well the ELK code (and ultimately, DFT) can model this anisotropy. As such, calculating and measuring the *2D Electron Momentum Density* (2D-EMD) means the anisotropy can be easily identified. Unlike the RHF approach which yields spherically symmetric MCPs (a perfect circle on a 2D-EMD), a smaller

order of symmetry should be identified if the theoretical calculation is to reflect the observed results. Figure 7.10 plots the 2D-EMD for a CeB_6 calculation using the LDA and GGA exchange correlation functionals using 456 k points inside the IBZ. Unlike the lattice optimisation, no k point offset was used. The LDA estimates the localisation of

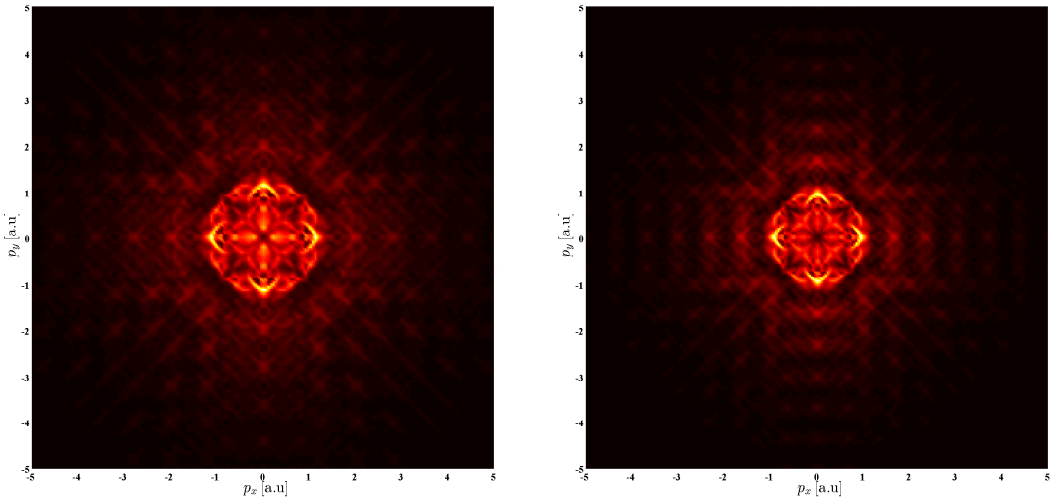

Figure 7.10: Theoretical 2D-EMDs calculated using the ELK code for CeB_6. The LDA (left) and GGA (right) calculations have subtle deviations from each other at low momentum.

the electrons to be slightly higher than that of the GGA with its increased broadness. Both 2D-EMDs calculate a very slight anisotropy indicated by the low order, four-fold symmetry in the 2D-EMD. In both calculations, the Umklapp features have been preserved with the GGA calculation exhibiting a higher degree of sharpness.

The differences are accented when comparing the 1D-EMD (MCP) plots to the experimental data collected. The theoretical [100] and [110] ELK MCPs have been plotted against the experimental data in figure 7.11. The profiles have been convoluted using a Gaussian with a FWHM of 0.44 a.u. Much like the anisotropy in the experimental data, the theoretical [110] profile replicates a smaller contribution at low momenta compared to the [100] direction. The [110] profile additionally manages to capture the broadness of the experimental data, only failing to replicate the very low momentum dip in the experimental profile. Regarding the [100] direction, the theoretical profile fails at capturing the broadness nor the higher contributions to the MCP at low momenta. The

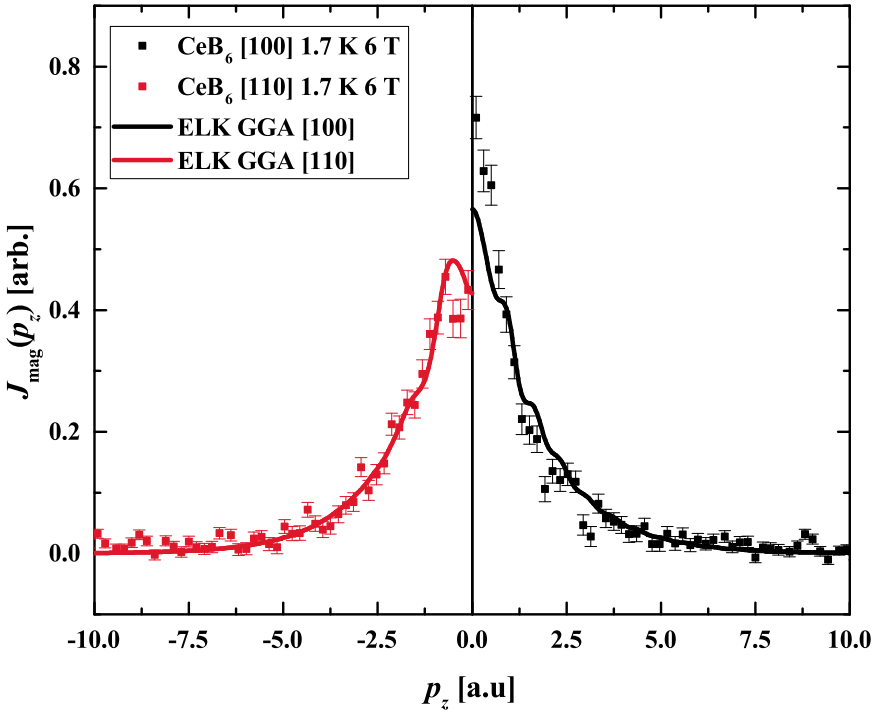

Figure 7.11: Experimental profiles of CeB_6 [100] and [110] measured at 1.7 K at a field of 6 T compared to theoretical ELK profiles calculated using the GGA exchange correlation functional. The anisotropy in the experimental data is replicated reasonably with the theoretical calculation.

calculation for the [100] does however calculate the Umklapp features which appear in the experimental profile although the features in the experimental data may be noise due to the statistical quality. Finally, this calculation finds the EMD to originate entirely from the Ce ion. No contributions are found to originate from the B_6 octahedra.

7.5.1 MCP Orbital Contributions using GAMESS

The GAMESS LCAO method was used to calculate the orbital contributions to the MCP for the [100] and [110] directions. This work focuses on the $4f$ contributions to the profile, continuing from the DFT in which the $4f$ orbital was treated in the valence. Due to the discussion in §7.1.2, it is the $4f$ electron of Ce which will be studied as this is the model which is supported by recent studies. As such, identifying which of the seven available $4f$ orbitals is the main goal of this body of work.

A CeB_6 unit cell was surrounded by 290 point charges with charge $+3e$ for the Ce and charge $-0.5e$ for the B. This crystallographic environment approximates a $3 \times 3 \times 3$ unit cell whilst minimising the overhead from such a calculation with negligible impact on accuracy. The *Well-Tempered Gaussian Basis Set* (WTBS) was used for both the Ce and B atoms.[172,173] The calculation yielded a *cubic* set of $4f$ orbitals.

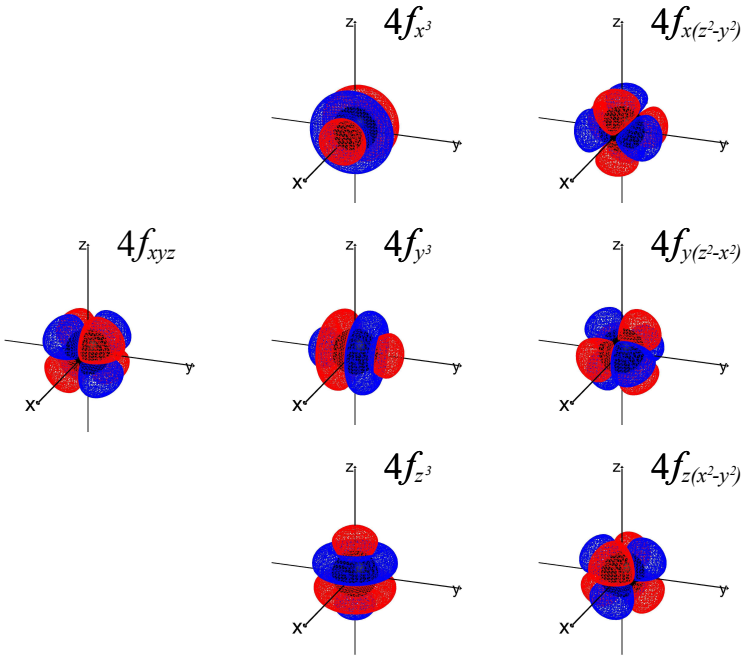

Figure 7.12: The seven cubic $4f$ orbitals of the Ce ion (●) as calculated using GAMESS with the WTBS basis set. The B ions have been omitted. Image courtesy of Ian Maskery.[174]

These orbitals are identified when the $4f$ ion is in a crystal environment with cubic symmetry (as is the case with CeB_6). Figure 7.12 plots the seven cubic $4f$ wavefunctions. Conversion from a GAMESS wavefunction to a direction MCP was performed using the prescription described in figure 3.3. The calculated MCPs have been plotted in figure 7.13. A significant anisotropy has been reproduced in the calculation for a majority of the orbitals as evidenced by the differences between the [100] and [110] MCPs. Since the Ce^{3+} ion will at most, possess a single $4f$ electron, identifying which orbital is occupied by this electron is possible by fitting the GAMESS MCPs to the experimental data. The prime candidate for the most applicable $4f$ orbital is the $4f_{x(z^2-y^2)}$ which has a narrow but sharp characteristic in the [100] direction and a wider, less sharp character

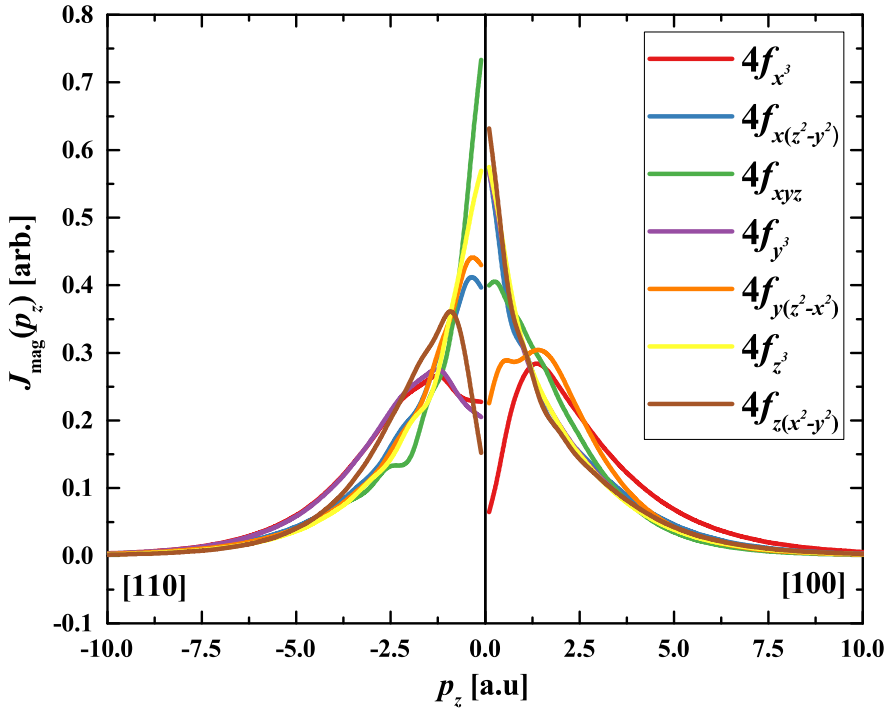

Figure 7.13: The seven $4f$ orbital dependent MCPs calculated using the GAMESS code for CeB_6. A significant anisotropy is reproduced for all profiles except the $4f_{z^3}$ orbital which is isotropic in the *a*-*b* plane (and thus, is reflected in the minor difference between the [100] and [110] profiles). For the [100] direction, the $4f_{x^3}$ and $4f_{y^3}$ profiles are degenerate.

in the [110] direction. In the [100] direction, the $4f_{x(z^2-y^2)}$, $4f_{z^3}$ and $4f_{z(x^2-y^2)}$ are approximately degenerate however the $4f_{z^3}$ orbital has no anisotropy (which is expected due to the isotropic nature of its wavefunction) and the $4f_{z(x^2-y^2)}$ is too broad in the [110]. This means only the $4f_{x(z^2-y^2)}$ is suitable for describing the data.

The fitting of the $4f_{x(z^2-y^2)}$ orbital to the CeB_6 experimental data for the [100] and [110] directions is plotted in figure 7.14. The results are consistent with those of the ELK calculation presented in figure 7.11. The [110] profile adequately describes the experimental profile although the theoretical profile is slightly broader than the experimental data. Unlike the ELK calculation, this profile describes the very low momentum dip more successfully. As was the case with the ELK calculation, the [100] profile produced from the GAMESS calculation fails to capture the broadness of the experimental data,

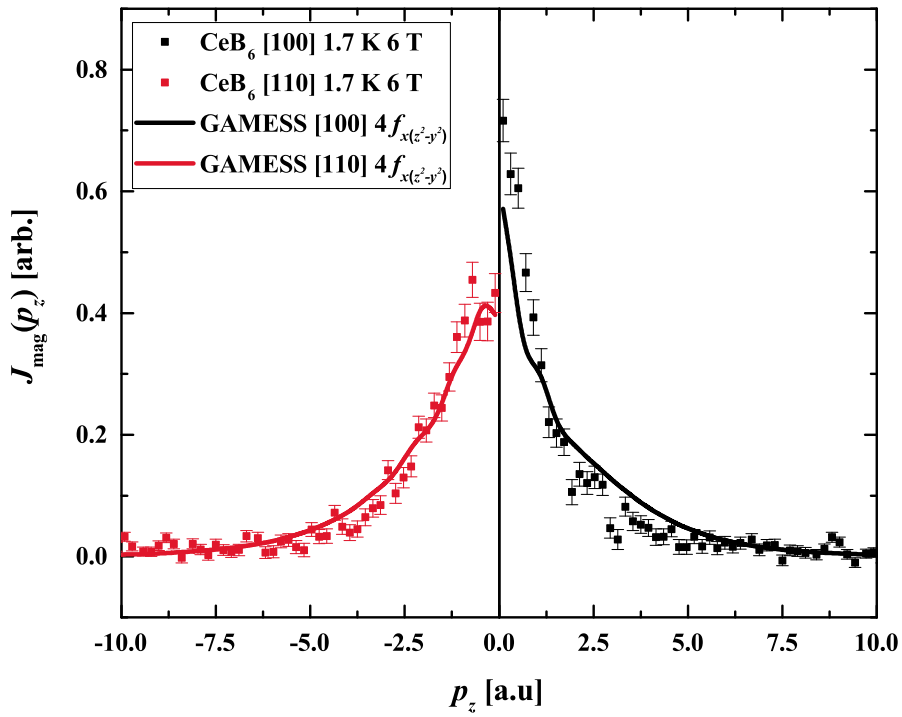

Figure 7.14: Experimental profiles of CeB_6 [100] and [110] measured at 1.7 K at a field of 6 T plotted against the $4f_{x(z^2-y^2)}$ directional MCPs computed from GAMESS. All profiles have been normalised to an area of 1. The anisotropy observed experimentally is reproduced in the calculation with the [110] profile having a smaller contribution at low momentum compared to the [100] direction. As is the case with the ELK calculation, the [100] calculation has poor agreement with the experimental data.

overestimating the contributions at $\sim 1.5 \leq p_z \leq 5$ a.u. At very low momentum, the GAMESS profile underestimates the contributions to the experimental data, resulting in a less narrow peak. Unlike the ELK calculation, no periodic Umklapp features are apparent in the GAMESS profile.

The fact that both calculation methods underestimate the [100] profile at low momentum suggests a systematic error in the modelling of this system. One possible reason for this is that the strongly correlated nature of the Ce $4f$ electron makes it too difficult to model using a free electron, RHF-based method (as is GAMESS). Similarly, it suggests that the GGA XC functional (and the DFT calculation as a whole) is too primitive to describe the complicated physics which define the magnetism of the system. However, another possible reason is that there is an additional spin density contributing to the

total MCP which is not calculated in the DFT, nor has it been included in the Ce ion GAMESS calculations. The underestimation of the experimental MCP at very low momentum could be accounted for by the very narrow $2p$ MCP of B.

7.5.2 Potential B $2p$ Contribution to the EMD

A possible reason for the theoretical MCPs underestimating the CeB_6 [100] profile could be the calculations' lack of a B contribution to the EMD. The ELK calculation predicts no B magnetic moment and the GAMESS calculation finds no hybridisation between the Ce $4f$ wavefunctions and the B $2p$ wavefunctions.

In order to investigate the possible B contribution to the EMD, two different calculations were performed. The first was a free atom of B and the second was a B_6 octahedron (present in the CeB_6 unit cell) surrounded by Ce and B point charges in a $3 \times 3 \times 3$ CeB_6 unit cell. Both models were calculated using the GAMESS code. The WTBS basis set was used for both calculations. Figure 7.15 plots the 2D-EMD of the B and B_6 $2p_z$ orbitals. The B calculation results in a spherically symmetric EMD which as

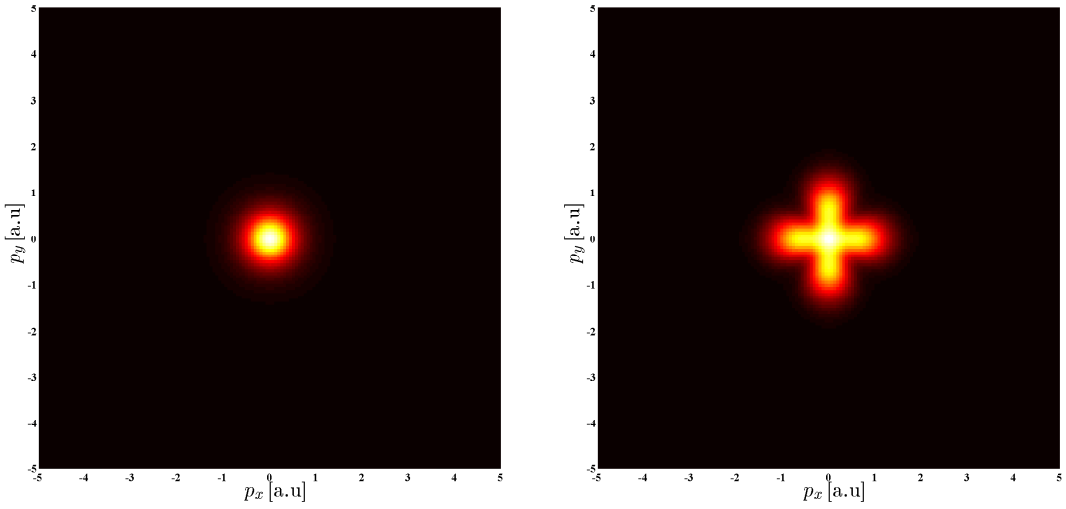

Figure 7.15: Calculated 2D projections of the $2p_z$ EMD for a free B atom (left) and a B_6 octahedra surrounded by Ce ion point charges (right). The projections are different since the B calculation is spherically symmetric whereas the B_6 calculation exhibits a significant anisotropy.

a result, will show no anisotropy in the [100] and [110] projections. Furthermore, this

calculation could be considered simplistic since it does not take into account crystal field effects or interactions with the Ce ions. This also contradicts Hanzawa's spin density results which suggest the B and Ce spin densities are hybridised. The B_6 calculation does reproduce an anisotropy and in comparison, is a more sophisticated calculation as it considers all six B atoms as well as the Ce ions (which have been treated as point charges).

The calculated B_6 $2p_z$ MCP was fitted with the Ce $4f_{x(z^2-y^2)}$ profile to both the [100] and [110] data sets. The fit was constrained to both data sets in order to keep the Ce:B ratios the same. The resultant fitting has been plotted in figure 7.16. The fitting finds

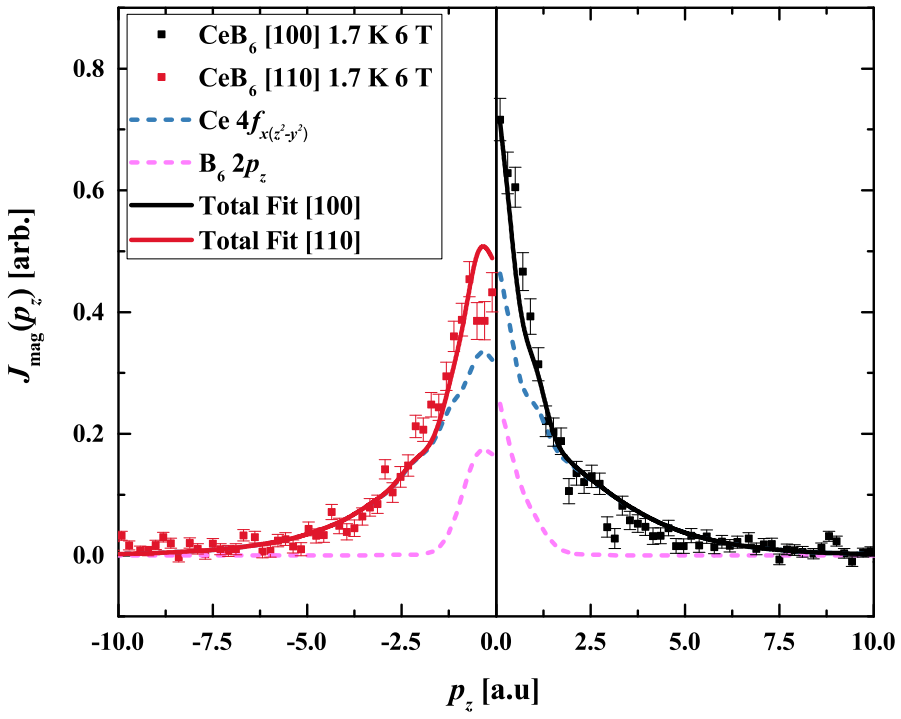

Figure 7.16: Experimental profiles of CeB_6 [100] and [110] measured at 1.7 K at a field of 6 T plotted against GAMESS calculated Ce $4f_{x(z^2-y^2)}$ and B $2p_z$ profiles (dashed lines). The fitting was performed within a range of $0 \leq p_z \leq 5$ a.u. The resultant total fits are comprised of 81 % Ce $4f$ and 19 % B $2p$. The inclusion of a small B $2p$ moment significantly improves the fits compared to the purely Ce calculations displayed in figures 7.11 and 7.14.

a small B moment contributes to the the total MCP, parallel to the Ce moment. The calculated spin moments have been summarised in table 7.3. These results disagree with

Direction	Ce $4f_{x(z^2-y^2)}$ [μ_B]	B_6 $2p$ [μ_B]	Total [μ_B]
[100]	-0.232 ± 0.006	-0.046 ± 0.001	-0.278 ± 0.006
[110]	-0.204 ± 0.005	-0.040 ± 0.001	-0.244 ± 0.005

Table 7.3: The calculated spin moments of CeB_6 as a result of the fitting of the [100] and [110] profiles of Ce $4f_{x(z^2-y^2)}$ and B_6 $2p$ profiles.

the ELK DFT calculation which suggests a negligible B moment antiparallel to the Ce. The calculated profiles agree with the data significantly better compared to the previous calculations. The very narrow profiles of the B $2p$ [100] and [110] are responsible for the significant improvements to the fits for both the [100] and [110] directions. The inclusion of a small B $2p$ moment enables the [100] profile to match the broadness of the experimental data far better than without. In the [110] direction, the inclusion of the small B $2p$ moment means the higher momentum agreement ($2.5 \leq p_z \leq 7.5$ a.u) is much better than with an absence of a B contribution. This does however cause the very low momentum contribution to increase, creating a deviation from the experimental data at $p_z < 1.5$ a.u. The calculated total spin moments find the [110] to have a slightly higher moment compared to the [100] direction however this is likely due to the overestimation of the experimental MCP at low momentum. To conclude, the inclusion of a small B moment to the calculation creates a significant improvement to the agreement with the experimental data. This model is more successful in describing the measured MCPs compared to the purely Ce models generated by ELK and GAMESS.

7.5.3 Forcing a B contribution using FSM-DFT

The novel result suggesting a B contribution to the EMD was as previously discussed, absent in the ELK DFT calculations on the system. Instead, calculation of the EMD found it to be purely Ce-*like* in character. A *fixed spin moment* (FSM) calculation[175,176] can be performed which restricts the total number of electrons in the various bands of the system. In this case, forcing a small B moment on the six B sites in the crystal. In the following calculation, the spin moment values determined from the GAMESS Ce + B_6 fitting were used to fix the Ce and B moments in the ELK FSM calculation. The Ce moment was fixed to be -0.23 μ_B and the B moments were fixed to 0.008 μ_B.

This value was obtained by dividing the B_6 spin moment (-0.040 μ_B) equally amongst the six B atoms in the unit cell. The calculated MCPs have been compared to the experimental data in figure 7.17. The calculated profiles' agreement does not appear

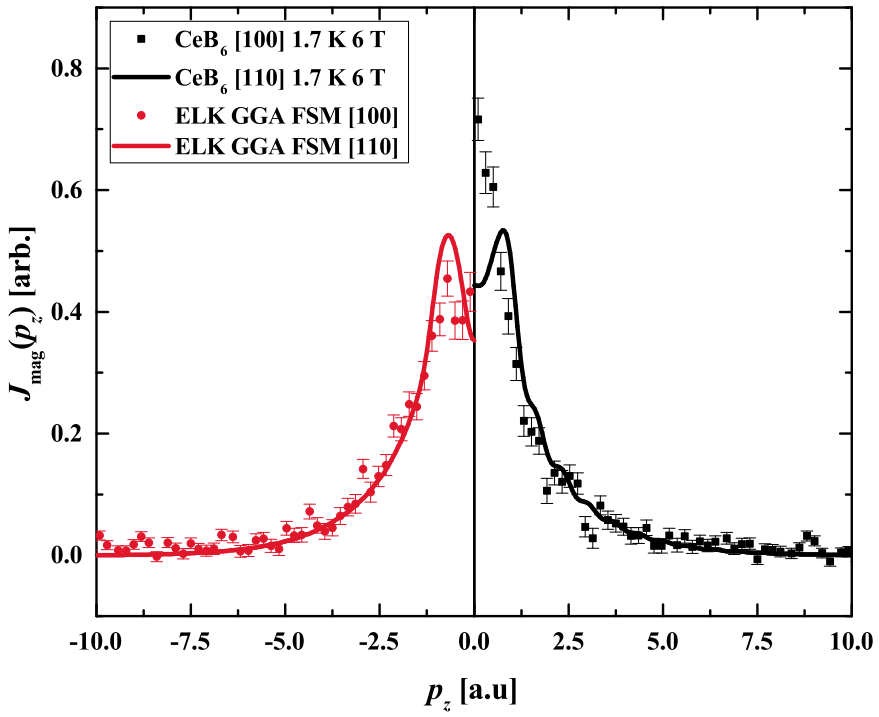

Figure 7.17: Experimental profiles of CeB_6 [100] and [110] measured at 1.7 K at a field of 6 T plotted against the FSM ELK calculated MCPs. The agreement with $p_z \geq 1$ a.u is significantly improved compared to the original ELK calculation.

to have improved over the original ELK calculated MCPs (figure 7.11). Much like the original ELK calculation, the [100] profile's agreement at $p_z \leq 1$ a.u is poor due to the lack of low momentum contributions in the profile. However, the FSM calculation creates a slightly more broad profile at low momentum, creating worse agreement at low momentum compare to the original calculation. The broadness of the [110] direction is similarly, not described as successfully in the FSM calculation as there is a larger contribution to the peak at low momentum. Comparing the [100] and [110] profiles, the anisotropy is less pronounced in the FSM calculation when compared to the original calculation. Both directions in the FSM calculation develop low momentum dips, which isn't the case for the original calculation.

Compared to the original calculation, the FSM calculation's agreement with the experimental data is slightly worse. Neither calculation manages to find good agreement with the experimental data in the [100] direction. A further investigation into producing a B moment with FSM calculations is necessary to study this change in agreement further.

7.6 Concluding Remarks

7.6.1 Summary

The CeB_6 spin density was measured on the BL08W beamline of SPring-8 at 1.7 K in a field of 6 T. Due to the magnet upgrade, CeB_6 was measured to test the system's capabilities when studying materials with low spin moments. An anisotropy was discovered between the [100] and [110] directions prompting a further study of the system. The enhancement in statistics refuted the proposal that CeB_6 has a Ce $5d$ character due to the poor agreement between the new experimental data and the Ce $4f$ and $5d$ RHF profiles.

Theoretically, the system was modelled with DFT using the ELK code. The GAMESS code was also used to model the wavefunctions of the Ce^{3+} and B ions. The ELK code predicted no B moment, attributing the spin moment entirely to the Ce $4f$ band. The ELK calculation agreed well with literature but when compared to the experimental data, failed to capture the essential features. This is attributed to an overly broad [100] profile, however the [110] profile agreed better. This issue is similarly present in the GAMESS calculation where it was proposed that the $4f_{x(y^2-z^2)}$ orbital is responsible for the magnetism in CeB_6. Much as was the case in the ELK calculation, the sole $4f$ model is too broad to agree with the [100] experimental data. To rectify this issue, an inclusion of a small B moment was proposed by modelling the B $2p$ band using GAMESS. The narrow $2p$ profile improved the fits for both directions significantly, comprising ~ 19 % of the total spin moment. In conclusion, this work suggests that the magnetism in CeB_6 does not originate solely from the Ce ion, but is comprised of a Ce $4f$ moment and a B $2p$ moment.

7.6.2 Future Work

Whilst being constrained to fit two different directions is beneficial for testing the robustness of the proposed Ce:B_6 spin-density model, measuring a third direction (such as the [111]) will give an additional constraint on the fitting, enabling a more rigorous study of how successful this model is. Regarding the future use of DFT calculations, a different electronic structure has been proposed by Gürel *et al.*[177] which puts the $5p^6$, $5d^1$, $4f^1$ and $6s^2$ states of the Ce and the $2s^2$ and $2p^1$ states of the B into the valence. Studying the system using this electronic structure may provide novel results for studying the system.

Outside the scope of MCS, perhaps XMCD could be employed to probe the potential B spin moment. This type of measurement may be non-trivial however due to the very low energy of the B K-edge and the requirement that the system be studied at $T < 2$ K. Few facilities are available which can provide this laboratory environment.

Chapter 8

Orbital Occupation of the 1D Complex Oxide $Ca_3Co_2O_6$

Low dimensional quantum spin systems have generated considerable experimental and theoretical interest due to their complex phase diagrams and novel physics. One such material is the 1D complex oxide $Ca_3Co_2O_6$, which at low temperatures, has several steps in its magnetisation curve, reminiscent of quantum tunnelling effects. The origin of this step-like behaviour and furthermore, the origin of these magnetic contributions is still an open area of discussion. MCS presents an ideal method of studying the magnetism in this system. By combining the experimental MCS data with theoretical and analytical techniques, the orbital occupations (and thus, the band structure) can be explored. A sample of $Ca_3Co_2O_6$ was measured on the BL08W beamline at SPring-8, taking full advantage of the new experimental capacity and improved statistics available because of the magnet upgrade. The band structure of the system was calculated using the SPR-KKR DFT code and an orbital study was performed using the GAMESS code. This work presents a new orbital model for the system, in disagreement with the literature and previous experimental work.

8.1 Introduction

Low dimensional systems, in which there is a restriction to one or more spatial dimensions in the material, exhibit a plethora of exotic phases and physical phenomena. The one-dimensional (1D) Cobaltate $Ca_3Co_2O_6$ and in fact, the isostructural compounds of the form $A_3MM'O_6$ (where A is an alkaline-earth metal and M, M' are transition metals) all have attracted considerable interest due to their unique crystal structure and unusual properties.[178] Among the metal oxides, *low dimensionality* refers to systems where the metal-metal separations are short within a plane or along a chain of atoms. $Ca_3Co_2O_6$ is characterised by its rhombohedral structure (space group R-3c where $a = 9.061$ Å and $c = 10.367$ Å) which is comprised of 1D chains of CoO_6 prisms alternating between a trigonal structure and an octahedral structure along the c direction of a hexagonal unit cell.[179] These chains are separated by Ca ions and in turn, form a hexagonal lattice in the a-b plane. The crystal structure has been plotted in figure 8.1.

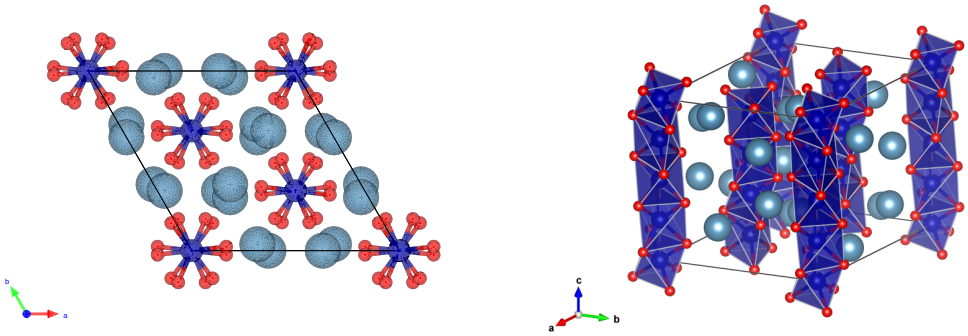

(a) (b)

Figure 8.1: The R-3c crystal structure of $Ca_3Co_2O_6$ (●, ● and ● respectively). (a) is a projection in the a-b plane showing the triangular arrangement of the Co-O chains which gives rise to the geometric frustration in the system. (b) shows the Co-O chains which align along the c axis.

Over the years, there has been intense controversy over the valency of the trigonal and octahedral sites with two dominant models being proposed.[180] Either both Co are in the 3+ state, or the octahedral Co_{oct} is in the tetravalent 4+ state and the trigonal Co_{trig} is in the divalent 2+ state.[181–187] Within the last decade, it has become widely

accepted that both Co ions are in the trivalent state (Co^{3+} with the outer orbital being $3d^6$) where the trigonal CoO_6 prism is in a high spin ($S = 2$) state while the octahedral CoO_6 prism is in a low spin ($S = 0$) state.[188–192] The trigonal crystal field and SOC generate an Ising-style magnetic anisotropy on the trigonal CoO_6 sites with the easy axis aligned parallel to the chains. Spins are aligned ferromagnetically along the chains while a weaker antioferromagnetic interaction couples adjacent chains along helical pathways, leading to magnetic frustration.[193,194] To add further complexity to this already elaborate phase diagram, below T_N, a new magnetic order is obtained via a longitudinal amplitude-modulated spin-density wave which propagates along the c axis with a periodicity of ~ 1000 Å.[195,196]

An additional topic of controversy relates to $Ca_3Co_2O_6$'s conductivity. Experimentally, $Ca_3Co_2O_6$ has been found repeatedly to be an insulator[197–199] whilst theoretically, $Ca_3Co_2O_6$ has been predicted to be a half-metal.[182,188,190] Electronic structure calculations will only predict an insulating phase when a U term is applied to the Hamiltonian to account for correlation effects.[191,200]

8.1.1 Proposed Electronic Structure

The work by Wu *et al.*[191] built the framework for the modern theory of $Ca_3Co_2O_6$'s band structure. Their initial LDA results find $Ca_3Co_2O_6$ to be a ferromagnetic half-metal where for the trigonal CoO_6 prism, the crystal field does not cause the Co $3d$ orbitals to split into the typical e_g and t_{2g} bands. Instead, a degeneracy is found between the $3d_{x^2-y^2}$ and $3d_{xy}$ orbitals and the $3d_{xz}$ and $3d_{yz}$ orbitals. With SOC turned on, this degeneracy is lifted. This orbital picture has been plotted in figure 8.2. This significant change in the energy levels due to the SOC generates a large impact on the magnetic properties of the system in the form of a large, unquenched orbital moment. Each of the SOC d energy levels accommodates one spin-up electron except for d_2 which also accommodates a spin-down electron. This results in an orbital contribution to the magnetic moment greater than what is typically observed in Co or Fe ions in O_h symmetry. An ionic d_2 would give an orbital moment of 2 μ_B however the calculation of Wu *et al.* finds this value suppressed to an orbital moment of 1.57 μ_B. This is due to

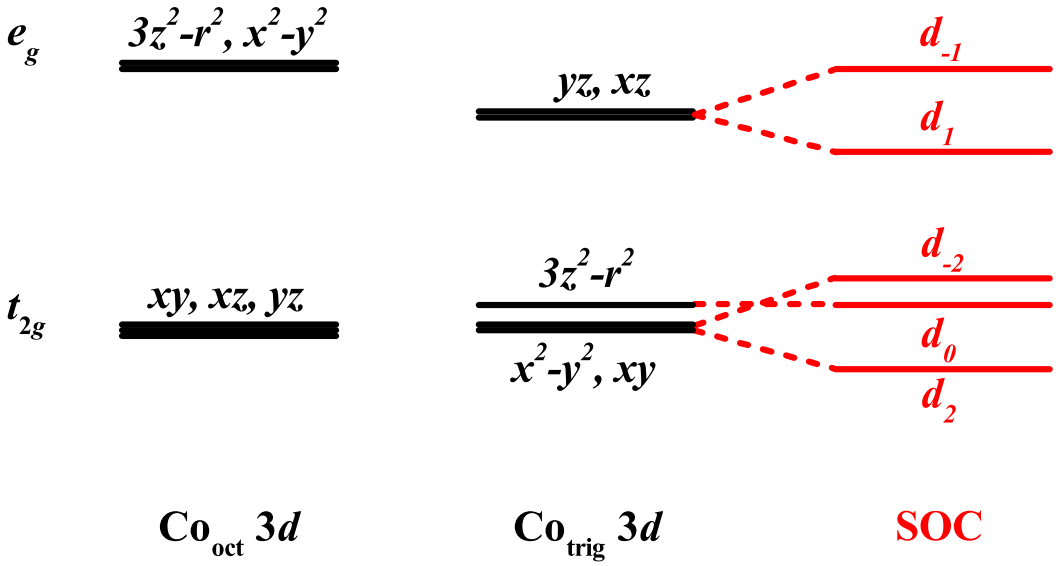

Figure 8.2: Energy levels of the Co 3d orbitals for the octahedral (left) and trigonal (right) CoO_6 clusters. Highlighted in red is the lifting of the degeneracy of the trigonal orbitals due to SOC.

the covalency of the Co bonds in addition to the fact that the trigonal prism is slightly distorted.

The initial LDA+SOC calculation predicted the material to be a ferromagnetic half metal. In order to converge the calculation to an insulating state, the LDA+SOC+U method was required. Using $U = 5$ eV and $J = 0.9$ eV, the results of the calculation determined $Ca_3Co_2O_6$ to be a ferromagnetic insulator, in stark contrast to the LDA+SOC calculation. Converging the calculation to give $Ca_3Co_2O_6$'s experimentally determined insulating states suggests the system to be a correlated insulator.[201] Finally, Wu *et al.* suggests the charge distribution corresponds to that of the trigonal Co^{2+}, octahedral Co^{4+} state, in disagreement with the available literature which suggests otherwise.

8.2 Experimental Work

The same set of crystals used at ESRF[207] were used for this MCS experiment at SPring-8. Single crystal samples of $Ca_3Co_2O_6$ were grown in a KCO_3 flux using a $Ca_3Co_2O_6$ powder synthesised via a solid state reaction.[195] The quality of these samples was verified

using Laue X-ray diffraction which verified the single crystal nature of the sample, showing very clear Laue patterns free of any twinning or defects. Since the c-axis is of exclusive interest, multiple single crystals were orientated along the direction and attached to a sample mount in order to improve the magnetic signal. These samples have been measured in other experiments.[195,196,202–206]

MCS data was collected on the BL08W beamline at SPring-8 in December 2013. The sample was cooled to 10 K and a magnetic field of 5 T was applied along the c-axis of the sample.

Originally for testing purposes, the new SPring-8 data was compared to the experimental data and theoretical model of Butchers.[207] The model suggests a large contribution from the $3d_{xz,yz}$ orbital, with a small contribution from the $3d_{x^2-y^2,xy}$ orbital and a very small contribution from the $3d_{3z^2-r^2}$ orbital. The results of this comparison have been plotted in figure 8.3. The experimental profile measured at SPring-8 is entirely consistent with the shape and broadness of the profile measured by Butchers at ESRF, albeit with significantly improved statistics. Concerning the theoretical model however, the new data emphasises the model's unsuccessful description of the MCP. Above 2 a.u, the model underestimates the broadness of both data sets, invalidating its applicability to describing the physics of the system.

This testing exercise proved to stress the importance of a a new orbital occupation study which must be performed in order to describe this new data set. This theoretical study was performed using the SPR-KKR and GAMESS codes.

8.3 Electronic Structure Calculations

The electronic structure of $Ca_3Co_2O_6$ was calculated using the SPR-KKR code. The fully-relativistic simulation was calculated using the GGA exchange-correlation functional with 1000 k points inside the IBZ. An initial estimate of a 5 μ_B total moment was allocated to the trigonal Co-site in order to converge the calculation at the physical ground-state. The calculated DOS has been plotted in figure 8.4. The calculation con-

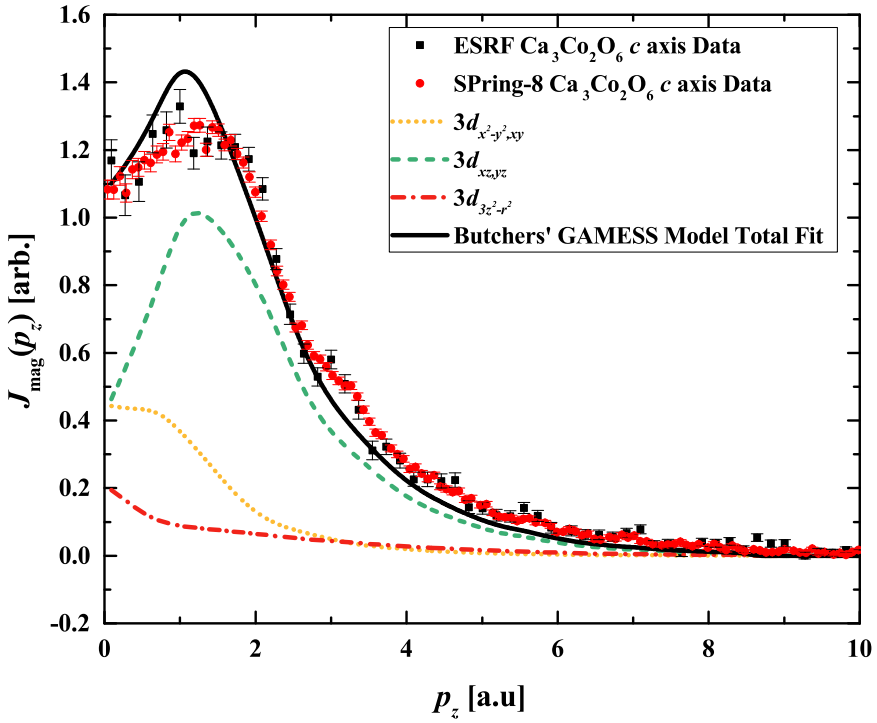

Figure 8.3: The old experimental $Ca_3Co_2O_6$ measured at ESRF plotted against the new $Ca_3Co_2O_6$ data measured at SPring-8. The model is from Butchers' thesis. The shapes of both experimental MCPs is consistent, with the SPring-8 having higher statistical quality. Butchers' model is unsuccessful in describing the measured MCPs.

verges to find $Ca_3Co_2O_6$ is a ferromagnetic half-metal with a total spin moment of 3.93 μ_B and a small orbital moment of 0.01 μ_B. In agreement with the theoretical work of Wu *et al.*, E_F is dominated by trigonal Co 3*d* minority states comprised of the $3d_{x^2-y^2,xy}$ and $3d_{3z^2-r^2}$ states. The $3d_{xz,yz}$ states are found above E_F. The spin moment is comprised mainly of the trigonal Co site with a small contribution originating from the Ca and O. No moment is attributed to the octahedral Co site. The orbital moment is found to originate entirely from the trigonal Co site. A table summarising the magnetic contributions is presented in table 8.1. The calculated MCP projected along the [001] direction has been plotted in figure 8.5. The agreement with the experimental data is very poor. Due to the calculation's predicted half-metallic properties, periodic Umklapp features have developed in the theoretical profile. These features are not present in the measured MCP due to the compound's lack of conductivity. In addition, the peaks at

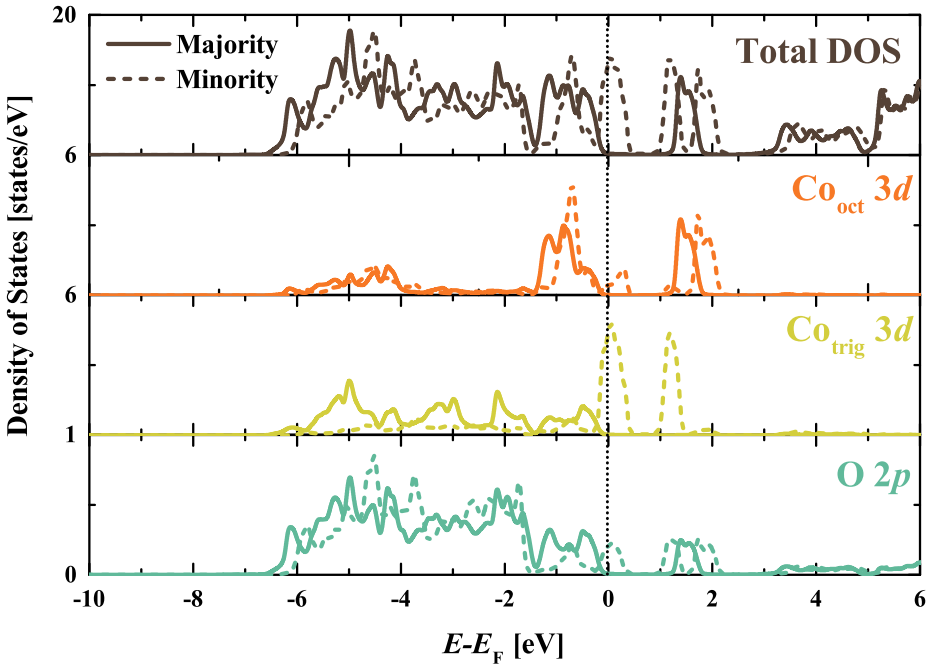

Figure 8.4: The calculated DOS of $Ca_3Co_2O_6$ using the GGA exchange-correlation functional. The calculation finds $Ca_3Co_2O_6$ to be a ferromagnetic half-metal. In addition to the total DOS, the partial DOS of the octahedral and trigonal Co $3d$ states have been plotted in addition to the partial DOS of the O $2p$ states.

~ 2 a.u and ~ 0.5 a.u are missing in the experimental data, which has a single peak at ~ 1.5 a.u. It can be argued that the broadness of the theoretical profile matches that of the experimental profile. The oscillations in the profile make this conclusion difficult to justify however.

8.4 Orbital Occupation Study using GAMESS

The magnetic properties of $Ca_3Co_2O_6$ as discussed previously in §8.1 are attributed entirely to the high spin, trigonal CoO_6 cluster. Since the theoretical MCP generated by the SPR-KKR fails to agree with the experimental data, an alternative approach is the wavefunction-based GAMESS code. A study using the same methodology was performed by Koizumi *et al.*[208] on $La_{2-2x}Sr_{1+2x}Mn_2O_7$ where they found the measured MCP to be dominated by a $3d_{x^2-y^2}$ contribution. Several different approaches to modelling

Site	Spin Moment [μ_B]	Orbital Moment [μ_B]
Ca	0.2121	-0.0024
$Co_{trigonal}$	1.4618	0.05342
$Co_{octahedral}$	0.0001	0.0001
O	0.2976	-0.0042
Total	3.9434	0.0936

Table 8.1: Fully-relativistic GGA calculated spin and orbital moment contributions of $Ca_3Co_2O_6$.

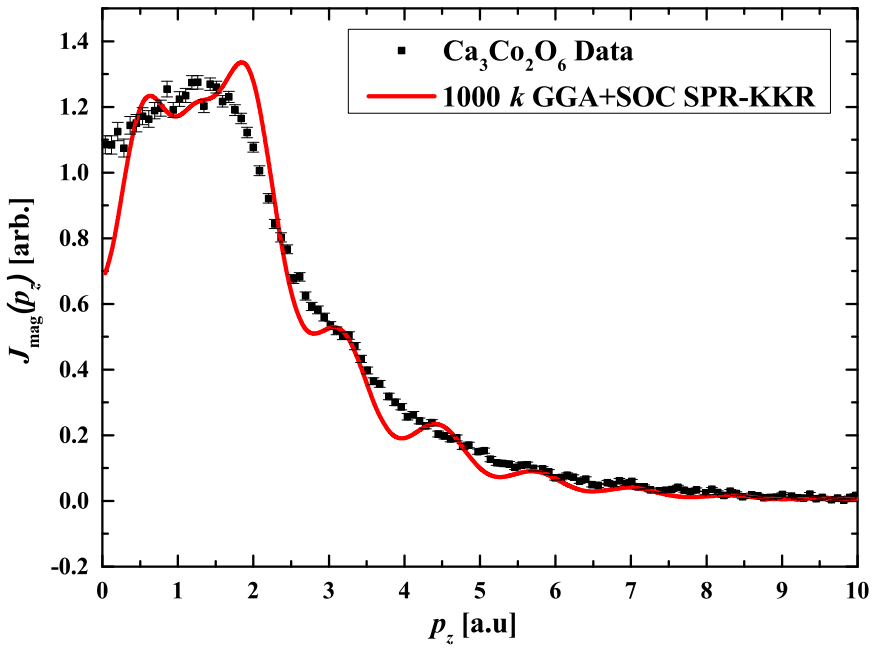

Figure 8.5: Experimental [001] profile of $Ca_3Co_2O_6$ measured at 10 K with an applied field of 5 T plotted against the SPR-KKR calculation. The broadness is arguably captured but the essential features of the theoretical profile are all missing in the experimental data.

this system have been considered. Since the SPR-KKR calculation allocates a sizeable moment to the O of the CoO_6 trigonal site, this will be the first cluster modelled in GAMESS. This cluster was then extended to Co_3O_{12} and Co_5O_{18} to examine how the periodicity of the cluster may impact the theoretical profile. Finally, the O atoms were removed from the cluster in order to study how their absence affected the calculated profiles.

8.4.1 Modelling the CoO_6 Cluster

A CoO_6 cluster was surrounded in 1991 point charges which emulated the surrounding atoms and unit cells. The valencies of the Ca, Co and O atoms were $+2e$, $+3e$ and $-2e$ respectively. This crystallographic environment approximates a $3 \times 3 \times 3$ unit cell whilst only the CoO_6 trigonal cluster is treated *ab initio*[1]. The Ahlrich TZV basis set was used for both the Co and O atoms.[209] The outer electron configuration of Co is $3d^7 4s^2$. Consequently, using Hund's rules,[21] the Co in the 3+ state has a spin quantum number of $m_s = 2$. The O in the 2− state has a fully occupied $2p$ orbital and so has $m_s = 0$. As a result, the multiplicity of the cluster was found to be $M = 5$.[210]

The calculation yielded five $3d$ orbitals from the CoO_6 trigonal cluster which are shown in figure 8.6. It is important to note that these orbitals are not purely of Co $3d$ character

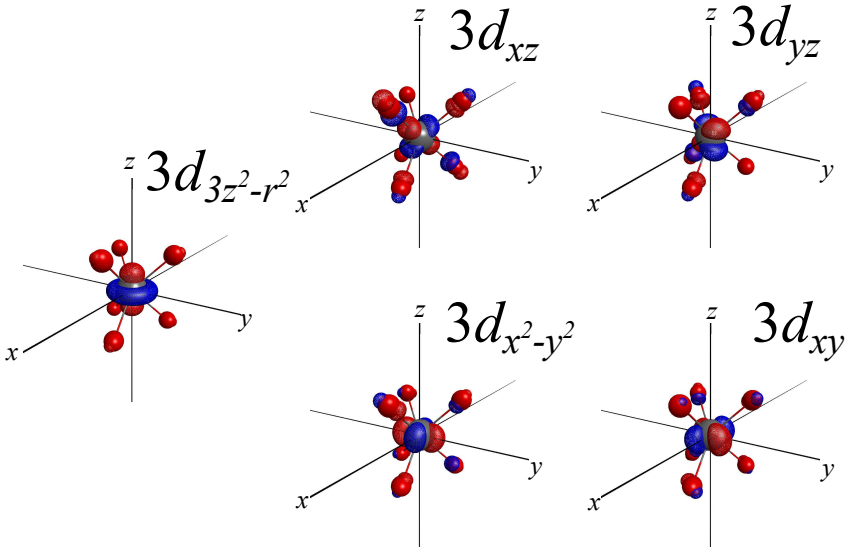

Figure 8.6: The five $3d$ orbitals of the CoO_6 trigonal cluster calculated using GAMESS with the Ahlrichs TZV basis set.

as there is some hybridisation with the O $2p$ orbital as well.

From these orbitals, the MCPs have been calculated and projected along the c-axis. The profiles have been plotted in figure 8.7. As predicted by Wu *et al.*, the $3d_{x^2-y^2}$ and $3d_{xy}$ and the $3d_{xz}$ and $3d_{yz}$ orbitals were found to be degenerate in the GAMESS

[1]These are the atoms which are specified in the `$DATA` section of a GAMESS input file. The atoms specified in this group are represented using explicitly defined basis functions.

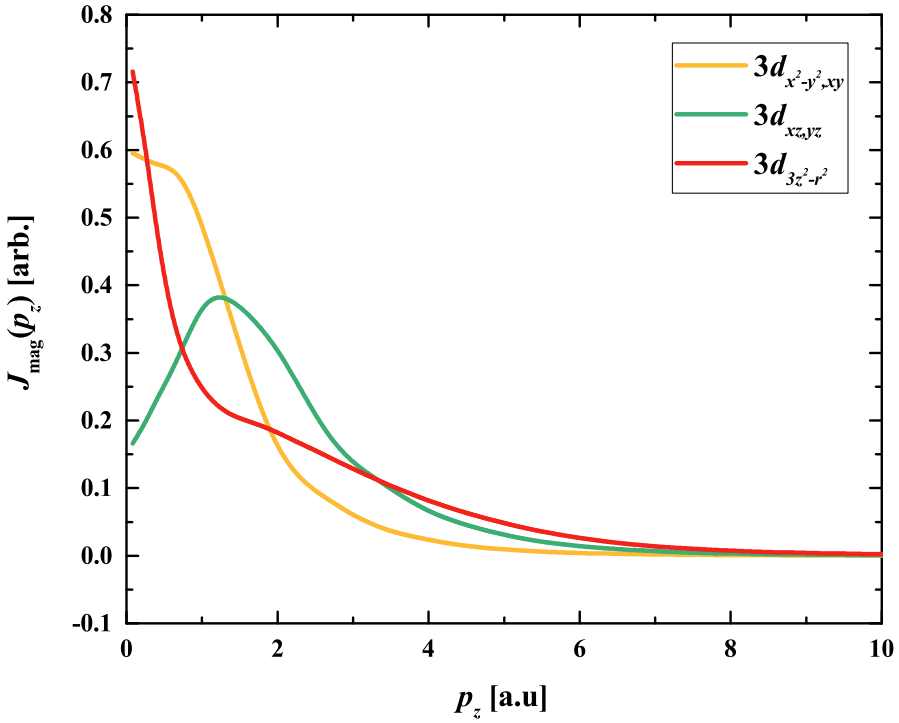

Figure 8.7: The theoretical $3d$ MCPs of the trigonal CoO_6 cluster projected along the c-axis, computed using the GAMESS code. The $3d_{x^2-y^2}$ and $3d_{xy}$ are degenerate as are the $3d_{xz}$ and $3d_{yz}$.

calculation. This is reflected in the shapes of the MCPs where the respective MCPs were found to have an identical character. The presence of point charges in the calculation is crucial to the degeneracy of the orbitals. In the absence of these point charges, the degeneracy of the orbitals is lifted and the shapes of the theoretical MCPs start to differ. This degeneracy is important because its physical interpretation is that these degenerate orbital MCPs can exceed 1 μ_B of spin moment and instead, reach a spin moment of 2 μ_B.

Two approaches were taken when fitting the theoretical calculations to the experimental data. The first approach utilised an *unconstrained* fit, where the parameterisation used to scale the individual orbital MCPs is unrestricted and allowed to vary freely. The second approach was a *constrained* fit. In this case, all orbitals were restricted to be positive. The sign of the MCP is indicative of the spin moment's direction. Having all

the MCPs be positive suggests all the spin moments are parallel to each other. This is expected to be the case when the sample is saturated in a magnetic field of 5 T. If the spin moments of specific orbitals are found to be anti-parallel to each other, this result would be considered non-physical in the presence of a magnetic field. In both cases, the experimental data has been normalised to the experimentally determined spin moment of 3.93 μ_B. The results of this fitting have been plotted in figure 8.8.

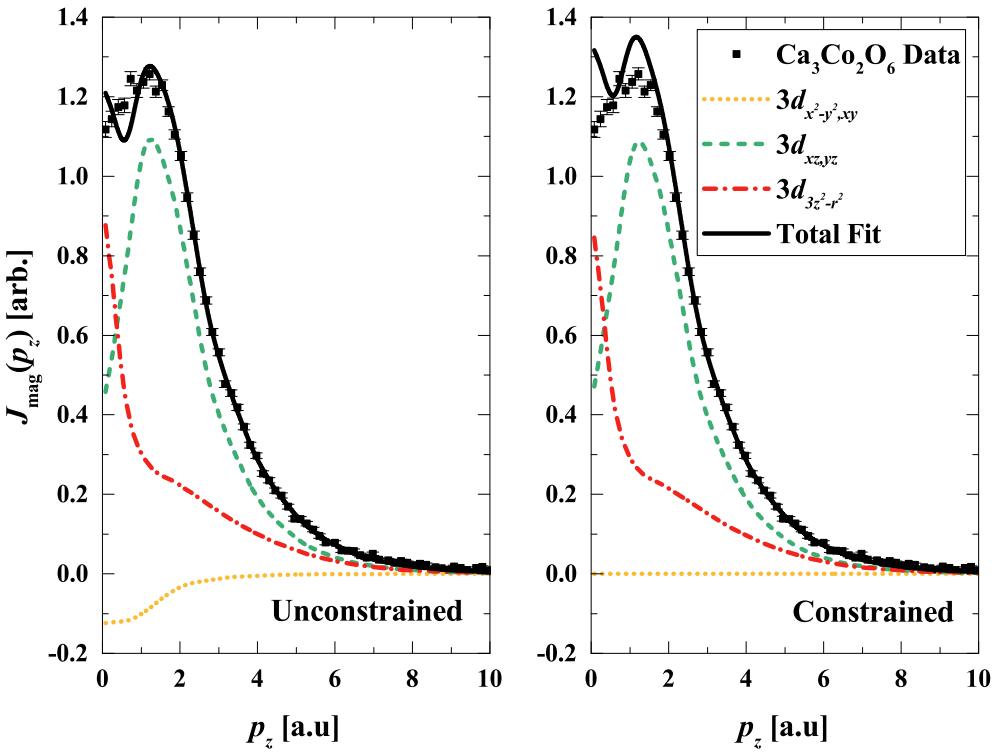

Figure 8.8: Unconstrained (left) and constrained (right) fitting of the trigonal CoO_6 GAMESS profiles to the newly collected experimental data. Both fitting paradigms find very good agreement with the experimental data. However, neither of these results are deemed physical when following the outline presented by Wu *et al.*

On initial inspection, both fitting paradigms are found to give good agreement with the experimental data. It is when the individual orbital contributions are examined that this agreement fails under scrutiny. Table 8.2 compares the orbital spin moment contributions to the total spin moment for both fitting paradigms. The values highlighted in red are non-physical. Focusing on the unconstrained regime, the $3d_{xz,yz}$ degenerate orbital has a spin moment significantly higher than its maximum allowed spin moment

Fitting Regime	x^2-y^2, xy [μ_B]	xz, yz [μ_B]	$3z^2-r^2$ [μ_B]	Total Spin Moment [μ_B]
Unconstrained	-0.21	2.86	1.22	3.88
Constrained	0	2.85	1.18	4.03

Table 8.2: Orbital specific spin moment contributions to the total spin moment of the new $Ca_3Co_2O_6$ experimental data. The values highlighted in red are deemed non-physical.

(2 μ_B). While a degree of Co $3d$ - O $2p$ hybridisation can be inferred from this value (and is indeed expected), an excess of almost 1 μ_B of moment is far too much due (solely) to hybridisation and is therefore deemed non-physical. Additionally, the $3d_{x^2-y^2,xy}$ degenerate orbital is found to have a spin moment anti-parallel to the total spin moment of the trigonal CoO_6 cluster. This is in complete disagreement with Wu *et al.*'s work in which the polarisation of the orbitals is found to be parallel. A result which finds one of the orbital contributing negative (anti-parallel to the other orbitals) is in complete disagreement with their result.

Examining the results of the constrained fitting finds similar disagreement. The $3d_{xz,yz}$ degenerate orbital also has a spin moment which is significantly higher than what is allowed. In disagreement with Wu *et al.*'s work, the $3d_{x^2-y^2,xy}$ degenerate orbital contributes 0 to the total MCP. The fact that *forcing* a constraint on the fitting procedure is required to make all the contributions positive is telling that this model is unable to adequately describe the experimental data.

A conclusion from this theoretical model is that this simple model, where only the trigonal CoO_6 cluster is treated in the *ab initio* cluster, is insufficient in modelling the magnetic properties of $Ca_3Co_2O_6$. While the octahedral CoO_6 cluster is in the low spin state (and therefore contributes 0 moment to the EMD), its inclusion in the calculation may factor-in potential long range order effects which would otherwise not be present in the calculation.

8.4.2 Modelling of Higher Order Co-O Clusters

With the fitting of the trigonal CoO_6 orbitals to the new experimental data, the results were found to be non-physical. An attempt to rectify this issue is to increase the

order of the clusters modelled *ab initio* in GAMESS as their inclusion may improve the physicality of the fitting to the experimental data. The inclusion of the additional Co-O clusters in the chain will have an effect on the calculated wavefunctions which will as a result, change the shape of the calculated MCPs.

The various chains modelled in GAMESS are shown in figure 8.9. In all calculations, the

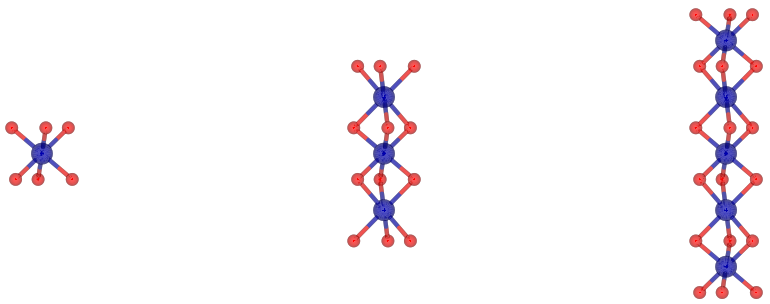

CoO_6 Co_3O_{12} Co_5O_{18}

Figure 8.9: The Co-O chains calculated using the GAMESS code in an attempt to model experimental MCS data.

trigonal CoO_6 cluster was situated at the origin of the coordinate system as this is the high spin site. The Co_3O_{12} and Co_5O_{18} calculations were chose due to their inherent symmetry which is retained when compared to *even-numbered* Co calculations which would generate asymmetric wavefunctions. The Co_3O_{12} cluster incorporates an octahedral cluster above and below the trigonal site whilst the Co_5O_{18} calculation contains both an additional set of octahedral clusters and an additional set of trigonal clusters.

A Co_3O_{12} cluster was surrounded by 1983 point charges in order to simulate the crystallographic environment. A similar calculation was performed on a Co_5O_{18} cluster which was surrounded by 1975 point charges. This crystallographic environment translates to a total of $3 \times 3 \times 3$ unit cells. As was the case with the calculation described in §8.4, the Ahlrich TZV basis set was used to describe both the Co and the O atoms treated in each cluster. No constraints were applied to the fitting. The results of these two calculations have been plotted in figure 8.10. Table 8.3 summarises the calculated moments for the unconstrained Co_3O_{12} and Co_5O_{18} cluster calculations. The Co_3O_{12} calculation will be discussed first. The resulting calculation is considerably different to that of its CoO_6 counterpart. The inclusion of the two octahedral clusters above and below the

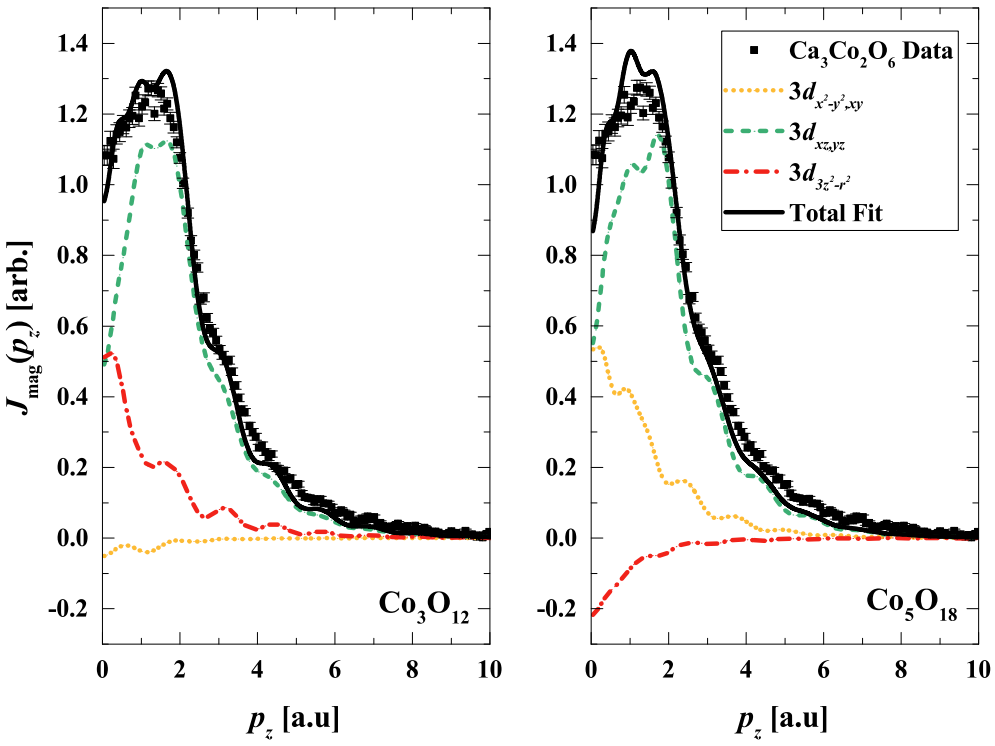

Figure 8.10: Unconstrained fitting of the trigonal Co_3O_{12} and Co_5O_{12} GAMESS calculations, fit to the experimental data collected at SPring-8. The incorporation of the additional octahedral clusters sees the development of periodic features in the calculated MCP for both calculations. These periodic features are not well observed in the experimental data.

Cluster	x^2-y^2, xy [μ_B]	xz, yz [μ_B]	$3z^2-r^2$ [μ_B]	Total Moment [μ_B]
Co_3O_{12}	-0.07	3.09	0.80	3.81
Co_5O_{18}	0.97	3.07	-0.24	3.82

Table 8.3: Orbital specific spin moment contributions to the total spin moment for the unconstrained Co_3O_{12} and Co_5O_{15} cluster calculations.

trigonal cluster have given rise to periodic features which were previously absent in the calculation. The appearance of periodic features like these are generally attributed to Fermi surface features in the EMD. This is not the case however. Instead, these periodic features arise due to the Co-Co interference along the chain in the cluster. This gives a reason for why periodic features can exist in $Ca_3Co_2O_6$ even when there's an absence of a Fermi surface (due to the system's insulating phase).

Consistent with the CoO_6 cluster calculation, the Co_3O_{12} allocates a non-physical set

of contributions to the calculated $3d$ orbitals. The unconstrained fitting finds the total theoretical spin moment to be 3.81 μ_B. This is comprised mostly of the $3d_{xz,yz}$ degenerate orbital which contributes 3.1 μ_B spin moment to the total MCP. This enormous spin moment cannot possibly be achieved solely from this orbital and is not a realistic result. The $3d_{x^2-y^2,xy}$ doubly degenerate orbital much as was the case in the unconstrained fitting of the CoO_6 model gives a small negative contribution to the total spin moment. Again, this violates the work of Wu *et al.* and has no theoretical basis for occurring.

Turning attention to the Co_5O_{18} calculation, similar to the Co_3O_{12} cluster calculation, periodic features have developed in the $3d$ orbitals. Much like the CoO_6 and Co_3O_{12} cluster calculations, the contributions to the total MCP are found to be non-physical. However, the results for Co_5O_{18} are found to be inconsistent with the consistently non-physical results of the CoO_6 and Co_3O_{12} calculations. The calculation finds a negative -0.24 μ_B contribution originating from the $3d_{3z^2-r^2}$ orbital instead of the $3d_{x^2-y^2,xy}$ doubly degenerate orbitals. Consistent with the previous two calculations, a significant majority of the moment is attributed to the $3d_{xz,yz}$ doubly degenerate orbital, which allocates 3.07 μ_B to the MCP - a very non-physical result. Finally, the calculation attributes 0.97 μ_B to the $3d_{x^2-y^2,xy}$ doubly degenerate orbitals, which is not the case for the previous two calculations.

Regardless of which type of Co-O cluster modelled using GAMESS, the agreement between the theoretical calculations and experimental data is poor, and the calculated contributions to the total MCPs are non-physical. The overemphasis of the $3d_{xz,yz}$ orbitals is a significant problem in all three of these calculations. The following section attempts to rectify this issue by removing the O atoms from the cluster, instead treating them as point charges.

8.4.3 Absence of O in the Cluster

The calculations performed on the Co-O clusters give rise to, non-physical results which place too much moment on the $3d_{xz,yz}$ and give poor agreement with the experimental data. In addition, the DFT calculations described in §8.3 are also incapable of adequately

describing the EMD of the system. The failure of these models may be due to the heavy hybridisation observed in the calculation between the Co $3d$ and O $2p$ wavefunctions. A possible counter-investigation to this observed phenomena is to remove the O atoms from the trigonal CoO_6 cluster. Instead, these O atoms will be treated as point charges much as the rest of the atoms outside the trigonal and octahedral clusters. This means the wavefunctions exported by the GAMESS code will be purely Co in character, and not be comprised of any O wavefunction contributions. This is in stark contrast to the work of Wu *et al.* where an O moment is suggested.

In total, four calculations were performed where the O atoms were treated as point charges. Visual representations of these calculations have been plotted in figure 8.11. The calculations used a maximum of 1997 point charges representative of a $3 \times 3 \times 3$

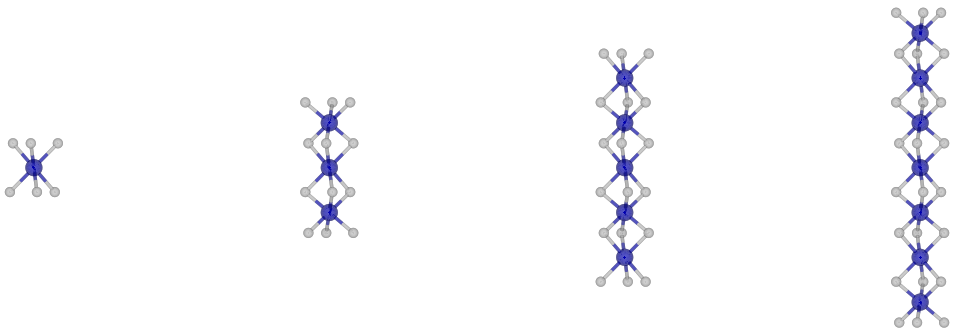

Figure 8.11: The four Co-O calculations where the O atoms are now treated as point charges (◉). Each cluster is surrounded by up to 1997 point charges which represent a $3 \times 3 \times 3$ unit cell.

$Ca_3Co_2O_6$ unit cell. As with the previous calculations, the Co atom is in the 3+ valency. The Co clusters were all situated at the center of the point charge regions to ensure a symmetric point charge distribution around the *ab initio* cluster. The fitting was performed within a range of $0 \leq p_z \leq 10$.

The fitting for the single Co atom cluster is plotted in figure 8.12. The absence of any treated O atoms makes a significant difference to the shapes of the orbital dependent MCPs (and subsequently, the net, total fit). Most significantly is the presence of a sizeable $3d_{x^2-y^2,xy}$ contribution to the total MCP. Unlike any of the calculations which

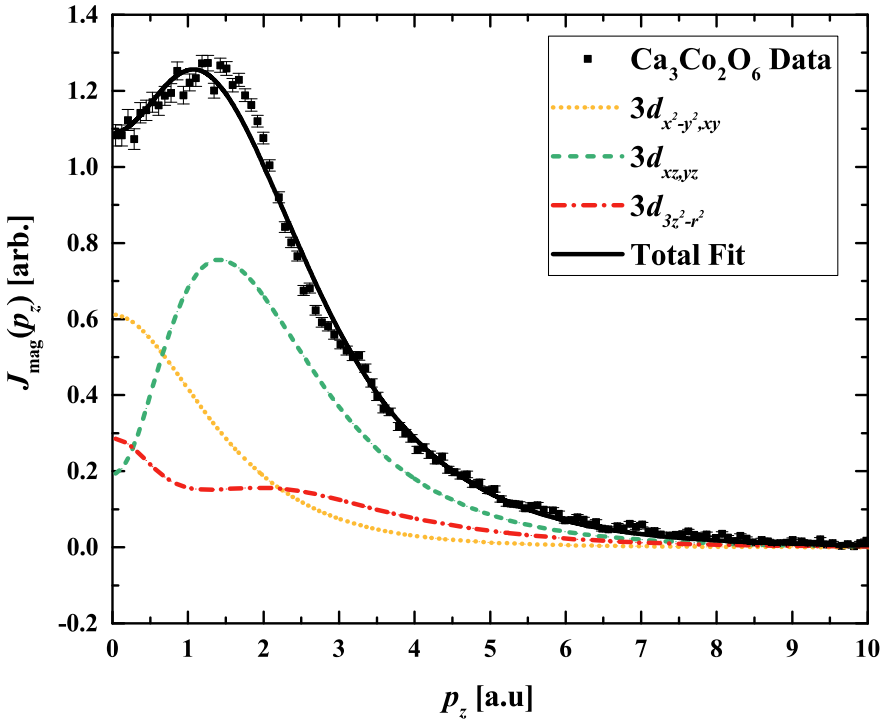

Figure 8.12: The O absent Co cluster calculation model plotted against the experimental data. The fitting is a significantly more physical and realistic result.

Cluster	x^2-y^2, xy [μ_B]	xz, yz [μ_B]	$3z^2-r^2$ [μ_B]	Total Moment [μ_B]
Co	1.01	2.15	0.74	3.90

Table 8.4: Orbital specific spin moment contributions to the total spin moment for the Co cluster calculation.

contained O in the cluster, the absence results in a much more physically appropriate model for describing the experimental data. The total fit estimates the total spin moment to be 3.90 μ_B, in excellent agreement with the observed spin moment of 3.93 μ_B. The calculated spin moments have been summarised in 8.4. The resultant fitting marks a significant improvement in physicality of the calculated spin moments. While the $3d_{xz,yz}$ contribution is still slightly above 2 μ_B, this value is within the error due to the fitting paradigm and furthermore, marks a significant improvement in physicality in comparison to the previous Co-O models. The contributions are also all positive (parallel) to each other, in agreement with the theoretical model presented in figure 8.2.

One deviation from the experimental data is the lack of a bump in the theoretical MCP at $\sim$ 3.25 a.u. The Co cluster calculation predicts the MCP to be smooth with no periodic features which is not the case in the experimental MCP.

The fitting for the higher order chains is presented in figure 8.13. For the purpose of comparison, all extended chain fits use the contributions calculated from the base Co calculation. Much as what was seen in §8.4.2, extending the chain in c introduces peri-

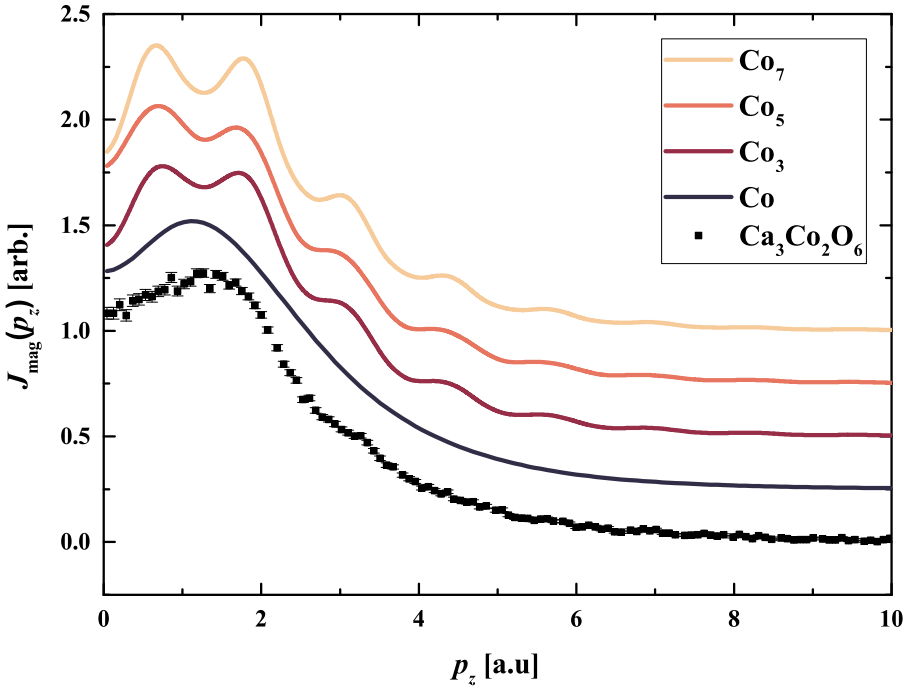

Figure 8.13: The four O free Co chain MCP total fits calculated using GAMESS plotted with the experimental data. Each profile is offset by 0.25. The total fits are dependent on the contributions calculated from the base Co calculation. Extended the chain to higher orders introduces periodic features to the MCP which are not observed in the experimental data.

odic features into the MCPs. Comparison between the experimental data and the Co_7 calculation is presented in figure 8.14. The development of periodic features is immediately noticeable in the $3d_{z^2-r^2}$ orbital which is the primary source of these periodic features. In addition to this, the $3d_{x^2-y^2,xy}$ and $3d_{xz,yz}$ also start to develop periodic features. Unlike the calculation which includes O in the cluster, the results from the O-free calculations again, return physical results for the resultant fitting. Much as is

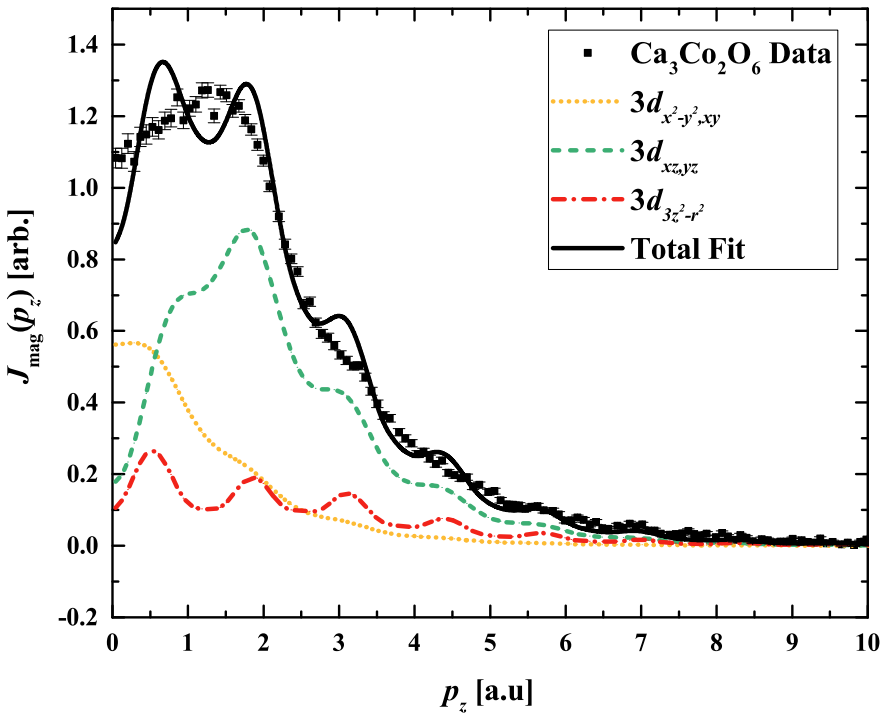

Figure 8.14: The experimental data fit with $3d$ orbitals calculated from the Co_7 calculation (the last calculation in figure 8.11). Compared to the base Co calculation (figure 8.12), the agreement is significantly worse due to the development of periodic features in all three calculated orbitals.

the case for the calculation with only a single Co atom in the cluster, these calculations find an MCP which is predominantly of $3d_{xz,yz}$ with a sizeable $3d_{x^2-y^2,xy}$ contribution. The periodic features in the extended Co cluster calculations do not reproduce the experimental bump at $\sim$ 3.25 a.u. The failure in the theoretical work to describe this bump in the MCP suggests that either the theoretical model still is not adequate in describing the experimental data, or alternatively, the bump in the experimental MCP is anomalous.

A reason for the introduction of periodic features in the MCPs is due to hybridisation of the Co-Co wavefunctions. This interaction does not appear to extend to the next nearest neighbours as no *observable*[2] difference can be seen. Furthermore, the fact these periodic

[2]Due to the convolution used to mimic the experimental resolution, any difference in the theoretical MCPs which may be witnessed cannot be observed experimentally, hence the difference is not *observable*.

features are not observed in the experimental data could suggest that screening effects are in play, resulting in no hybridisation (or substantially less) between the neighbouring Co wavefunctions. This may also explain the drastic improvement in agreement with experiment when the O atoms are removed from the cluster. The lack of any O spin density in these calculations combined with the significant improvement in agreement with the experimental data suggests the O wavefunctions are localised entirely on their atomic sites and provide no overlap with the Co $3d$ wavefunctions. Perhaps a source of this screening could be the localised O $2p$ wavefunctions which screen the Co-Co interaction.

While this model presents a significant improvement in the description of the experimental MCP, the result is controversial. The lack of any O spin-density in the calculation is a controversial result which disagrees with the theoretical work of Wu *et al.* and the breadth of DFT calculations which have been used to study the system. In addition, since this model sets the trigonal Co atom to be in the 3+ valence, this work also disagrees with the conclusion that the trigonal Co atom is in the 2+ state. However, since the DFT calculations which have been performed in lieu of their work are inadequate in describing the MCP of the system adequately, presenting theoretical work which is successful in describing the measured MCP is of much intellectual value, even if the results are in disagreement with alternative theoretical methods and studies.

8.5 Concluding Remarks

8.5.1 Summary

The c direction of $Ca_3Co_2O_6$ was measured on the BL08W beamline of SPring-8 using the newly installed magnet setup. By measuring the sample at 10 K using an applied magnetic field of 5 T, a dataset with high quality statistics was acquired for the system. The theoretical model used to describe the experimental data of Butchers was found to be inadequate in modelling the essential physics of the newly acquired data. In addition, the MCP calculated using SPR-KKR failed to describe the experimental data. Using

GAMESS, the CoO_6 trigonal site was modelled and while agreement with the measured MCP was good, the orbital contributions to the total MCP were non-physical. This lack of physicality was also apparent when the CoO_6 trigonal cluster was extended along the 1D chain. The higher order clusters also developed periodic features which weren't observed in the base CoO_6 calculation.

A breakthrough in the modelling of this system came from removing the O atoms from the *ab initio* cluster, effectively modelling a single Co atom in the $Ca_3Co_2O_6$ crystallographic environment. The agreement with experiment was far more successful, very adequately describing the measured MCP and giving physical spin moment contributions from the individual orbitals. Longer chains of Co atoms were also calculated however these developed the periodic features characteristic of the Co-Co hybridisation observed in previous GAMESS calculations. The results of this study suggest that the spin-density of the system originates entirely from the trigonal Co site and that no O spin-density is required to describe the EMD. Introducing an O spin-density to the description destroys the physicality of the results. This is a controversial result as previous theoretical studies of this system have proposed models which are comprised of trigonal Co, O and even a small Ca contribution to the magnetism of the system. Furthermore, all theoretical studies treated the trigonal Co atom as being in the 3+ state. The success of this model refutes the possibility that the trigonal Co atom is in the 2+ state and consequently, that the octahedral Co atom is in the 4+ state. This work encompasses much of what makes MCS a valuable tool in the study of electronic structure, demonstrating how the electronic properties and orbital occupations can be analytically determined with the combination of theory and experiment.

8.5.2 Future Work

The limits of what can be achieved using wavefunction based codes for determining the electronic structure of $Ca_3Co_2O_6$ have been reached in this thesis. Practically, all of the potential calculations modelling various aspects of the Co-Co and Co-O wavefunctions have been studied. On a theoretical basis, further pursuits into modelling this system will have to use DFT-based methods. The work of Butchers (in addition to the work

of various collaborators) has demonstrated that the LDA, GGA and LDA+U methods are unsuitable for modelling this system as the theoretical results do not agree with the measured experimental profiles. One possible avenue to explore would be similar to that which has been presented in section 7.17, where (in the case of CeB_6) the B moments were fixed to be non-zero. In the case of $Ca_3Co_2O_6$, the O moments could be set to zero to simulate the effects of the GAMESS calculations. If the hypothesis, that no O moment contributes to the spin density of $Ca_3Co_2O_6$ is true, doing like-wise with the DFT calculations will provide further insight into this claim. If the agreement between the experimental data and the FSM-DFT calculations is significantly improved with this model, this will provide a serious case that O makes no contribution to the spin density and instead, the spin-density of $Ca_3Co_2O_6$ is entirely Co $3d$ in nature.

Chapter 9

Conclusions

The existing hardware of the SPring-8 BL08W beamline has been upgraded by replacing the previous magnet with the 9 T Oxford Instruments magnet which originally resided on ESRF's ID15 beamline. To complement this upgrade, the control software had to be updated to accommodate this change in hardware. Due to the vastly improved experimental capacity achieved through this upgrade, a range of MCS experiments have been conducted over the last three years which have taken full advantage of the improved hardware capabilities. The spin-densities of Co_2MnSi, CeB_6 and $Ca_3Co_2O_6$ were all measured, taking full advantage of the improved hardware. The modelling of these compounds was performed primarily using either the ELK or GAMESS codes. New paradigms for developing models were used which have previously been unavailable due to hardware restrictions and lack of functionality in the codes used. Finally, complimenting the experimental MCS work of these compounds has been a breadth of supplementary experimental techniques ranging from SQuID magnetometry to Powder XRD. Their contributions have helped provide further insight into the magnetic structure and stoichiometry of these materials. The success in probing the spin-densities of these compounds, and the advent of further developed analytical methods to study them, will pave the way for future studies of the spin-densities of novel, exotic phenomena.

9.1 Summary of Results

9.1.1 BL08W Magnet Upgrade

The initial goal of this project was to upgrade the experimental capabilities of BL08W by transferring the 9 T Oxford Instruments magnet from the ESRF ID15 beamline to the SPring-8 BL08W beamline. To facilitate this upgrade, the software which controlled the experimental functions of the beamline needed to be modified to accommodate the new magnet.

Testing (as well as some of the experiments described in this thesis) found the configuration produced data with significantly improved statistics which agreed with the previously collected data from both the ID15 and BL08W beamlines. A larger range of phenomena can now be explored due to the improved experimental capacity provided by the upgrade.

9.1.2 Co_2MnSi

Half-metallicity, even after its initial postulation in the mid 1980s, has remained a fervently studied area of research due to the lack of materials which have been experimentally determined to possess 100 % spin-polarised band structures. The Co-based full Heusler alloys are currently a promising candidate and recent results on thin films have been very promising.

The EMD of Co_2MnSi was probed along three high symmetry [100], [110] and [111] directions at a temperature of 300 K with an applied magnetic field of 1 T. These results were compared to a theoretical model calculated using the ELK FP-LAPW DFT code. Significant agreement between the experimental data and the theoretical model was found, with the three directional curves describing the tails of the MCPs very adequately. Only at very low momentum, where contributions from the more correlated, itinerant electrons are present in the MCPs, do the theoretical curves deviate from the experimental values. In addition to the experimental MCPs, the experimental and theoretical anisotropies were determined and compared to give an extra comparison layer.

By removing the less anisotropic core electrons (which contribute to the tails of the MCPs), data which is more itinerant in character can be compared to the theoretical work. Here, very good agreement is found, with the theoretical anisotropies very accurately modelling the anisotropies calculated from the experimental data.

Due to the good agreement between the MCS experimental data and the theoretical model, examining the stoichiometry of the compound, and how deviations in its structure affect its macroscopic properties was important to test the validity and robustness of Co_2MnSi. Theoretically, variations in the lattice parameter of up to 6 %, while shifting the magnetic contributions of the Co and Mn sites in the sample, did not impact the total moment of the system, finding Co_2MnSi to still be a half-metal (theoretically). Additionally, introducing correlation to the system using the GGA+U model found the system to still retain its half-metallicity until large values of U were applied. Experimentally, the system was found to have a slight Silicon excess which sat on the Co sites of 2 %. A further investigation into the stoichiometry of the system through comparing the Powder XRD data of two sources (Cu K_α and Co K_α) was attempted. However, the quality of the data was questionable due to a large background in the Co K_α source data. This resulted in the determined disorder parameters being dubious, suggesting further measurements need to be taken.

To summarise, the theoretical work was found to be in very good agreement with the experimental MCS work. Small changes to the band structure introduced through lattice variations and correlation made no impact on the total moment, allowing Co_2MnSi to retain its half-metallicity, suggesting that small deviations in stoichiometry may not break the half-metallicity of the system. These results propose Co_2MnSi to be a robust half-metal and this work is the first bulk measurement of the compound which finds Co_2MnSi to be a potential half-metal.

9.1.3 CeB_6

The heavy fermion, complex Kondo material CeB_6 has remained controversial due to the nature of its magnetism and phase diagram. Recent work has suggested this to be

of $4f$ while previous MCS studies have suggested it to possess the character of the $5d$ electrons. The poor statistics and primitive models used to analyse the measured MCP, combined with the revised interest in the compound presented a fantastic opportunity to use the new hardware installed on BL08W.

A much improved measurement of CeB_6 was performed, measuring primarily the [100] and [110] directions at 1.7 K using an applied magnetic field of 6 T - a measurement which was not possible using the previous hardware. The spin moments were found to be -0.284 ± 0.006 μ_B along the [100] direction and -0.27 ± 0.01 μ_B along the [110] direction. An anisotropy in the EMD was found from comparing the shapes of [100] and [110] profiles.

The system was modelled using two different codes, the ELK FP-LAPW DFT code, and the GAMESS code. The ELK work while agreeing with the literature (in particular, the Fermi surface modelling of CeB_6 and LaB_6) found poor agreement with the experimental MCPs. While a small anisotropy was calculated between the [100] and [110] directions, the broadness of the [100] profile could not be replicated in the ELK calculation. In GAMESS, modelling the CeB_6 unit cell found the $4f_{x(z^2-y^2)}$ orbital to describe the EMD the most successfully. Like the ELK calculation, the [100]'s broadness fails to be described with the GAMESS calculation.

Success was found upon the study of a potential B contribution to the EMD. The possibility of a B spin-density is not a well researched area, and very little literature has examined this possibility. Introducing a small B $2p$ contribution dramatically improved the agreement with experiment. The narrow profile of the $2p$ MCP in superposition with the broad $4f$ profile of the Ce provides a very apt description of the CeB_6 EMD, along both the [100] and [110] directions. Attempting to account for the possible B contribution through the use of a FSM calculation in ELK found an improvement in the broadness of the calculated MCP, although this profile still did not determine the low momentum contributions correctly.

In summary, only with the inclusion of a B contribution, can the experimental MCS work be adequately described theoretically. The results of this find that a B contribution to

the EMD, in combination with a $4f$ contribution from the Ce, very adequately describes the measured EMD of CeB_6. This supports the recent work in the literature which suggests the magnetism to originate from the $4f$ band. However, the inclusion of a B moment is potentially novel and is in need of further study. Additionally, this work finds that modern DFT codes are unsuccessful in calculating the ground-state properties of CeB_6. The inclusion of a B moment in DFT calculations may aid in the study of this system.

9.1.4 $Ca_3Co_2O_6$

The 1D complex oxide $Ca_3Co_2O_6$ has been the topic of numerous experimental and theoretical studies. Recent band structure models of the system failed to agree experimental work. DFT calculations find the system to be a ferromagnetic half-metal when the system has repeatedly been found to be an insulator. The inclusion of U and SOC is necessary to converge the system into an insulating state. Furthermore, there is controversy surrounding the valencies of the trigonal and octahedral Co sites in the system. Early MCS work found disagreement with a range of DFT calculations and was ill-described with a proposed model calculated using GAMESS. In order to test the new, upgraded experimental setup on BL08W, the system was measured again, taking full advantage of the improved hardware now available on BL08W.

A measurement along the c axis of $Ca_3Co_2O_6$ was made at a temperature of 10 K using an applied magnetic field of 5 T. The new data expressed a significant improvement in statistics compared to the old data and emphasised the previous model's inability to describe the data adequately. This prompted a new study into the system, taking full advantage of the new hardware in addition to new theoretical techniques.

Multiple approaches were taking to studying the CoO_6 trigonal site which is found to contribute to the spin-density of the system. The initial calculations involved modelling three different chains of these trigonal *clusters*: CoO_6, Co_3O_{12} and Co_5O_{18}. The fitting (both unconstrained and constrained) found that while the curves well very adequate in describing the MCP, the spin moment contributions from the orbitals were non-physical.

In addition, as the chains were extended, the development of periodic features were observed in the theoretical MCPs. In order to improve upon this model, the O atoms were removed from the cluster and instead, treated as point charges. Co, Co_3, Co_5 and Co_7 chains were modelled and compared to the experimental data. Regarding the Co cluster calculation, the fitting found a significant improvement in the physicality of the results, whilst also giving very good agreement with the experimental data. Much like with the Co-O cluster calculations, extending the chain was found to develop periodic features in the theoretical MCPs.

The conclusion from this work suggests solely the trigonal Co site in the 3+ state, contributes to the EMD in $Ca_3Co_2O_6$. The incorporation of an O moment destroys the physicality of the results and is not necessary to adequately describe the EMD. Not only do DFT calculations predict the system to be half-metallic (unless a sufficient U is applied), but the allocation of moment to the O sites may be what is causing disagreement between the theoretical calculations and the experimental work. This is a controversial result as previous theoretical models of the system all incorporate an O moment (and a small Ca moment) into their descriptions of the magnetism. Furthermore, this work suggests the periodic features which development in the MCP are not due to Fermi surface features (indicative of a metallic state), but instead are interference effects which occur due to the hybridisation of the Co-Co wavefunctions along the 1D chain. Their absence in the experimental data suggests that some form of screening may be occuring which is why their presence is muted.

9.2 Future Work

Suggestions for future work relating to the three measured samples are presented in their respective chapters. This section is therefore a discussion relating to the future of magnetic Compton scattering on BL08W.

While the improvements to the statistics have been demonstrated in this thesis, further improvements can be made. Shifts in the sample position were observed on many of the high field experiments due to the shrinking (and subsequent expanding) of the apparatus

during field flips. An upgrade to the magnet is possible which will eliminate this sample movement, which will provide an even greater improvement to the statistics.

The complex, highly correlated systems which have been studied in this thesis have demonstrated the difficulty DFT has in describing these systems. It has been proposed for both CeB_6 and $Ca_3Co_2O_6$ that a possible solution to this may be through the use of FSM calculations as both chapters have argued against the predicted spin-density allocations calculated by DFT calculations. A primary issue with an over dependence on this paradigm is how it causes the calculation to no longer be *ab initio*. The user is required to input the predicted moments of the constituent atoms instead of the DFT code. If correlated systems require this level of user input to calculate the observed physics of a system, it indicates a potential underlying issue in the codes' predictive capabilities.

Bibliography

[1] J.R. Hook and H.E. Hall. *Solid State Physics*. Manchester Physics Series. Wiley, 2013.

[2] C. Kittel. *Introduction to Solid State Physics*. Wiley, 2004.

[3] J. Callaway. *Quantum theory of the solid state*. Academic Press, 1991.

[4] B.E. Warren. *X-ray Diffraction*. Addison-Wesley Series in Metallurgy and Materials Engineering. Dover Publications, 1969.

[5] V.E. Naish and R.P. Ozerov. *Neutron Diffraction of Magnetic Materials*. Springer US, 2012.

[6] Leonid A. Bendersky and Frank W. Gayle. Electron Diffraction Using Transmission Electron Microscopy. *Journal of Research of the National Institute of Standards and Technology*, 106(6), 2001.

[7] N.W. Ashcroft and N.D. Mermin. *Solid State Physics*. HRW international editions. Holt, Rinehart and Winston, 1976.

[8] S. Hassani. *Mathematical Methods: For Students of Physics and Related Fields*. Undergraduate Texts in Contemporary Physics. Springer New York, 2000.

[9] C.J. Foot. *Atomic physics*. Oxford master series in physics. Oxford University Press, 2005.

[10] J. E. Jones. On the Determination of Molecular Fields. II. From the Equation of State of a Gas. *Proceedings of the Royal Society of London A: Mathematical, Physical and Engineering Sciences*, 106(738):463–477, 1924.

[11] J. Tersoff. New Empirical Approach for the Structure and Energy of Covalent Systems. *Phys. Rev. B*, 37:6991–7000, Apr 1988.

[12] Donald W. Brenner. Empirical Potential for Hydrocarbons for use in Simulating the Chemical Vapor Deposition of Diamond Films. *Phys. Rev. B*, 42:9458–9471, Nov 1990.

[13] P. Hofmann. *Solid State Physics: An Introduction*. Physics textbook. Wiley, 2011.

[14] P. Drude. Zur Elektronentheorie der Metalle. *Annalen der Physik*, 306(3):566–613, 1900.

[15] P. Drude. Zur Elektronentheorie der Metalle; II. Teil. Galvanomagnetische und thermomagnetische Effecte. *Annalen der Physik*, 308(11):369–402, 1900.

[16] E. Merzbacher. *Quantum Mechanics*. Wiley, 1998.

[17] Robert B. Leighton. The Vibrational Spectrum and Specific Heat of a Face-Centered Cubic Crystal. *Rev. Mod. Phys.*, 20:165–174, Jan 1948.

[18] J. Singleton. *Band Theory and Electronic Properties of Solids*. Oxford Master Series in Condensed Matter Physics. OUP Oxford, 2001.

[19] D. Greig. *Electrons in metals and semiconductors*. European physics series. McGraw-Hill, 1969.

[20] R. Hull and INSPEC (Information service). *Properties of Crystalline Silicon*. EMIS datareviews series. INSPEC, the Institution of Electrical Engineers, 1999.

[21] T. Engel and P.J. Reid. *Physical chemistry*. Pearson Benjamin Cummings, 2006.

[22] R.M. White. *Quantum Theory of Magnetism: Magnetic Properties of Materials*. Springer Series in Solid-State Sciences. Springer, 2007.

[23] S. Blundell. *Magnetism in Condensed Matter*. Oxford Master Series in Condensed Matter Physics. OUP Oxford, 2001.

[24] M A G Dixon, J A Duffy, S Gardelis, J E McCarthy, M J Cooper, S B Dugdale, T Jarlborg, and D N Timms. Spin Density in Ferromagnetic Nickel: a Magnetic

Compton Scattering Study. *Journal of Physics: Condensed Matter*, 10(12):2759, 1998.

[25] Barry N. Taylor of the Data Center in close collaboration with Peter J. Mohr of the Physical Measurement Laboratory's Atomic Physics Division. The NIST Reference on Constants, Units and Uncertainty. http://physics.nist.gov/cuu/index.html, 2015. Accessed: 23/09/2015.

[26] D.J. Griffiths. *Introduction to Quantum Mechanics*. Pearson international edition. Pearson Prentice Hall, 2005.

[27] J. C. Slater. A Simplification of the Hartree-Fock Method. *Phys. Rev.*, 81:385–390, Feb 1951.

[28] P. Hohenberg and W. Kohn. Inhomogeneous Electron Gas. *Phys. Rev.*, 136:B864–B871, Nov 1964.

[29] R.K. Nesbet. *Variational Principles and Methods in Theoretical Physics and Chemistry*. Cambridge University Press, 2002.

[30] W. Kohn and L. J. Sham. Self-Consistent Equations Including Exchange and Correlation Effects. *Phys. Rev.*, 140:A1133–A1138, Nov 1965.

[31] John P. Perdew and Yue Wang. Accurate and Simple Analytic Representation of the Electron-Gas Correlation Energy. *Phys. Rev. B*, 45:13244–13249, Jun 1992.

[32] John P. Perdew, Kieron Burke, and Matthias Ernzerhof. Generalized Gradient Approximation Made Simple. *Phys. Rev. Lett.*, 77:3865–3868, Oct 1996.

[33] E L Peltzer y Blanc, C O Rodrguez, J Shitu, and D L Novikov. Degree of Localization of the Exchange-Correlation Hole and its Influence on the Ground-State (Structural and Magnetic) Properties of 3*d* Metals. *Journal of Physics: Condensed Matter*, 13(42):9463, 2001.

[34] G P Srivastava. Broyden's Method for Self-Consistent Field Convergence Acceleration. *Journal of Physics A: Mathematical and General*, 17(6):L317, 1984.

[35] D.J. Singh and L. Nordstrom. *Planewaves, Pseudopotentials, and the LAPW Method*. Springer, 2006.

[36] Kay Dewhurst, Sangeeta Sharma, and Lars Nordstrm. The ELK FP-LAPW Code. `http://elk.sourceforge.net/`, 2015. Accessed: 02-03-2015.

[37] Michael W. Schmidt, Kim K. Baldridge, Jerry A. Boatz, Steven T. Elbert, Mark S. Gordon, Jan H. Jensen, Shiro Koseki, Nikita Matsunaga, Kiet A. Nguyen, Shujun Su, Theresa L. Windus, Michel Dupuis, and John A. Montgomery. General Atomic and Molecular Electronic Structure System. *Journal of Computational Chemistry*, 14(11):1347–1363, 1993.

[38] Karen L. Schuchardt, Brett T. Didier, Todd Elsethagen, Lisong Sun, Vidhya Gurumoorthi, Jared Chase, Jun Li, and Theresa L. Windus. Basis Set Exchange: A Community Database for Computational Sciences. *Journal of Chemical Information and Modeling*, 47(3):1045–1052, 2007. PMID: 17428029.

[39] Peter M.W. Gill. Molecular integrals Over Gaussian Basis Functions. volume 25 of *Advances in Quantum Chemistry*, pages 141 – 205. Academic Press, 1994.

[40] Brett M. Bode and Mark S. Gordon. Macmolplt: a Graphical User Interface for GAMESS. *Journal of Molecular Graphics and Modelling*, 16(3):133 – 138, 1998.

[41] Alejandro Saenz, Tanja Asthalter, and Wolf Weyrich. Methods for the Calculation of Spherically Averaged Compton Profiles with GTOs. *International Journal of Quantum Chemistry*, 65(3):213–223, 1997.

[42] H Ebert, D Kdderitzsch, and J Minr. Calculating Condensed Matter Properties using the KKR-Green's Function MethodRecent Developments and Applications. *Reports on Progress in Physics*, 74(9):096501, 2011.

[43] J Korringa. On the Calculation of the Energy of a Bloch Wave in a Metal. *Physica*, 13(67):392 – 400, 1947.

[44] W. Kohn and N. Rostoker. Solution of the Schrödinger Equation in Periodic Lattices with an Application to Metallic Lithium. *Phys. Rev.*, 94:1111–1120, Jun 1954.

[45] Paul Soven. Coherent-Potential Model of Substitutional Disordered Alloys. *Phys. Rev.*, 156:809–813, Apr 1967.

[46] M. Cooper, P. Mijnarends, N. Shiotani, N. Sakai, and A. Bansil. *X-Ray Compton Scattering*. Oxford Series on Synchrotron Radiation. OUP Oxford, 2004.

[47] Arthur H. Compton. A Quantum Theory of the Scattering of X-rays by Light Elements. *Phys. Rev.*, 21:483–502, May 1923.

[48] R.H. Stuewer. *The History of the Compton Effect*. Number v. 1 in The History of the Compton Effect. University of Wisconsin–Madison, 1968.

[49] O. Klein and T. Nishina. Über die Streuung von Strahlung durch freie Elektronen nach der neuen relativistischen Quantendynamik von Dirac. *Zeitschrift fur Physik*, 52:853–868, November 1929.

[50] F.W. Lipps and H.A. Tolhoek. Polarization Phenomena of Electrons and Photons. I: General Method and Application to Compton Scattering. *Physica*, 20(16):85 – 98, 1954.

[51] F.W. Lipps and H.A. Tolhoek. Polarization Phenomena of Electrons and Photons. II: Results for Compton Scattering. *Physica*, 20(16):385 – 405, 1954.

[52] J.E McCarthy, M.J Cooper, V Honkimki, T Tschentscher, P Suortti, S Gardelis, K Hmlinen, S.O Manninen, and D.N Timms. The Cross-Section for Magnetic Compton Scattering up to 1 MeV. *Nuclear Instruments and Methods in Physics Research Section A: Accelerators, Spectrometers, Detectors and Associated Equipment*, 401(23):463 – 475, 1997.

[53] M.J. Cooper, C. Shenton-Taylor, J.A. Duffy, C.A. Steer, and L.V. Blaauw. A Short History of Magnetic Compton Scattering. *Nuclear Instruments and Methods in Physics Research Section A: Accelerators, Spectrometers, Detectors and Associated Equipment*, 580(1):1 – 7, 2007. Proceedings of the 10 th International Symposium on Radiation Physics {ISRP} 10.

[54] M J Cooper, E Zukowski, S P Collins, D N Timms, F Itoh, and H Sakurai. Does Magnetic Compton Scattering only Measure Spin Magnetization? *Journal of Physics: Condensed Matter*, 4(29):L399, 1992.

[55] J. E. McCarthy, J. A. Duffy, C. Detlefs, M. J. Cooper, and P. C. Canfield. $4f$ Spin Density in the Reentrant Ferromagnet $smmn_2ge_2$. *Phys. Rev. B*, 62:R6073–R6076, Sep 2000.

[56] Iucr and A. J. C. Wilson. *International Tables for Crystallography, Volume C: Mathematical, physical and chemical tables International Tables for Crystallography.* Kluwer Academic Publishers, Dordrecht, Boston, London, 1992.

[57] Peter Holm. Relativistic Compton Cross-Section for General Central-Field Hartree-Fock Wavefunctions. *Phys. Rev. A*, 37:3706–3719, May 1988.

[58] D. N. Joanes and C. A. Gill. Comparing measures of sample skewness and kurtosis. *Journal of the Royal Statistical Society: Series D (The Statistician)*, 47(1):183–189, 1998.

[59] I. Hughes and T. Hase. *Measurements and their Uncertainties: A practical guide to modern error analysis.* OUP Oxford, 2010.

[60] Y. Kubo and S. Asano. Magnetic Compton profiles of iron and nickel. *Phys. Rev. B*, 42:4431–4446, Sep 1990.

[61] H. Danan, A. Herr, and A. J. P. Meyer. New Determinations of the Saturation Magnetization of Nickel and Iron. *Journal of Applied Physics*, 39(2):669–670, 1968.

[62] CIAAW. Atomic weights of the elements. `ciaaw.org/atomic-weights.htm`, August 2015.

[63] D. O. Smith. Development of a Vibrating Coil Magnetometer. *Review of Scientific Instruments*, 27(5):261–268, 1956.

[64] Simon Foner. Versatile and Sensitive Vibrating Sample Magnetometer. *Review of Scientific Instruments*, 30(7):548–557, 1959.

[65] J. Goldstein. *Scanning Electron Microscopy and X-ray Microanalysis: Third Edition*. Scanning Electron Microscopy and X-ray Microanalysis. Springer US, 2003.

[66] P. Willmott. *An Introduction to Synchrotron Radiation: Techniques and Applications*. Wiley, 2011.

[67] G. Margaritondo. *Introduction to synchrotron radiation*. Oxford University Press, 1988.

[68] J. Als-Nielsen and D. McMorrow. *Elements of Modern X-ray Physics*. Wiley, 2001.

[69] Aleksandar Gjurchinovski. Relativistic Aberration of Light as a Corollary of the Relativity of Simultaneity. *European Journal of Physics*, 27(4):703, 2006.

[70] Pascal Elleaume. Insertion Devices for the New Generation of Synchrotron Sources: A review (invited). *Review of Scientific Instruments*, 63(1):321–326, 1992.

[71] Herman Winick, George Brown, Klaus Halbach, and John Harris. Wiggler and Undulator Magnets. *Physics Today*, 34:50–63, 1981.

[72] X. M. Marchal, T. Tanaka, and H. Kitamura. An Elliptical Wiggler for SPring-8. *Review of Scientific Instruments*, 66(2):1937–1939, 1995.

[73] Jos Goulon, Pascal Elleaume, and Denis Raoux. Special Multipole Wiggler Design Producing Circularly Polarized Synchrotron Radiation. *Nuclear Instruments and Methods in Physics Research Section A: Accelerators, Spectrometers, Detectors and Associated Equipment*, 254(1):192 – 201, 1987.

[74] G.F. Knoll. *Radiation Detection and Measurement*. John Wiley & Sons, 2010.

[75] D.J. Griffiths. *Introduction to Electrodynamics*. Prentice Hall, 1999.

[76] S. A. Wolf, D. D. Awschalom, R. A. Buhrman, J. M. Daughton, S. von Molnr, M. L. Roukes, A. Y. Chtchelkanova, and D. M. Treger. Spintronics: A Spin-Based Electronics Vision for the Future. *Science*, 294(5546):1488–1495, 2001.

[77] Tanja Graf, Claudia Felser, and Stuart S.P. Parkin. Simple Rules for the Understanding of Heusler Compounds. *Progress in Solid State Chemistry*, 39(1):1 – 50, 2011.

[78] S Fujii, S Sugimura, Ishida, and S Asano. Hyperfine Fields and Electronic Structures of the Heusler Alloys Co_2MnX (X=Al, Ga, Si, Ge, Sn). *Journal of Physics: Condensed Matter*, 2(43):8583, 1990.

[79] Shoji Ishida, Shinpei Fujii, Shoei Kashiwagi, and Setsuro Asano. Search for Half-Metallic Compounds in Co2MnZ (Z=IIIb, IVb, Vb Element). *Journal of the Physical Society of Japan*, 64(6):2152–2157, 1995.

[80] L. Chioncel, Y. Sakuraba, E. Arrigoni, M. I. Katsnelson, M. Oogane, Y. Ando, T. Miyazaki, E. Burzo, and A. I. Lichtenstein. Nonquasiparticle States in Co_2MnSi Evidenced through Magnetic Tunnel Junction Spectroscopy Measurements. *Phys. Rev. Lett.*, 100:086402, Feb 2008.

[81] Markus Meinert, Christoph Friedrich, Günter Reiss, and Stefan Blügel. *GW* study of the half-metallic Heusler compounds Co_2MnSi and Co_2FeSi. *Phys. Rev. B*, 86:245115, Dec 2012.

[82] S. Ishida, T. Masaki, S. Fujii, and S. Asano. Theoretical search for half-metalliic films of Co2MnZ (Z = Si, Ge). *Physica B: Condensed Matter*, 245(1):1 – 8, 1998.

[83] P.J. Webster. Magnetic and Chemical Order in Heusler Alloys containing Cobalt and Manganese. *Journal of Physics and Chemistry of Solids*, 32(6):1221 – 1231, 1971.

[84] T. Daibou, M. Shinano, Y. Sakuraba, M. Oogane, and T. Miyazaki. Tunnel Magnetoresistance Effect in CoFeB/MgO/Heusler Alloys(Co2FeSi, Co2MnSi) Tunnel Junctions. In *Magnetics Conference, 2006. INTERMAG 2006. IEEE International*, pages 724–724, May 2006.

[85] P J Brown, K U Neumann, P J Webster, and K R A Ziebeck. The Magnetization Distributions in some Heusler Alloys Proposed as Half-metallic Ferromagnets. *Journal of Physics: Condensed Matter*, 12(8):1827, 2000.

[86] C. N. Borca, Takashi Komesu, Hae-Kyung Jeong, P. A. Dowben, Delia Ristoiu, Ch. Hordequin, J. P. Nozières, J. Pierre, Shane Stadler, and Y. U. Idzerda. Evidence for Temperature Dependent Moments Ordering in Ferromagnetic NiMnSb(100). *Phys. Rev. B*, 64:052409, Jul 2001.

[87] M. P. Raphael, B. Ravel, Q. Huang, M. A. Willard, S. F. Cheng, B. N. Das, R. M. Stroud, K. M. Bussmann, J. H. Claassen, and V. G. Harris. Presence of Antisite Disorder and its Characterization in the Predicted Half-metal Co_2MnSi. *Phys. Rev. B*, 66:104429, Sep 2002.

[88] R. A. Dunlap and D. F. Jones. Mössbauer-effect study of Sn-impurity-site Hyperfine Fields in the Heusler Alloys Co_2MnZ ($Z = \mathrm{Al}, \mathrm{Ga}, \mathrm{Si}, \mathrm{Ge}, \mathrm{Sn}$). *Phys. Rev. B*, 26:6013–6018, Dec 1982.

[89] Rie Y. Umetsu, Kosei Kobayashi, Asaya Fujita, Ryosuke Kainuma, and Kiyohito Ishida. Phase Stability and Magnetic Properties of {L21} phase in $Co_2Mn(Al_{1-x}Si_x)$ Heusler Alloys. *Scripta Materialia*, 58(9):723 – 726, 2008.

[90] R. A. de Groot, F. M. Mueller, P. G. van Engen, and K. H. J. Buschow. New Class of Materials: Half-Metallic Ferromagnets. *Phys. Rev. Lett.*, 50:2024–2027, Jun 1983.

[91] Lance Ritchie, Gang Xiao, Y. Ji, T. Y. Chen, C. L. Chien, Ming Zhang, Jinglan Chen, Zhuhong Liu, Guangheng Wu, and X. X. Zhang. Magnetic, Structural, and Transport Properties of the Heusler alloys Co_2MnSi and NiMnSb. *Phys. Rev. B*, 68:104430, Sep 2003.

[92] I. Galanakis, P. H. Dederichs, and N. Papanikolaou. Slater-Pauling Behavior and Origin of the Half-metallicity of the Full-Heusler Alloys. *Phys. Rev. B*, 66:174429, Nov 2002.

[93] Mario F. Borunda, H. Hennig, and Eric J. Heller. Ballistic versus Diffusive Transport in Graphene. *Phys. Rev. B*, 88:125415, Sep 2013.

[94] I. I. Mazin. How to Define and Calculate the Degree of Spin Polarization in Ferromagnets. *Phys. Rev. Lett.*, 83:1427–1430, Aug 1999.

[95] M. J. M. de Jong and C. W. J. Beenakker. Andreev Reflection in Ferromagnet-Superconductor Junctions. *Phys. Rev. Lett.*, 74:1657–1660, Feb 1995.

[96] R. J. Soulen, J. M. Byers, M. S. Osofsky, B. Nadgorny, T. Ambrose, S. F. Cheng, P. R. Broussard, C. T. Tanaka, J. Nowak, J. S. Moodera, A. Barry, and J. M. D. Coey. Measuring the Spin Polarization of a Metal with a Superconducting Point Contact. *Science*, 282(5386):85–88, 1998.

[97] Shashi K. Upadhyay, Akilan Palanisami, Richard N. Louie, and R. A. Buhrman. Probing Ferromagnets with Andreev Reflection. *Phys. Rev. Lett.*, 81:3247–3250, Oct 1998.

[98] Y. Ji, G. J. Strijkers, F. Y. Yang, C. L. Chien, J. M. Byers, A. Anguelouch, Gang Xiao, and A. Gupta. Determination of the Spin Polarization of Half-Metallic cro$_2$ by Point Contact Andreev Reflection. *Phys. Rev. Lett.*, 86:5585–5588, Jun 2001.

[99] Yu. S. Dedkov, U. Rüdiger, and G. Güntherodt. Evidence for the Half-metallic Ferromagnetic State of fe$_3$o$_4$ by Spin-resolved Photoelectron Spectroscopy. *Phys. Rev. B*, 65:064417, Jan 2002.

[100] K. P. Kämper, W. Schmitt, G. Güntherodt, R. J. Gambino, and R. Ruf. CrO_2 - A New Half-Metallic Ferromagnet? *Phys. Rev. Lett.*, 59:2788–2791, Dec 1987.

[101] M Fonin, Yu S Dedkov, R Pentcheva, U Rdiger, and G Gntherodt. Spin-resolved Photoelectron Spectroscopy of Fe_3O_4 revisited. *Journal of Physics: Condensed Matter*, 20(14):142201, 2008.

[102] W.H. Wang, M. Przybylski, W. Kuch, L.I. Chelaru, J. Wang, Y.F. Lu, J. Barthel, and J. Kirschner. Spin Polarization of Single-crystalline Co_2MnSi Films Grown by {PLD} on GaAs(0 0 1). *Journal of Magnetism and Magnetic Materials*, 286:336 – 339, 2005. Proceedings of the 5th International Symposium on Metallic Multilayers.

[103] W. H. Wang, M. Przybylski, W. Kuch, L. I. Chelaru, J. Wang, Y. F. Lu, J. Barthel, H. L. Meyerheim, and J. Kirschner. Magnetic Properties and Spin Polarization of

Co_2MnSi Heusler Alloy Thin Films Epitaxially Grown on GaAs(001). *Phys. Rev. B*, 71:144416, Apr 2005.

[104] X. Y. Dong, C. Adelmann, J. Q. Xie, C. J. Palmstrm, X. Lou, J. Strand, P. A. Crowell, J.-P. Barnes, and A. K. Petford-Long. Spin Injection Fromom the Heusler alloy Co_2MnGe into $Al_{0.1}Ga_{0.9}As$-GaAs Heterostructures. *Applied Physics Letters*, 86(10):–, 2005.

[105] G. Hu and Y. Suzuki. Negative Spin Polarization of Fe_3O_4 in Magnetite/Manganite-Based Junctions. *Phys. Rev. Lett.*, 89:276601, Dec 2002.

[106] L. B. Zhao, W. B. Mi, E. Y. Jiang, and H. L. Bai. Spin-polarized Transport of Electrons from Polycrystalline Fe_3O_4 to Amorphous Si. *Applied Physics Letters*, 91(5):–, 2007.

[107] C. M. Fang, G. A. de Wijs, and R. A. de Groot. Spin-polarization in Half-metals (invited). *Journal of Applied Physics*, 91(10):8340–8344, 2002.

[108] J. Schmalhorst, A. Thomas, S. Kämmerer, O. Schebaum, D. Ebke, M. D. Sacher, G. Reiss, A. Hütten, A. Turchanin, A. Gölzhäuser, and E. Arenholz. Transport Properties of Magnetic Tunnel Junctions with Co_2MnSi Electrodes: The Influence of Temperature-dependent Interface Magnetization and Electronic Band Structure. *Phys. Rev. B*, 75:014403, Jan 2007.

[109] Christian Herbort, Elena Arbelo Jorge, and Martin Jourdan. Morphology Induced Magnetoresistance Enhancement of Tunneling Junctions with the Heusler Electrode $Co_2Cr_{0.6}Fe_{0.4}Al$. *Applied Physics Letters*, 94(14):–, 2009.

[110] Y. Sakuraba, M. Hattori, M. Oogane, Y. Ando, H. Kato, A. Sakuma, T. Miyazaki, and H. Kubota. Giant Tunneling Magnetoresistance in Co_2MnSi/AlO/Co_2MnSi Magnetic Tunnel Junctions. *Applied Physics Letters*, 88(19):–, 2006.

[111] M. Jourdan, J. Minr, J. Braun, A. Kronenberg, S. Chadov, B. Balke, A. Gloskovskii, M. Kolbe, H.J. Elmers, G. Schnhense, H. Ebert, C. Felser, and M. Klui. Direct Observation of Half-metallicity in the Heusler compound Co_2MnSi. *Nat Commun*, 5:–, May 2014.

[112] P. J. Hasnip, J. H. Smith, and V. K. Lazarov. Ab initio Studies of Disorder in the full Heusler Alloy $Co_2Fe_xMn_{1-x}Si$. *Journal of Applied Physics*, 113(17):–, 2013.

[113] Yoshio Miura, Kazutaka Nagao, and Masafumi Shirai. Atomic Disorder Effects on Half-metallicity of the Full-Heusler Alloys $Co_2Fe_xMn_{1-x}Si$: A First-principles study. *Phys. Rev. B*, 69:144413, Apr 2004.

[114] B.S.D.Ch.S. Varaprasad, A. Srinivasan, Y.K. Takahashi, M. Hayashi, A. Rajanikanth, and K. Hono. Spin Polarization and Gilbert Damping of $Co_2Fe(Ga_xGe_{1-x})$ Heusler Alloys. *Acta Materialia*, 60(18):6257 – 6265, 2012.

[115] Francis Birch. Finite Elastic Strain of Cubic Crystals. *Phys. Rev.*, 71:809–824, Jun 1947.

[116] M. P. Raphael, B. Ravel, M. A. Willard, S. F. Cheng, B. N. Das, R. M. Stroud, K. M. Bussmann, J. H. Claassen, and V. G. Harris. Magnetic, Structural, and Transport Properties of Thin Film and Single Crystal Co_2MnSi. *Applied Physics Letters*, 79(26):4396–4398, 2001.

[117] S. Amari, R. Mebsout, S. Mabih, B. Abbar, and B. Bouhafs. First-principle Study of Magnetic, Elastic and Thermal Properties of Full Heusler Co_2MnSi. *Intermetallics*, 44(0):26 – 30, 2014.

[118] Gökoglu, G. and Gülseren, O. Electronic Structure of Half-metallic Ferromagnet Co_2MnSi at High-pressure. *Eur. Phys. J. B*, 76(2):321–326, 2010.

[119] S. Picozzi, A. Continenza, and A. J. Freeman. Co_2MnX (X = Si, Ge, Sn) Heusler compounds: An *ab initio* Study of their Structural, Electronic, and Magnetic Properties at Zero and Elevated Pressure. *Phys. Rev. B*, 66:094421, Sep 2002.

[120] Xing-Qiu Chen, R. Podloucky, and P. Rogl. *Ab initio* Prediction of Half-metallic Properties for the Ferromagnetic Heusler Alloys Co_2MSi(M=Ti,V,Cr). *Journal of Applied Physics*, 100(11):–, 2006.

[121] Yasemin Kurtulus, Richard Dronskowski, German D. Samolyuk, and Vladimir P. Antropov. Electronic structure and Magnetic Exchange Coupling in Ferromagnetic Full Heusler Alloys. *Phys. Rev. B*, 71:014425, Jan 2005.

[122] J A Duffy. What we can learn from Magnetic Compton Scattering: Application to the Determination of Spin Polarization. *Journal of Physics: Conference Series*, 443(1):012011, 2013.

[123] Hem Chandra Kandpal, Gerhard H. Fecher, Claudia Felser, and Gerd Schönhense. Correlation in the Transition-Metal-Based Heusler Compounds Co_2MnSi and Co_2FeSi. *Phys. Rev. B*, 73:094422, Mar 2006.

[124] Burak Himmetoglu, Andrea Floris, Stefano de Gironcoli, and Matteo Cococcioni. Hubbard-corrected DFT Energy Functionals: The LDA+U Description of Correlated Systems. *International Journal of Quantum Chemistry*, 114(1):14–49, 2014.

[125] Erik R. Ylvisaker, Warren E. Pickett, and Klaus Koepernik. Anisotropy and Magnetism in the LSDA + U Method. *Phys. Rev. B*, 79:035103, Jan 2009.

[126] S. Picozzi, A. Continenza, and A. J. Freeman. Role of Structural Defects on the Half-metallic Character of Co_2MnGe and Co_2MnSi Heusler Alloys. *Phys. Rev. B*, 69:094423, Mar 2004.

[127] I. Galanakis, K. Özdoğan, B. Aktaş, and E. Şaşşoğlu. Effect of Doping and Disorder on the Half-metallicity of Full Heusler Alloys. *Applied Physics Letters*, 89(4):–, 2006.

[128] H. Pandey, R. Prasad, and R. C. Budhani. Correlation between Site Disorder and Magnetic Moment in Full-Heusler Co_2FeSi. *JPS Conference Proceedings*, 3(017037), 2014.

[129] H. M. Rietveld. A profile refinement method for nuclear and magnetic structures. *Journal of Applied Crystallography*, 2(2):65–71, Jun 1969.

[130] A.C. Larson and R.B. Von Dreele. General Structure Analysis System (GSAS). *Los Alamos National Laboratory Report LAUR*, 86:748, 1994.

[131] Brian H. Toby. *EXPGUI*, a graphical user interface for *GSAS*. *Journal of Applied Crystallography*, 34(2):210–213, Apr 2001.

[132] Yota Takamura, Ryosho Nakane, and Satoshi Sugahara. Quantitative Analysis of Atomic Disorders in Full-Heusler Co_2FeSi Alloy Thin Films using X-ray Diffraction with Co K_α and Cu K_α sources. *Journal of Applied Physics*, 107:09B111, 2010.

[133] A. J. Bradley and J. W. Rodgers. The Crystal Structure of the Heusler Alloys. *Proceedings of the Royal Society of London A: Mathematical, Physical and Engineering Sciences*, 144(852):340–359, 1934.

[134] V. Niculescu, K. Raj, T. J. Burch, and J. I. Budnick. Correlation of the Internal Fields, Magnetic Moments, and Site Preferences in $Fe_{3-x}Mn_xSi$ Alloys. *Phys. Rev. B*, 13:3167–3174, Apr 1976.

[135] E. Prince. International Diffraction Tables for Crystallography, Volumes C and D. *Springer*, 2006.

[136] S. Kunii, T. Kasuya, K. Kadowaki, M. Date, and S.B. Woods. Electron Tunneling into Superconducting YB_6. *Solid State Communications*, 52(7):659 – 661, 1984.

[137] Pavol Szab, Jozef Ka?mar?k, Peter Samuely, Jn Girovsk, Slavomir Gabni, Karol Flachbart, and Takao Mori. Superconducting energy gap of {YB6} studied by point-contact spectroscopy. *Physica C: Superconductivity and its Applications*, 460462, Part 1:626 – 627, 2007. Proceedings of the 8th International Conference on Materials and Mechanisms of Superconductivity and High Temperature SuperconductorsM2S-HTSC {VIII}.

[138] H Nozaki, T Tanaka, and Y Ishizawa. Magnetic Behaviour and Structure Change of GdB_6 Single Crystals at Low Temperatures. *Journal of Physics C: Solid State Physics*, 13(14):2751, 1980.

[139] G.E. Grechnev, A.V. Logosha, A.S. Panfilov, and N.Yu. Shitsevalova. Pressure Effects on Magnetic Properties and Electronic Structure of EuB_6 and GdB_6. *Journal of Alloys and Compounds*, 511(1):5 – 8, 2012.

[140] T. Kasuya, M. Kasaya, K. Takegahara, T. Fujita, T. Goto, A. Tamaki, M. Takigawa, and H. Yasuoka. Mechanisms for Anomalous Properties in SmB_6. *Journal*

of Magnetism and Magnetic Materials, 3134, Part 1:447 – 450, 1983.

[141] G. Li, Z. Xiang, F. Yu, T. Asaba, B. Lawson, P. Cai, C. Tinsman, A. Berkley, S. Wolgast, Y. S. Eo, Dae-Jeong Kim, C. Kurdak, J. W. Allen, K. Sun, X. H. Chen, Y. Y. Wang, Z. Fisk, and Lu Li. Two-dimensional Fermi surfaces in Kondo insulator SmB_6. *Science*, 346(6214):1208–1212, 2014.

[142] T. Komatsubara, N. Sato, S. Kunii, I. Oguro, Y. Furukawa, Y. Ōnuki, and T. Kasuya. Dense Kondo behavior in CeB_6 and its Alloys. *Journal of Magnetism and Magnetic Materials*, 31:368 – 372, 1983.

[143] P. Blum and F. Bertaut. Contribution l'tude des borures teneur leve en bore. *Acta Crystallographica*, 7(1):81–86, 1954.

[144] J.M. Effantin, J. Rossat-Mignod, P. Burlet, H. Bartholin, S. Kunii, and T. Kasuya. Magnetic phase diagram of CeB_6. *Journal of Magnetism and Magnetic Materials*, 4748(0):145 – 148, 1985.

[145] T. Fujita, M. Suzuki, T. Komatsubara, S. Kunii, T. Kasuya, and T. Ohtsuka. Anomalous specific heat of CeB_6. *Solid State Communications*, 35(7):569 – 572, 1980.

[146] G Uimin, Yoshio Kuramoto, and Noboru Fukushima. Mode Coupling Effects on the Quadrupolar Ordering in CeB_6. *Solid State Communications*, 97(7):595 – 598, 1996.

[147] Gennadi Uimin. Quadrupolar and magnetic ordering in CeB_6. *Phys. Rev. B*, 55:8267–8279, Apr 1997.

[148] W.A.C. Erkelens, L.P. Regnault, P. Burlet, J. Rossat-Mignod, S. Kunii, and T. Kasuya. Neutron Scattering Study of the Antiferroquadrupolar Ordering in CeB_6 and $Ce_{0.75}La_{0.25}B_6$. *Journal of Magnetism and Magnetic Materials*, 6364(0):61 – 63, 1987.

[149] Masashi Takigawa, Hiroshi Yasuoka, Takaho Tanaka, and Yoshio Ishizawa. NMR Study on the Spin Structure of CeB_6. *Journal of the Physical Society of Japan*, 52(3):728–731, 1983.

[150] J.-H. Han, M.-T. Tran, and K.-S. Kim. The Kondo Effect Revisited: RG-improved Perturbation Theory based on the Schwinger-Boson Representation. *ArXiv e-prints*, January 2015.

[151] L. Kouwenhoven and L. Glazman. Revival of the Kondo effect. *eprint arXiv:cond-mat/0104100*, April 2001.

[152] A. Takase, K. Kojima, T. Komatsubara, and T. Kasuya. Electrical Resistivity and Magnetoresistance of CeB_6. *Solid State Communications*, 36(5):461 – 464, 1980.

[153] Katsurou Hanzawa and Tadao Kasuya. Antiferro-Quadrupolar Ordering in CeB_6. *Journal of the Physical Society of Japan*, 53(5):1809–1818, 1984.

[154] Ryousuke Shiina, Hiroyuki Shiba, and Peter Thalmeier. Magnetic-Field Effects on Quadrupolar Ordering in a Γ 8-Quartet System CeB_6. *Journal of the Physical Society of Japan*, 66(6):1741–1755, 1997.

[155] Noboru Fukushima and Yoshio Kuramoto. Fluctuation Effects on the Quadrupolar Ordering in Magnetic Field. *Journal of the Physical Society of Japan*, 67(7):2460–2468, 1998.

[156] E. Zirngiebl, B. Hillebrands, S. Blumenröder, G. Güntherodt, M. Loewenhaupt, J. M. Carpenter, K. Winzer, and Z. Fisk. Crystal-field Excitations in CeB_6 studied by Raman and Neutron Spectroscopy. *Phys. Rev. B*, 30:4052–4054, Oct 1984.

[157] Fusayoshi J. Ohkawa. Orbital Antiferromagnetism in CeB_6. *Journal of the Physical Society of Japan*, 54(10):3909–3914, 1985.

[158] Hironori Nakao, Ko ichi Magishi, Yusuke Wakabayashi, Youichi Murakami, Kuniyuki Koyama, Kazuma Hirota, Yasuo Endoh, and Satoru Kunii. Antiferro-Quadrupole Ordering of CeB_6 Studied by Resonant X-Ray Scattering. *Journal of the Physical Society of Japan*, 70(7):1857–1860, 2001.

[159] J.X. Boucherle and J. Schweizer. Magnetic Form Factor in Anomalous Intermetallic Ce Compounds. *Physica B+C*, 130(1):337 – 346, 1985.

[160] Masahiro Saitoh, Noriko Okada, Eiji Nishibori, Hiroyuki Takagiwa, Tetsuya Yokoo, Masakazu Nishi, Kazuhisa Kakurai, Satoru Kunii, Masaki Takata, Makoto Sakata, and Jun Akimitsu. Anomalous Spin Density Distribution in CeB_6. *Journal of the Physical Society of Japan*, 71(10):2369–2372, 2002.

[161] F Givord, J-X Boucherle, P Burlet, B Gillon, and S Kunii. Non-anomalous Magnetization Density Distribution in CeB_6. *Journal of Physics: Condensed Matter*, 15(19):3095, 2003.

[162] Katsurou Hanzawa. Spin Density on B Sites and Magnetic Structure Factors of CeB_6. *Journal of the Physical Society of Japan*, 70(7):1900–1903, 2001.

[163] Hoyoung Jang, G. Friemel, J. Ollivier, A. V. Dukhnenko, N. Yu. Shitsevalova, V. B. Filipov, B. Keimer, and D. S. Inosov. Intense Low-energy Ferromagnetic Fluctuations in the Antiferromagnetic Heavy-fermion Metal CeB_6. *Nat Mater*, 13(7):682–687, July 2014.

[164] G. Friemel, Yuan Li, A.V. Dukhnenko, N.Y. Shitsevalova, N.E. Sluchanko, A. Ivanov, V.B. Filipov, B. Keimer, and D.S. Inosov. Resonant Magnetic Exciton Mode in the Heavy-fermion Antiferromagnet CeB_6. *Nat Commun*, 3:830–, May 2012.

[165] M.J. Cooper, J.A. Duffy, Z.F. Banfield, A.M. Bebb, L. Blaauw, C. Shenton-Taylor, C. Steer, and J.W. Taylor. Compton scattering studies of 4f ferromagnetism. *Radiation Physics and Chemistry*, 75(11):1638 – 1645, 2006. Proceedings of the 20th International Conference on X-ray and Inner-Shell Processes 4-8 July 2005, Melbourne, Australia Proceedings of the 20th International Conference on X-ray and Inner-Shell Processes.

[166] Y. Tanaka, U. Staub, K. Katsumata, S. W. Lovesey, J. E. Lorenzo, Y. Narumi, V. Scagnoli, S. Shimomura, Y. Tabata, Y. Onuki, Y. Kuramoto, A. Kikkawa, T. Ishikawa, and H. Kitamura. Direct and Quantitative Determination of the Orbital Ordering in CeB_6 by X-ray Diffraction. *EPL (Europhysics Letters)*, 68(5):671, 2004.

[167] M B Suvasini, G Y Guo, W M Temmerman, G A Gehring, and M Biasini. The Fermi surface of CeB_6. *Journal of Physics: Condensed Matter*, 8(38):7105, 1996.

[168] Sandeep, M P Ghimire, D P Rai, P K Patra, A K Mohanty, and R K Thapa. Study of Bulk Modulus, Volume, Energy, Lattice Parameters and Magnetic Moments in Rare Earth Hexaborides using Density Functional Theory. *Journal of Physics: Conference Series*, 377(1):012084, 2012.

[169] H. Ebert. Two Ways to Perform Spin-polarized Relativistic Linear Muffin-Tin-Orbital Calculations. *Phys. Rev. B*, 38:9390–9397, Nov 1988.

[170] Yoshichika Ōnuki, Takemi Komatsubara, Paul H. P. Reinders, and Mike Springford. Fermi Surface and Cyclotron Mass of CeB_6. *Journal of the Physical Society of Japan*, 58(10):3698–3704, 1989.

[171] M. Biasini, H. M. Fretwell, S. B. Dugdale, M. A. Alam, Y. Kubo, H. Harima, and N. Sato. Positron Annihilation Study of the Electronic Structure of LaB_6 and CeB_6. *Phys. Rev. B*, 56:10192–10199, Oct 1997.

[172] S. Huzinaga and B. Miguel. A Comparison of the Geometrical Sequence Formula and the Well-tempered Formulas for Generating {GTO} Basis Orbital Exponents. *Chemical Physics Letters*, 175(4):289 – 291, 1990.

[173] Sigeru Huzinaga and Mariusz Klobukowski. Well-tempered Gaussian basis sets for the Calculation of Matrix HartreeFock Wavefunctions. *Chemical Physics Letters*, 212(34):260 – 264, 1993.

[174] Ian Maskery. *Spin densities in 4f and 3d magnetic systems*. PhD thesis, University of Warwick, 2013.

[175] J. Häglund. Fixed-spin-moment Calculations on BCC and FCC Iron using the Generalized Gradient Approximation. *Phys. Rev. B*, 47:566–569, Jan 1993.

[176] K Schwarz and P Mohn. Itinerant Metamagnetism in YCO_2. *Journal of Physics F: Metal Physics*, 14(7):L129, 1984.

[177] Tanju Gürel and Resul Eryiğit. *Ab initio* Lattice Dynamics and Thermodynamics of Rare-earth Hexaborides LaB_6 and CeB_6. *Phys. Rev. B*, 82:104302, Sep 2010.

[178] Seiji Niitaka, Hiroshi Kageyama, Masaki Kato, Kazuyoshi Yoshimura, and Koji Kosuge. Synthesis, Crystal Structure, and Magnetic Properties of New One-Dimensional Oxides Ca_3CoRhO_6 and Ca_3FeRhO_6. *Journal of Solid State Chemistry*, 146(1):137 – 143, 1999.

[179] Helmer Fjellvg, Egil Gulbrandsen, Siv Aasland, Arne Olsen, and Bjrn C. Hauback. Crystal Structure and Possible Charge Ordering in One-Dimensional $Ca_3Co_2O_6$. *Journal of Solid State Chemistry*, 124(1):190 – 194, 1996.

[180] Hiroshi Kageyama, Kazuyoshi Yoshimura, Koji Kosuge, Hiroyuki Mitamura, and Tsuneaki Goto. Field-Induced Magnetic Transitions in the One-Dimensional Compound $Ca_3Co_2O_6$. *Journal of the Physical Society of Japan*, 66(6):1607–1610, 1997.

[181] S. Aasland, H. Fjellvg, and B. Hauback. Magnetic Properties of the One Dimensional $Ca_3Co_2O_6$. *Solid State Communications*, 101(3):187 – 192, 1997.

[182] R. Vidya, P. Ravindran, H. Fjellvåg, A. Kjekshus, and O. Eriksson. Tailor-Made Electronic and Magnetic Properties in One-Dimensional Pure and Y-Substituted $Ca_3Co_2O_6$. *Phys. Rev. Lett.*, 91:186404, Oct 2003.

[183] D. Flahaut, A. Maignan, S. Hébert, C. Martin, R. Retoux, and V. Hardy. Chromium Site Selective Substitution in $Ca_3Co_2O_6$: Influence on the Magnetic Properties of an Ising-like Triangular Lattice. *Phys. Rev. B*, 70:094418, Sep 2004.

[184] A. Maignan, V. Hardy, S. Hebert, M. Drillon, M. R. Lees, O. Petrenko, D. Mc K. Paul, and D. Khomskii. Quantum Tunneling of the Magnetization in the Ising Chain Compound $Ca_3Co_2O_6$. *J. Mater. Chem.*, 14:1231–1234, 2004.

[185] V. Hardy, D. Flahaut, M. R. Lees, and O. A. Petrenko. Magnetic Quantum Tunneling in $Ca_3Co_2O_6$ Studied by AC Susceptibility: Temperature and Magnetic-field Dependence of the Spin-relaxation Time. *Phys. Rev. B*, 70:214439, Dec 2004.

[186] E. V. Sampathkumaran, N. Fujiwara, S. Rayaprol, P. K. Madhu, and Y. Uwatoko. Magnetic Behavior of Co ions in the Exotic Spin-chain Compound $Ca_3Co_2O_6$ from ^{59}Co NMR Studies. *Phys. Rev. B*, 70:014437, Jul 2004.

[187] V. Hardy, S. Lambert, M. R. Lees, and D. McK. Paul. Specific Heat and Magnetization Study on Single Crystals of the Frustrated Quasi-one-dimensional Oxide $Ca_3Co_2O_6$. *Phys. Rev. B*, 68:014424, Jul 2003.

[188] M.-H Whangbo, D Dai, H.-J Koo, and S Jobic. Investigations of the Oxidation States and Spin Distributions in $Ca_3Co_2O_6$ and Ca_3CoRhO_6 by Spin-polarized Electronic Band Structure Calculations. *Solid State Communications*, 125(78):413 – 417, 2003.

[189] K. Takubo, T. Mizokawa, S. Hirata, J.-Y. Son, A. Fujimori, D. Topwal, D. D. Sarma, S. Rayaprol, and E.-V. Sampathkumaran. Electronic Structure of Ca_3XO_6 (X = Co, Rh, Ir) Studied by X-ray Photoemission Spectroscopy. *Phys. Rev. B*, 71:073406, Feb 2005.

[190] V. Eyert, C. Laschinger, T. Kopp, and R. Frsard. Extended Moment Formation and Magnetic Ordering in the Trigonal Chain Compound $Ca_3Co_2O_6$. *Chemical Physics Letters*, 385(34):249 – 254, 2004.

[191] Hua Wu, M. W. Haverkort, Z. Hu, D. I. Khomskii, and L. H. Tjeng. Nature of Magnetism in $Ca_3Co_2O_6$. *Phys. Rev. Lett.*, 95:186401, Oct 2005.

[192] Hiroshi Kageyama, Kazuyoshi Yoshimura, Koji Kosuge, Masaki Azuma, Mikio Takano, Hiroyuki Mitamura, and Tsuneaki Goto. Magnetic Anisotropy of $Ca_3Co_2O_6$ with Ferromagnetic Ising Chains. *Journal of the Physical Society of Japan*, 66(12):3996–4000, 1997.

[193] Raymond Frésard, Christian Laschinger, Thilo Kopp, and Volker Eyert. Origin of Magnetic Interactions in $Ca_3Co_2O_6$. *Phys. Rev. B*, 69:140405, Apr 2004.

[194] L. C. Chapon. Origin of the Long-wavelength Magnetic Modulation in $Ca_3Co_2O_6$. *Phys. Rev. B*, 80:172405, Nov 2009.

[195] S. Agrestini, L. C. Chapon, A. Daoud-Aladine, J. Schefer, A. Gukasov, C. Mazzoli, M. R. Lees, and O. A. Petrenko. Nature of the Magnetic Order in $Ca_3Co_2O_6$. *Phys. Rev. Lett.*, 101:097207, Aug 2008.

[196] S. Agrestini, C. Mazzoli, A. Bombardi, and M. R. Lees. Incommensurate Magnetic Ground State Revealed by Resonant X-ray Scattering in the Frustrated Spin System $Ca_3Co_2O_6$. *Phys. Rev. B*, 77:140403, Apr 2008.

[197] Maignan, A., Michel, C., Masset, A. C., Martin, C., and Raveau, B. Single Crystal Study of the One Dimensional $Ca_3Co_2O_6$ Compound: Five Stable Configurations for the Ising Triangular Lattice. *Eur. Phys. J. B*, 15(4):657–663, 2000.

[198] B. Raquet, M. N. Baibich, J. M. Broto, H. Rakoto, S. Lambert, and A. Maignan. Hopping Conductivity in One-dimensional $Ca_3Co_2O_6$ Single Crystals. *Phys. Rev. B*, 65:104442, Mar 2002.

[199] Antoine Maignan, Sylvie Hbert, Christine Martin, and Delphine Flahaut. One Dimensional Compounds with Large Thermoelectric Power: $Ca_3Co_2O_6$ and Ca_3CoMO_6 with M=Ir^{4+} and Rh^{4+}. *Materials Science and Engineering: B*, 104(3):121 – 125, 2003. Proceedings of the International Workshop on the Applications of Oxide Materials.

[200] Antoine Villesuzanne and Myung-Hwan Whangbo. Comparative Electronic Band Structure Study of the Intrachain Ferromagnetic versus Antiferromagnetic Coupling in the Magnetic Oxides $Ca_3Co_2O_6$ and Ca_3FeRhO_6. *Inorganic Chemistry*, 44(18):6339–6345, 2005. PMID: 16124813.

[201] J. Zaanen, G. A. Sawatzky, and J. W. Allen. Band Gaps and Electronic Structure of Transition-metal Compounds. *Phys. Rev. Lett.*, 55:418–421, Jul 1985.

[202] S. Agrestini, C. L. Fleck, L. C. Chapon, C. Mazzoli, A. Bombardi, M. R. Lees, and O. A. Petrenko. Slow Magnetic Order-Order Transition in the Spin Chain Antiferromagnet $Ca_3Co_2O_6$. *Phys. Rev. Lett.*, 106:197204, May 2011.

[203] C. L. Fleck, M. R. Lees, S. Agrestini, G. J. McIntyre, and O. A. Petrenko. Field-driven Magnetisation Steps in $Ca_3Co_2O_6$: A Single-crystal Neutron-diffraction

Study. *EPL (Europhysics Letters)*, 90(6):67006, 2010.

[204] G. Allodi, R. De Renzi, S. Agrestini, C. Mazzoli, and M. R. Lees. NMR study of magnetic order, metamagnetic transitions, and low-temperature spin freezing in $Ca_3Co_2O_6$. *Phys. Rev. B*, 83:104408, Mar 2011.

[205] C. Mazzoli, A. Bombardi, S. Agrestini, and M.R. Lees. Resonant X-ray Scattering Study of Ground State: Preliminary Results of Magnetic Field Effects. *Physica B: Condensed Matter*, 404(19):3042 – 3044, 2009. Proceedings of the International Conference on Strongly Correlated Electron Systems.

[206] A. Bombardi, C. Mazzoli, S. Agrestini, and M. R. Lees. Resonant X-ray Scattering Investigation of the Multipolar Ordering in $Ca_3Co_2O_6$. *Phys. Rev. B*, 78:100406, Sep 2008.

[207] Matthew Butchers. *Magnetic Compton Scattering Studies of Novel Phases.* PhD thesis, University of Warwick, 2013.

[208] Akihisa Koizumi, Satoru Miyaki, Yukinobu Kakutani, Hiroyasu Koizumi, Nozomu Hiraoka, Kenji Makoshi, Nobuhiko Sakai, Kazuma Hirota, and Yoichi Murakami. Study of the e_g Orbitals in the Bilayer Manganite $La_{2-2x}Sr_{1+2x}Mn_2O_7$ by Using Magnetic Compton-Profile Measurement. *Phys. Rev. Lett.*, 86:5589–5592, Jun 2001.

[209] Ansgar Schäfer, Christian Huber, and Reinhart Ahlrichs. Fully Optimized Contracted Gaussian Basis Sets of Triple Zeta Valence Quality for Atoms Li to Kr. *The Journal of Chemical Physics*, 100(8):5829–5835, 1994.

[210] P. Atkins and J. de Paula. *Atkins' Physical Chemistry.* OUP Oxford, 2014.